

DISS. ETH NO. 25423

**Combinatorial investigation of hardening
mechanisms in compositional gradient
and multilayer thin films**

A thesis submitted to attain the degree of
DOCTOR OF SCIENCES of ETH ZURICH
(Dr. sc. ETH Zurich)

presented by

KEITH BENNETT THOMAS

M.Sc., Friedrich-Alexander Universität Erlangen-Nürnberg

born on 12.08.1988

citizen of

the United States of America

accepted on the recommendation of

Prof. Dr. Ralph Spolenak, examiner

Dr. Johann Michler, co-examiner

Prof. Dr. Dipl.-Ing. Dr. mont. Daniel Kiener, co-examiner

Prof. Dr. Jörg F. Löffler, co-examiner

2018

"...it was a cherished experience. I feel I got the chance to see the inner workings of the grand order of things. In the overall scheme of things, it proves that men can do about anything they want to if they work hard enough at it, and I knew that I could do it, and that's a good thought. And that leads, of course, to a strong suspicion that everybody else can do it if they want to."

-Scott Carpenter, reflecting on his 1962 orbital spaceflight

Abstract

A combinatorial experimental approach was used to investigate the mechanical properties of thin films deposited by sputtering. Nanoindentation and micropillar compression experiments performed at various temperatures and strain rates were used to evaluate the operative deformation mechanisms within the films as a function of their architecture and the testing conditions. Three classes of films were investigated: lateral compositional gradient films, periodic bilayer multilayer films, and nanoparticle-dispersion metal matrix composites. A number of different materials systems were investigated in addition to the copper-tungsten combination used for all of the listed film architectures.

Lateral compositional gradient films were prepared via co-sputtering and by annealing thickness-gradient multilayer films. Both binary (two-component) and ternary (three-component) compositional gradient films were deposited and investigated. Nanoindentation was used to map the hardness and reduced modulus of these films across large-area substrates. In general a simple rule-of-mixtures is sufficient to predict the modulus of a compositional gradient film, while the hardness can be evaluated using a superposition of various hardening mechanisms. Metastable solid solutions were observed in the Cu-W films. Laser ablation experiments and optical reflectometry experiments were performed on the Al-Cu-Ni compositional gradient film and demonstrate the utility of the combinatorial approach beyond mechanical characterization.

Multilayer thin films with incoherent interfaces were also investigated. Material systems included Cu-W, Cu-TiN, and Mg-Nb. A combinatorial approach utilizing thickness-gradient films was applied to investigate the role of both layer thickness and the ratio of film components on the mechanical properties of the film. Previous experiments in the literature have addressed only the effect of layer thickness while largely neglecting the influence of non-equal volumetric ratios. The combinatorial approach used here highlights the potential for investigating a larger number of parameters influencing the mechanical behavior of multilayer thin films with only a modest increase in experimental effort. Elevated temperature micropillar compression experiments were performed on both Cu-TiN and Mg-Nb thin films. In the case of both materials systems diffusion-based deformation mechanisms are shown to dominate material plasticity at elevated temperatures, a novel finding in a field where deformation behavior has been classically explained using dislocation-based deformation mechanisms. Cryogenic tests were also performed on the Mg-Nb multilayer films and revealed the onset of brittle fracture within BCC-magnesium at low temperatures.

Finally, a co-deposition method for preparing nanoparticles dispersed in a metal matrix composite is presented. While the nanoparticles do not have any discernable impact on the strength of the film, they do aid in the preservation of a nanocrystalline microstructure at elevated temperatures through grain boundary pinning. The benefits of a nanocrystalline microstructure can be thereby maintained at temperatures beyond those for which such materials are typically stable. The above methods for achieving material strengthening are discussed and placed into the context of existing thin film mechanics literature. Design strategies which can be applied to provide even further enhancement to the mechanical properties of thin films are discussed.

Zusammenfassung

Eine kombinatorische Vorgehensweise wurde verwendet um die mechanischen Eigenschaften von Dünnschichten, die durch Kathodenzerstäubung erzeugt wurden, zu untersuchen. Nanoindentation und Mikrokompression wurden bei verschiedenen Temperaturen und Dehnraten durchgeführt um die aktiven Verformungsmechanismen in den Dünnschichten als Funktion des Schichtaufbaus und experimentellen Bedingungen zu bestimmen. Drei verschiedene Dünnschichtarchitekturen wurden dabei untersucht: Schichten mit lateralen Gradienten in der chemischen Zusammensetzung, periodische Multilagen und Nanopartikel-verstärkte Komposite mit einer metallischen Matrix. Eine Vielzahl von verschiedenen Materialsystemen wurde untersucht sowie Kupfer-Wolfram für alle Schichtarchitekturen.

Die Schichten mit lateralen Gradienten in der chemischen Zusammensetzung wurden durch simultane Kathodenzerstäubung und das anschließende Wärmebehandlung von Multilagenschichten hergestellt. Binäre (zwei Komponenten) und ternäre (drei Komponenten) Schichten wurden hergestellt und untersucht. Nanoindentation wurde verwendet um die Härte und Elastizitätsmodul über großflächige Substrate zu messen. Im Allgemeine reicht eine einfache Mischungsregel um das Modul der Elastizität zu beschreiben während die Härte durch die Superpositionierung von verschiedenen Härtemechanismen beschrieben wird. Metastabile Mischkristalle wurden in den Cu-W Dünnschichten vorgefunden. Laser-Ablations-Versuche und optische Reflektometrie wurden auf den Al-Cu-Ni Proben durchgeführt und zeigen die vielfältige Einsetzbarkeit der kombinatorischen Vorgehensweise.

Multilagen Dünnschichten mit inkohärenten Grenzflächen wurden auch untersucht. Materialsysteme erfassten Cu-W, Cu-TiN und Mg-Nb. Eine kombinatorische Vorgehensweise basierend auf Dickengradienten wurde verwendet um die Rolle von einzelnen Schichten sowie des Volumenverhältnisses zwischen den Komponenten auf die mechanischen Eigenschaften der Schicht zu bestimmen. Experimentelle Versuche die schon in der Literatur beschrieben sind setzten sich meistens nur mit dem Effekt von Schichtdicken auseinander, während das Volumenverhältnis weitgehend vernachlässigt wird. Hoch-Temperatur Mikrosäulen Kompressionsversuche wurden an Cu-TiN sowie Mg-Nb Multilagenbeschichtungen. In beiden Materialsystemen wurden diffusionsbasierte Deformationsmechanismen nachgewiesen die plastische Verformung des Materials zu dominieren. Da alle herkömmlichen Modelle für die mechanischen Eigenschaften von Multilagen auf Versetzungsbewegungen basieren, ist dies ein neues und bisher wenig erforschtes Phänomen. Tieftemperaturversuche wurden auch an den Mg-Nb Multilagen durchgeführt um den Übergang von plastischem zu sprödem Verhalten des Materials zu demonstrieren.

Schlussendlich ist auch eine Methode zur Herstellung von Nanopartikel-verstärktem Metall-Matrix-Kompositen vorgestellt. Bei Raumtemperatur haben die Nanopartikel keinen Einfluss auf die mechanischen Eigenschaften der Beschichtung da sie von der hohen Dichte an Zwillingsgrenzen dominiert wird. Bei erhöhten Temperaturen wirken die Nanopartikel stabilisierend auf die Kornstruktur durch den sogenannten „Zener-Pinning“ Effekt. Die erwünschten Eigenschaften von der nanokristallinen Mikrostruktur können deshalb auch bei höheren Temperaturen ausgenutzt werden. Zum Schluss werden die oben genannten Methoden für Materialverstärkung diskutiert und im Kontext der vorhandenen Literatur verglichen. Strategien um noch höhere mechanische Festigkeiten zu erreichen werden diskutiert.

Contents

1	Introduction	8
1.1	Combinatorial Science	8
1.2	Micro- and Nanomechanical Testing	9
1.3	Thesis Objectives	10
1.4	Thesis Outline.....	11
2	Background in Crystal Mechanics and Mechanical Testing.....	12
2.1	Crystalline Materials	12
2.1.1	Point Defects	12
2.1.2	Line Defects	13
2.1.3	Area Defects	15
2.1.4	Volume Defects	16
2.2	Deformation Mechanisms.....	16
2.2.1	Dislocation-based Mechanisms.....	16
2.2.2	Diffusion-based Mechanisms	18
2.2.3	Grain-based Mechanisms.....	19
2.2.4	Deformation Mechanism Maps	20
2.3	Strengthening Mechanisms.....	21
2.4	Mechanical Testing Strategies.....	23
2.4.1	Variable Temperature Mechanical Testing.....	23
2.4.2	Variable Strain Rate Mechanical Testing.....	24
2.4.3	Activation Volume and Activation Energy.....	24
3	Experimental Methods.....	26
3.1	Film Deposition	26
3.1.1	Co-Sputtered Compositional Gradient Films	29
3.1.2	Multilayer Thin Films	30
3.1.3	Nanoparticle Condensation	30
3.1.4	Focused Ion Beam Milling.....	31
3.2	Material Selection.....	32
3.3	Material Characterization	33
3.3.1	Chemical Composition	33
3.3.2	Microstructure	34

3.3.3	Mechanical Properties	34
4	Compositional Gradient Films	35
4.1	Copper-Tungsten	35
4.1.1	Introduction	35
4.1.2	Materials and methods	37
4.1.3	Results.....	39
4.1.4	Discussion.....	42
4.1.5	Conclusions.....	47
4.2	Aluminum-Copper-Nickel	48
4.2.1	Introduction	48
4.2.2	Experimental.....	48
4.2.3	Results.....	50
4.2.4	Discussion.....	55
4.2.5	Conclusions.....	56
5	Multilayer Thin Films	58
5.1	Copper-Tungsten	59
5.1.1	Introduction	59
5.1.2	Experimental.....	60
5.1.3	Results and discussion.....	62
5.1.4	Conclusions.....	66
5.2	Copper-Titanium Nitride	67
5.2.1	Introduction	67
5.2.2	Experimental.....	67
5.2.3	Results.....	69
5.2.4	Discussion.....	77
5.2.5	Conclusions.....	80
5.3	Magnesium-Niobium.....	81
5.3.1	Introduction	81
5.3.2	Experimental.....	81
5.3.3	Results.....	84
5.3.4	Discussion.....	92
5.3.5	Conclusions.....	95

6	Nanoparticle Composite Films	97
6.1	Introduction	97
6.2	Experimental	98
6.3	Results	100
6.3.1	Tungsten nanoparticle deposition	100
6.3.2	Thickness gradient sample	100
6.3.3	Nanoparticle density gradient sample	102
6.3.4	High particle density in thin films (100 nm)	105
6.3.5	High particle density in thick films (1 μ m)	107
6.4	Discussion	108
6.5	Conclusions and Outlook	109
7	Strengthening Mechanisms in Sputtered Films	111
7.1	Co-Sputtered Thin Films	113
7.1.1	Rule-of-Mixtures	113
7.1.2	Solid Solution Strengthening	113
7.1.3	Grain Size Strengthening	113
7.1.4	Superposition of Hardening Mechanisms	114
7.2	Multilayer Thin Films	114
7.2.1	Temperature-Dependent Deformation in Multilayers	115
7.3	Nanoparticle Metal Matrix Composites	118
8	Summary and Outlook	120
9	Bibliography	123
	Curriculum Vitae	133
	Personal Information	133
	Education	133
	Publications and Presentations	134
	Peer-reviewed journal publications	134
	Oral presentations	135
	Poster presentations	135

List of Abbreviations

AFM – atomic force microscope
AR – aspect ratio
BCC – body-centered cubic
CLS – confined layer slip
CRSS – critical resolved shear stress
CSR – continuous strain rate
CTE – coefficient of thermal expansion
DBTT – ductile-to-brittle transition temperature
DMM – deformation mechanism map
DoE – design of experiments
EDX – energy-dispersive X-ray spectroscopy
FCC – face-centered cubic
FCDC – face-centered diamond cubic
FEM – finite element method
FIB – focused ion beam
FWHM – full width at half maximum
GBS – grain boundary sliding
GND – geometrically necessary dislocation
HAADF – high-angle annular dark-field imaging
HCP – hexagonal close pack
HIPIMS – high-power impulse magnetron sputtering
HP – Hall-Petch
MMC – metal matrix composite
PLC – power law creep
PVD – physical vapor deposition
RF – radio frequency
RT – room temperature
ROM – rule of mixtures
SAD – selected area diffraction
SCCM – standard cubic centimeters per minute
SEM – scanning electron microscope
SFE – stacking fault energy
SPD – severe plastic deformation
SRJ – strain rate jump
SZM – structure zone model
TAC – tip-to-area calibration
TEM – transmission electron microscope
TGC – terminated gas condensation
XRD – X-ray diffraction
XRF – X-ray fluorescence
ZAF – atomic number, absorption, fluorescence

1 Introduction

1.1 Combinatorial Science

The scientific method is an iterative process of observation, experimentation, and evaluation used to gain understanding of the world around us. Historically a small number of simple experiments have been sufficient to obtain insight into many natural phenomena, but as the complexity of the investigated subject increases, so do the experimental demands. Combinatorial science was developed to fulfill this need to perform large numbers of experiments with a high degree of automation. Samples are produced in parallel to minimize the experimental effort required while rapid, automatable characterization techniques are used to quickly obtain the information of interest. High-throughput screening, a branch of combinatorial science, is already widely implemented in the drug development and other biological fields. Similar approaches have begun to gain traction in materials science, particularly in the investigation of thin film properties where only very small volumes of sample are required for characterization [1]. With such approaches the possibilities for discovery through experimental work are greatly expounded by drastic reduction in the time and effort needed for sample preparation and characterization.

The samples most frequently used in combinatorial materials science are thin films with a large lateral variation in chemical composition, commonly known as materials libraries. The most common and convenient method for preparing materials libraries is co-deposition, where multiple elements are simultaneously deposited onto large area substrates. Sputtering is the preferred method of deposition as it is more stable and easily controlled than other physical vapor deposition (PVD) methods like evaporation. Large substrates are used to maximize the amount of the binary or ternary phase diagram which can be covered by a single substrate. Most suitable deposition systems can readily deposit more than half of a binary diagram or one quarter of a ternary diagram [2], though the exact performance depends on the deposition flux variation profile. Binary and ternary materials libraries are the most common, though higher order systems can also be realized through the incorporation of additional sputter targets.

Electron beam evaporation has been used to deposit ternary materials libraries onto large steel and molybdenum film substrates as early as 1965 [3]. Substrate heating was employed to ensure that equilibrium phases formed during deposition. While samples could be prepared in an expedient fashion, the absence of rapid characterization techniques for chemical composition and crystal structure prevented the method from immediately gaining popularity. Co-deposition was soon adapted to sputtering to deposit both binary and ternary thin film material libraries as improved control over deposition rate is provided. Using known sputter flux profiles, the absence of a rapid means for chemical composition characterization could be somewhat circumvented by using sparse film thickness measurements and known sputter flux profiles to locally calculate the chemical composition of the film. The superconducting transition temperature and electrical resistivity across 70% of the Mg-Mo binary phase diagram was determined in this manner [4].

The chemical composition of thin films can now be quickly determined in an automated fashion using a variety of techniques, including X-ray fluorescence (XRF), energy-dispersive X-ray spectroscopy (EDX), and electron probe microanalysis (EPMA). With rapid means available for sample preparation and chemical analysis, modern research focuses on the development of other suitable characterization techniques and approaches to evaluate the large quantity of data produced by combinatorial techniques [5].

1.2 Micro- and Nanomechanical Testing

Mechanical testing is perhaps the most fundamental branch of materials characterization as the mechanical properties of a material often dictate the structural and engineering applications for which a given material is suited. A number of common testing strategies have been developed which vary according to the type of mechanical property to be determined and the sample geometry. Compression, tensile, and indentation experiments are described below as they are the large-scale tests most readily adaptable for smaller specimens.

Indentation is perhaps the most prevalent mechanical test owing to its simplicity, quickness, and nearly universal applicability to a large number of samples. The absence of sample preparation, however, comes at a cost of a complex stress state within the sample and sometimes challenging interpretation. Nanoindentation is the local extension of conventional indentation applied to a much smaller scale. In principle the tests are identical in the respect that both use a hard indenter to penetrate the sample, but the data acquisition for the two differs greatly. Conventional indentation relies upon optical measurement of the residual impression left in the sample after indentation whereas nanoindentation relies on instrumentation to monitor the force applied to the indenter and the indentation depth during the indentation process itself. Knowledge of the exact indenter tip shape is needed to calculate the sample hardness and a reduced elastic modulus.

Micropillar compression is analogous to conventional compression experiments, but also has several important differences. Samples of a defined geometry are typically prepared using focused ion beam (FIB) milling. Standard test specimens are cylindrical pillars, though square cross-sections and other specimen geometries are sometimes used. The conventional annular milling strategy, where the ion beam is orthogonal to the sample surface, results in pillar taper and damage to the pillar surface in the form of implanted gallium atoms, dislocations, surface amorphization, and a number of other potential defects. Another important difference between conventional and microscale micropillar compression is that the test apparatus is only in direct contact with the upper surface of the micropillar. The micropillar thin film is supported from below by a substrate, adhesive, and mounting stub. Each of these additional elements increases the compliance of the test apparatus and must be accounted for. This is especially critical for the pedestal, the portion of the substrate which is inevitably included in the micropillar to some degree.

Micro- and nanomechanical testing are the logical extension of macroscale testing for miniaturized parts. Thin film coatings, integrated circuits (ICs), microelectromechanical systems (MEMS), and many other small-scale devices rely on the mechanical robustness of components smaller than those which can be tested directly using conventional techniques. It is typically not possible to simply extrapolate the mechanical properties obtained at larger scales since material properties can be radically different at small scales. In the case of combinatorial investigations the samples produced are of a very small size and there is simply not enough sample material produced to rely on conventional mechanical testing methods. Small scale testing methods like nanoindentation and micropillar compression are ideally suited for extracting the mechanical properties of small volumes of material.

1.3 Thesis Objectives

The core aim of this thesis is to apply a combinatorial approach to investigating the mechanical properties of compositional gradient and multilayer thin films. In order to achieve this overarching target, the following concrete objectives are realized:

- Combinatorial methods are developed as a useful strategy for testing the mechanics of thin films. A shutter system is developed and implemented which permits an alternative strategy for producing complete materials libraries.
- Complex film architectures are produced through advanced sputtering techniques. These include metastable solid solutions of otherwise immiscible materials, periodic bilayer multilayer films, a multilayer film containing a pseudomorphic phase stabilized by an epitaxial interface, and a nanoparticle-reinforced metal matrix composite (MMC).
- The mechanical properties of the deposited films are investigated using both nanoindentation and micropillar compression.
- Variable temperature micropillar compression experiments are performed from cryogenic temperatures to elevated temperatures of 250°C.
- Transient testing techniques including strain rate jumps (SRJs), stress relaxation, and creep experiments are implemented to gain insight into operative deformation mechanisms.
- The usefulness of established hardening models for describing the mechanics of novel film architectures is evaluated. Where deficiencies are found, an attempt is made to reconcile the experimental data with alternative models.

The copper-tungsten materials system was used to investigate all three of the film architectures discussed in this work, namely compositional gradient films, multilayer films, and nanoparticle metal matrix composites. Copper and tungsten are mutually insoluble across their entire range of compositions and possess widely differing materials properties. The insolubility is critical since it enables the investigation of both metastable phases and film architectures where clearly defined interfaces between two constituent materials are required. Copper and tungsten are readily distinguishable from one another via electron microscopy and X-ray techniques due to the large difference in atomic number, so the chemical composition of the deposited films can be readily determined with a high degree of certainty. A number of potential commercial applications for copper-tungsten materials exist as well, most notably as high-voltage electrical contacts where erosion through sparking and abrasion is of concern. There is also interest in using copper-tungsten materials as radiation-hard, thermally conductive components for nuclear reactors. In short, the copper-tungsten system is an ideal model system for understanding many of the interface- and solubility-related effects addressed in this work. Other materials systems are investigated as well for the various film architectures as an extension of the applicability of findings from the unifying copper-tungsten system to other materials.

The first specific question to be answered pertains to the applicability of using co-sputtering of compositional gradient films to perform combinatorial studies. Theoretically the samples are ideal for such studies as they require comparatively little preparation time and offer a wide range of material compositions for investigation. There are, however, a number of issues to be addressed. Sputtering occurs far from thermal equilibrium and therefore is capable of producing meta-stable phases which can exist despite not appearing on any equilibrium phase diagrams. The copper-tungsten materials system was selected for study as two metastable phases have been observed previously. The chemical composition range was selected such that the sample covers nearly the entire range over which the metastable BCC-phase exists. Another potential issue with using co-sputtered compositional gradient samples for combinatorial studies is the difficulty of specifically controlling factors aside from chemical composition. Since the entire sample is deposited simultaneously, deposition occurs under identical conditions across the wafer. The deposition flux gradient, however, results in each area of the film being deposit-

ed at a slightly different rate. The spatial arrangement of the targets and substrate is also specifically selected so that there is a large difference in distance travelled by sputtered ions when reaching the extreme ends of the substrate. The angle at which the sputtered ions arrive at the substrate also varies appreciably. All of these factors can have significant influence on the texture, microstructure, and surface topology of the films, which can have a dramatic influence on the film mechanical properties and ease of testing. The Zr-Nb materials system was selected to investigate these effects since niobium is only soluble within zirconium up to 0.6 atomic % at room temperature. For the rest of the phase diagram niobium is present in its BCC β -phase and magnesium is present in its HCP α -phase. The HCP-BCC materials combination is selected for investigation as incorporating the two components into a single metastable phase, as is often the case for co-sputtered metals, can exhibit properties not associated with either of the two constituent materials.

Multilayer thin films have a long history of study due to their interesting mechanical properties and the ease with which the operative hardening mechanisms at different length scales can be investigated. There are a few materials combinations which have been studied far more extensively than others, most notably Cu-Ni and Cu-Nb. For this work the broader applicability of conclusions drawn from these specific materials was testing by first applying similar materials combinations and then moving to less-extensively studied systems. Cu-W was selected as the first system due to its similarity with the well-studied Cu-Nb system. The copper component is identical while the tungsten and niobium share many basic materials properties. Both are refractory metals with a BCC crystal structure, similar atomic radii, and a high melting point. This is important since many of the models developed for other multilayer systems rely on the nature of the interface to determine the ease with which dislocations can cross it. Materials systems with identical crystal structures and similar lattice spacing are described as "coherent", such as Cu-Ni. Systems with drastically differing lattice spacing or different crystal structures are referred to as being incoherent. Among the incoherent systems, FCC-BCC combinations are the most widely studied. Recent research trends have begun exploring other incoherent combinations as well, most notably the HCP-BCC combination. This is especially interesting at smaller length scales where a reduction of interface energy can stabilize atypical crystal phases. This is the case for the Mg-Nb materials system, where sufficient reduction in layer thickness can stabilize a BCC magnesium phase. A combinatorial approach to investigating Mg-Nb multilayer films would enable the study of the exact nature of this phase and the conditions required to successfully stabilize it. In addition to Cu-W and Mg-Nb multilayers, metal-ceramic interfaces are studied as well using the Cu-TiN materials system. The titanium nitride layers were deposited using reactive sputtering and have the same immiscibility advantage as the strictly metallic multilayer combinations investigated here.

1.4 Thesis Outline

This thesis is arranged into eight distinct chapters. First, a general introduction to combinatorial science and micro- and nanomechanical testing is given along with a brief summary of the thesis objectives. The second chapter provides the necessary background information concerning crystalline materials, the mechanisms which govern their mechanical behavior, and the general approach used to synthesize and test samples. The third chapter describes the scientific equipment used in the subsequent chapters along with a brief description of the physics behind each of the characterization techniques. Chapters 4, 5, and 6 present the bulk of the results obtained during this work. The chapters are divided by film architecture; with several materials systems investigated using each film architecture. Chapter 4 covers compositional gradient films, chapter 5 pertains to multilayer thin films, and chapter 6 discusses nanoparticle reinforced composites. Chapter 7 then draws upon the knowledge gained in the previous three chapters to discuss the strengthening mechanisms available in thin films in general. The results from this work are set into the context of the existing literature. The final chapter summarizes the work and provides an outlook for further investigation.

2 Background in Crystal Mechanics and Mechanical Testing

2.1 Crystalline Materials

The vast majority of metallic, semiconductor, and ceramic materials have a crystalline microstructure. A crystal is defined as a solid material whose constituent elements (typically atoms) are arranged in an ordered, periodic fashion with translational symmetry. Theoretically a perfect crystal possesses no deviation from this structure, continuing into infinity with each lattice site being occupied by a single, exactly place atom. The properties of such a crystal are invariant and easy to predict, but are in general not a good representation of reality. In the physical world there are a number of defects and deviations from the ideal crystal which determine the actual properties and behavior of crystalline materials. Understanding the possible types of defects and their effect on the crystal is essential to accurately interpreting measured data from crystalline material. The various types of crystal defects can be classified by size and dimensionality as point, line, area, or volume defects. All defects require energy for their formation and are generally present in all crystalline materials.

2.1.1 Point Defects

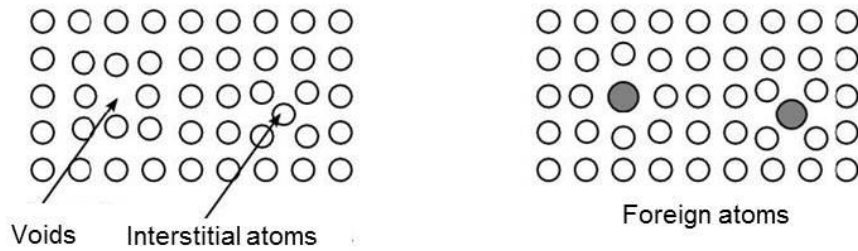
The simplest point defect occurs when a single lattice site is left unoccupied. This type of defect is known as a vacancy. The surrounding crystal lattice will generally contract somewhat, resulting in a tensile stress field around the vacant lattice site. A related crystal point defect occurs when an atom occupies a position between regular lattice sites. This type of defect is referred to as an interstitial and results in a compressive stress field surrounding the interstitial atom. Vacancies and interstitials can occur together when sufficient energy is provided to an atom to leave its lattice site. Even modest thermal energy is sufficient to create vacancies. The quantity of vacancies in a metal as a function of temperature can be generally estimated by Equation 1:

$$N_v = \frac{\rho N_A}{A} \exp\left(-\frac{Q_v}{k_B T}\right) \quad \text{Equation 1}$$

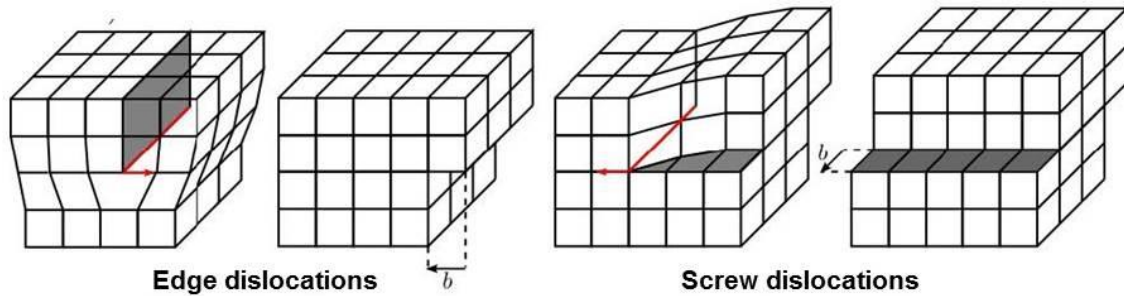
where N_v is the vacancy concentration, ρ is the density, N_A is the Avogadro constant, A is the atomic mass, Q_v is the energy required for vacancy formation, k_B = Boltzmann constant, and T is the temperature.

Interstitial point defects are also possible when an atom of a different species occupies a position between lattice sites. Smaller atoms impose less compressive stress on the lattice and can readily occupy interstitial locations. Most steels, for example, rely on carbon interstitials within an iron crystal to provide their excellent hardness. Foreign atoms which are too large to occupy an interstitial position can instead replace an atom in the host material to form another type of point defect, known as a substitutional. Substitutional atoms can provide either a compressive or tensile stress to the surrounding crystal lattice, depending on whether the substitutional atom is larger or smaller than the atoms of the host crystal. All of the point defects occur frequently in real world materials as the amount of energy required to generate such defects is small.

Point defects



Line defects



Area defects

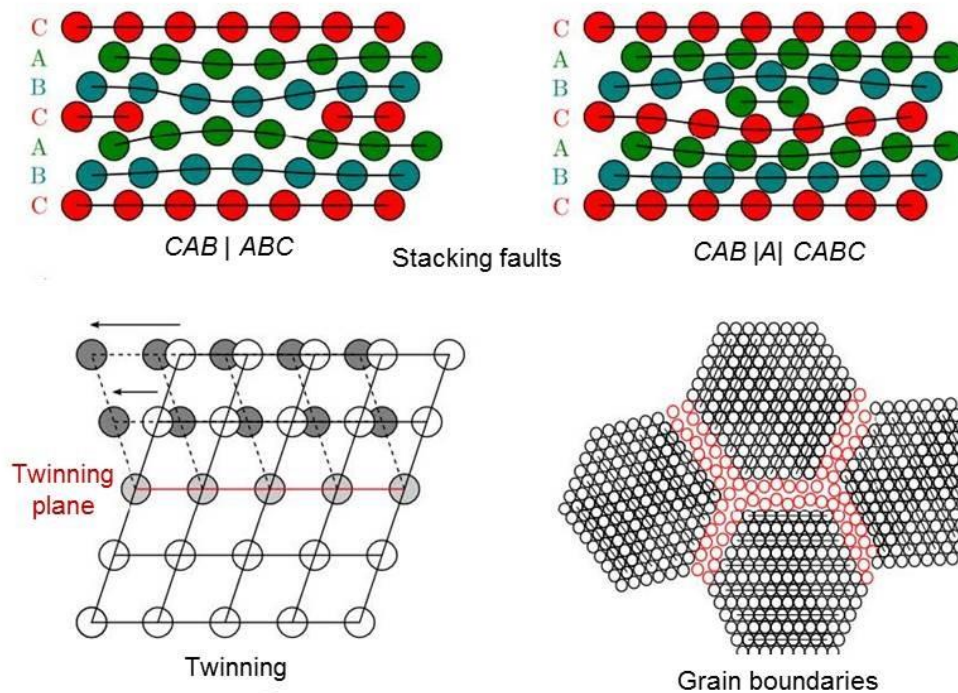


Figure 1: Common defects found within crystalline materials. *Figure provided by Juri Wehrs.*

2.1.2 Line Defects

Perhaps the most interesting crystal defect for the study of crystal plasticity is the edge dislocation. Edge dislocations occur when a crystallographic plane terminates within the crystal, leaving a region of compressive stress on the side with the extra plane of atoms and a tensile stress at the region beyond the terminated plane. The regions to the side of the dislocation consist are subject to shear stress. The asymmetric stress field caused by edge dislocations is very important as it dictates the movement and

interaction possibilities of the dislocation. Edge dislocations are commonly represented an inverted **T** symbol where the single vertical arm represents the additional partial plane of atoms. Two metrics are used to describe an edge dislocation: the line direction and the Burgers vector. The line direction describes the termination of the extra partial atomic plane while the Burgers vector b is used to describe the magnitude and direction of the lattice distortion as a result of the dislocation's presence.

In a perfect crystal the shear strength is given by Equation 2:

$$\tau_m = \frac{G}{2\pi} \quad \text{Equation 2}$$

where τ_m is the shear strength and G is the shear modulus. Considering the shear modulus of magnesium (17 GPa) and tungsten (161 GPa) as representative soft and hard metals, shear strengths on the order of a few to tens of GPa are expected. In reality the shear strength of most metals lies in the single MPa range, three full orders of magnitude below that expected for a perfect crystal. Dislocations are responsible for this drastic difference since they enable plastic deformation to occur one atomic plane at a time rather than throughout the entire crystal simultaneously. Through breaking one set of bonds and forming bonds with the adjacent plane, dislocations travel through the crystal and accommodate plastic deformation at even modest shear stresses. A second mode of edge dislocation movement called climb enables the dislocation to move into a parallel glide plane. This requires a vacancy to interact with the dislocation, and is therefore far more significant at elevated temperatures where vacancies have enhanced mobility.

Screw dislocations are formed when a crystal plane is sheared in such a way that the atoms resting in that plane are bonded with atoms resting in the adjacent plane. Screw dislocations impose a radially symmetric pure shear strain which decays in intensity with increasing distance from the center of the screw dislocation, otherwise known as the dislocation core. Most dislocations are neither purely edge or screw dislocations, but rather a mixture of the two. It is also possible for a dislocation to double back onto itself, forming a dislocation loop. When two edge or screw dislocations with perpendicular Burgers vectors intersect, either a jog or a kink is formed. A jog describes the situation where the step changes the slip plane of the dislocation while a kink displaces the dislocation within the same slip plane.

Beyond the basic edge and screw dislocations, there are also a number of other line defects known as partial dislocations. Partial dislocations form through the decomposition of an edge or screw dislocation into a pair of components, one leading and the other trailing. They are generally much more complicated to visualize since they possess a non-translational Burgers vector, but are prevalent and relevant to the deformation in many materials. Two of the most common types of partial dislocations are Shockley partial dislocations, with a Burgers vector of $b=a/6\langle 112 \rangle$, and Frank partial dislocations, with a Burgers vector of $b=a/3\langle 111 \rangle$. Shockley partial dislocations are glissile while Frank partial dislocations are sessile. For FCC metals with nanoscale confinement, partial dislocations become the dominant deformation mechanism [6]. The formation of partial dislocations also results in the formation of a stacking fault, an area defect described in the next section. When two leading Shockley partial dislocations combine a Lomer-Cottrell junction is formed. This junction is sessile and therefore sometimes termed a "lock" which prevents additional dislocation glide. It is also sometime referred to as a stair-rod dislocation. The Hirth lock dislocation, with a Burgers vector of $b=a/3\langle 100 \rangle$, is another related arrangement. Partial dislocations are only present in close-packed crystal lattices, namely FCC and HCP crystals. The presence of partial dislocation has not been demonstrated in BCC materials, largely due to the high stacking fault energies which would be involved.

Dislocations can be generated a number of ways. They can be formed as intrinsic defects during the original growth of the crystal, such as during a PVD or CVD process. Deposited atoms which lack sufficient mobility to occupy their ideal lattice sites and minor misalignment of crystallites joining from separate nucleation sites can both readily result in the formation of dislocations during the crystal growth process. Otherwise dislocations can be generated through applied stress after the growth of the crystal. Agglomeration of vacancies or interstitials (most notably in the case of Si) provides a simple means for dislocations to form. Irregular grain boundaries can also serve as a nucleation point for dislocation generation when an appropriate stress is applied. Phase transformation can also result in the generation of new dislocations as the volumetric change in the crystal needs to be accommodated under their presence of external dimensional constraints. A dislocation which exists to satisfy geometrical requirements is referred to as a geometrically necessary dislocation (GND). Another especially interesting dislocation source is the Frank-Reed source, a defect arrangement which allows for many dislocations to be generated from the same site. A dislocation arm sweeps the space around the Frank-Reed source under applied stress and emits a unique dislocation with each complete sweep. A single Frank-Reed source can emit dislocations nearly indefinitely, becoming depleted only when its atomic arrangement is disturbed.

There are also a number of dislocation annihilation mechanisms which are possible. The simplest occurs when the dislocation travels through the crystal and reaches either a free surface or grain boundary. The dislocation can exit the crystal, leaving an atomic step on the surface or interface in its place. Dislocations can also be eliminated within the crystal. In order for this to occur for line dislocations, two dislocations of inverse orientation need to meet along the same slip plane. Upon recombination an extra complete plane of atoms is added to the crystal. Screw dislocations can annihilate upon joining with a co-axial dislocation with the opposite sign. Partial dislocations can also be eliminated through combination with their leading or trailing counterpart, correcting the stacking fault through their elimination. Thermal annealing provides sufficient energy to enhance dislocation mobility to the point that many of the dislocations can annihilate with their opposites or exit the crystal. This is the primary effect targeted through thermal annealing after cold-working a material.

2.1.3 Area Defects

As mentioned in the previous section, the dissociation of a dislocation into two partial dislocations is also accompanied by the generation of a planar defect known as a stacking fault. Stacking faults can be visualized by imagining the closest-packed planes of a crystal as viewed from above. In an FCC crystal any one of three positions can be occupied by the atoms of a given plane, represented by the letters A, B, and C. The subsequent layer then has two remaining possible sites. In a defect-free crystal the stacking order follows a simple, repeating ABCABCABC stacking order. A simple stacking fault occurs when this order is violated. For an FCC crystal a stacking fault, shown in bold, possesses the following stacking order: ABCABC**BC**ABC. For an HCP crystal, where the basal plane is the most densely packed and the ideal stacking order consists of only two potential sites, the ideal stacking order is given as ABABABABAB. When a stacking fault is introduced the stacking order involves the displacement of one layer to a third site: ABABAB**CB**ABAB. Stacking faults in which the same site is occupied in consecutive atomic layers (AA, BB, or CC) are generally not observed due to the high energy required for their existence. Stacking faults, like all types of crystal defects, are in a higher energy state than the ideal crystal and therefore require a given stacking fault energy (SFE) for their generation.

A special case of stacking fault occurs when there is not just one misplaced atomic layer in the stack, but the conventional stacking order is reversed. This type of defect is known as a twin grain boundary, or simply a twin. A twin is a mirror-image plane about which the conventional stacking order is reflected: ABCABC**CB**ACBA. Twins are readily identified by their planar nature and commonly take the appearance of a banded or layered structure when multiple twins occur with close spacing. In general twins

are a desirable defect since they do not degrade the electrical properties of a crystal despite providing improvements to the crystal's mechanical properties.

Grain boundaries are another type of two-dimensional crystal defect which can be roughly divided into two classes: low-angle grain boundaries and high-angle grain boundaries. A grain boundary which has a different material on the other side is termed an interface while a grain boundary without anything on the other side is known as a free surface.

2.1.4 Volume Defects

Larger defects are also present in most materials and can also play a significant role in their mechanical behavior. Voids are empty or gas-filled volumes trapped within bulk material. They diminish the density of a material and compromise its physical integrity through stress concentration and missing material. Most fabrications processes strive to eliminate the presence of voids, with foams and other porous materials providing a notable exception. Cracks can also be viewed as a type of volume defect, with the sharp crack tip as a site of intense stress concentration. Ceramics and other brittle materials are prone to failure through crack propagation. Precipitates, small volumes of a foreign substance trapped within a crystal, can also be considered a type of volume defect. More broadly any type of secondary phase particle, whether it is introduced via precipitation or not, can be considered a type of volume defect.

2.2 Deformation Mechanisms

In crystalline materials there are a number of mechanisms which are available to accommodate plastic deformation. In general many of these mechanisms will be operative, but under a given set of conditions it is likely that one will be more dominant than the others. For a given polycrystalline material, three factors determine the dominant deformation mechanism: temperature, strain rate, and stress field. These deformation mechanisms can be roughly divided into three main categories: dislocation-based mechanisms, diffusion based-mechanisms, and grain-based mechanisms. There are also a number of combined mechanisms in which atomic diffusion facilitates dislocation or grain movement.

2.2.1 Dislocation-based Mechanisms

Dislocation glide is among the most important deformation mechanisms in crystalline materials. It occurs readily along densely packed planes and is the simplest method of dislocation movement, occurring when bonds in adjacent planes sequentially broken and re-formed. Under appropriate circumstances dislocation glide is even somewhat reversible by applying a load in the opposite direction. Dislocation glide is a reaction to shear stress, which will exist to some degree in all crystallographic directions neither parallel nor perpendicular to a uniaxial applied load. The minimum stress necessary to initiate dislocation glide is defined by the Peierls stress. This threshold is dependent on the dislocation geometry and is lower for larger atomic spacing. As such, slip tends to occur along closely-packed planes, where the distance between adjacent planes is the greatest. The Peierls stress, also known as the Peierls-Nabarro stress, is given by:

$$\tau_{PN} = Ge^{-\frac{2\pi W}{b}} \quad \text{Equation 3}$$

where τ_{PN} is the Peierls-Nabarro stress, $W = a/(1 - \nu)$ and represents the dislocation width, G is the shear modulus, ν is the Poisson's ratio, b is the interatomic spacing, and a is the interplanar spacing.

Another important metric for determining the planes upon which slip is most likely to occur is the Schmid factor. The Schmid factor is a purely geometrical factor, meaning that for a given crystal it can be defined for any direction relative to an applied tensile or compressive stress. The critical resolved shear stress (CRSS), or the shear stress component of the applied stress in the direction in which slip occurs, is the highest for planes and directions in which the Schmid factor is the highest. This slip system is therefore known as the primary slip system and is the first in which slip occurs. Further increase in stress will result in the activation of other slip systems as each of their respective CRSS thresholds is reached. Schmid's Law is given as:

$$\tau_c = \sigma \cdot m \quad \text{Equation 4}$$

where τ_c is the critically resolved shear stress, σ is the applied stress, $m = \cos(\varphi)\cos(\lambda)$ is the Schmid factor, φ is the angle between the applied stress and the glide plane, and λ is the angle between the applied stress and the glide direction.

For both FCC and BCC crystals there are a total of twelve slip systems, while exactly five are needed to accommodate an arbitrary deformation. HCP crystals, however, possess just two independent slip systems and therefore tend to fail in a brittle fashion after fracture is initiated. BCC crystals will also tend to become brittle at lower temperatures where there is insufficient thermal energy to activate all five slip systems. The ductile-to-brittle transition temperature (DBTT) often marks the point at which an important slip system has become deactivated. The primary slip system for FCC crystals is along the $\{111\}$ plane, for BCC crystals along the $\{110\}$, and for HCP crystals along the basal $\{0001\}$ plane. Considering a statistically random distribution of grains within a polycrystalline material, the average Schmid factor of a crystal system can be used to predict the yield strength of a material. The Taylor factor considers not only the statistical orientation of the grains, but also their compatibility. For an FCC crystal with sufficiently large grains to preclude grain-boundary strengthening, the yield strength is predicted to be 2.24 times the shear strength. This is the lower limit of the yield strength as there are a number of other mechanisms which can contribute to the overall strength.

As the Schmid factor tends to underestimate the observed yield strength, subsequent attempts have been made to improve on this basic model. Using the assumption that all of the grains within a polycrystalline material deform the same amount, Taylor proposed the use of an alternative orientation factor. The Taylor factor tends to provide a more realistic estimate of the yield strength, though the Schmid factor still is widely utilized.

In addition to dislocation glide, dislocation generation and annihilation are two further dislocation-based mechanisms through which plastic deformation can be accommodated. Dislocation nucleation has been commonly observed from Frank-Reed sources and other dislocation source arrangements, but it can also occur from the surface of a grain, at a grain boundary, or at an interface with another material. The energy required for dislocation nucleation to occur is generally higher than from a source within the crystal, therefore it is only expected to provide a major contribution to plasticity for crystals of sufficiently small size that internal dislocation sources are not available. Dislocation annihilation can also occur either within the crystal or at a free surface, grain boundary, or interface. When a dislocation exits the crystal by any of the latter means, a step is left at the surface since the additional partial plane of atoms is then located on the outside of the crystal rather than within it.

A final mechanism of dislocation-based deformation is known as climb. Climb describes the process by which a dislocation can circumvent a barrier by traveling perpendicular to its glide plane. This can only occur if there is sufficient thermal energy within the crystal to permit the diffusion of vacancies. Bypassing a larger obstacle will generally require more time and more thermal energy as multiple diffu-

sion steps must occur. Climb is the primary mechanism by which a dislocation can bypass a barrier to its slip plane and can be thought of as a combined dislocation-diffusion mechanism. This is also known as power-law creep. In general all deformation mechanisms are rate-dependent, but those relying solely on dislocation movement tend to be far less rate-sensitive than those with a diffusional component.

2.2.2 Diffusion-based Mechanisms

Diffusion-based mechanisms make up the second group of common deformation mechanisms. Diffusion is a thermal process by which atoms and vacancies can change their positions within a crystal. Fundamentally diffusion is always driven by the presence of an energetic gradient within the crystal. In the simplest case without any externally applied gradient, diffusion is driven solely by the local thermal variations within the crystal. As atoms vibrate about their lattice sites a sufficiently large energetic gradient can occur which allows a vacancy or atom to change sites. Conceptually it is often more convenient to refer to vacancy diffusion rather than atomic diffusion since a different atom will change position during each diffusion event. The vacancy, analogous to the concept of a hole when referring to electron transport, can be treated as a single mobile particle even though it is really just the absence of a particle where one is expected. Without any higher length-scale gradients the vacancy will follow a random walk throughout the crystal. When atoms or vacancies diffuse within the crystal, this is referred to as bulk or lattice diffusion. The Peierls stress within the crystal tends to provide a significant amount of resistance to lattice diffusion, so it tends only to occur with significant frequency at elevated temperatures or around defects within the crystal.

Far less resistance to diffusion is offered at a free surface, where the Peierls stress is only present on the side of the surface atoms in contact with the rest of the crystal. A number of mechanisms are possible at the surface, including hopping, atomic exchange, and longer-range jumps among others. Surface diffusion is one of the primary deformation mechanisms during sintering and Ostwald ripening processes. The amount of energy needed for surface diffusion to occur is generally around half that required for lattice diffusion to occur. In general, the more disorder within the crystal, the more likely diffusion is to occur. Grain boundaries, while not as energetically favorable as a free surface, also offer conditions for facilitating diffusion processes. Diffusion occurs more readily along large-angle grain boundaries than shallow angle grain boundaries for this reason. Diffusion can also occur along interfaces between different materials. How readily diffusion occurs depends heavily on the nature of the interface and can be difficult to verify experimentally. A perfectly epitaxial interface will provide a less efficient pathway for diffusion as compared to one with misfit dislocations or no clear epitaxial relationship between the two materials.

Diffusion is commonly associated with creep, deformation which occurs over a longer time scale when a mechanical load is applied and not removed. Creep can be divided into a number of sub-categories. Coble creep occurs when vacancies diffuse along grain boundaries, resulting in grain boundary sliding. The strain rate is proportional to d^{-3} , where d is the grain size. Coble creep tends to occur at lower temperatures, where insufficient energy is available for vacancies to easily diffuse through the bulk crystal. Herring-Nabarro creep describes the situation when vacancy diffusion occurs through the crystal grains instead of along grain boundaries. This only really occurs as a dominant deformation mechanism at low stresses in fine-grained materials. The strain rate increases linearly with applied stress. As compared to Coble creep, Herring-Nabarro creep exhibits a d^{-2} proportionality relationship with grain size. Herring-Nabarro creep tends to be dominant at higher temperatures. Other criteria can also be used to distinguish between various types of creep. One such criterion is the change in creep rate over time. This is then used to classify three distinct stages of creep: primary, secondary, and tertiary creep. During primary creep there is initially a higher creep rate, which then reduces with time. Secondary

creep describes the portion for which the creep rate is relatively constant. Tertiary creep is said to have begun when the creep rate again increases and ultimately culminates in specimen rupture.

Although creep is strongly associated with diffusion-based deformation, dislocation movement also has a dynamic component and can contribute to creep phenomena, albeit primarily at lower temperatures. Power-law creep (PLC) is the most prominent example of dislocation-mediated creep. PLC can be further subdivided into low- and high-temperature creep, expressed as a function of the melting temperature of the material. PLC covers a very broad range of creep rates, from as low as 10^{-10} s^{-1} to as high as 1 s^{-1} in extreme cases. At higher temperatures (typically above 0.7 of the melting temperature) within the PLC regime materials can undergo dynamic recrystallization during deformation. As direct experimental observation of creep processes is very difficult to attain, the various creep mechanisms are generally distinguished on the basis of their rate dependency at different temperature and loading conditions.

2.2.3 Grain-based Mechanisms

The third major class of deformation mechanisms involves mechanisms in which entire grains contribute to plastic deformation. These mechanisms become significant as the grain size decreases and are typically observed in nanocrystalline materials. They too are only operative in conjunction with dislocation- and diffusion-based mechanisms, most often occurring at the grain boundaries.

Grain rotation, though not truly an independent deformation mechanism, is also occasionally described as a method for accommodating deformation. Grain rotation, like grain boundary sliding, requires that the grain boundaries exhibit a higher degree of deformability than the grains themselves. Grain rotation is readily identifiable by a change in crystalline texture after the material has undergone plastic deformation. The textures which arise after severe plastic deformation (SPD), forging, rolling, and drawing are a result of grain rotation during the deformation processes. Not only the orientation, but also the shape size, and number of grains can vary during deformation. Grain growth and coalescence can occur at the expense of smaller grains being consumed or the grain shape can become elongated. In some cases new grains can form when dislocations arrange to form a low-angle grain boundary, as process which as an integral part of dynamic recovery.

The grain boundaries are sometimes subject to deformation while the grains themselves remain relatively intact. This type of process can be broadly termed as grain boundary sliding (GBS). GBS is also sometimes referred to as either granular or superplastic flow. It occurs in conjunction with Coble creep. Typically grain boundary sliding occurs at high homologous temperatures and relatively modest strain rates. Grain boundary sliding is most common in ceramic materials where the disordered, glass-like grain boundaries can deform while the crystalline grains themselves maintain their structure.

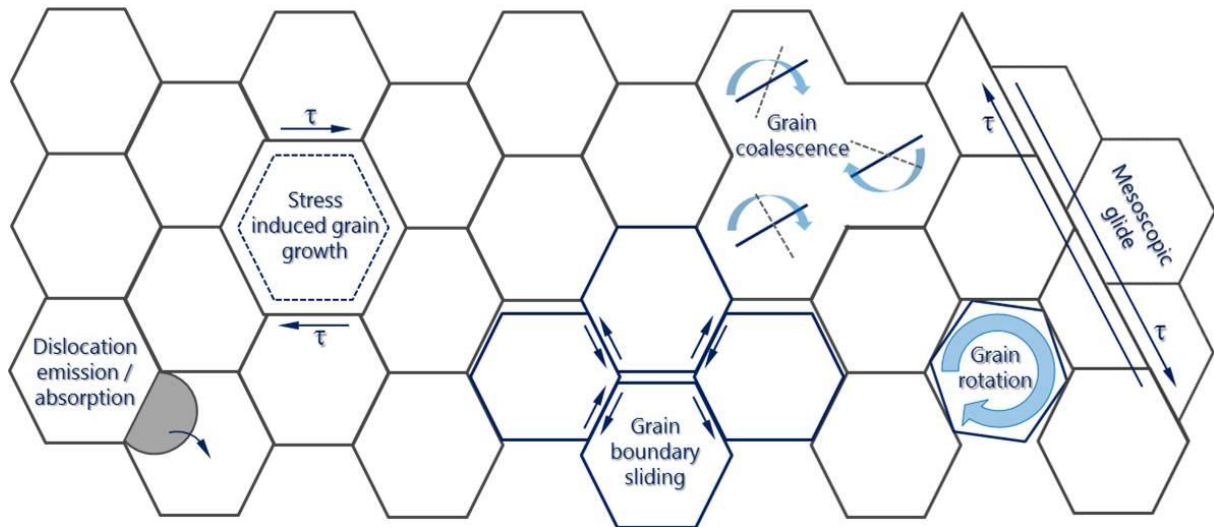


Figure 2: In addition to dislocation- and diffusion-based mechanisms, a number of grain-based mechanisms are also available for accommodating plastic deformation. *Figure created by Juri Wehrs.*

2.2.4 Deformation Mechanism Maps

With so many potential competing mechanisms and the relatively complex arrangement of microstructure and defects, it can be difficult to fully understand which mechanisms dictate the plastic behavior of a material. In general it can be assumed that many mechanisms are operating simultaneously, but that there is one primary mechanism dictating the bulk behavior of the material. Since these mechanisms operate in parallel, the mechanism with the highest rate will be dominant. General deformation mechanism maps (DMM) for a wide variety of materials have been constructed which indicate the conditions under which a given deformation mechanism is considered to be dominant. Though far from extensive, and technically only valid for materials whose microstructure closely matches the material use to generate the maps, they have demonstrated their utility for providing an atomic level interpretation of observations collected from bulk materials.

For a material of a given microstructure, the dominant deformation mechanism depends on three primary factors: the applied stress, the temperature of the material, and the strain rate. The most common method for presenting this data is on a plot of temperature versus shear stress. The map is divided into distinct areas, representing the range of conditions under which a given deformation mechanism is dominant. Although solid lines are used to separate these areas, it is accepted that there is always a transition zone between adjacent areas and that the exact point at which one mechanism gives way to another is typically not explicitly defined. Constant strain rate contours are drawn onto the map to indicate the effect of strain rate. Using two dimensional plots, two other arrangements of the data are possible. The temperature can be plotted versus strain rate or the stress can be plotted versus the strain rate. In either case the third variable can be added to the plot as a contour. All three variable can be plotted as a three-dimensional plot, but this is typically avoided in the literature in the interest of preserving clarity.

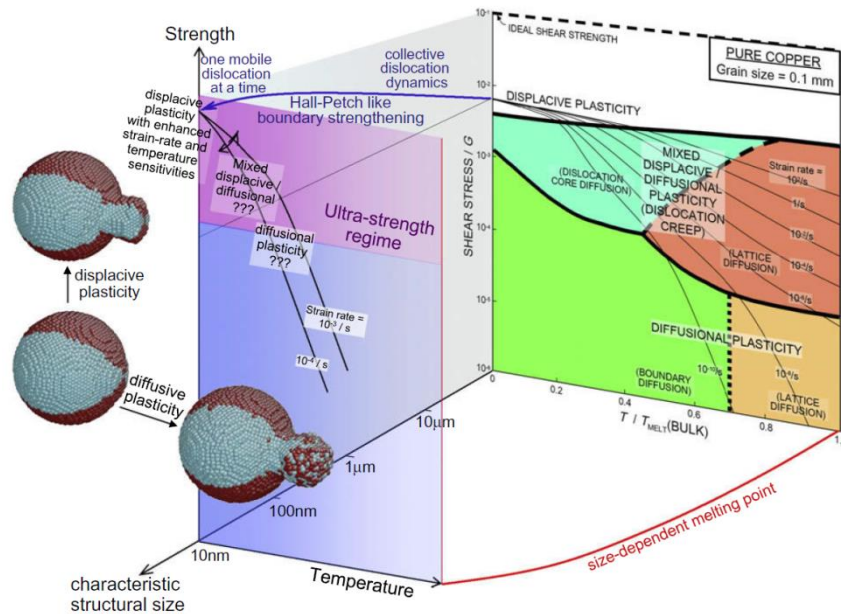


Figure 3: A typical temperature-shear stress deformation mechanism map for pure copper with a grain size of 0.1 mm [7].

2.3 Strengthening Mechanisms

In order to design strong materials, the specific deformation mechanisms operating under testing conditions need to be considered and addressed. There are a number of potential strategies for adding to the strength of a material, each which seeks to address and inhibit a specific mechanism. In cases in which a particular deformation mechanism cannot be entirely eliminated it is often possible to slow the deformation mechanism rate to a point that a competing mechanism will become more relevant for governing material plasticity.

Most traditional strengthening strategies are designed to impede dislocation movement as for most materials dislocation-based mechanisms are the most relevant at room temperature. As discussed previously, dislocations impose a local strain on the crystal lattice. This strain interacts with other strains within the crystal and with obstacles within the crystal. By providing an appropriate obstacle, dislocation movement can be impeded. Dislocations themselves can serve as effective obstacles for other dislocations. This is the principle behind work hardening, in which an artificially large dislocation density is introduced to the material, typically by means of high-stress deformation. Work hardening is sometimes referred to as cold working or strain hardening, depending on the process which is used for its application to the material. Within a single grain dislocations have a mixed character and can follow rather convoluted paths through the grain. When a sufficient number of dislocations are introduced to the crystal grain the likelihood of a dislocation passing through the grain unencumbered becomes increasingly small. The dislocation can easily become entangled with other dislocations. This type of strengthening mechanism is referred to as forest hardening.

Forest hardening is closely related to dislocation pileup, the strengthening mechanism governing the Hall-Petch relationship of material strength dependence with grain size. Smaller grained materials exhibit improved strength and toughness as the grain size is reduced from the micrometer to the nanometer scale. This trend continues until the single-digit nanometer scale, below which the material can exhibit a variety of different behaviors. Dislocations, unable to easily exit the grain, become congested near the grain boundary and inhibit the movement of subsequent dislocations.

Dislocation movement can also be inhibited through the introduction of a foreign species of atoms. For soluble atoms, whether substitutional or interstitial, the crystal lattice is distorted and dislocations cannot glide easily along their slip planes. This is referred to as solid solution hardening and tends to have a comparatively small contribution to material strength since the barrier to glide is not especially large. Precipitate hardening, in which the foreign species forms a second phase, tends to be a more effective hardening mechanism. More generally this can be referred to as dispersion strengthening since it is possible to introduce the secondary phase particles by means other than precipitation.

Additional strengthening can be derived from the specimen dimensions themselves, which is often the case for films. Thin films are naturally harder than their bulk counterparts of the same composition for a number of reasons. Firstly, the deposition process lends itself to the production of small grain sizes, so the Hall-Petch effect tends to be quite pronounced in thin films. Secondly, the substrate upon which the film is deposited can provide strength to the film, even if it is only indirectly. Elastic modulus mismatch between the film and substrate can generate a mirror or imaging stress, which contributes to the film hardness by increasing the isostatic stress during testing. There is also a general size effect which occurs within the film itself. Measurements applied at the small scale will show increased strength with decreasing test volumes. This can be attributed to the difference in mechanical properties between the surface and bulk of a material and the decreased likelihood of probing a weak defect within a small volume.

More complex film structures introduce a number of additional hardening mechanisms. This can be seen in periodic bilayer multilayer films, where two materials are deposited in alternating layers to incorporate a large number of interfaces into a small volume. The strength of such multilayer films is strongly dependent on the thickness of the individual layers and the nature of the interfaces between them. Four regimes are defined for such multilayer films. The first occurs from the large-scale to micrometer scale when the multilayer exhibits properties well-approximated by the lower bound rule-of-mixtures. As the layers become thinner a strengthening trend similar to that observed in the Hall-Petch relationship defines the strength of the multilayer. Dislocations pile up near the layer interfaces, analogous to pile-up at grain boundaries. At length scales of several tens of nanometers the layers become too thin to accommodate multiple dislocations. Instead dislocations bridge between the upper and lower interfaces. The curvature of the confined dislocation produces a bow similar to that observed in Orowan hardening. At even further reduced length scales the behavior of a multilayer film is dominated by interface crossing, the resistance encountered when a dislocation passes between dissimilar materials.

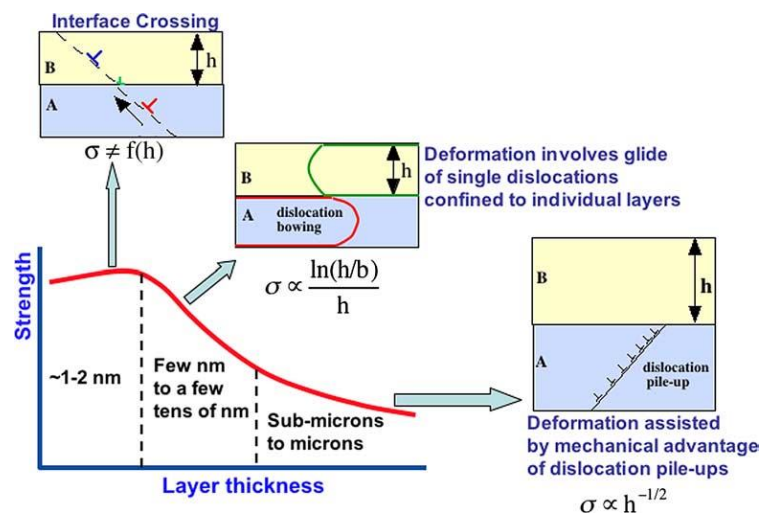


Figure 4: The strengthening mechanisms for multilayer materials change as a function of layer thickness. In general thinner layers provide improved strength down to the single-digit nanometer range [8].

2.4 Mechanical Testing Strategies

As the active deformation mechanisms in a given material depend strongly on the temperature, stress, and strain rate, it is necessary to develop testing techniques in which these three variables can be varied. Applying different levels of stress and strain rate are relatively straightforward, but special test apparatus are required for variable temperature testing. A number of standardized experimental setups have been developed (tensile tests, micropillar compression, nanoindentation, etc.), but all share common principles related to the test parameters of stress, strain rate, and temperature.

2.4.1 Variable Temperature Mechanical Testing

Variable temperature tests are not only useful for understanding the strength of a material across a range of temperatures, but also provide insight into the operative deformation mechanisms within the material. Any given deformation consists of both thermal and non-thermal components, the magnitude of which can be determined through variable temperature testing. A drastic change in strength with changing temperature indicates that there is high activation energy for the dominant deformation mechanism. Decreasing the testing temperature tends to result in increased strength and decreased ductility. The ideal strength of a crystal is achieved at 0 K since there is no energy available to assist any thermally activated deformation mechanisms. The ideal strength can be approximated as one-twentieth of the elastic modulus for FCC materials and one-tenth of the elastic modulus for BCC materials, as calculated using the Lennard-Jones potential [9].

The simplest experimental setup for cryogenic testing involves submerging the sample and sample holder into a boiling liquid since its temperature will remain constant and no active temperature control is needed. At atmospheric pressure liquid helium can be used to achieve a temperature around 4 K (-269°C) while liquid nitrogen can be used to reach 77 K (-196°C). While useful for reaching very low temperatures, the immersion method does not permit experiments to be performed in-situ and is limited to only fixed temperatures for which an appropriate boiling liquid is available. A much more versatile method relies on active temperature control, permitting arbitrary temperatures to be achieved within the limits of the testing equipment. Cooling is typically achieved using liquid nitrogen, either connected to the test apparatus via a thermally conductive pathway or actively chilled by pumping the liquid nitrogen or evaporating nitrogen through a chilling circuit. Thermal equilibrium between the indenter and sample is necessary prior to conducting the experiments to ensure that there is no heat transfer, which could lead to unwanted expansion or contraction. Temperatures as low as 173 K (-100°C) can be realized using a typical indenter, though further design improvements may see temperatures near that of liquid nitrogen achieved. Resistive heaters embedded in the indenter and sample holder can be used to guarantee identical temperatures before the experiments are performed.

Elevated temperature experiments are more easily realized than cryogenic experiments since only a heat source is required and no liquids or gases need to be pumped through the system. Elevated temperature testing is typically conducted under either vacuum or an inert gas atmosphere to prevent the sample from oxidizing or reacting with moisture in the air. Temperatures above 1000 K have been reported in the literature for elevated temperature micromechanical testing [10]. Heating occurs either through the use of resistive heaters or lasers. Since only a small volume of material needs to be heated and there are no convective losses under vacuum, modest heating power is still capable of reaching high temperatures. The main concern is often providing sufficient thermal insulation to protect load and displacement instrumentation from the high temperatures in the indenter and sample.

2.4.2 Variable Strain Rate Mechanical Testing

The second major factor influencing the active deformation mechanisms in a material is the strain rate at which the material is deformed. There are a number of testing strategies through which the strain rate sensitivity of a material can be investigated. The simplest is to use a strain-rate controlled testing apparatus and to test various samples at different strain rates. In principle this is sufficient to determine the strain rate sensitivity of a material, but in practice the variation in sample geometry and material inhomogeneity within micromechanical test specimens can introduce more variation in the results than is produced through the various strain rates. As such, a prohibitively high number of specimens would need to be tested before the statistical significance of the strain rate sensitivity could be established.

An alternative method to constant strain rate tests performed on multiple samples is the strain rate jump (SRJ) test. During a SRJ test the applied strain rate is instantaneously varied after the onset of plastic deformation within the test specimen. Since the change in strain rate is near instantaneous, the sample microstructure, dislocation density, and geometry can be assumed to be identical immediately preceding and following the strain rate jump. The change in flow stress as a function of strain rate can be immediately discerned without concern about variation between samples. Depending on the strain-hardening behavior of the material, it can be possible to test many different strain rates on the same sample. In general the first and last segment of the loading curve are tested at the same strain rate in order to allow a constant strain rate stress-strain curve to be interpolated and used as a baseline against which the strain rate jump segments can be compared. There is generally a short period of time required after each SRJ for the flow to stabilize. This point of stabilization is identified as when the slope of the loading curve is identical to the interpolated slope between the first and the last loading segments. The SRJ test is generally the preferred method for strain rate sensitivity (SRS) determination due to its advantages of testing multiple strain rates per test specimen and guarantee of identical structure before and after each SRJ.

Other tests adapted from conventional mechanical testing can also be applied to micromechanical specimens to determine time-dependent material behavior. Stress relaxation tests apply a fixed strain to the test specimen and monitor the decay in stress with time. Several variation of creep tests have also been recently applied to micromechanical testing. These are performed in load-control mode or in a pseudo-load-control mode in which a control loop maintains a constant stress throughout the test. The stress rupture test, in which a constant force is applied and the sample is allowed to deform until failure, is another such test.

2.4.3 Activation Volume and Activation Energy

Activation energy is used to describe any thermally activated process. The Arrhenius equation expresses the fundamental relationship between temperature, activation energy, and strain rate:

$$\dot{\epsilon} = \dot{\epsilon}_0 e^{-\frac{Q}{kT}} \quad \text{Equation 5}$$

where $\dot{\epsilon}$ is the creep rate, Q is the activation energy, k is the Boltzmann constant, and T is the temperature. While originally developed to describe the amount of energy necessary to initiate a chemical reaction, the concept of activation energy can be applied to any situation in which an energy barrier must first be overcome before an energetically favorable process can take place. In the context of mechanical testing, the activation energy represents the amount of energy required to initiate a given deformation mechanism. The activation energy can be calculated by:

$$Q = \frac{1}{m} R \left[\frac{\partial \ln \sigma}{\partial (1/T)} \right] \quad \text{Equation 6}$$

where m is the strain-rate sensitivity exponent, R is the universal gas constant, σ is the stress, and T is the temperature. A second activation parameter, the activation volume, is needed to calculate the activation energy and can also provide insight into the operation of specific deformation mechanisms. The activation volume is determined through investigating the strain rate sensitivity of the flow stress. The activation volume describes the volume of material needed for a specific mechanism to operate. As such the activation volume for a process like lattice diffusion can be below the volume of a single unit cell (1 b^3) while dislocation bowing can exhibit an activation volume of more than a 1000 b^3 . The activation volume is given by:

$$V_a = \frac{\sqrt{3}kT}{m\sigma_f} \quad \text{Equation 7}$$

where k is the Boltzmann's constant, T is temperature, m is the strain-rate sensitivity exponent, and σ_f is the flow stress. In order to calculate the activation volume the strain rate sensitivity of the material in question must first be determined. For bulk samples, the strain rate sensitivity exponent has traditionally been determined using a series of monotonic mechanical tests performed on near-identical samples. This is sufficient only when there is minimal variation in the dimensions, microstructure, and dislocation density between the samples used. For micromechanical testing, where the stochastic variability between test specimens is often large, strain-rate sensitivity is determined utilizing strain-rate jump tests in which the applied strain-rate is changed instantaneously. For a strain-rate sensitive material, the stress within the material will also change instantaneously. For most materials, a higher strain rate results in a higher stress within the material since there is insufficient time for relaxation, diffusion, and other time-dependent processes to initiate. Strain-rate jump testing is especially effective for micromechanical testing since the dimensions, microstructure, and dislocation density of the test specimen are essentially identical immediately before and after applying the strain-rate jump. For samples capable of withstanding a large strain before failure it is possible to perform multiple strain-rate jumps on a single test specimen, greatly reducing the experimental effort needed to collect a useful amount of data. The strain-rate sensitivity exponent, m , is given by:

$$m = \left. \frac{\partial \ln \sigma}{\partial \ln \dot{\epsilon}} \right|_T \quad \text{Equation 8}$$

Taken together, the activation volume, and activation energy provide three useful metrics through which the dominant deformation mechanism can be determined. These parameters are calculated through observed changes in strength as a function of temperature and strain-rate.

3 Experimental Methods

3.1 Film Deposition

Sputtering is a means of physical vapor deposition (PVD) in which a target material is eroded by a plasma, with ejected material deposited onto a substrate. Both the substrate and target are enclosed in a vacuum chamber which is emptied of atmosphere to provide a controlled environment with as few contaminants as possible. A sputtering gas is introduced to the chamber to provide the plasma and momentum transfer to the target. By applying a voltage between the cathode and anode within the chamber plasma is generated above the target. Ions within the plasma bombard the target, slamming into its surface, ejecting atoms through the impact. The atoms then traverse the deposition chamber, potentially changing their direction or losing energy through collisions with sputtering gas. In the case of reactive sputtering it is also possible to form ceramics and other compounds through reaction between the sputtered material and the sputtering gas. The sputtered material then reaches the substrate where it adheres and results in film growth.

All of the thin films investigated throughout this work were produced through sputter deposition. Sputter deposition, colloquially referred to as sputtering, is one of the most common methods of physical vapor deposition (PVD). Sputtering occurs when gas ions (typically Ar^+) are accelerated toward a cathode by an imposed electric field. The cathode is referred to as the target and can be composed of nearly any material. As the initial sputtering gas ions strike the target a cascade of secondary electrons are emitted from the target. These electrons then serve to ionize more of the surrounding sputtering gas and ultimately plasma is generated in the vicinity of the target. The plasma is said to be ignited once it has reached a self-sustaining state. Ions continue to bombard the target with sufficient momentum transfer to eject atoms from the target, which then pass through the plasma and sputtering gas to reach a substrate. The ejected material coalesces on this substrate to form the desired thin film.

The deposited atoms have a much higher kinetic energy and surface diffusivity compared to those generated by other PVD methods like evaporation, which results in several significant differences between the film microstructures. Sputtered films tend to have a higher number of defects from the high-energy impacts and more impurities due to the presence of the sputtering gas within the deposition chamber. Although the deposition chamber is typically evacuated to quite low pressures ($\sim 10^{-6}$ torr) prior to sputtering, the actual deposition occurs at around 0.1 torr after the sputtering gas has been introduced. When compared to evaporation, which occurs at pressures between 10^{-6} and 10^{-10} torr, there are simply more opportunities for contamination to be introduced. Where sputtering truly shines, however, is in its excellent versatility and controllability. A wide variety of materials can be sputtered, significantly better stoichiometric control is possible when multiple elements are being deposited, more uniform film thickness is achievable through the large area target and multiple deflections which occur while the atoms travel through the sputtering gas, and the film microstructure can be varied between amorphous to near-epitaxial.

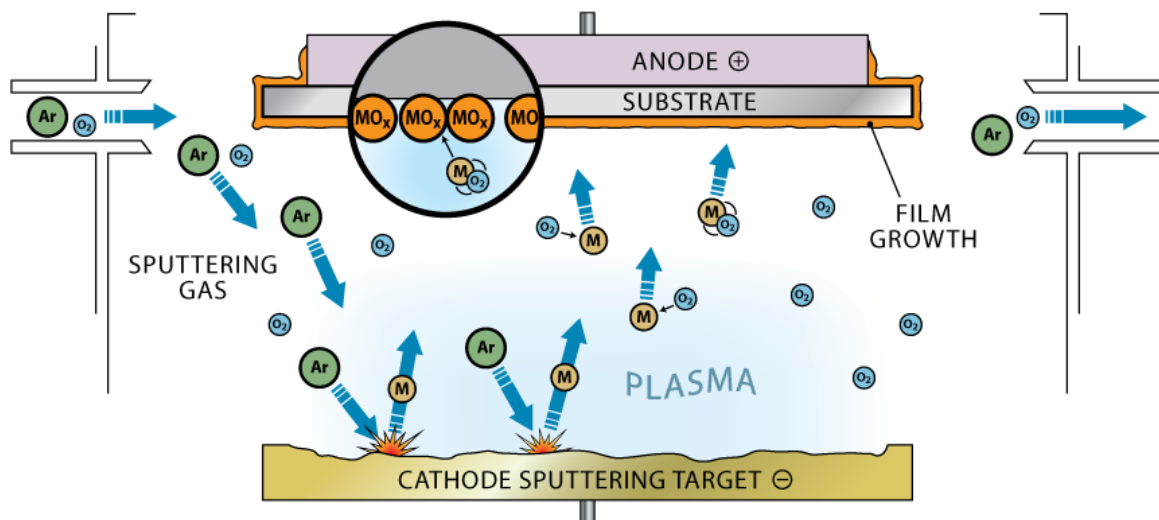


Figure 5: The basic components of magnetron sputtering include the sputtering target, the substrate, anode, sputtering gas, and plasma. Image taken from <http://clearmetalsinc.com/technology/>

The microstructure and stresses within the deposited film are strongly dependent upon the substrate temperature and the energy which with the sputtered material arrives at the substrate. Secondary factors include the direction and flux of deposited material, the atom adsorption probability, surface site density, and adatom mobility. The energy can be controlled directly through the applied voltage or by changing the pressure during the sputtering process. At higher pressures the mean free path of the particles within the chamber is reduced and there are more opportunities for momentum transfer to the sputtering gas. The temperature of the substrate dictates the adatom mobility on the substrate surface, with higher temperatures providing improved mobility. Various film microstructures, divided into three primary zones and a transition zone, are defined based on increasing substrate temperature and energy of the deposited atoms and shown in the structure zone model (SZM).

- Zone 1 occurs at low temperatures and low energies. With minimal adatom mobility growth occurs in the direction of the sputtering target and grain boundaries tend to contain many voids. Films exhibit a nanocrystalline columnar grain structure with a smooth sample surface. It is not uncommon for an intrinsic tensile stress to be present.
- Zone T is a transition zone in which surface diffusion becomes active. During the initial stages of growth there is competitive growth between grains of different orientations, resulting in an initially random texture which becomes more pronounced with increasing film thickness. The films in the transition zone exhibit a high surface roughness from potentially faceted growth. There is a fairly broad distribution of grain sizes within the film, packed densely into fibrous grains.
- Zone 2 is known as the reconstruction zone. Both surface and bulk diffusion take place extensively during deposition. The grain size is large while surface roughness is low. The film maintains a columnar grain structure.
- Zone 3 type films are deposited at the highest temperatures and energies. At this point there is sufficient mobility that a recrystallized grain structure with rather large grains is formed. Larger grains can consume larger ones during film growth and the orientation, while still textured, is more random than in the other structure zones.

Ideally films are sputtered to contain a modest intrinsic compressive stress to ensure that the film is fully dense, but will not buckle or delaminate from internal stresses. The intrinsic stress can be moni-

tored either during the deposition using a number of metrology methods, with laser-based wafer curvature methods being the most common. For most metals the intrinsic stress can be best regulated by controlling the pressure of the sputtering gas. At low pressures the film tends to exhibit a high density of columnar grain boundaries and an intrinsic in-plane tensile strain. By increasing the sputtering pressure a transition from tensile stress to compressive stress within the deposited film can be induced. Pulsed sputtering techniques, such as high-power impulse magnetron sputtering (HIPIMS), produce smoother and denser films than conventional magnetron sputtering.

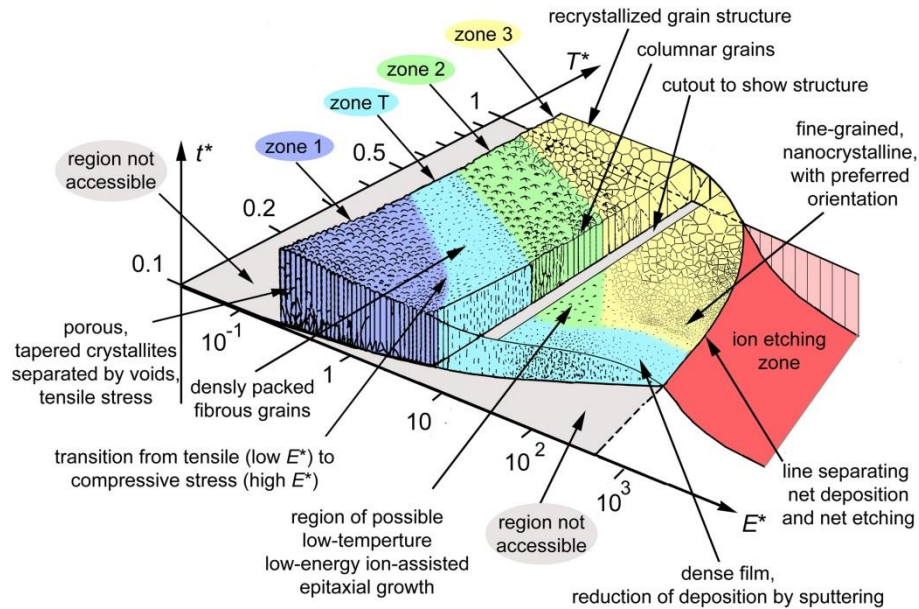


Figure 6: The structure zone diagram for sputtered films displays the relationship between film microstructure, temperature, and the energy with which the deposited material reaches the substrate [11], as originally reported by Thornton [12].

A number of variations on basic cathodic sputtering are used to achieve even greater versatility and more desirable film properties. Magnetron sputtering is a simple enhancement in which a magnetic field near the target helps to confine the plasma and improve the deposition rate by around two orders of magnitude, enabling deposition rates of several tens to hundreds of angstroms per second, depending on the material. Standard sputtering uses a direct current (DC) electrical field, but it is also possible to use alternating current (AC). This typically takes the form of radio frequency (RF) sputtering where typical frequencies range between 5 and 30 MHz. An electrical bias can be applied to the substrate as well to vary the energy and flux of the deposited material. High-power impulse magnetron sputtering (HIPIMS), in which brief ($\sim 100 \mu\text{s}$), intense ($\text{kW}\cdot\text{cm}^{-2}$) energy pulses are applied intermittently, produces dense, smooth films without overheating the target.

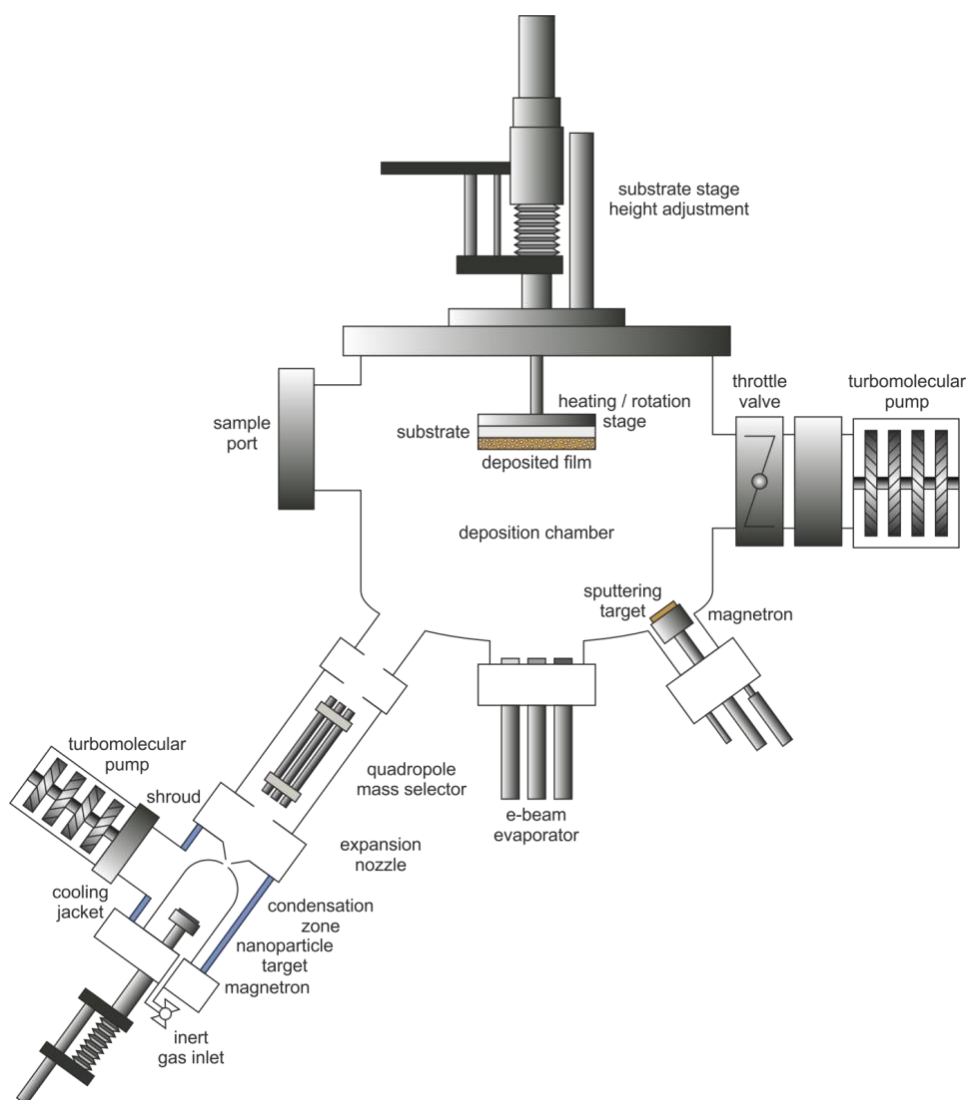


Figure 7: Schematic detailing the thin film deposition system used for the majority of the films deposited for this work. The deposition arrangement is from the bottom up to prevent unwanted particles, flakes, and other contamination from being incorporated into the films. Cusps around the base of deposition chamber can be used interchangeably for three types of deposition: sputtering, evaporation, terminated gas condensation of nanoparticles.

3.1.1 Co-Sputtered Compositional Gradient Films

Sputtering was used to deposit films containing multiple elements through simultaneous deposition, or co-sputtering. In the simplest case the a single composite target containing the desired film constituents can be used, but this offers limited control over the film stoichiometry. By instead using multiple targets, with each mounted in a separate magnetron gun, the deposition rate of each constituent element was adjusted independently through the individual magnetron gun power. For uniform film thickness and composition, the substrate was rotated throughout the deposition. However, it is also possible to use a stationary substrate to intentionally produce a film with a lateral compositional gradient. This effect is enhanced by arranging the spatial arrangement of the substrate and magnetron guns to maximize the difference in deposition flux across the substrate. Binary and ternary compositional gradients are common, but in principle the number of elements is limited only by the number of sputter guns available. If the sputter rate of each target is similar and an approximately linear deposition flux gradient is present, it is still possible to maintain a film with acceptable thickness uniformity despite the compositional variation. Since sputtering takes place far from thermodynamic equilibrium

it is possible for metastable phases to be present in co-sputtered samples. Limited diffusivity at the substrate often leads to the formation of solid solutions which can only be realized through co-deposition. If these metastable phases are not desired substrate heating can be employed during deposition to enhance adatom mobility or the entire sample can be annealed after deposition to ensure only equilibrium phases are present within the film.

3.1.2 Multilayer Thin Films

For a periodic bilayer of specified materials there are two variables: the bilayer thickness (often referred to as wavelength, Λ) and the ratio of one material to the other. For the sake of simplicity a constant volumetric ratio of 1:1 is used for most experimental investigations. Other volumetric ratios are also of interest, but experimental limitations usually restrict researchers to just investigating the basic size effect of varying the layer thickness. By adapting the stationary substrate approach used for co-sputtering materials libraries, however, a combinatorial approach to multilayer samples can also be pursued. Continuous thickness gradients in each layer are realized across the substrate using variable deposition flux. Each layer then has a wedge-shaped cross-sectional profile. When the two sputter targets are arranged at opposite ends of the substrate the volumetric ratio of the two component materials is varied while maintaining a film with acceptable thickness uniformity. By instead arranging the sputtering targets orthogonal to one another and the substrate it is possible to simultaneously explore all combinations of bilayer periodicity and thickness between the maximum and minimum individual film thicknesses, though this comes at the expense of having a variable film thickness.

Even greater control over sputtered multilayer films for combinatorial experiments can be achieved through the use of a shutter system for shielding parts of the substrate from the deposition flux. Rather than utilizing variable deposition flux, variable deposition time is used to incorporate thickness variation into the individual layers. This can be performed either continuously or stepwise, in which discrete patches of uniform thickness can be deposited. This is especially useful when larger areas of uniform sample are needed. More complicated strategies using shadow masks are also possible, but for the purpose of these experiments a more versatile shutter system was developed. Multilayer samples produced both with and without the shutter system have the potential to be used to produce compositional gradient films by depositing thin layers and performing a post-deposition anneal.

3.1.3 Nanoparticle Condensation

Nanoparticles were created using a variation of conventional sputtering using a process known as terminated gas condensation (TGC). In TGC sputtered ions condense in-flight within a separate chilled chamber to form nanoparticles before they are transported to the substrate in the main deposition chamber, as shown in Figure 7. The size of the nanoparticles produced can be varied from aggregates containing as few as 30 atoms to particles with a diameter of up to 20 nm. For these experiments single crystal nanoparticles with a diameter between 4 and 8 nm were produced. Three factors can be easily controlled to influence the nanoparticles produced: aggregation length, gas flow rate, and power used to sputter the target. Longer aggregation lengths and lower gas flow rates result in the formation of larger diameter particles, while sputtering power has little impact on the particles size [13].

The condensation zone is kept at a higher pressure to reduce the mean free path of the sputtered atoms and promote aggregation. Nanoparticles are conveyed to the main deposition chamber via a pressure difference, while the charged fraction of the particles can be manipulated electrostatically. This can be used to filter the particles by mass using a quadrupole, to modify the velocity with which the particles reach the substrate, or even focus the particles onto a smaller area. Both soft (minimal nanoparticle deformation) and hard (impacts where the nanoparticles deform appreciably) landings on

a substrate are possible depending on the electrostatic field used to accelerate the particles toward the substrate. Since TGC provides nearly the same degree of material versatility as conventional sputtering, it is possible to produce nanoparticle-reinforced films made of nearly arbitrary materials combinations. This is performed by co-depositing nanoparticles and sputtering a separate material simultaneously, as enabled by the differential pumping between the main deposition chamber and the TGC condensation chamber.

3.1.4 Focused Ion Beam Milling

Focused ion beam (FIB) milling is the standard route for preparation of micropillar for compression experiments. FIBs are in many ways analogous to scanning electron microscopes (SEMs), but utilize a beam of charged ions rather than an electron beam. While it is possible to use a number of different ions in a FIB, gallium has been established as the most convenient source owing to its low melting point, low volatility, and adequate mass to provide high milling rates. Most FIBs are used in conjunction with a SEM in a “dual-beam” system in order to facilitate visualization and modification of samples from different angles. The sample is manipulated within a vacuum chamber and is positioned at the intersection of the electron and ion beams for milling and imaging operations. The FIB impinges on the sample surface and can be used to remove material in a similar fashion to sputtering, albeit with significantly improved spatial resolution provided at the expense of overall material removal rate. Nanometer to micrometer sized features can be readily created using FIB milling.

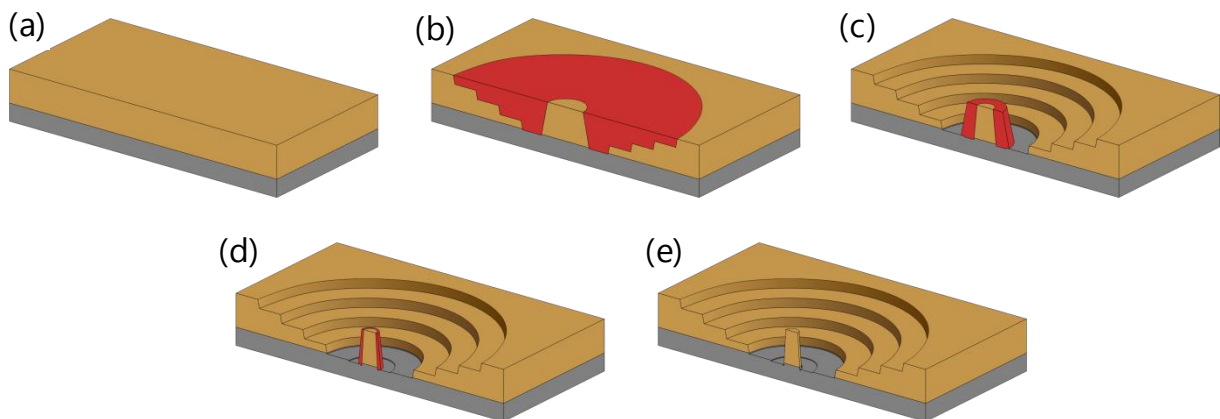


Figure 8: The standard 3-step FIB-milling procedure for producing a micropillar from a thin film is shown in cross-section. Red regions correspond to the volume removed in each step, the substrate is shown in gray, and the film is copper. The film and substrate (a) undergo rough milling (b), fine milling (c) and polishing (d) to produce a finalized micropillar (e). Reduction in milling current with each subsequent step minimizes the FIB damage imparted to the micropillar surface and helps to reduce the amount of sidewall taper. Care should be taken to prevent excessive milling into the substrate as it can be difficult to observe the pedestal height if there is excessive undercut, particularly in the final polishing step.

In general it is necessary to produce many micropillars for experiments as there is an inherently large scatter in most micropillar compression data. This scatter can be traced to the small volume of material being tested and microstructure-related local inhomogeneity within the sample. Micropillars are typically milled in compact arrays to enable a series of compression experiments to be performed without necessitating large sample movements. It is important that the craters produced in the rough milling step do not overlap since they also help to protect adjacent pillars from re-deposited material. FIB milling is essentially a localized sputtering process, so most of the material removed will ultimately end up deposited on another surface. Maintaining distinct craters for each micropillar obstructs any line-of-sight material re-deposition from accumulating on neighboring pillars. The final polishing step also helps to ensure that the pillar surface is pristine after manufacture.

The calculation of stress within the micropillars requires accurate knowledge of their physical dimensions, which will inevitably vary somewhat even if identical milling parameters are used for each micropillar. Pre-compression imaging is performed in a SEM, preferably from multiple viewing angles to ensure that all of the pillars are radially symmetric and free of major voids, damage, or defects. At least one oblique view and view from the sample surface normal are collected for each micropillar. In-situ imaging during the compression experiments can be utilized in order to gain insight into the pillar deformation mechanisms. Post-compression imaging offers a view of the pillar unobstructed by the indenter and provides higher resolution images than can be collected during the compression experiments.

Standard TEM lamellae preparation was performed using FIB milling and liftout. Trenches are milled adjacent to the area of interest and the lamella is attached to a needle using FIB-deposited platinum. The lamella is then cut free from the surrounding material and transferred to a TEM grid, where it is attached using additional FIB-deposited platinum and cut free from the needle. After the lift-out process it is necessary to thin the lamella further, improving electron transparency and reducing the amount of FIB-imparted surface damage. This surface damage from FIB milling is manifest in a variety of forms, including the formation an amorphous surface layer, implanted gallium ions, generation of dislocations, intermetallic phases, changes in grain size and orientation [14], and a number of other lesser effects. The depth of the damaged layer ranges from a few nanometers to several tens of nanometers and depends most strongly on the accelerating voltage used [15]. For TEM lamella preparation accelerating voltages as low as 1 kV are used for the final polishing step to ensure that the damaged surface layer is as thin as possible.

3.2 Material Selection

A number of different materials were used for the experiments presented in this thesis. Most of the films were metallic, so the crystal structure was one of the first selection criteria, while the atomic radius has a strong influence on the solubility and potential orientation relationship between different metals. For co-sputtered films it is possible to produce metastable solid solutions if the size difference between atoms is not too large. For multilayer films the crystal structure of the pure elements determines the nature of the interface. Totally incoherent interfaces, epitaxial interfaces, and other intermediate forms of alignment (Kurdjumov-Sachs, etc.) are possible. More generally any two materials with a strongly differing material property of interest can be chosen in order to produce composites with unique material properties.

Element	#	Structure	radius	Melting Point	Modulus	CTE
name	z	-	pm	K	GPa	$\mu\text{m}/\text{mK}$
Aluminum	13	FCC	143	933.47	70	23.1
Copper	29	FCC	128	1357.77	110-128	16.5
Magnesium	12	HCP	160	923	45	24.8
Nickel	28	FCC	124	1728	200	13.4
Niobium	41	BCC	146	2750	105	7.3
Silicon	14	FCDC	111	1687	130-188	2.6
Tungsten	74	BCC	139	3695	411	4.5
Zirconium	40	HCP	160	2128	88	5.7

Table 1: The basic material properties of select elements used in this work are given.

A number of basic material properties were considered in choosing appropriate materials for the studied films. The melting point is critical for tests which will be conducted at elevated temperatures. This is not only due to the softening which occurs at higher homologous temperatures, but also due to the increase in diffusion. Materials close to their melting temperature can diffuse much more readily. The coefficient of thermal expansion (CTE) is also a very important parameter for samples which will be tested at various temperatures. Temperature changes in composites with a large difference in CTE can result in very large stresses being generated.

The nature of the interface between the materials chosen for the multilayer films is another important factor which was considered. Titanium nitride was selected as ceramics provide totally incoherent interfaces which are impervious to dislocation transmission. The copper-tungsten material combination was chosen as the common material for all film architectures due to several criteria. Copper and tungsten are mutually insoluble, provide a hard/soft material combination, and offer an incoherent FCC/BCC interface. This data complements the wide body of literature for the well-studied Cu-Nb system and offers chance to compare broader applicability of models developed principally based on Cu-Nb findings.

3.3 Material Characterization

The combinatorial approach used during sample preparation results in large area samples with significant compositional variation. It is therefore critical that local material characterization can be, ideally quickly and non-destructively. The chemical composition and film thickness can typically be characterized quite quickly through several different techniques described below, though the sample microstructure is generally more involved. In general X-ray techniques are ideal as they allow rapid for rapid characterization without permanently altering or damaging the sample. Regardless of the characterization technique in question, the availability of a programmable sample stage with at least two axes is necessary to minimize the operator time required to complete sample characterization. Most modern instruments are equipped with a programmable x-y stage, enabling characterization routines to be programmed and left to run automatically over several hours or days. This process is sometimes described as “wafer mapping” since site-specific information is collected across a larger substrate.

3.3.1 Chemical Composition

Following sample deposition, the first material property of interest is the chemical composition of the deposited film. For pure elemental films this is typically already known, but chemical characterization is still worthwhile in order to ensure that impurities and contamination were not included in the film during deposition. For reactively sputtered and co-sputtered films the stoichiometry of the film is typically not known exactly after deposition and should be determined experimentally. Three methods were used to determine the chemical composition of the films produced during this work: X-ray fluorescence, energy dispersive X-ray spectroscopy, and glow discharge optical emission spectroscopy.

X-Ray Fluorescence (XRF) functions by using an X-ray source to excite the atoms within the sample, which subsequently relax and emit characteristic X-rays of their own. A Fischerscope X-Ray XDV was operated at 50 kV using a rhodium source excited at 50 kV. The utilized spectrum consists of both broadband Bremsstrahlung and rhodium’s intense characteristic X-rays. These X-rays are generated within a vacuum tube by accelerating electrons toward the rhodium anode from a tungsten cathode filament using a voltage around 50 kV. Elements heavier than rhodium and excited using the higher-energy Bremsstrahlung portion of the spectrum, while lighter elements are mainly excited by rhodium’s characteristic X-rays. This X-rays displace a core electron within the sample atoms, leaving a hole

in their place. An outer shell electron then replaces this hole, emitting a characteristic X-ray during its transition to a lower energy state. The wavelength of the characteristic X-ray emitted during this transition depends on the starting and ending energy of the electron. Siegbahn notation is commonly used to describe the characteristic X-rays which can be emitted. The energies and relative intensities of these fluorescent transitions provide an identifying "fingerprint" for each element. Energy dispersive X-ray spectroscopy (EDX), also utilizes characteristic X-rays to identify and quantify the chemical composition of a sample. EDX measurements were performed using an EDAX system mounted onto a Hitachi S-4800 SEM.

Glow discharge optical emission spectroscopy (GDOES) was used for chemical depth profiling, employing a Jobin Yvon 5000 RF system. GDOES is a destructive characterization technique, so sufficient sample should remain undamaged to perform any other desired tests. At least a 5-mm-diameter circle of material is needed to ensure that the vacuum seal is spanned by the sample. After clamping the sample in place, a vacuum is drawn before filling the test chamber with inert gas. Plasma is generated in a fashion similar to that described for sputtering, but with the sample of interest used as the cathode. The plasma erodes the sample uniformly, removing material for as long as the experiment is allowed to run. The eroded atoms are excited within the plasma and emit characteristic photons, which are in turn detected by a spectrophotometer. Monitoring the spectral variation as a function of erosion depth permits a chemical composition depth profile to be generated. In general some optimization of the gas pressure and power is needed to ensure that the crater remains smooth throughout the process.

3.3.2 Microstructure

The three primary tools used for the characterization of the film microstructure used in this work are scanning electron microscopy (SEM), X-ray diffraction (XRD), and transmission electron microscopy (TEM). Several different SEMs were used, including a Hitachi S-4800, a cold-cathode Tescan SEM, and a tungsten-filament Tescan SEM. A Jeol 2200 FS was used for the TEM measurements. A Bruker D8 Discover unit was used for all XRD measurements.

3.3.3 Mechanical Properties

A Hysitron Ubi nanoindenter was used to perform room temperature nanoindentation experiments using a diamond Berkovich tip. Elevated temperature nanoindentation was performed using an Anton Paar nanoindenter operated within a vacuum chamber to prevent sample oxidation during testing. Micropillar compression experiments were performed using two separate Alemnis nanoindenters, one equipped with the standard high temperature module and another modified for performing cryogenic experiments.

4 Compositional Gradient Films

Combinatorial science, the simultaneous preparation of many samples using a single process, drastically reduces the effort required to obtain experimental data. This approach is readily applicable to thin films deposited by physical vapor deposition. Co-sputtering is one of the simplest and earliest methods developed for preparing a combinatorial materials library [4]. Sputter targets are positioned to deliver a variable flux over a large, stationary substrate. The deposited film possesses a continuous lateral variation in chemical composition with minimal variation throughout the film thickness. Dubbed the Continuous Composition Spread (CCS) technique [2], large portions of binary and ternary phase diagrams can be covered in a single deposition through appropriate geometric arrangement of the targets and substrate. For screening applications the continuous composition spread approach is often preferable to the related discrete combinatorial synthesis (DCS) approach [16] as the likelihood of overlooking a composition of interest is reduced. The most critical consideration when implementing the CCS approach is that the film should be homogeneous within the characterization volume, so strongly localized methods are needed. As with all combinatorial approaches, rapid, automatable materials characterization techniques must be utilized to efficiently process the many sampling sites across the film.

4.1 Copper-Tungsten

4.1.1 Introduction

Copper and tungsten possess strongly differing mechanical and thermal properties, usually restricting their use to quite different engineering applications. Combinations of these two metals can be designed to exploit each of their respective strengths and develop high-performance materials. The high electrical and thermal conductivity of copper coupled with tungsten's exceptional abrasion resistance and refractory properties are effectively combined in modern arcing contacts for use in high-voltage circuit breakers, welding electrodes, and heat sinks for use in harsh environments. These parts are generally fabricated using powder metallurgy and infiltration to form a metal matrix composite in which copper and tungsten are present as chemically distinct phases. The formation of Cu-W alloys using traditional melt-based processing is not possible as the Cu-W binary materials system is immiscible across its entire range of compositions [17,18]. The immiscibility of Cu and W has been overcome to create actual Cu-W alloys in the form of films using a number of alternative techniques including ion implantation, co-evaporation, and co-sputtering. Ion implantation has been used to achieve tungsten contents of up to 10 atomic % in copper [19], whereas vapor condensation methods like co-sputtering and co-evaporation allow for any desired composition to be realized [20–22]. Depending on the deposition conditions used, the as-deposited film can be either amorphous or a metastable solid solution. The immiscibility of copper and tungsten can be circumvented by using fabrication processes operating far from equilibrium, enabling otherwise unachievable crystalline phases to be realized [23].

The immiscibility of Cu and W has been overcome to create actual Cu-W alloys in the form of films using a number of alternative techniques including ion implantation, co-evaporation, and co-sputtering. Ion implantation has been used to achieve tungsten contents of up to 10 atomic percent [19], whereas vapor condensation methods like co-sputtering and co-evaporation allow for any desired composition to be realized [20–22]. Compositional gradients in thin films obtained by co-evaporation or co-sputtering of multiple target materials enable a wide range of material combinations to be investigated through local microstructural and mechanical probing without the necessity of processing and studying individual composition specimens [3,4,24]. This 'multi-specimen' concept of compositional gradient or 'phase spread' thin films has been used for assessment of phase diagram sections in ter-

nary or multi- component systems [3,25] determination of optimal compositions for superconductivity, dielectricity [2], magnetism, etc. and has evolved to the combinatorial synthesis approach [1].

Previous work with co-deposited Cu-W alloy films has investigated material microstructure using scanning electron microscopy (SEM) and x-ray diffraction (XRD). Samples deposited at or near room temperature are described as having an amorphous microstructure due to the broad diffraction peak (FWHM of several degrees) present at 2θ values in the $39\text{--}44^\circ$ range and lack of obvious grains on the micrometer scale. This initial microstructure begins to form distinct crystalline phases after heating, beginning first with copper precipitation around 420 K and the formation of a metastable BCC solid solution at 670 K [20]. A triode sputtering setup has also been used to achieve notably thicker films (50-200 μm) exhibiting two distinct phases after deposition, the first with an amorphous appearance followed by an abrupt but jagged transition to a metastable BCC Cu-W intermetallic alloy. The amorphous-looking phase is most dominant when the W content lies between 40 and 45 atomic percent. Knoop microhardness tests showed increasing hardness with increasing copper content with the amorphous-looking being slightly softer than the BCC intermetallic alloy at identical chemical compositions [21]. While these two preliminary works have established the presence of metastable Cu-W intermetallic compounds and a potential metallic glass (amorphous phase), enough questions remain regarding the structure and mechanical properties of such films to merit further investigation.

Two metastable solid solutions have been reported in the literature: one face centred cubic (FCC) substitutional solid solution on the copper-rich side of the phase diagram [19,26] and one body centred cubic (BCC) substitutional solid solution on the tungsten-rich side of the phase diagram [22,27]. While initial reports estimated that the BCC to FCC transition occurred between 40 and 60 atomic % copper [27], no general consensus has yet been reached. Pinpointing the transition via experimental means is challenging as an amorphous region is sometimes encountered between the two metastable solid solutions, depending on the deposition conditions used. In one case this amorphous region occupies the entire region between 30 and 80 atomic % Cu [28]. More recent publications report the transition occurring at roughly 70 atomic % Cu [29], with *ab initio* simulations placing the transition at even higher copper contents, somewhere between 77 and 79 atomic % Cu [30,31]. These simulations are based on the assumption that kinetic limitations prevent the as-deposited film from forming separate Cu and W phases. The diffusion lengths of the deposited atoms determine which metastable solid solution is energetically favorable. As such the phase transition point is predicted to occur over a small range, depending on the deposition flux and substrate temperature.

In the case of amorphous films, a gentle annealing step results in the formation of a metastable solid solution whereas higher temperature annealing will result in complete separation into pure copper and pure tungsten phases [22,32]. For ion implanted films this phase separation has been reported to occur at annealing temperatures between 400°C and 600°C [19]. For sputtered films an exhaustive experimental study covering the entire compositional range utilized an annealing temperature of 750°C and annealing times of up to ten hours to separate metastable solid solution films into their constituent elemental phases [29]. Hardness is of upmost importance for Cu-W parts as wear-resistance and durability are essential. For this reason, most commercially relevant Cu-W alloys are on the tungsten-heavy side of the phase diagram. This is also the region selected here for study, ranging from 12 to 45 atomic % Cu. Vapor-phase deposition techniques for combinatorial studies of structural materials have been precluded in previous studies due to a desire for the bulk mechanical properties, and not those of a thin film [33]. The use of thin films is, however, completely justified for screening experiments and investigations of compositional trends, even if the quantitative strengths achieved are superior to those obtainable in bulk materials.

Early microhardness tests of BCC solid solutions (0-50 atomic % Cu) reported a hardness maximum at 18 atomic % Cu which exceeds that of pure tungsten by nearly 30%. [21] These tests were performed

using a Knoop indenter in very thick films (40-150 μm) and have not been repeated. Considering the columnar microstructure of the pure tungsten films, difficulty in obtaining fully dense tungsten films, and the potential for splitting grain boundaries with a Knoop indenter, it seems plausible that the pure tungsten film hardness was underestimated. A subsequent microhardness test performed in an amorphous film with 50 at. % Cu showed enhanced Vickers hardness over pure W, but the pure W films were noted to have a columnar porous structure with many large voids [34]. With only two compositions tested along with pure Cu and W films, insufficient data was provided to draw any conclusions about hardness trends. A third study by Zong *et al.* using nanoindentation also reported superior hardness to pure tungsten in metastable BCC solid solutions containing 9 and 21 atomic % Cu, whereas amorphous films with higher Cu content had hardness inferior to the Voigt model for rule of mixtures [28]. The low modulus of amorphous films was explained by reduced film density, but no explanation was given for the enhanced hardness in BCC solid solutions. Although the compositions at which hardness values exceed pure tungsten varied between these three consecutive reports, substitutional solid solution strengthening is the implied mechanism for increased hardness values.

The thorough evaluation of the Cu-W materials system recently performed by Vüllers and Spolenak, however, does not indicate any hardness enhancement whatsoever to pure tungsten with the addition of copper [29]. For copper contents above 40 atomic %, the hardness data from Zong and Vüllers is in good agreement, but between 0 and 40 atomic % the data from Zong *et al.* [28] is significantly higher, and in some cases double, that given by Vüllers and Spolenak [29].

This research seeks to address these discrepancies using nanoindentation to determine if enhanced hardness in tungsten is achievable through addition of copper. The contribution of various strengthening mechanisms and applicability of a simple rule-of-mixtures is discussed. X-ray diffraction and transmission electron microscopy are used to obtain microstructural information including crystallite size and lattice plane spacing. Microstructural variation as a function of chemical composition is also addressed.

4.1.2 Materials and methods

The Cu-W compositional gradient film was deposited on a 4-inch silicon (100) wafer (Semiconductor Wafer) by direct current (DC) magnetron sputtering system (Mantis Deposition Ltd, UK, Model: QPrep). The sputtering targets were copper (99.99% pure, 76.2 mm diameter \times 3 mm thick) and tungsten (99.95% pure, 76.2 mm diameter \times 3.18 mm thick). Prior to deposition the silicon substrate was cleaned in two subsequent 15-minute ultrasonic baths: first in ethyl acetate and then isopropanol. Pressurized nitrogen gas was used to dry the wafer before introduction into the deposition chamber. A base pressure below 1×10^{-5} Pa was achieved prior to deposition utilizing a turbo molecular pump backed by a dry rotary pump. In order to obtain a large compositional gradient the substrate was positioned closer to the sputter targets than for a typical deposition.

The sputtering of Cu and W was carried out in a pure argon atmosphere by continuous flow of argon gas through a mass flow controller into the chamber. Both of the targets underwent an argon sputter cleaning for 10 minutes with closed shutters to remove surface contaminants before deposition onto the substrate. The sputtering parameters for Cu-W film are given in **Table 2**. Pure copper and pure tungsten films were deposited in addition to the composition-spread sample to be used as references. Sputtering conditions for these films were identical to those used for the composition-spread sample, but with longer deposition time to reach a film thickness of 1 μm .

Base pressure	1×10^{-5} Pa
Sputtering gas	Argon
Gas flow rate	35 sccm
Sputtering pressure	0.22 Pa
Deposition time	3.5 hours
Cu target power	35 W
W target power	84 W
Substrate temperature	Room temperature

Table 2: Sputtering parameters used to deposit the Cu-W films

X-Ray Fluorescence (XRF) was used to characterize the thickness and chemical composition of the compositional gradient film. A Fischerscope X-Ray XDV was operated at 50 kV with a spot size of 3 mm to measure a rectangular grid of 8 cm \times 4 cm with 1 cm spacing between measurement points. A Hitachi S-4800 Scanning Electron Microscope (SEM) was used to obtain all micrographs. An accelerating voltage of 1.5 keV and a current of 100 pA were used to image the sample surface at a working distance of 5 mm. The mechanical behavior of the thin film with the compositional gradient film was studied by using a Hysitron Ubi Nanoindenter. The hardness & elastic modulus were extracted from the load-displacement curves obtained on impinging a Berkovich tip into the films by using the Oliver and Pharr analysis [35]. Maximum loads ranging from 1 to 5 mN were used in order to restrict the penetration depths to 10% of the total thicknesses of all the films with loading/unloading rates of 0.1 mN/s and a pause time at maximum load of 10 s.

When performing X-ray diffraction (XRD) measurements on a continuous composition spread film, it is necessary that the sample area illuminated by the X-rays exhibit sufficiently small variation in chemical composition to be considered homogeneous. For ternary composition spread samples a point focus is necessary, even when the compositional variation is gentle. Binary composition spread samples, however, can exhibit sufficient lateral homogeneity to permit the use of a line-focus configuration, keeping diffraction intensity high and measurement time manageable. The copper-tungsten sample prepared here exhibited minimal compositional variation across its 4 cm of width, making it an ideal candidate for characterization using a line-focus setup on a lab-scale diffractometer. A Bruker Discover D8 with Cu K $_{\alpha}$ radiation was used to collect the data shown in Figure 10. Initial measurements from 13 sites centered along the sample meridian at 5 mm intervals were collected across a 2 θ range from 30° to 110° with a step size of 0.2° and a collection time per step of 576 seconds. A 2° offset was used when performing the initial ω -2 θ scans to suppress diffraction peaks from the single-crystalline silicon substrate. A total of 68 detailed scans were then collected along the sample meridian at 1 mm intervals across a 2 θ range from 39° to 44° with a step size of 0.025° and a collection time per step of 384 seconds. These detailed scans were collected without any offset since there are no silicon peaks present across this 2 θ range.

A focused ion beam workstation (FIB, Tescan Vela) was used to produce three cross-sectional lamellae for transmission electron microscopy (TEM, FEI Tecnai F30) by the lift-out process. These three sites correspond to 15.4, 19.0, and 41.3 atomic % copper content and were selected owing to the enhanced X-ray diffraction intensity at these chemical compositions. The accelerating voltage of the ion beam was stepped down from 15 kV to 5 kV during ion polishing of the samples in order to reduce the thickness of the damage layer at the surface and minimize the energy input into the sample. The samples were left relatively thick prior to TEM analysis (~150 nm) in order to ensure that the metastable microstructure was not affected. Bright field imaging (BFTEM) and selected area diffraction of the film

was performed on each of the three samples. Additionally, high angle annular dark field scanning TEM and energy dispersive X-ray spectroscopy were performed on the three samples in order to investigate the compositional uniformity of the samples through the film thickness.

4.1.3 Results

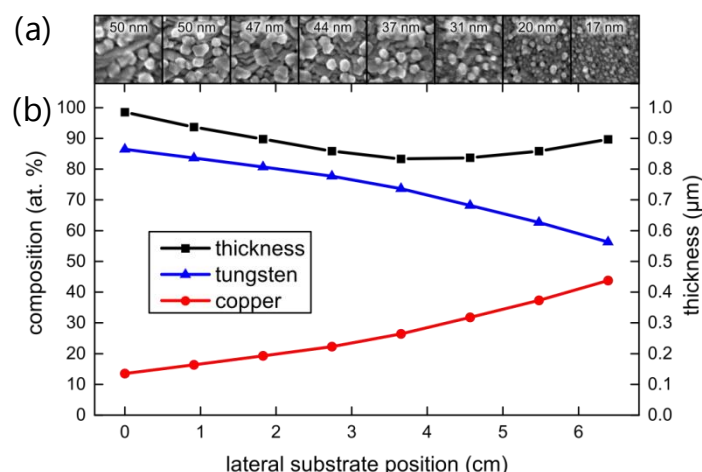


Figure 9: (a) SEM surface micrographs and their average surface feature diameters, exhibiting decreasing surface microstructure size with higher copper content along Cu-W compositional gradient film (b) smooth, continuous spatial variation of chemical composition and film thickness variation between 850 nm and 1000 nm as measured by XRF.

SEM surface micrographs across the length of the sample are shown in Figure 9(a). The faceted crystalline surface structures are largest near the tungsten-rich side of the sample and decrease steadily in diameter with increasing copper content. The diameter of these surface structures cannot be taken conclusively as the grain size since each feature could potentially contain smaller crystalline domains. As the sample was kept under vacuum for several hours after deposition it is not expected that any significant amount of surface oxidation has occurred as the sample returned to room temperature. *ImageJ* image analysis software was used to calculate the average diameter of these surface features.

Figure 9(b) displays the film thickness and chemical composition as measured by XRF. Data from the medial line is shown as excellent lateral homogeneity was achieved. Over a width of four centimeters perpendicular to the compositional gradient no significant change in chemical composition was observed. This enables a line-focus rather than a spot-focus to be employed for X-ray diffraction characterization of the film. A smooth, continuous compositional gradient is present in the film, ranging from 12 to 45 atomic % Cu. The film thickness varies slightly between 850 nm in the center to 1 μm near the ends, sufficiently small variation to perform nanoindentation experiments without significant influence from the substrate.

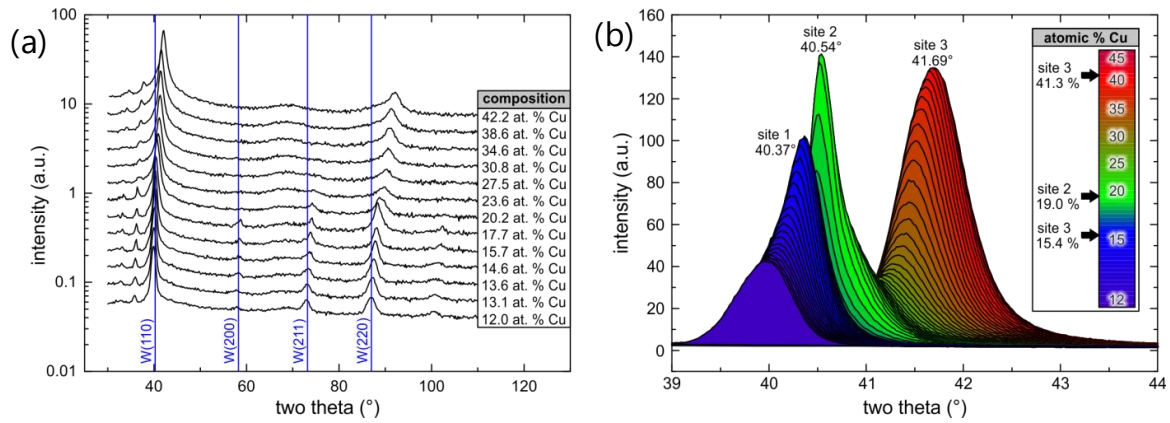


Figure 10: (a) Offset logarithmic plot of XRD scans from 30° to 110° consistent with a single BCC phase with no significant change in texture with changing chemical composition (b) Detailed scans from 39° to 44° with continuous variation in the diffraction angle and intensity of the {110} diffraction peak. Three sites diffract more strongly than the others, indicating enhanced long-range order at these chemical compositions.

The XRD scans shown in Figure 10(a) indicate a single BCC phase with a strong (110) fiber texture. A logarithmic representation of the data is necessary to see the weak (200) and (211) peaks, which are even then only detectable where there is low copper content in the film. Another small peak whose center shifts from 35.8° to 37.4° with increasing copper content is visible. This peak is attributed to the small amount of Cu-K β radiation passing through the nickel filter and also corresponds to the (110) peak of the BCC solid solution. More detailed scans of the strongly pronounced (110) peak between 39 and 44 degrees is given in Figure 10(b).

The main diffraction peak is observed to shift between the {110} peak for tungsten (40.34°) and the {111} peak for copper (43.32°) with increasing copper content. The absence of any discontinuities in peak position is indicative of a single solid solution phase with variation in average lattice parameter. Molecular dynamics simulations have been used to calculate the X-ray diffraction patterns for the similarly immiscible copper-tantalum system [36]. A continuous shift of peak positions was both predicted computationally and observed experimentally in this system, though the diffraction intensity was shown to abate with increasing concentration of solute atoms. In the copper-tungsten films presented here, three local intensity maxima are observed. As there is no significant change in film texture, it is hypothesized that these chemical compositions exhibit enhanced long-range order, leading to stronger diffraction.

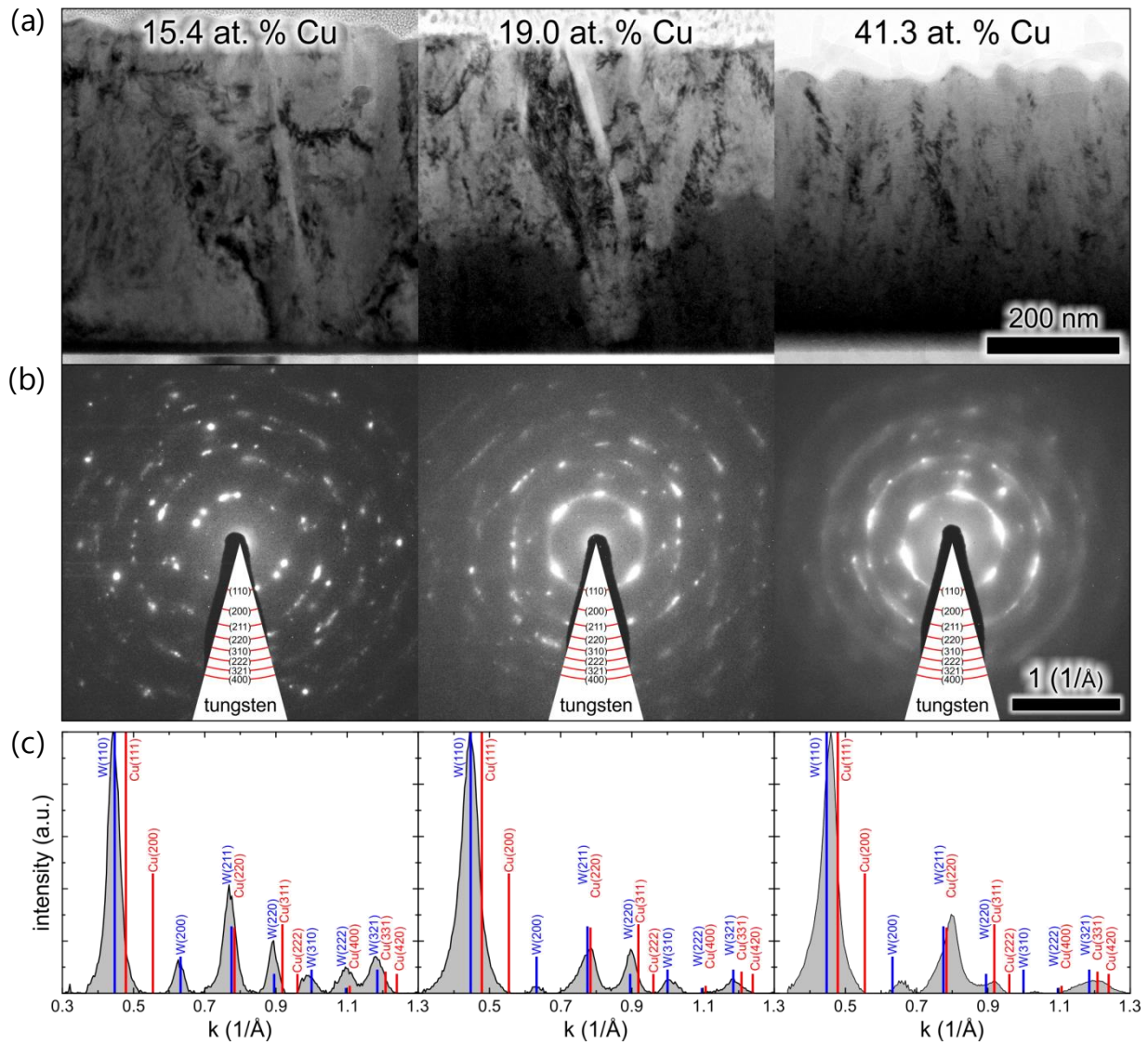


Figure 11: (a) BFTEM (b) SAD patterns and (c) radially integrated SAD intensity at the three chemical compositions for which the strongest X-ray diffraction was observed.

The microstructure and crystalline structure of the alloy at the compositions corresponding to the three XRD diffraction maxima were investigated using Bright Field Transmission Electron Microscopy (BFTEM) and Selected Area Diffraction (SAD), as shown in Figure 11. With the exception of a thin (18 nm) layer formed at the interface between the substrate and film for the 15.4 atomic % lamella, no evidence of secondary phase formation was observed. This interface layer is thin enough not to have had any impact on either the XRD or nanoindentation data. Initial BFTEM micrographs collected at 200 kV exhibited insufficient detail, therefore the BFTEM micrographs shown in Figure 11(a) were collected several months after the lamellae were produced at 300 kV to obtain higher resolution images and observe potential sample aging. The SAD patterns all correspond to a BCC crystal structure whose lattice parameter decreases with increasing copper content, and corresponds well to the more precise calculation of the plane spacing obtained via XRD. Multiple grains from within the film are diffracting in each SAD, though noticeably more grains, and therefore smaller grain size, are observed in the 41.3 atomic % Cu sample. All of the SAD patterns were collected using the same aperture diameter. Crucially, the TEM cross-sections confirmed that the films have deposited without porosity or grain boundary cracks; this is important for the measurement of mechanical properties via nanoindentation.

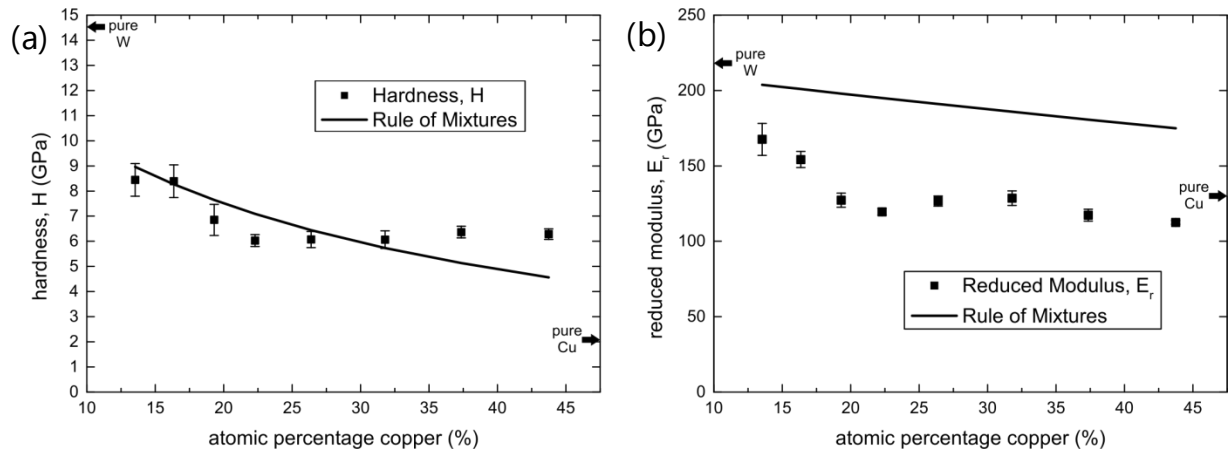


Figure 12: (a) Hardness and (b) reduced modulus of Cu-W compositional gradient film together with rule of mixture fits calculated from the measured values of pure copper and pure tungsten.

Figure 12(a) shows the change in hardness of the thin film with the compositional gradient as a function of the chemical composition while Figure 12(b) displays the reduced modulus. Values for pure copper and tungsten films are included as well. The copper film exhibited a hardness of 2.1 ± 0.1 GPa and a reduced modulus of 130 ± 5 GPa. The tungsten film exhibited a hardness of 14.5 ± 1.1 GPa and a reduced modulus of 218 ± 9 GPa. The hardness values for all compositions lay between the values for pure copper and pure tungsten, while the reduced modulus was inferior to that of pure copper across much of the investigated compositional range. Only once the chemical composition dropped below 20 atomic % copper was any improvement in modulus observed. Hardness values of the pure elemental films exceed those of their bulk counterparts, largely due to their nanocrystalline nature. In the case of copper additional contributions can arise owing to the higher elastic modulus of the silicon substrate.

4.1.4 Discussion

Despite the mutual insolubility of copper and tungsten under equilibrium conditions, a BCC solid solution was formed across the investigated compositional range. The (110) and (220) peaks were by far the most pronounced in the ω -2 θ XRD scans, which indicates a strong texture with the closest packed planes aligning parallel to the substrate surface, as is commonly observed in sputtered films. Due to the strong texture, the preparation of TEM lamellae and collection of SAD patterns was necessary to confirm the BCC crystal structure. The lattice parameter of this BCC solid solution decreases with increasing copper content and has been observed in previous studies [28,29], but the strong variation in diffraction intensity shown here has not been previously observed. As no additional peaks appear elsewhere, it is unlikely that the variations in intensity are due to a change in texture. Instead it seems plausible that these local maxima correspond to compositions at which the diffracting crystal domains are larger. As there is little variation in temperature and deposition rate across the substrate, locally enhanced surface diffusion at select compositions is potentially responsible for larger grain size. Although these maxima do not correspond to any discrete stoichiometric relations, they are hypothesized to correspond to atomic arrangements of improved stability. Surface diffusion arguments like those presented in Chang's model for metastable phase formation [30] could be extended to account for microstructural features as well.

Local minima in the diffraction peak full width at half-maximum (FWHM) correspond to the sites exhibiting the highest diffraction intensity. Amorphous films in this compositional range [28] exhibit a FWHM of 6.5° , whereas the FWHM of these films is generally around 0.7° . At the most pronounced diffraction point a FWHM of only 0.35° is observed. The crystallite size can be calculated using the well-known Scherrer equation [37]. Modifications to the Scherrer equation exist to compensate for system-

atic errors [38], but they rely on using multiple XRD peaks from the same phase. Owing to the strong texture of this sample, only the (110) peak was observed with sufficient intensity to apply the classical Scherrer equation (Equation 9) for calculating the lower limit of crystallite size, seen in Figure 13(b).

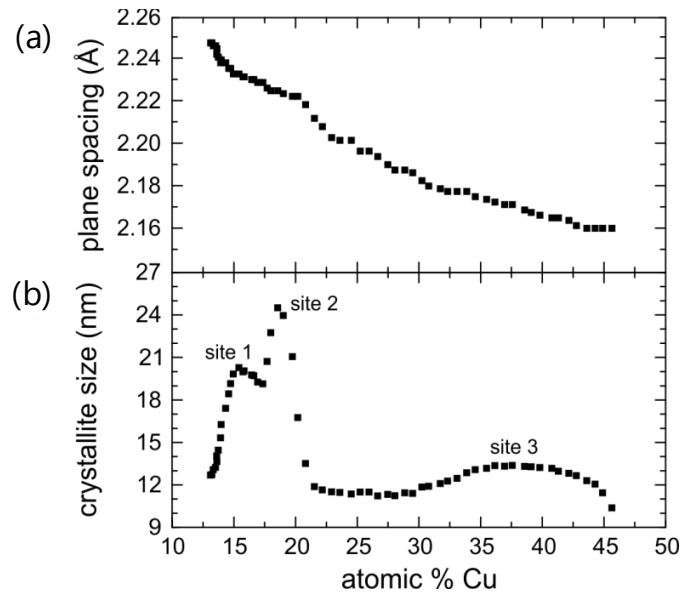


Figure 13: (a) Plane spacing and (b) crystallite size calculated using the Scherrer equation and the data from the detailed XRD scans seen in Figure 2(b)

$$\tau = \frac{0.9\lambda}{\beta \cos\theta} \quad \text{Equation 9}$$

In Equation 9, τ is the crystallite size, λ is the wavelength of radiation, β is the Full Width Half Maximum (FWHM) of the peak, and θ is the Bragg angle. There are a number of factors other than crystallite size which can contribute to peak broadening, though for this sample they are assumed to be near equivalent as the deposition was performed in a single run. The crystallite size calculated underestimates the actual grain size, but is sufficient for the purpose of relative comparisons within this sample. A strong correlation between total diffraction intensity and local minima in FWHM supports the hypothesis that larger grain size is responsible for the increased diffraction intensity.

Additional information can also be gleaned from the center position of the main diffraction peak, used to calculate the plane spacing shown in Figure 13(a). A negative deviation from Vegard's Law is observed as the plane spacing and volume of the solid solution are less than that predicted. This is not surprising as the interatomic spacing of tungsten along the close-packed [111] direction is 2.741 Å while the spacing of Cu along the close-packed [110] direction is 2.543 Å, i.e. Cu atoms are around 7.2% smaller. Deviation from Vegard's law [39] is commonly observed in solid solutions where the constituent atoms possess significantly different lattice parameters.

After several months of storage, extensive whisker growth was observed in the 41.3% at. % Cu TEM lamella. Energy Dispersive X-Ray Spectroscopy (EDS) revealed these whiskers to consist entirely of copper. These whiskers and the lamellar spinodal decomposition of the metastable metastable BCC solid solution into distinct copper and tungsten phases can be seen in Figure 11(a). The XRD experiments on this portion of the sample were repeated to determine if separation had occurred in the sample or just the TEM lamella. No change was observed in the XRD pattern, so the phase separation only occurs when a large free surface is available and sufficient time for diffusion is provided. The separation of the metastable copper-tungsten solid solution into an oriented, layered structure is presum-

ably related to the strong texture present in the as-deposited film. Similar microstructure through lamellar spinodal decomposition has been observed in copper-cobalt material [40]. While this phase separation is interesting when considering the long-term stability of these samples or as a potential strategy for preparing multilayer structures, it does not have any bearing on the mechanical properties of the film shortly after deposition since the metastable solid solution is still intact.

No hardness increase in tungsten films was observed through the addition of copper in this work. Prior reports of hardness enhancement are likely attributable to porosity within the pure tungsten films used for comparison [21,28,34]. Though the hardness does not exceed that of pure tungsten, there is a general trend for improved hardness with increasing tungsten content. Two approaches were followed to understand this hardness trend: first using superposition of hardening mechanisms calculated from models available in the literature and subsequently by applying a simple rule of mixtures. The well-known Tabor relationship [41] was used to convert the flow stress contributions to measured hardness by multiplying by a factor of 2.7. If the various strengthening mechanisms are assumed to be independent of one another it is sufficient to simply add the contribution of their individual effects to the hardness. The calculated hardness contribution for three models is plotted alongside the measured hardness data in Figure 12.

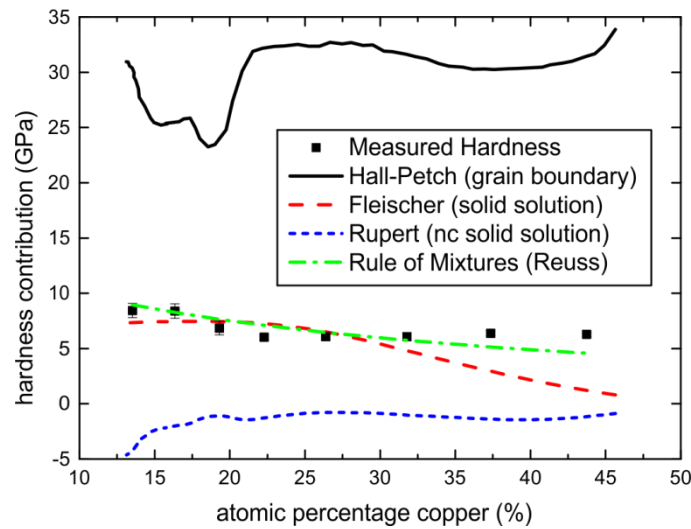


Figure 14: Calculated hardness contributions for Hall-Petch (grain boundary), Fleischer (solid solution), and Rupert (nanocrystalline solid solution) strengthening models together with measured film hardness.

4.1.4.1 Grain size strengthening

Additional strengthening is provided by the small grain size in this film. Grain boundaries inhibit the transmission of dislocations from adjacent grains, resulting in dislocation pile-up. This is described using the Hall-Petch relationship, given in Equation 10.

$$\sigma_y = \sigma_0 + \frac{k_y}{\sqrt{d}} \quad \text{Equation 10}$$

In Equation 10 σ_y is the yield stress contribution of grain boundary hardening, σ_0 and k_y are the empirically determined Hall-Petch constants, and d is the average grain size. Since the film investigated here contains more tungsten than copper and has a BCC crystal structure, the Hall-Petch constants for tungsten ($H_0 = 350 \text{ kg/mm}^2$, $k_y = 10 \text{ kg/mm}^{-3/2}$, given in terms of hardness) [42] were used rather than those for copper ($\sigma_0 = 30.4 \text{ MPa}$, $k_y = 0.15 \text{ MPa}\cdot\text{m}^{1/2}$, given in terms of yield stress) [43]. Several meth-

ods for grain size determination are possible. Firstly, the grain size can be treated as being equivalent to the crystallite size calculated using the Scherrer equation from the XRD data shown in Figure 10(b). This should be considered a lower bound of grain size and tends to overestimate the hardness contribution of grain boundaries. The surface micrographs of the sample cannot be used as the grain size as there is no guarantee that the surface features represent a typical grain within the material and not a surface oxide. The BFTEM micrographs provide another potential means for confirming the grain size, but grain boundaries were difficult to identify reliably for two of the samples as the grains are typically smaller than the lamella thickness. For these reasons the crystallite size from the XRD measurements was used for all of the following calculations necessitating grain size information [42]. At the smallest grain sizes the predicted hardness contribution approaches 35 GPa. Such high hardness is typically only observed in ceramics and other ultra-hard materials. For a metallic film, even one consisting largely of refractory material, this is an unrealistically high value for hardness. The Hall-Petch constants were determined using experimental data collected from grain sizes ranging from 100 μm down to roughly 250 nm. It is therefore suggested that the Hall-Petch constants reported in the literature are not valid at grain sizes below 100 nm. The applicability of Hall-Petch hardening is not evident in the data collected here as there is no obvious correlation between grain size and measured hardness. There is, however, a general trend of decreasing hardness with increasing copper solute concentration.

4.1.4.2 Solid solution strengthening

The introduction of foreign atoms into a pure material is a common tactic for improving flow strength, as first described by Fleischer using a discrete obstacle model [44]. In the model for substitutional solid solutions, hardening is achieved through the elastic interaction energy present due to both size and modulus effects. The energy contribution due to the size difference between the solute and solvent atoms is proportional to the lattice distortion term, as calculated using Equation 11:

$$\epsilon_a = \frac{1}{a_{\text{solvent}}} \cdot \frac{\partial a}{\partial c} \quad \text{Equation 11}$$

In Equation 11 the lattice distortion term ϵ_a is equivalent to the slope of lattice spacing versus solute concentration, and is typically obtained via X-ray diffraction. The lattice constant of the solvent is given by a_{solvent} and c is solute concentration. Over small ranges of solute concentration it is often sufficient to use a linear approximation and treat ϵ_a as a constant. Over a larger range the relationship may deviate significantly from linearity and a higher order fit may be necessary. For this data set a second order polynomial fit was applied to the data given in Figure 13(b), with the first derivative of this fit equivalent to the lattice distortion term at each site.

The energy contribution due to shear modulus difference between the solvent and solute is also determined empirically by calculating the shear modulus of the solid solution relative to the solvent. The shear modulus effect term is equivalent to the slope of the relative shear modulus vs. solute concentration plot, as given in Equation 12:

$$\epsilon_G = \frac{1}{G_{\text{solvent}}} \cdot \frac{\partial G}{\partial c} \quad \text{Equation 12}$$

Here ϵ_G is the local shear modulus change term, G_{solvent} is the shear modulus of the solvent, and c is again the solute concentration. In well-characterized systems, the shear modulus of the bulk material has been measured using torsion tests performed on samples spanning the range of solute concentrations of interest. Here, where bulk torsion samples of metastable Cu-W solid solutions cannot be readi-

ly produced, the shear modulus can be calculated using the measured elastic modulus from nanoindentation and assuming that the Poisson's ratio (ν) is equivalent to that of the solvent. In the case of tungsten, $\nu=0.28$. The relation between shear modulus G , elastic modulus E , and Poisson's ratio ν is shown in Equation 13:

$$G = \frac{E}{2(1 + \nu)} \quad \text{Equation 13}$$

After both the lattice distortion and shear modulus terms have been calculated, the total yield strength contribution for Fleischer's solid solution strengthening model is given by Equation 14:

$$\Delta\tau_{ss} = A \cdot G_{solvent} \left| \frac{\epsilon_G}{1 + \frac{1}{2} \cdot |\epsilon_G|} - \beta \cdot \epsilon_a \right|^{3/2} \sqrt{c} \quad \text{Equation 14}$$

Both A and β are empirical fitting terms, with A reflecting the magnitude of the strengthening while β reflects the relative contributions of the shear modulus and lattice spacing effects. In copper, a value for β of 3 is given, indicating that the modulus effect is the dominant hardening mechanism and that strengthening arises from interactions with screw dislocations [44]. In systems where the interaction between edge dislocations and lattice strains are dominant β takes a value between 16 and 32. The constant A is <1 , with a value of $1/700$ used where no specific fitting has been performed. [45]

The applicability of solid solution strengthening models over such a broad range of compositions is not widely established. Most solid solution strengthening models account for, at most, a few atomic percent of foreign atoms. Setting β as 25 and using the standard value of $1/700$ for A , a reasonable fit to the data can be obtained. While the exact trend is not closely followed, the hardness magnitude of several GPa and the decreasing hardening contribution with increasing solute content are both reflected in the Fleischer model. The total hardness, however, is less than that observed in pure tungsten. Similar softening behavior has been observed in many materials systems, particularly those with a BCC crystal structure [46]. This softening is not adequately addressed by use of the Fleischer model alone.

4.1.4.3 Nanocrystalline solid solution grain boundary pinning

A recent paper by Rupert et. al. [47] suggests that a new strengthening mechanism occurs in nanocrystalline solid solutions as an interaction between solutes and grain boundaries. This new mechanism was suggested based on the observation of a linear increase in yield strength with increasing solute content over a large concentration range of solute (0-20%), rather than the commonly observed square-root relationship observed in coarse-grained solid solutions. A model was derived using an approach similar to that used in the Fleischer model, but with an interaction parameter which considers global property changes rather than being limited to solute-dislocation interactions. The Rupert nanocrystalline solid solution model is given in Equation 15:

$$\Delta\tau_{nc,ss} \approx \frac{G_{solvent} \cdot b_{solvent}}{d} \cdot \left(\frac{1}{G_{solvent}} \frac{\partial G}{\partial c} + \frac{1}{b_{solvent}} \frac{\partial b}{\partial c} \right) \cdot c \quad \text{Equation 15}$$

The shear modulus is given by G , d represents the grain size, b is the length of the Burger's vector, and c is the solute concentration. This model accounts for both grain size and solid solution effects and can account for softening behavior in systems where solute addition results in a drop in shear modulus, as has been observed in nanocrystalline iron and nickel with copper solutes [48]. In both of these systems, the addition of copper reduces the shear modulus. For larger grain sizes there is a strengthening effect, but for nanocrystalline samples the addition of copper results in softening. As the addition of copper to tungsten also results in a reduction in shear modulus, this model predicts a softening effect across the full range of solute concentrations. The predicted softening, however, is strongest at low solute concentrations and does not fit the data well.

4.1.4.4 Rule of mixtures

None of the three above literature models provided an adequate fit to the data, nor did any combination of their contributions through superposition. The strengthening mechanisms considered do not appear to operate independently for this metastable copper-tungsten solid solution. The typical Hall-Petch grain boundary strengthening mechanism does not appear to be operative, either due to excessively small grain sizes or as a result of interference from other mechanisms. Solid solution softening rather than strengthening was observed as the sample hardness decreases with increasing solute content. Though no phase separation between copper and tungsten was observed, a simple rule of mixtures was also applied to model both hardness and reduced modulus. The Reuss model [49], given in Equation 16, is typically used to represent a lower bound value of the property of interest. This model, also known as the inverse rule of mixtures, is generally used to predict elastic modulus, though it can in principle be applied to any material property of interest.

$$H_{Reuss} = \left(\frac{V_f^{Cu}}{H_{Cu}} + \frac{V_f^W}{H_W} \right)^{-1} \quad \text{Equation 16}$$

The hardness H_{Reuss} of copper-tungsten mixtures is calculated using the respective volume fractions V_f and hardness, H , of pure copper and tungsten. This model provides a superior fit of film hardness compared to the other hardening models discussed, but systematically overestimates the reduced modulus of the film. As tungsten is elastically isotropic, the strong texture should have no impact on its elastic properties. The origin of the suppressed modulus values is unclear.

4.1.5 Conclusions

A combinatorial approach was used to deposit a copper-tungsten metastable BCC solid solution ranging from 12 to 45 atomic % copper. X-ray Diffraction (XRD) and Selected Area Diffraction (SAD) data show that a single BCC solid solution phase is present within the film. The shape, position, and intensity of the main XRD peak (110) vary continuously with copper content. Three local maxima are observed, corresponding to compositions at which larger grains have formed. The mechanical properties of the film, as determined via nanoindentation, vary with chemical composition. The hardness of pure tungsten was not improved upon by addition of copper, contrary to several previous reports, but corroborating the most recent investigations by Vüllers and Spolenak. Literature models for Hall-Petch hardening, solid solution hardening, and nanocrystalline solid solution softening were all applied in an effort to gain insight into the hardness of the film, though none provided an accurate representation of the observed hardness. In the absence of a more appropriate hardening model for the metastable copper-tungsten system, a simple rule of mixtures was applied and provides as an acceptable fit to the film hardness.

4.2 Aluminum-Copper-Nickel

4.2.1 Introduction

The aluminum-copper-nickel ternary materials system has attracted significant research attention, mainly due to its potential for use in shape-memory applications. At equilibrium there are a number of intermetallic phases which possess radically differing thermal, optical, and mechanical properties. For this experiment a ternary compositional gradient thin film is used to investigate the mechanical and optical properties of this materials system. Additional laser ablation experiments were performed to evaluate the applicability of using ternary compositional gradient wafers to evaluate film properties beyond the basic mechanical properties measured through nanoindentation. Laser ablation could be used to structure an array of smaller actuators within a sputtered Al-Cu-Ni film.

Laser machining has many advantages over conventional fabrication techniques [50,51]. Laser machining is often limited to simple 2D engraving and cutting patterns since three-dimensional machining of complex free-forms remains complex predict [52]. There are a number of competing mechanisms which influence the local material removal rates, making three-dimensional material removal with lasers much more complex than more traditional processes like CNC milling. One major reason for this complexity is the alteration of surface properties by the laser. Even small changes in the surface topology of the workpiece can lead to drastic differences in the laser-workpiece interaction. The absorption properties can change drastically, light can be reflected and absorbed elsewhere in the workpiece, and ablated material can even interfere with energy from the laser reaching the workpiece at all.

Time-resolved techniques have been used to study the dynamic aspects of laser ablation [53]. High speed imaging has also been used to understand the temporal development of laser-induced explosion phenomena during laser ablation on a microsecond scale [54]. Time-of-flight measurements have been used to monitor the individual ablation rates as a function of time for multi-component materials [55]. The influence of plume expansion on the laser-workpiece interaction must also be considered for accurate calculation of the workpiece's shape development during ablation [56]. Since there is no direct contact with the workpiece, laser ablation is an attractive technique for nearly all materials, ranging from pure metals[57], metal alloys [58], semiconductors [59], and many other materials. Even optically transparent materials are of interest [60]. For transparent materials the level of absorption should be high enough to initiate ablation. The plasma which is subsequently formed above the target area generally has a much higher absorptivity and leads to a drastic increase in the ablation rate after its formation.

4.2.2 Experimental

A combinatorial approach was used to study variation within the mechanical and optical behavior of Al-Cu-Ni thin films as a function of chemical composition. The ternary compositional gradient film used in this study was deposited on a 4-inch diameter silicon (100) wafer, in a magnetron sputtering facility (Mantis Deposition Ltd, UK, Model: QPrep). The targets used were aluminum, copper and nickel (99.95, 99.99 and 99.95% purity, respectively) and were sputtered simultaneously at different discharge powers to achieve the desired composition (RF—173 W, DC—67 W, DC—28 W, respectively). A turbo-molecular pump backed by a dry rotary pump ensured a base pressure of 2×10^{-4} Pa. The gradient was obtained by decreasing the target-to-substrate distance (8 cm) and deactivating substrate rotation. The sputtering gas used was pure argon ($\text{Ar} = 45$ sccm, 0.3 Pa) and the substrate was not actively heated. A total film thickness of 1 μm was targeted in order to provide sufficient material for both nanoindentation and laser ablation experiments to be conducted.

Both X-ray fluorescence (XRF) and energy-dispersive X-ray spectroscopy (EDX) were used to perform chemical mapping and film thickness measurements. The XRF measurements were performed using a Fischerscope X-Ray XDV with a rhodium X-ray source operated at 50 kV. Measurement times of 5 minutes per measurement site were necessary in order to obtain reliable measurement of the aluminum content due to the high absorption of aluminum's characteristic X-rays in atmosphere. EDX measurements were performed in a dual-beam FIB-SEM Tescan Lyra. Evaluation of chemical composition and film thickness was performed using STRATEGem film analysis software. An acquisition time of 1 minute was used for each of the measurement sites. Measurements for both XRF and EDX were performed in a grid with 1 cm spacing.

The laser ablation experiments were performed using a SPI G4 20 W HS Series L Type air-cooled nano-second pulsed fibre laser operated under atmospheric conditions. The laser wavelength was 1064 nm and had a focused spot size diameter of 49.8 μm . The sample was subdivided into square regions with a side length of 5 mm, with one set of experiments being performed in each sample sub-area. A constant laser fluence of 4.54 J/cm² and pulse duration of 30 nanoseconds was used to produce several dozen ablation craters in each sub-area. Longer pulse durations were not possible without completely ablating the film and reaching the silicon substrate. Prior to the laser ablation experiments optical characterization was performed using a Perkin Elmer UV-Vis-NIR Lambda 900 spectrophotometer. An integrating sphere was used to identify the total reflectivity of the film (both spectral and diffuse components) at 1064 nm (the wavelength of the laser used for the ablation experiments). The beam size was roughly a 5 \times 10 mm rectangle. A mask was used to ensure that only the region of interest was measured. Reflectivity measurements were conducted in a square grid with 1 cm spacing.

Sample imaging was performed using scanning electron microscopy (SEM, Hitachi S-4800). Sample surfaces were imaged after deposition, after the laser ablation experiments had been conducted, and after cross-sections of the laser ablation craters were prepared by focused ion beam (FIB) milling. A dual-beam SEM-FIB Tescan Vela instrument was used to prepare cross-sections using a two-step process. First, a rough cutting step with high Ga ion beam (30 kV beam and 3 nA probe current) was used to mill a rectangular trench, followed by a fine polishing step (30 kV and 1 nA) in the area of interest. The size of surface features was determined from the micrographs using ImageJ software. Atomic force microscopy was also performed to determine the film roughness and the size of surface features. An AFM NT-MDT Solver Pro-M was operated in tapping mode using a tip with a nominal radius with 15 nm. Topographic parameters (root mean square roughness and height–height correlation length) were obtained from the 10 \times 10 μm^2 AFM scans using Gwyddion software.

Nanoindentation was performed using a Hysitron Ubi nanoindenter using a diamond Berkovich indenter tip. The indenter was operated in load control using loading, hold, and unloading times of 10 seconds. Sixteen indents were performed at each test site with the load increasing from 4 to 10 mN. The average hardness and reduced modulus values for all sixteen indents are given.

The dimensions of each laser ablation crater were measured using an optical microscope (Alicona InfiniteFocus). Three-dimensional reconstruction of the ablation craters was performed using focus variation. A magnification of 20 \times was used, with a corresponding resolution of 50 nm vertically and 2.93 μm laterally. The ablated volume per crater in any area of constant chemical composition was calculated by averaging the values measured across ten different craters. The analyzed craters were chosen away from the line ends to avoid the distortions in laser footprint which can occur at the beginning and end of each line due to variation in feed speed. The ablated volume was calculated as the difference in volume between the crater volume beneath the reference plane and the volume of the rim of re-solidified material, which rises above the target surface Figure 15. In some cases error can be introduced through enclosed voids in the re-solidified material, but generally this error is small.

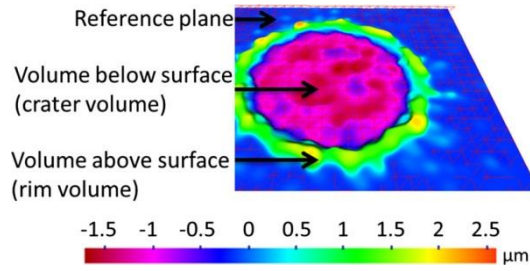


Figure 15: A typical site exposed to laser flux results in an ablated crater and a raised rim around the crater circumference of re-deposited material. The ablation volume is taken to be the difference between the crater volume and that of the re-deposited rim. Surface topology measurements were performed by varying the focus of an optical microscope.

4.2.3 Results

The Al-Cu-Ni compositional gradient thin film covers a chemical composition range between approximately 0 and 50 atomic percent aluminum, 25 and 75 atomic percent copper, and between 25 and 75 atomic percent nickel. This area represents one-fourth of the total ternary phase diagram, roughly half of which is covered by the wafer sample. As such, one-eighth of the entire ternary phase diagram is represented by this single sample. The area along with the chemical composition of the measurement sites are shown in the diagram on the left in Figure 16. Several distinct regions of the equilibrium phase diagram are contained within this experimental region, containing a total of four different phases, given in Table 3.

Symbol	Phase	Structure
α	Ni-Cu	FCC solid solution
α_1	$\text{Ni}_3\text{Al-Ni}_2\text{CuAl}$	FCC superlattice
β_2	NiAl	BCC superlattice
γ	Cu_9Al_4	Complex cubic

Table 3: Equilibrium phases present in the portion of the Cu-Al-Ni ternary phase diagram covered by the lateral compositional gradient sample.

The reflectivity of the film was also mapped in a similar fashion to the chemical composition mapping, as seen in the diagram on the right in Figure 16. The reflectivity was only measured at 1064 nm since this is the wavelength used for the laser ablation experiments. Visual inspection of the sample reveals a minor change in color while the entire film has a metallic, mirror-like appearance. This indicates that the spectral component of the film reflectivity is quite high and that surface roughness is sufficiently small to prevent much diffuse reflection from occurring. The reflectivity increases from 63% to nearly 70% with increasing aluminum content.

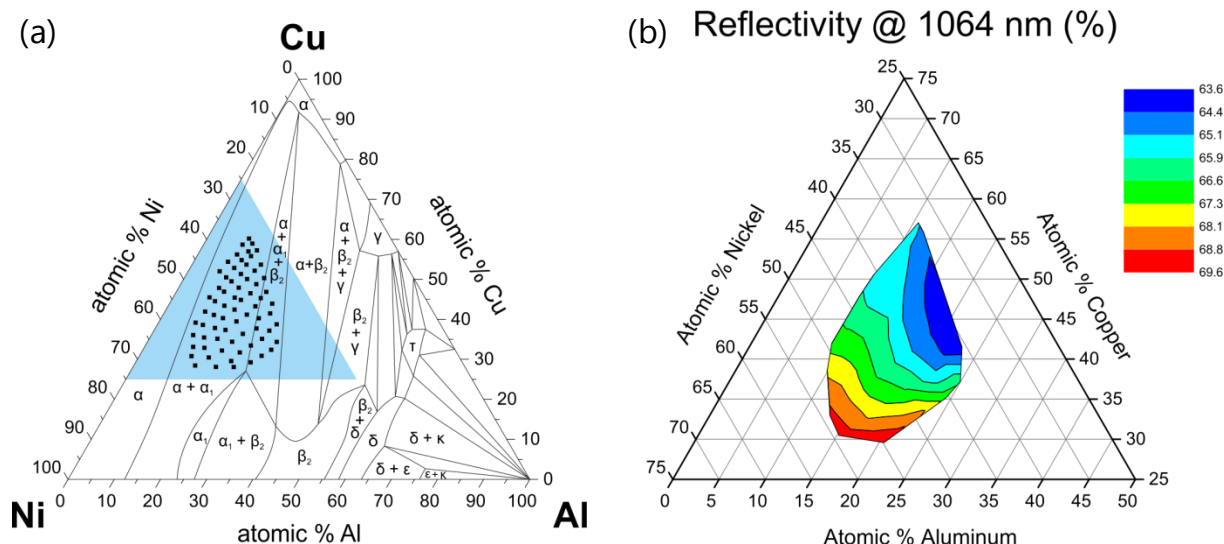


Figure 16: An equilibrium phase diagram for the ternary Al-Cu-Ni system is presented (a). The sputtered compositional gradient sample contains near equal parts of each component. Four distinct phases can occur within this region of the phase diagram, though the actual number can vary according to the presence of metastable phases or insufficient kinetics for the film to reach an equilibrium phase. The total film reflectivity at a wavelength of 1064 nm is presented in (b).

Since the Al-Cu-Ni materials system is well-known for its shape-memory alloy applications, the microstructure of the film was also investigated using X-ray diffraction. A strong diffraction peak corresponding to the (111) reflection of a face-centered cubic crystal was observed across the entire wafer, though the exact diffraction angle and full-width half-maximum of the peak varied. The position of the peak was used to determine the d-spacing of the (111) planes and the Scherrer equation was applied to determine the crystallite size as a function of chemical composition. These results are shown in Figure 17. The d-spacing values are accurate since the values given represent the average plane spacing within the area of the sample illuminated by the X-ray spot. The crystallite size, however, cannot be interpreted quantitatively since it is calculated from the width of the peak. The measured peak is essentially a convolution of all the material under the illuminated spot.

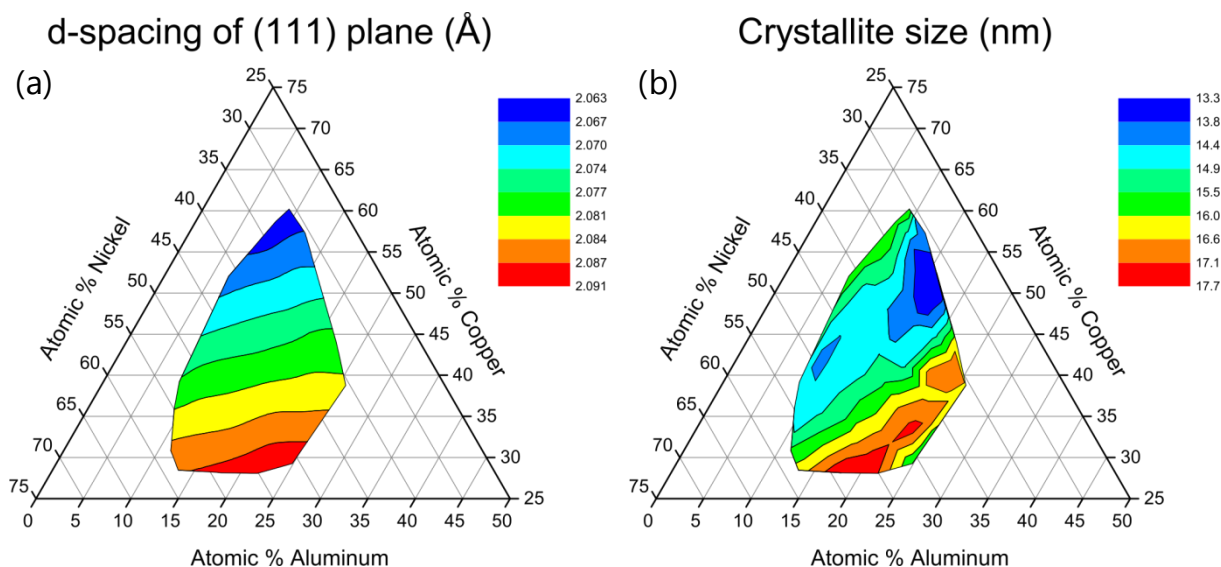


Figure 17: X-ray diffraction mapping of the Al-Cu-Ni combinatorial gradient sample reveals an increasing lattice constant with decreasing copper content and, to a lesser extent, increasing aluminum content (a). The Scherrer equation was used to calculate the crystallite size (b). Significant peak broadening occurs due to the large beam size and variation in chemical composition, therefore the values given are not quantitative, but rather give an impression of relative crystallite size between different sites on the wafer.

The surface of the sample was also inspected using a scanning electron microscope (SEM) in order to ascertain if there were any local changes as a result of the different chemical compositions. A selection of five surface micrographs representing the characteristic surface topology is shown in Figure 18. Each of these sites was also scanned using an atomic force microscope (AFM) to quantify the surface roughness. Portions of the film with a high copper content tended to be the smoothest, with only small surface features visible. Where aluminum content is the highest the surface is drastically rougher and is visibly covered in tooth-like surface features. These denticle protrusions are oriented in a fashion which suggests that the oblique positioning of the sputtering target may play a role in their formation. The larger structures roughly correspond with the portions of the wafer at which larger crystallite sizes were calculated, indicating that they are likely crystalline.

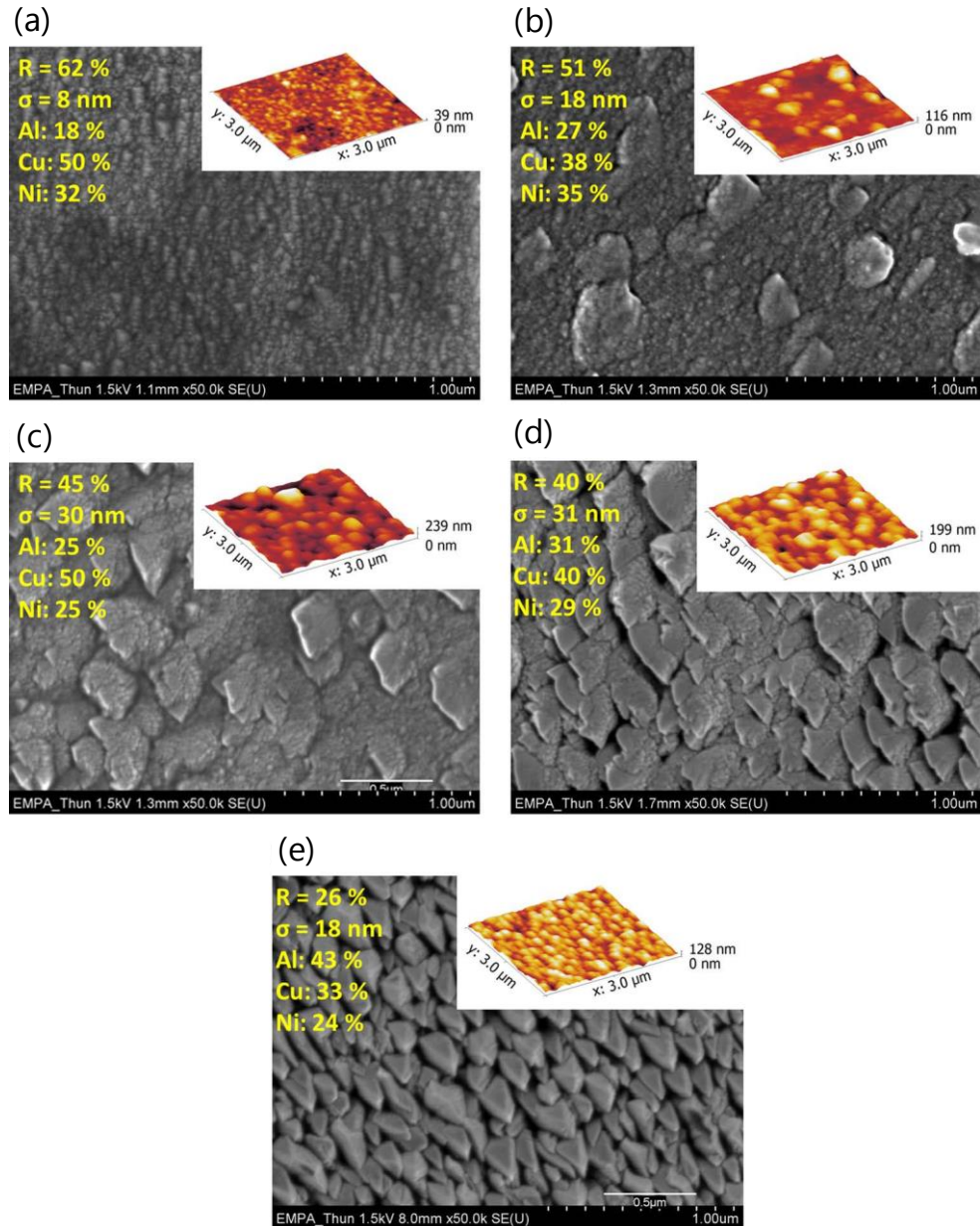


Figure 18: SEM micrographs are shown alongside AFM scans for representative site on the Al-Cu-Ni compositional gradient film. A wide variation in surface topology is observed, ranging from smooth surfaces (a) to denticle protrusions (e).

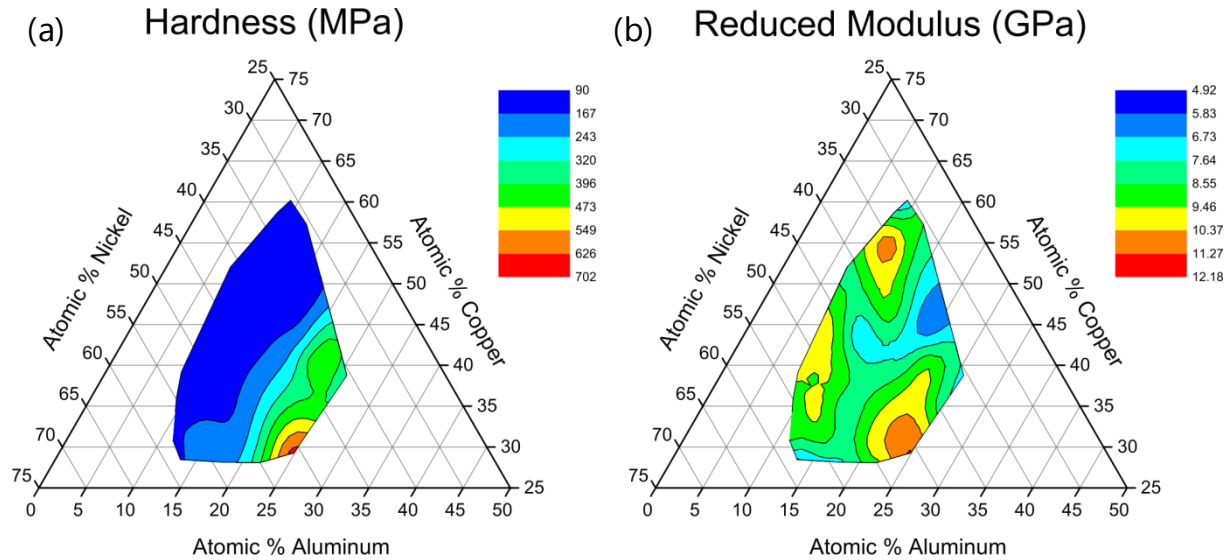


Figure 19: Nanoindentation was used to map both the hardness and reduced modulus of the Al-Cu-Ni compositional gradient film as a function of chemical composition. Film hardness increased with increasing aluminum content, whereas the modulus exhibited several local maxima.

Figure 19 shows the results of the nanoindentation experiments. The hardness varies drastically across the film and falls a clear trend of increasing hardness with increasing aluminum content. Where the aluminum content is the highest, the hardness reaches 700 MPa, as opposed to just 90 MPa where the aluminum content is the lowest. The reduced modulus does not exhibit a clear trend like the hardness, but still varies significantly between 5 and 13 GPa.

Figure 20 shows the characteristic crater profiles for several sites across the compositional gradient film. Again, a clear trend as a function of aluminum content is observed. Large lips of raised material form at the edge of the ablation craters where the aluminum content is the lowest. Increasing the aluminum content somewhat causes the overall depth of the ablation crater to decrease slightly while the height of the crater lip decreases appreciably. At even higher aluminum content the crater depth and diameter increase while the raised lip at the crater edge disappears completely.

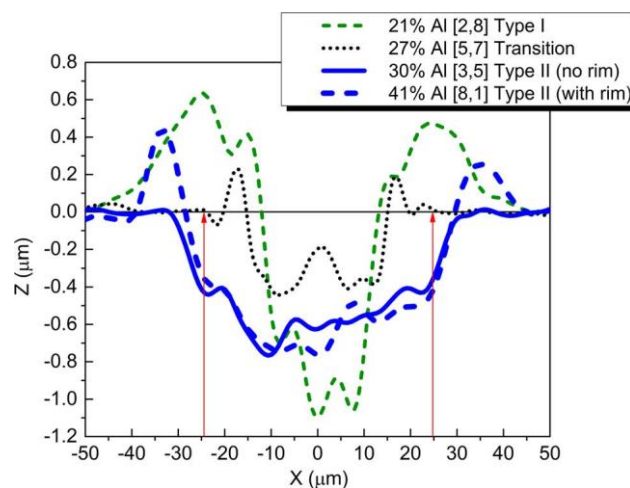


Figure 20: Increasing the aluminum content while maintaining the ratio of copper-to-nickel results in a steady progression to higher ablation volumes. Craters with low aluminum content had a small diameter and a wide rim of re-solidified material. At aluminum content of 30 atomic % the ablation craters did not show any raised lip whatsoever. Increasing the aluminum content further to 41% resulted in a sharp, relatively pronounced lip. The red arrows indicate the beam diameter.

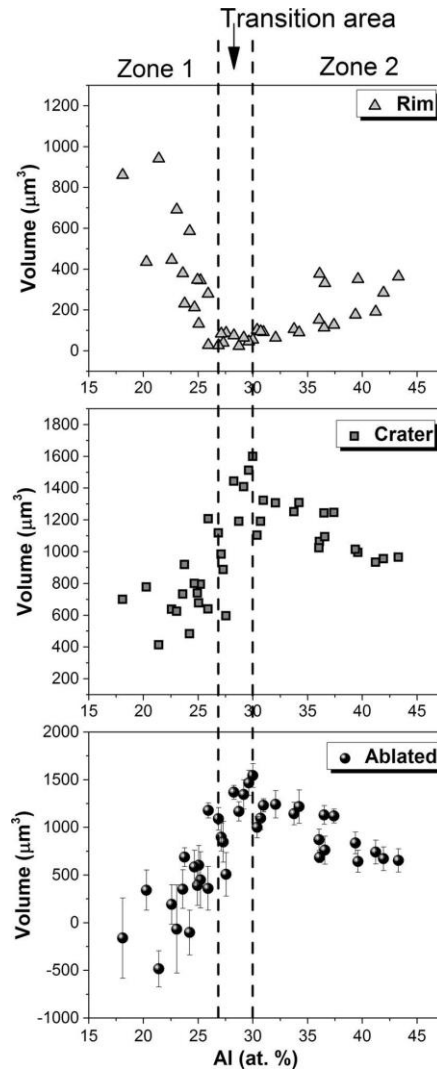


Figure 21: Rim (top), crater (middle), and ablated (bottom) volumes given as a function of aluminum content. A transition zone between 27 and 30 atomic % aluminum is observed, above which the ablation volume increases drastically. Further increases in the aluminum content results in a gradual decrease in ablation volume.

Figure 21 shows the measured volume of the raised rim, the ablation crater, and the difference in volume between the two. Two distinct zones are identified based on the aluminum content, separated by a narrow transition region. In the first zone, where the least aluminum is present, the volume of the raised rim on the perimeter of the crater is observed to decrease with increasing aluminum content. In this zone the ablated volume of the crater is observed to increase. This trend continues up to 30 atomic % aluminum. At this point the maximum ablation volume and smallest rim volume are reached. As the aluminum concentration continues to increase there is a gradual decrease in the total volume of the ablation crater as the rim feature reappears.

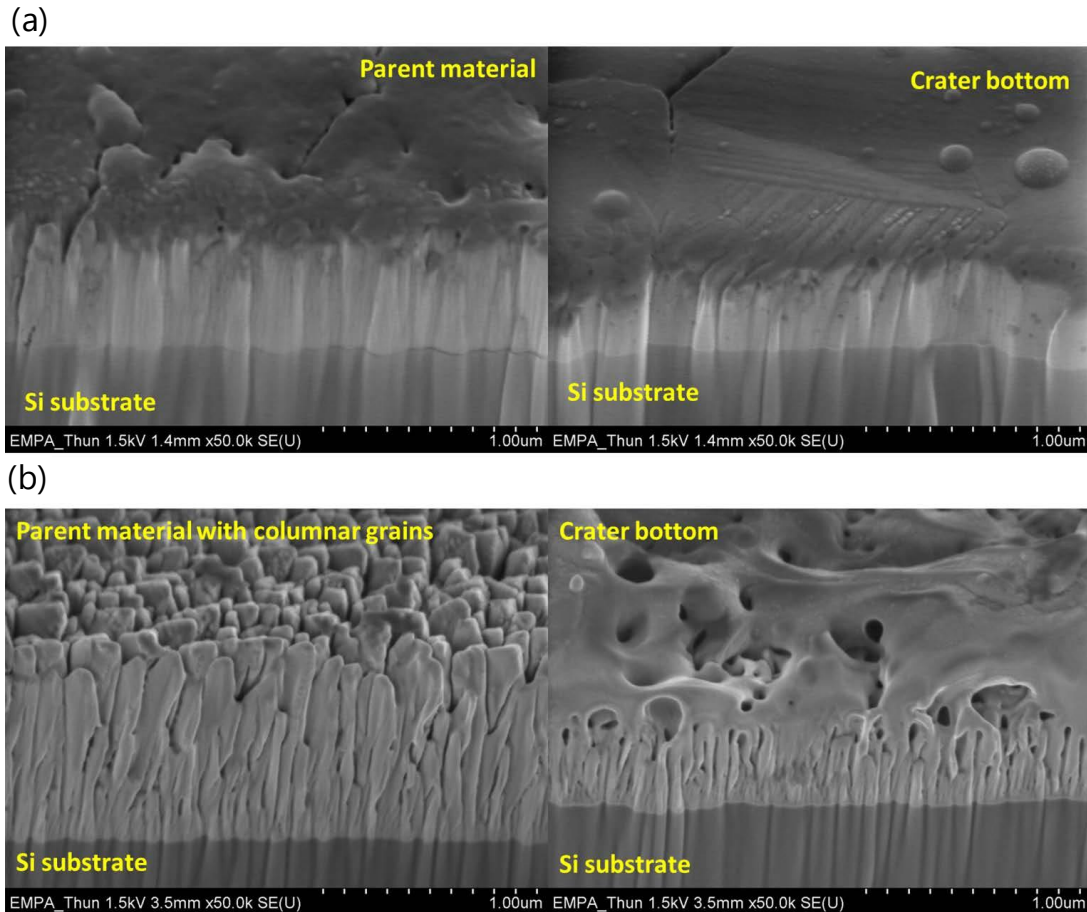


Figure 22: SEM images of film cross-sections prepared by FIB milling show the as-deposited film (left= and bottom of the ablation crater (right). Portions of the film exhibiting a low volume of ablated material (a) do not show the significant signs of melting and re-solidification that are seen in areas of the film which resulted in larger ablation volumes (b).

4.2.4 Discussion

One-eighth of the Al-Cu-Ni ternary diagram could be covered using a single compositional gradient sample. X-ray diffraction demonstrates that the lattice parameter of the solid solution increases with increasing aluminum content. Considering the lattice parameters the pure elements (aluminum = 404.95 pm, copper = 361.49 pm, and nickel = 352.4 pm), this trend is in agreement with the size of the individual atoms. By overlaying the portion of the ternary diagram covered by this sample with the equilibrium phase diagram it can be concluded that there are three possible chemical phases contained within the wafer. The film hardness improves markedly with the addition of aluminum, indicating that the NiAl phase is the major contributor to film hardness. The modulus could not be determined with sufficient precision to draw any conclusion about its dependence upon chemical composition.

The 30-ns IR laser irradiation of a metal thin film places the ablation process in the thermal regime, which consists of three main steps. (1) Laser radiation is absorbed by the workpiece in an area under the surface equal to the skin depth (several nm in the case of metals irradiated with IR), and the amount of energy delivered to the sample is directly related to its reflectance at the laser wavelength (1064 nm). (2) The energy is then distributed to the rest of the material by heat transfer. The maximum temperature and depth are dictated by the thermal properties (e.g. thermal diffusivity, fusion and boiling points, melting and evaporation enthalpies) of the thin film, as well as the surface morphology and topography. Particularly in the case of thin films, heat transfer is influenced by the thickness of the thin

film, substrate type and the nature of the interface between the two. (3) Significant ablation occurs when the surface reaches the vaporization temperature, or even sooner (around the melting point), depending on the pressure at the target surface. Depending on the laser pulse duration and thermal properties of the thin film, heat transfer to the substrate may become important and lead to the ablation of both film and substrate.

The sample thickness varied between 1 and 1.35 μm and was used as a reference when analyzing crater depth. Previous experiments on laser ablation of metallic thin films have demonstrated that the ablation threshold increases linearly with the film thickness up to the thermal diffusion length, after which it remains constant [61]. A simple calculation of the thermal diffusion length for each of the elemental film components is useful for understanding heat transfer in these experiments. Using a film thickness of 1 μm and a pulse duration $\tau=30\text{ns}$, the thermal diffusion length is given by Equation 17:

$$\delta_{th} = \sqrt{2\tau \left(\frac{k}{\rho c} \right)} \quad \text{Equation 17}$$

where k is the thermal conductivity, ρ the density and c the specific heat of the material. The thermal diffusion length is therefore 2.25 μm for aluminum, 2.60 μm for copper, and 1.16 μm for nickel. The thermal diffusivity at room temperature for all three materials was taken from [62]. As the film thickness is less than the thermal diffusion length and the beam diameter in focus is around 50 μm , heat conduction is effectively unidimensional and the thermal behavior of the system is affected by the properties of silicon, with the substrate acting as a heat sink in these experiments.

The reflectivity of the film is lower than the reflectivity of the respective pure metals at 1064 nm (Al ~ 80%, Cu ~ 90%, and Ni ~ 70% [63]). The film reflectivity depends not only on the chemical composition of the film, but also relies upon the surface finish. The SEM surface micrographs and AFM measurements of surface roughness indicate that there is a negative correlation between surface roughness and film reflectivity. Even the largest surface features are significant smaller than the laser wavelength, but they still provide additional scattering and absorption opportunities. At the highest aluminum concentration these surface features are the largest and most plentiful. The formation of these surface structures is postulated to be a combination of both the variation in chemical composition [64] and a result of the angle between the sputtering targets and the substrate during film deposition [12]. When sputtering from oblique angles it is not uncommon for the film to grow toward the sputtering target. This has been exploited in the path for producing films with tilted columnar grain boundaries and “zig-zag” films, in which the grain boundaries alternate their direction of tilt throughout the film thickness.

4.2.5 Conclusions

A smooth, continuous compositional gradient was produced through co-sputtering pure aluminum, copper, and nickel targets. Despite the difference in flux between the three targets, a fairly uniform film thickness was achieved, varying from 1 μm at the thinnest portion of the film to 1.35 μm at the thickest region. This film thickness was sufficient to perform nanoindentation, reflectivity, X-ray diffraction, and laser ablation experiments. The ablation threshold decreases with an increase in the aluminum percentage. Besides the compositional gradient, the target had a morphological gradient as well, which was similar to the distribution of aluminum in the sample. The structures varied in size (from 10 to 500 nm) and shape, and their presence might have played a role in both the decrease in the sample reflectivity (at 1064 nm) and the thermal contact between the thin film and the silicon substrate.

Based on the variations found in the geometrical and morphological characteristics of the craters and the sub-surface changes, as well as on the variations in the ablated volume, two regions were identified, separated by a transition area (between 27 and 30 at.% Al).

In the first region, the ablated volume was proportional to the amount of aluminum in the sample; the craters were deeper and narrower and the sub-surface was noticeably affected by heat; a higher amount of re-deposited material compared to the second region was present, which indicated that the energy delivered by the beam was close to the ablation threshold. In the second region, the craters were wider and shallower, and the sub-surface showed little heat damage; the variation of the volume was inversely proportional to the amount of aluminum, despite the threshold continuously decreasing. We have attributed this behavior to the increase in plasma density followed by partially decoupling of the workpiece from the incoming laser radiation.

Contributions: The laser ablation experiments and the topological characterization were performed by Simina Rebegea. Simina also drafted several of the figures used in this section. Selection of deposition parameters and sample deposition was performed by Laszlo Petho and Keith Thomas. FIB cross-sections of the ablation craters and SEM imaging were performed by Keith Thomas. Reflectivity measurements were also performed by Keith Thomas. All authors contributed to discussion while the text was prepared collaboratively between Simina Rebegea and Keith Thomas. The majority of these results have been published as "Laser ablation of a Cu–Al–Ni combinatorial thin film library: analysis of crater morphology and geometry " [65].

5 Multilayer Thin Films

By operating the different sputtering guns sequentially rather than simultaneously it is possible to deposit multilayer thin films as well. There are many practical applications for multilayer materials, including hard coatings, electrical interconnects, optical mirrors, and semiconductor devices just to name a few. Most of these applications use many layers of differing composition and thickness to fulfill different needs within the thin film (i.e. adhesion layers, diffusion barriers, etc.), while others employ periodic structures (Bragg reflectors, Göbel mirrors, etc.). Beyond their practical uses, periodic bilayers are also ideal structures for research purposes as they allow for the role of interfaces and size effects from different layer thicknesses to be investigated. A single bilayer stacked periodically enables the properties of very thin layers to be determined using methods which require larger sample volumes (nanoindentation, micropillar compression, etc.). These periodic bilayer structures are often referred to as nanolaminates or simply multilayers.

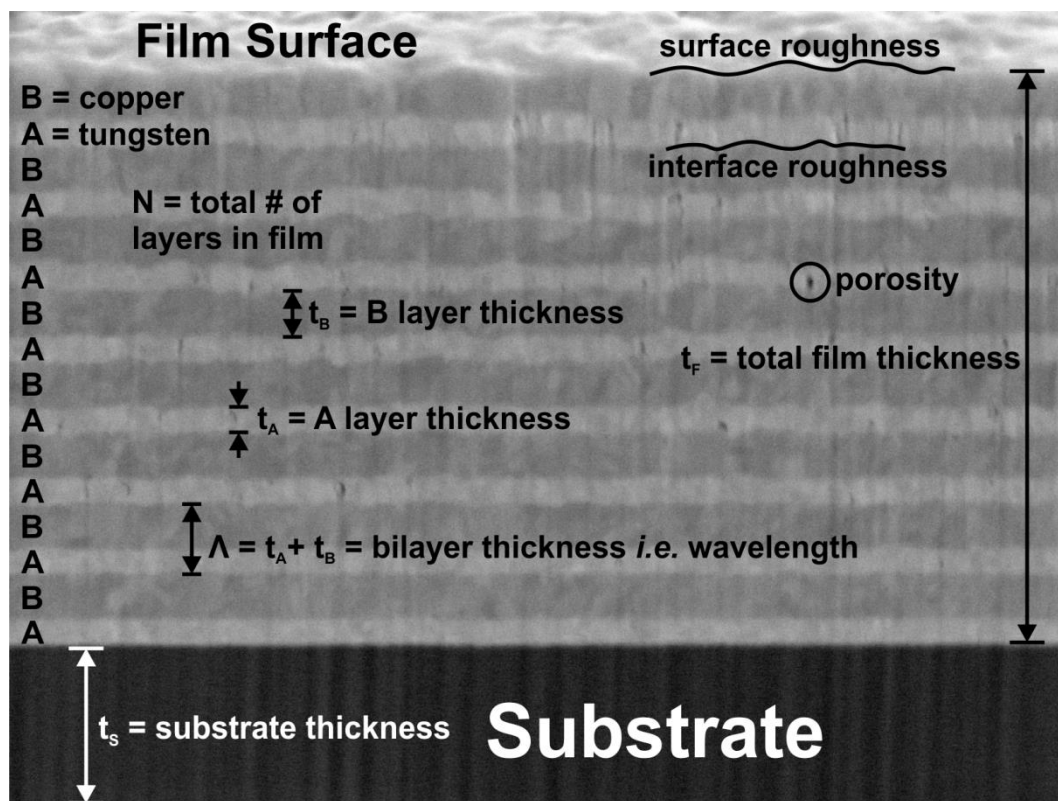


Figure 23: FIB cross-section of a Cu-W multilayer thin film with labels showing the terminology used to describe periodic bilayer films.

Multilayer films can be considered as two-dimensional laminar composites. The ideal loading orientation is therefore perpendicular to the film interfaces and surface. This makes their study via nanoindentation and micropillar compression very convenient, though other loading configurations have also been investigated. Tensile tests are more commonly performed transversely, with the tensile load being applied parallel to the layer interfaces. When sufficiently thick films are available it is also possible to mill micropillars in such a fashion as to allow compression experiments to be performed at oblique angles or even parallel to the interfaces as well [66].

Periodic bilayer thin films are generally useful as test structures for investigating the role of interfaces and size effects in addition to their use as optical elements (Bragg reflectors, Göbel X-Ray mirrors, and waveguides) and in semiconductor devices (lasers and LEDs). Periodic bilayers are a specific class of

multilayer films in which two materials are alternately deposited onto a substrate, keeping the individual layer thickness of each material constant. They are frequently used to investigate the mechanical strengthening observed at nanoscale periodicities, where a total film thickness on the micron scale enables nanoindentation, micropillar compression, micro-tensile testing, or a number of other mechanical tests to be performed. Loads applied perpendicular to the bilayer stack then effectively test a series of bilayers, allowing the mechanical properties of a single bilayer to be extracted through comparison with strengthening models.

Factors determining the strength of multilayers include the inherent strength of the constituent materials, differences between the elastic moduli of the materials used, the thickness of each layer, and the type of interface (coherent, incoherent, etc.). In metallic multilayers the various strengthening mechanisms function by inhibiting dislocation movement [67]. At thickness on the order of a few hundred nanometers to microns, dislocation pile-up provides strength in a fashion similar to the classical Hall-Petch relationship. Further reduction of layer thickness to tens of nanometers provides sufficient confinement to permit only a single dislocation to fit within each layer, bowing between the upper and lower interfaces. Misfit dislocations can reside at the interfaces to relieve some of the local stress [68]. Dislocation bowing is often described as being analogous to the Orowan mechanism in particle-reinforced composites. Once layer thicknesses reach the single-digit nanometer or thinner range, the resistance of the interface to dislocation movement and the nature of the interface become dominant. Depending on the constituent materials, this can result in either a strengthening or softening effect [8]. One notable exception to this general rule is the case in which there is a large elastic mismatch between the two materials. In this case it is not dislocations which are responsible for hardening, but rather the buildup of hydrostatic stress within the material with a lower modulus of elasticity. The stiffer material experiences a lateral tensile stress while the more compliant material is subject to the resultant compressive stress [69]. These stresses are largest in the center of the pillar and decays near the pillar edges, where the interface no longer provides as much lateral constraint. These "soft-hard" material combinations are especially interesting as they provide much higher strengths than would ordinarily be achievable with such high proportions of the softer material.

5.1 Copper-Tungsten

5.1.1 Introduction

Plasma-facing components in nuclear fusion reactors present another potential application for Cu-W composites. Tungsten has been the material of choice for these components in a number of projects including the international ITER project for fusion and in the ASDEX, EAST, and JET tokamaks due to its high melting point, low sputtering rate and low tritium retention [70,71]. Copper on the other hand is often selected when high thermal conductivity is of importance, as is the case in heat sinks [72,73]. Using tungsten-based alloys as the plasma-facing surface with a copper backing to facilitate cooling would be ideal, but this design is difficult to synthesize because of the difference in coefficients of thermal expansion. Functionally graded composites (compositional gradient in depth) have been formed by special sintering processes and electron beam welding to minimize the stress developed due to thermal stresses present in these components during operation [74,75]. Other promising designs combining the desirable properties of both copper and tungsten seem feasible, including nanolayered composites. Superior tolerance to radiation damage has been demonstrated in Cu-Nb nanolayered composites [76], so it seems reasonable to assume that Cu-W systems may exhibit similar radiation tolerance improvements.

5.1.2 Experimental

5.1.2.1 *Thickness gradient layers*

Traditional multilayer samples strive to achieve homogeneous layers, permitting only one design variation to be realized in each experimental run. By instead forgoing a uniformly thick layer and intentionally incorporating a thickness variation across the substrate, the experimentalist can create a continuous range of effective sub-samples in a single experimental run. Prerequisites for this strategy include:

1. The film growth method must allow variable film thicknesses to be deposited across the substrate. Physical vapor deposition (PVD) processes like sputtering, evaporation, and molecular beam epitaxy (MBE) are especially well suited for depositing thickness gradients. Two basic strategies for realizing this gradient exist: the movable shutter strategy and variable flux strategy. In the former strategy a shutter is slowly moved between the film material source and substrate to shade a variable region of the substrate, limiting deposition at any given time to the exposed substrate area. The shutter can be moved incrementally, allowing step-wise thickness variation and resultantly more homogeneous sub-sample areas. If substrate rotation is desired, the shutter must rotate along with it. In the latter strategy the film material source and substrate are positioned relative to one another such that a variable flux of film material impinges upon the substrate and film growth occurs at variable rates at different locations across the substrate. Substrate rotation should be eliminated completely. Figure 24 illustrates these two strategies schematically. Conformal film growth methods like atomic layer deposition (ALD) are unsuitable for growing thickness gradient films. Chemical vapor deposition (CVD) processes could potentially be adapted for thickness gradient growth by fixing the substrate and allowing for mass depletion in the reactive species, but the control of these processes would not be as straightforward as for PVD processes.
2. The area to be characterized should be small enough to be considered as having a homogeneous thickness. One advantage of the movable shutter strategy is especially apparent here as the substrate can be divided into homogeneous sub-samples areas of arbitrary sizes. Regardless which strategy is used to create the thickness gradient, automatable testing techniques will greatly facilitate speedy film characterization. Motorized XY linear translation stages can be readily programmed to move to different sites on the substrate, enabling a map of the entire substrate to be created.
3. The characterization method should be restricted to a localized subsample area and remain uninfluenced by the material outside of this area. For optical and mechanical measurements this is likely to be the case, but for thermal and electrical measurements it may be necessary to isolate the selected sub-sample area by means of a mesa etch or by dicing the substrate into physically separate sub-samples.

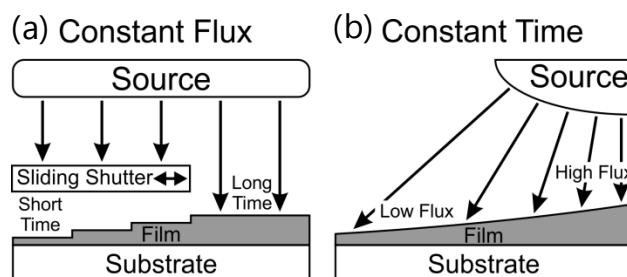


Figure 24: (a) sliding shutter and (b) oblique source methods for variable film thickness deposition

5.1.2.2 Orthogonal Wedge Geometry

An individual variable-thickness layer is useful on its own, but it does not allow for interactions between that layer and the rest of the multilayer film to be easily investigated. Incorporating a second variable-thickness layer with its thickness gradient perpendicular to the first provides a path for direct investigation of any interactions between the two layers. Figure 26 depicts a bimetallic multilayer film consisting of alternating copper and tungsten layers sputtered atop a silicon substrate. Cross-sections of the films were cut using a focused-ion beam (FIB) and then imaged using a scanning electron microscope (SEM) at 4 sites near the wafer perimeter to elucidate the film variation across the substrate. In this type of bi-material multilayer both the multilayer periodicity and thickness ratio of the two components are varied across the wafer. Most publications investigating the mechanical properties of two-component multilayers to date simply fix the volumetric ratio of component layers at 1:1 and vary layer thicknesses. Other studies have recognized the potential significance of component ratios and have chosen instead to fix one layer thickness and vary the component layer thickness ratio. An exhaustive investigation of both layer thicknesses and thickness ratios relying upon traditional sample geometry would require a prohibitively many experiments and as such has not yet been performed. The merits of the orthogonal wedge geometry are made especially clear in this regard as an enormous range of film thickness and material ratios can be investigated in just a few experimental runs.

A common strategy for investigating size effects in multilayers is to select a fixed thickness ratio of the two components (most commonly 1:1) and vary the bilayer periodicity (Λ) [77]. There is no guarantee that size effects within the two component materials appear at identical thicknesses, so some studies instead choose to keep one of the layer thicknesses constant and vary the layer thickness ratio [78]. Incorporating a thickness gradient into one of the component layers allows for a range of layer thickness ratios to be investigated on an individual substrate. These thickness gradient films are sometimes referred to as having wedge geometry because of their cross-sectional profile [79]. As was the case for compositional gradient films, the substrate should be kept stationary during deposition. Since this is a multilayer structure the targets are sputtered sequentially rather than simultaneously, with the inactive target being shielded from contamination by a shutter while the active target is being sputtered. Figure 25 shows the deposition setup needed to achieve wedge geometry films.

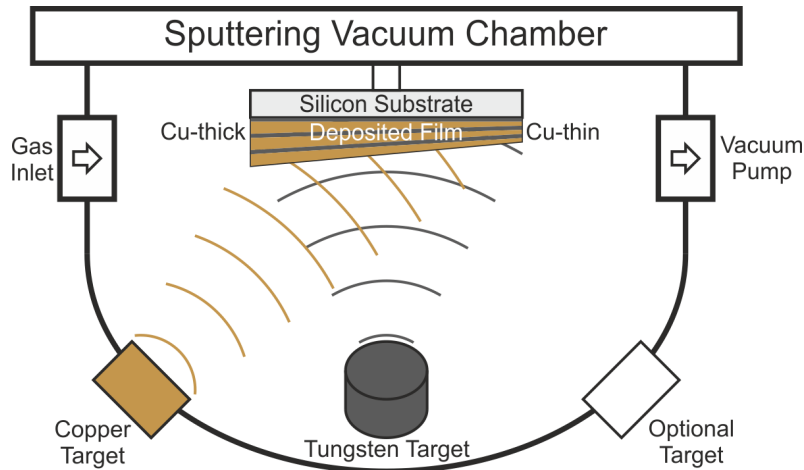


Figure 25: Schematic arrangement of the sputtering targets and substrate within the sputtering chamber for deposition of orthogonal wedge multilayer films.

While a single wedge component already saves a great deal of time in sample preparation, the use of thickness gradient films can be extended even further by orienting wedge-shaped films perpendicularly to one another. The Cu and W targets are positioned 90° apart from one another to create the orthogonal wedge geometry. In multilayer films consisting of repeating bilayers this allows a broad range of bilayer periodicities and layer thickness ratios to be investigated on a single substrate. Two orthogonal wedge samples were fabricated on full 4-inch silicon wafers. One sample consists of 80 bilayers with individual Cu-layer thickness varying from 6 to 21 nm and individual W-layer thickness varying from 8 to 18 nm. The other orthogonal wedge sample consists of just 8 bilayers with individual Cu-layer thicknesses varying between 100 and 350 nm and individual W-layer thicknesses between 60 and 200 nm.

5.1.3 Results and discussion

Cross-sections of the film were prepared using a focused ion beam (FIB) at each of the four cardinal points on the wafer to illustrate the bilayer thickness and thickness ratio modulation achieved. Figure 26 illustrates the orthogonal wedge sample geometry schematically and shows the SEM micrographs of each of the four cardinal cross-sections.

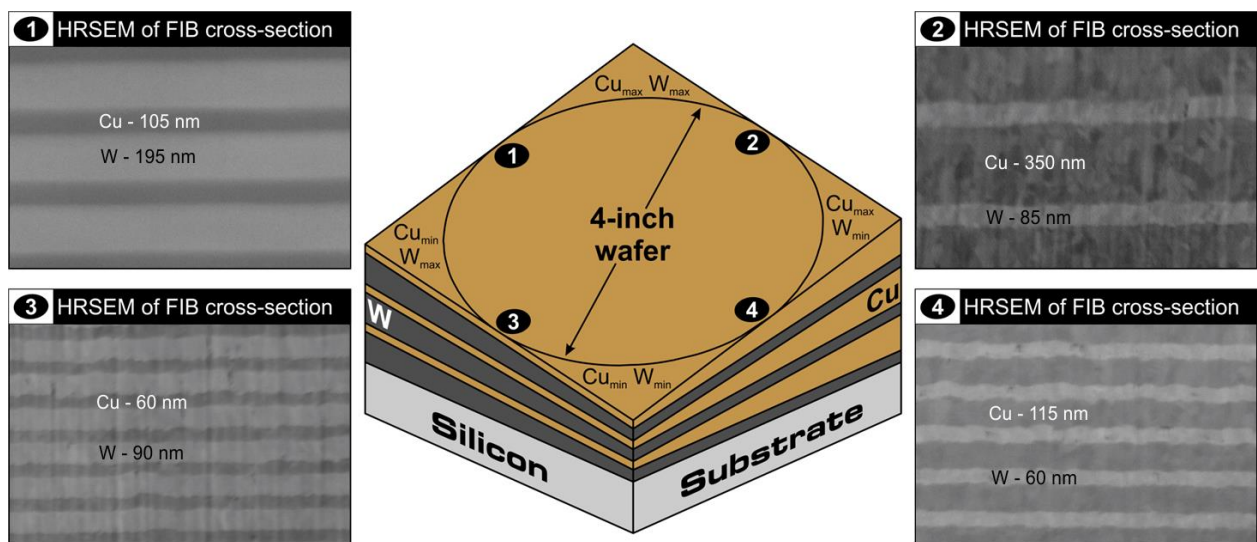


Figure 26: Orthogonal wedge multilayer sample geometry with 4 cardinal cross-section micrographs

One prerequisite to the use of compositional and thickness gradient films for study is that the gradients need to be shallow enough to facilitate characterization. As long as the characterization techniques are confined to a sufficiently small area of the gradient film it is reasonable to treat the film as being homogeneous within the tested area. This is seen clearly in the orthogonal wedge film cross-section micrographs in Figure 26, which are indistinguishable from micrographs taken of traditional parallel-planar nanolaminates. Nanoindentation inherently investigates adequately small areas while the x-ray fluorescence (XRF) and x-ray diffraction (XRD) spot sizes were reduced using x-ray optics to fulfill this requirement.

The mechanical behavior of the thin film with the nanolaminates was studied by using a Hysitron Ubi Nanoindenter. The hardness & elastic modulus were extracted from the load-displacement curves obtained on impinging a Berkovich tip into the films by using the Oliver and Pharr analysis [35]. Maximum loads ranging from 1 to 5 mN were used in order to restrict the penetration depths of 10 % of the total thicknesses of all the films with loading/unloading rates of 0.1 mN/s and pause time at maximum load of 10s. The volume fractions were estimated from atomic fractions using densities and atomic weights from standard sources.

The orthogonal wedge samples exhibited high intrinsic compressive stresses which ultimately led to the formation of telephone cord buckles, as seen in Figure 27. When the substrate containing 80 bi-layers was removed from the sputtering chamber there were no defects visible on the surface, but propagation of buckles began shortly after exposure to atmospheric conditions. The buckles were initiated from the edge of the substrate closest to the tungsten target during sputtering and grew radially outward. The buckles began as straight-sided buckles, but as time passed the developed into telephone-cord buckles. This transition is captured in Figure 27(a). The entire process took place at such a speed that it could be observed with the naked eye or under an optical microscope. The final buckles had a height of around 5 μm and a width of around 100 μm . Over time some pairs of adjacent telephone cord buckles joined to form a larger buckle with a width twice as large as the surrounding buckles, as is seen in Figure 27(b). In extreme cases even more buckles would form together to create large areas of film delamination. Following the iso-thickness lines for tungsten along the substrate it could be seen that the buckles remained shorter for the parts of the film where more copper was deposited. This indicates that the copper layers are loaded in biaxial tension and serve to compensate the high compressive stresses generated within the tungsten layers of the film.

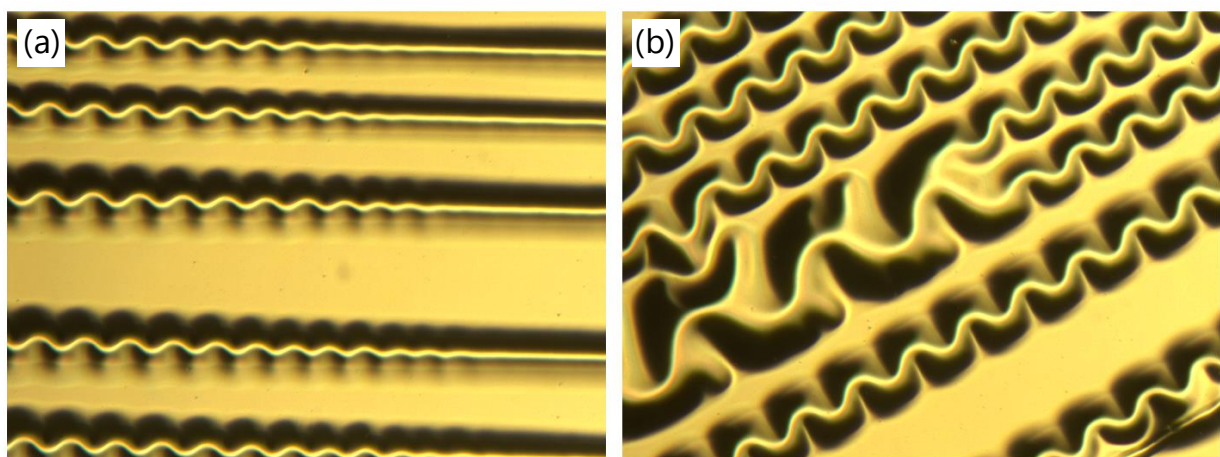


Figure 27: Telephone cord buckles begin as parallel buckles which gradually develop waviness as the film partially delaminates from the substrate. The film thickness decreases from left to right in (a) at the front where the buckles transition from straight to wavy. As delamination continues it is possible for adjacent buckles to combine into a larger buckle with twice the width of the original buckles, as seen in (b).

Two orthogonal wedge samples were prepared in order to investigate the influence of both bilayer thickness and the ratio of copper-to-tungsten on the film hardness. The first film consists of eight bilayers with copper layer thicknesses ranging from 80 to 165 nm and tungsten layer thicknesses varying from 50 to 300 nm. The hardness values obtained via nanoindentation along with three models for determining the hardness as a function of the individual layer thicknesses are presented in Figure 29. The second sample consists of 80 bilayers with copper layer thicknesses ranging from 4 to 17 nm and tungsten layer thicknesses varying from 3 to 26 nm. The measured hardness and hardness models for this film are presented in Figure 29.

The models developed for hard-soft multilayer combinations generally describe the mechanical behavior of the multilayer composite as being determined entirely by the weaker material. In cases where the difference in strength is large, this can be sufficient to describe the overall strength of the film. In general, however, it is necessary to consider the strength contributions of the individual layers. For conditions under which the material co-deforms, this is essential. A basic approach for describing the composite strength can be taken by evaluating the strength of the individual layers separately. The strength of the layers can be described using Hall-Petch models. A rule of mixtures can then be used to combine the results into a composite strength. Alternative approaches neglect the impact of non-equal volume fractions of material. Using a simple model describes the material strength as being independent of the thickness of the harder material.

The Hall-Petch coefficients used for copper were $H_0=2$ GPa and $k=10$ GPa·nm^{1/2} [80] while those used for tungsten were $H_0=4$ GPa and $k=30$ GPa·nm^{1/2} [81]. These constants are left in terms of hardness in order to allow direct comparison with the nanoindentation experiments from which they were derived. These constants are applied across the entire range of measured copper and tungsten layer thicknesses and are susceptible to inaccuracies at the extreme ends of the thickness range. Once the hardness for the individual layers was determined from the Hall-Petch relationship the results were combined in three ways: an upper bound rule of mixtures, a lower bound rule of mixtures, and a simple average of the copper and tungsten individual layer hardness.

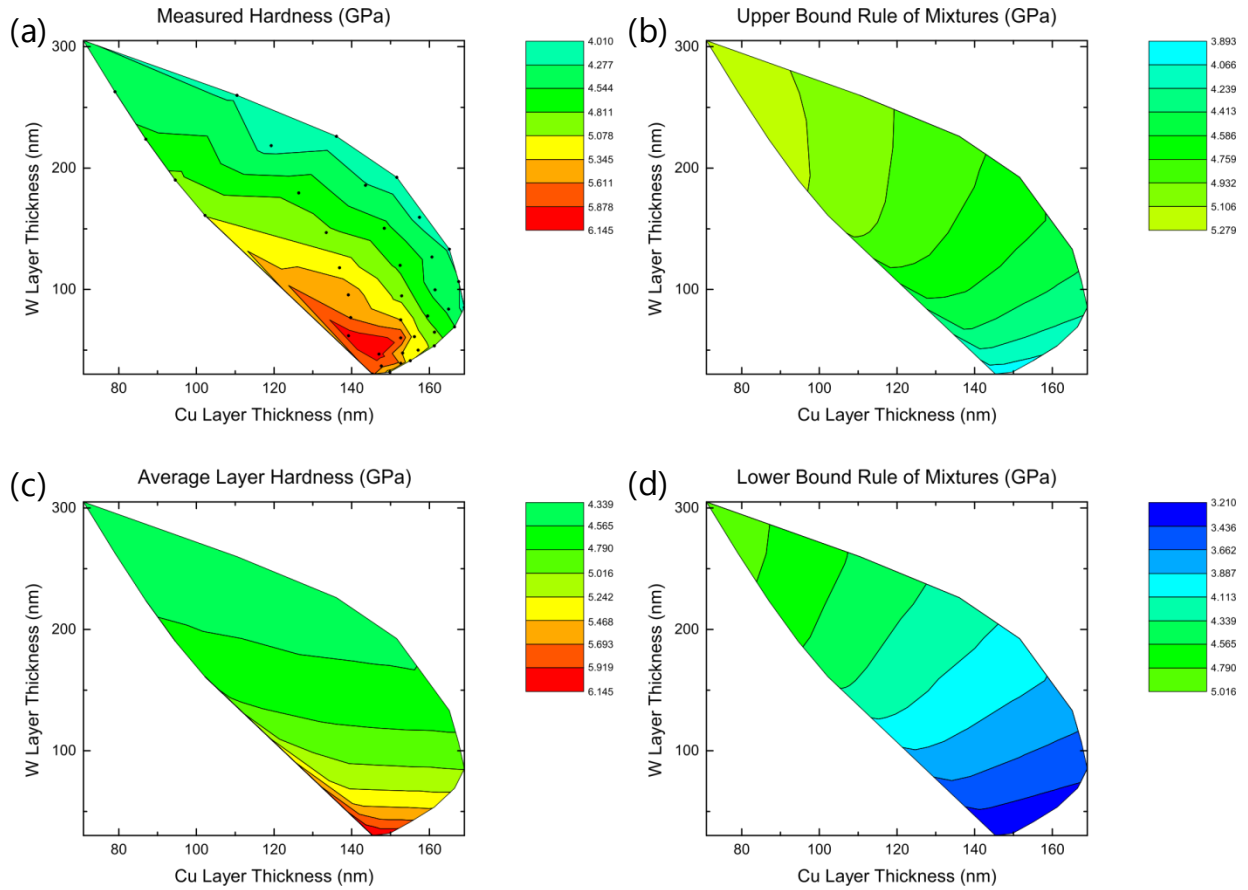


Figure 28: Nanoindentation and hardness model results for the orthogonal wedge combinatorial sample with thicker individual layers and a total of eight bilayers. The (a) measured hardness, (b) upper bound rule of mixtures, (c) average layer hardness, and (d) lower bound rule of mixtures are shown.

In the case of both samples there is a smooth, continuous gradient observed in the measured hardness. The film hardness is the highest where the tungsten layer thickness is the smallest. For fixed tungsten layer thicknesses hardness increases with decreasing copper layer thickness. The hardness is much more sensitive to the tungsten layer thickness than the copper layer thickness. Both the upper and lower bounds of the rule of mixtures predict that the copper, as the softer of the two components, has a larger effect on the film hardness. This behavior was not observed, indicating that treating the layers separately and applying a rule of mixtures is insufficient to capture the hardness development of the films both qualitatively and quantitatively. The average layer hardness, however, provides a reasonable model for predicting film hardness. The measured hardness gradient has a relatively constant slope while the averaging model predicts higher sensitivity when the tungsten layers are thinner. This result is somewhat surprising as it suggests that, at least for the copper-tungsten material combination, it is the harder phase which is responsible for determining the composite behavior and not the softer phase. As such further improvements to film hardness can be achieved by incorporating thinner layers of the reinforcing phase. The use of non-equivalent volume fractions in soft-hard material combinations is a promising strategy to achieve improved mechanical properties.

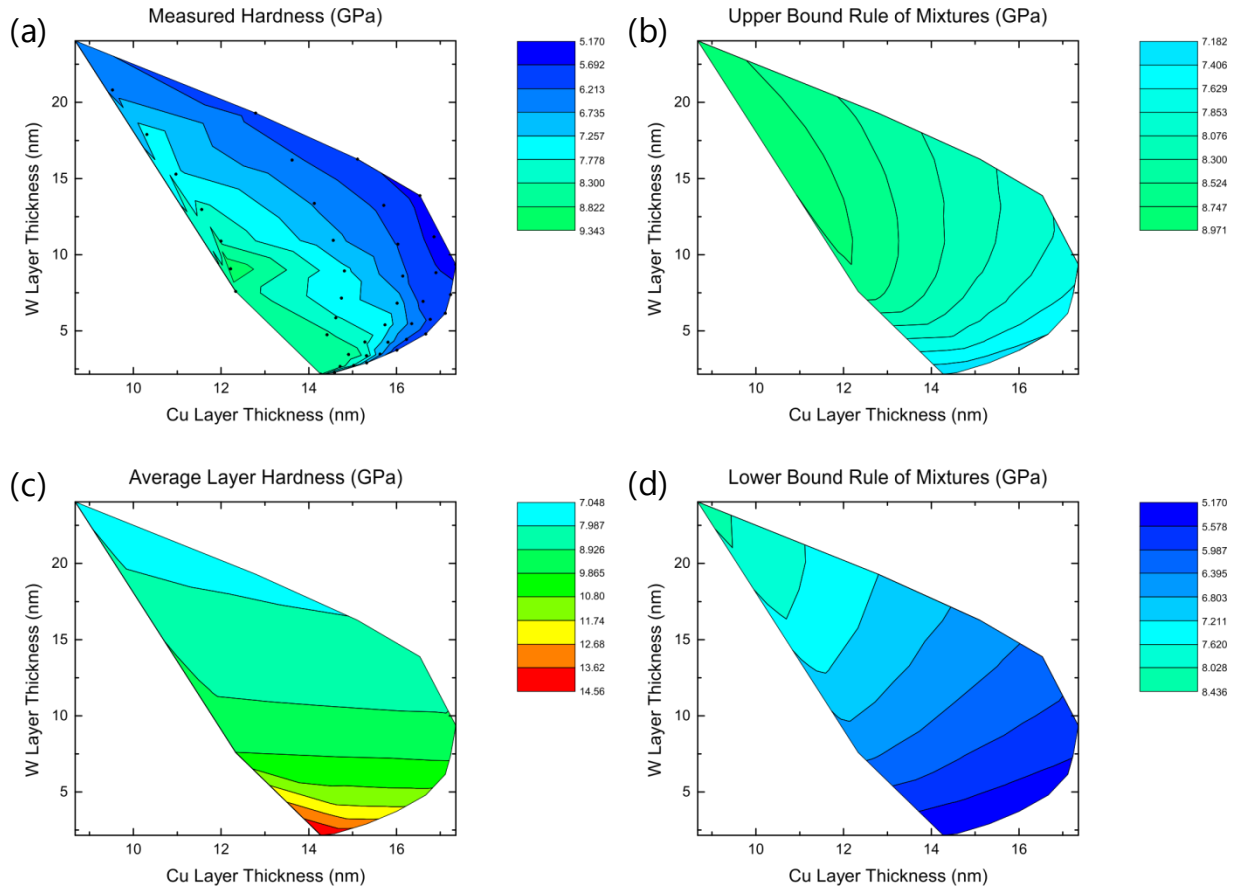


Figure 29: Nanoindentation and hardness model results for the orthogonal wedge combinatorial sample with thinner individual layers and a total of 80 bilayers. The (a) measured hardness, (b) upper bound rule of mixtures, (c) average layer hardness, and (d) lower bound rule of mixtures are shown.

5.1.4 Conclusions

Copper and tungsten can be combined in a variety of ways to create films with desirable mechanical and thermal properties. Co-sputtering permits the otherwise fully immiscible combination of Cu and W to form metastable phases. These phases are present in nanocrystalline form and do not possess an amorphous microstructure as reported in previous research. The hardness of such films can be predicted reasonably well by applying Hall-Petch hardening to the individual layers and averaging the hardness of the individual components. Nanolaminates show significant hardness improvement by incorporating even small volume fractions of tungsten between copper layers. Orthogonal wedge samples can be used to investigate a wide range of bilayer thicknesses and volume ratios in multilayer structures. If the film is deposited with an intrinsic compressive stress telephone cord buckles will form where the total force generated by the intrinsic stress exceeds the interface strength. The propagation of the telephone cord buckles in tungsten is initiated by a reaction with humidity or oxygen in the atmosphere. For a given total thickness of W, increasing the Cu layer thickness inhibits the formation of buckles, indicating that the Cu layers in these nanolaminates are under a biaxial tensile stress.

Contributions: Film deposition was performed together with Vipin Chawla.

5.2 Copper-Titanium Nitride

5.2.1 Introduction

Periodic bilayer films, a special class of multilayer thin films, utilize alternating layers of two materials in order to create a laminar composite film with more desirable properties than either of its constituent components. The use of periodic bilayer films can be used to improve both film strength [82,83] and film toughness [84–87]. Extensive investigation of multilayer films has been conducted to determine the parameters with the most pronounced effect on the mechanical properties of the films [8,88,89]. In general the use of thinner layers on the single-digit nanometer scale provides the most desirable mechanical properties [90]. The absolute strengthening limit in a given materials system depends on the nature of the interface between the two constituent materials. Interfaces which inhibit the transmission of dislocations have been shown to provide the highest degree of strengthening [67,91,92].

In order to ensure that dislocations cannot easily cross the interface between the two constituent materials, individual components are selected to have different crystal structures. A large difference in lattice parameter between the two materials can also be beneficial in ensuring a strong barrier to dislocation transmission across an interface. Beyond the classical metal-metal multilayers, it is also possible to utilize other combinations, such as metal-ceramic multilayers. This approach can be considered analogous to the biologically-inspired nacre structure in which the toughness of the brittle material is improved through the incorporation of a more ductile material in small quantities. A number of studies have been carried out investigating metal-ceramic material combinations in multilayers [93–101]. The totally incoherent interfaces in these systems preclude the direct transmission of dislocations across the interfaces. Failure tends to be dictated instead by either flow of the metallic layers (at elevated temperatures) or brittle fracture of the ceramic layers (at lower temperatures).

Metal-ceramic multilayers therefore offer an ideal combination for studying dislocation-impermeable interfaces. Previous studies utilizing an FCC metal and an amorphous ceramic in the case of Cu-PdSi were successful at demonstrating strength values approaching the metal's ideal strength [99]. Among the metal-ceramic materials where both phases are crystalline, Al-SiC is at present the most widely studied [97,100–102]. Both nanoindentation and micropillar compression experiments have been performed at room temperature and moderately elevated temperatures up to 100°C [101], providing insight into the deformation mechanisms operating across that temperature range and permitting comparisons between nanoindentation and micropillar compression data to be made. Various volumetric fractions of the two components were even investigated, demonstrating that the ratio between the two component materials also has a significant effect on the strength and failure mechanism of the films [102]. The Al-TiN materials system has demonstrated a number of attractive attributes as well, notably a markedly improved fracture toughness when constructed at a nanometer length scale [96,103].

The Cu-TiN studied here has the potential to exhibit many of the same desirable properties already observed in the Cu-PdSi and Al-TiN multilayer films. There is additional commercial relevance since copper is commonly used in conjunction with TiN in microelectronics, where TiN serves as a diffusion barrier to copper wires and interconnects [104].

5.2.2 Experimental

A total of five different films were prepared for this investigation: pure copper films, pure titanium nitride films, and three multilayer films. The nomenclature used to describe the multilayer films lists the

first layer deposited along with its nominal thickness followed by the second layer and its nominal thickness. Identical bilayers are then deposited to reach the total nominal film thickness of 5.5 μm . The three multilayer films studied here are Cu(5nm)-TiN(10nm), Cu(50nm)-TiN(100nm), and Cu(700nm)-TiN(1000nm). All films were deposited onto Si (100) substrates via DC magnetron sputtering (for Cu layers) and DC reactive magnetron sputtering (for TiN layers). Film deposition was performed at the Center of Advanced Surface Engineering in Cordovilla-Pamplona Spain. A short working distance of 7 cm and large sputtering targets ($200 \times 100 \times 6 \text{ mm}^3$) consisting of 99.96 atomic % pure copper and titanium were used. The Argon flow rate was held at 70 sccm throughout the entire deposition while an addition 6 sccm of Nitrogen was added during the reactive titanium deposition. A DC bias of -50 V was used during the deposition while the substrate temperature was maintained at 150°C.

The total film thickness, the individual layer thicknesses, and the abruptness of the interfaces were measured using GDOES (Jobin Yvon JY RF-5000). A gallium FIB (Tescan Lyra) was used to prepare cross-sections of each of the films at a current of 1 nA for the rough milling and 250 pA for the polishing step. The individual layer thickness and total film thickness were then measured by imaging the films in a SEM (Hitachi S-4800). The resolution of the SEM was insufficient for determining the individual layer thickness of the Cu(5nm)-TiN(10nm) film, so the thickness was calculated based on the sputtering times and the measured thickness for the Cu(50nm)-TiN(100nm) film. The pure TiN film exhibited pronounced columnar growth and a high surface roughness, so it was smoothed using an argon ion polisher (Balzers RES010) operated at 2 mA and 7 kV. The same FIB setup was used to prepare the micropillars used for compression experiments. A three-step fabrication process was followed at a constant accelerating voltage of 30 kV, stepping the current down from 5 nA to 1 nA and further to 200 pA for the final polishing step. A height-to-diameter aspect ratio of 2:1, though in some cases a slightly higher aspect ratio was produced when extra polishing was required to minimize the pillar taper.

A micromechanical testing platform (Alemnis) adapted for elevated temperature testing [105] was installed within a SEM (Zeiss DSM 962) in order to precisely align the indenter with the micropillars [106]. A diamond flat punch indenter with a diameter of 6 μm was used for all of the experiments. A constant displacement of $3 \times 10^{-3} \text{ s}^{-1}$ was used in order to give an approximately constant strain rate of $1 \times 10^{-3} \text{ s}^{-1}$, varying only slightly with the height variation between the micropillars. Micropillar imaging was performed using the aforementioned SEM prior to compression in order to precisely determine the dimensions of each micropillar and after compression to provide insight into the failure mechanism of each pillar. Micropillar compression experiments were initially conducted at room temperature before heating the samples to 400°C. The film and indenter temperature was allowed to stabilize over the course of an hour before performing the next round of compression experiments. The temperature was then reduced to 200°C and again allowed to stabilize before conducting the next round of micropillar compression experiments. Finally the temperature was returned to room temperature and several additional micropillars were compressed to ensure that no major microstructural changes had occurred within the samples during the elevated temperature tests.

ABAQUS© software was used to perform Finite Element (FE) simulations of the pure copper films, the Cu(50nm)-TiN(100nm) multilayers, and the Cu(700nm)-TiN(1000nm) multilayers at room temperature. A total of 20,236 quadrilateral elements were used in a radially symmetric 2D model for each of the micropillars. Boundary conditions were provided as a stationary pedestal at the bottom of the micropillar and a frictionless contact between the indenter and the upper surface of the micropillar. No size effect was considered for the TiN layers, which were treated as a perfectly elastic material sandwiched between the deformable copper layers.

5.2.3 Results

Cross-sections of the Cu-TiN multilayers and the two, single-component reference films are shown in Figure 30. The Cu(5nm)-TiN(10nm) film is not included as the SEM resolution was insufficient to distinguish the multilayer structure. The multilayers exhibit progressively increasing waviness as the film thickness increases. As such the interfaces near to the substrate are flat while those near the upper surface of the film exhibit pronounced waviness. This trend of increasing waviness with increasing film thickness has been observed previously and is not indicative of any intermixing between the two component materials [107]. The titanium nitride has grown in a highly ordered columnar structure, which leads to the pronounced curtaining effect from the FIB-preparation of the cross-section. The pure copper film is mainly nanocrystalline, but with one particularly large grain, interrupted by several twin boundaries, seen occupying the entire thickness of the film. The limited copper layer thickness in the multilayer films prevents such extensive grain growth from occurring. There are small, inter-columnar pores visible in the TiN layers in the multilayer films. These pores are rare enough that the films can be considered dense. There is a strong (111) film texture as is commonly reported for TiN films deposited by DC magnetron sputtering [108]. The film thicknesses as determined via SEM inspection are listed in Table 4: Film thicknesses were measured by preparing FIB cross-sections and observation within a SEM. The mechanical properties at room temperature were determined by micropillar compression. Table 4.

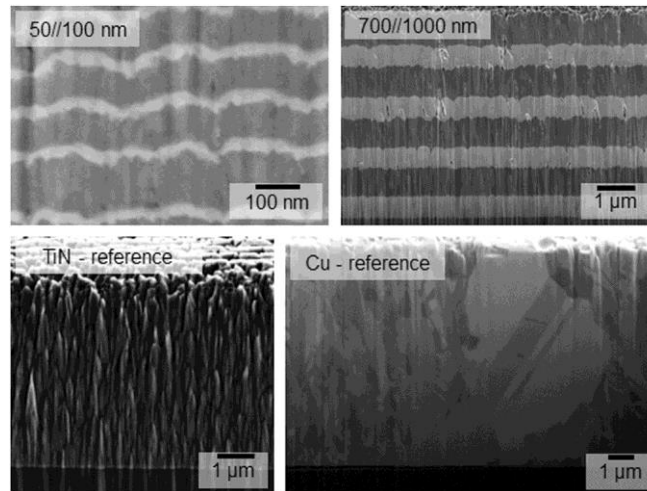


Figure 30: SEM micrographs of FIB cross-sections taken from the multilayers and single-component films used as references for the mechanical properties of copper and titanium nitride. Columnar growth in the TiN films is evidenced by a pronounced curtaining effect. Waviness present in the multilayers increases with increasing film thickness.

Film	Total Film Thickness	Individual Cu layer thickness	Individual TiN layer thickness	0.5% yield stress	Elastic modulus
-	μm	nm	nm	GPa	GPa
Cu(5nm)-TiN(10nm)	4.9	4.6	9.8	2.29±0.03	100±3
Cu(50nm)-TiN(100nm)	4.4	53	108	2.7±0.2	129±13
Cu(700nm)-TiN(1000nm)	6.5	717	1040	1.39±0.06	87±12
Pure TiN	5.4	-	5400	2.29±0.3	122±15
Pure Cu	4	4000	-	0.71±0.1	134±10

Table 4: Film thicknesses were measured by preparing FIB cross-sections and observation within a SEM. The mechanical properties at room temperature were determined by micropillar compression.

Typical engineering stress – engineering strain curves for the micropillars are shown in Figure 31a. The machine compliance was considered in the mechanical property calculations while the Sneddon correction [105,109] was applied to the data in order to compensate for the local substrate compliance beneath the micropillars. All of the multilayer films exhibit a higher yield stress and superior toughness to the single component films, with smaller layer thicknesses being associated with superior mechanical properties. The pure TiN films exhibit characteristic brittle ceramic behavior and are seen to have splintered apart along the columnar grain boundaries near the top of the micropillar (Figure 31b). The stress concentration at the top of the micropillar as a result of sidewall taper is especially apparent for brittle and strain-softening materials. The pure copper film shows typical metallic behavior, with a long strain-hardening region after the yield stress has been reached. The micropillar surface shows the onset of grains partially popping out of the micropillar (Figure 31c), indicating that the exceptionally large grains observed in the film cross-section may be a major contributor to the films overall mechanical behavior. A lower elastic modulus was calculated from the loading curves as compared to the unloading curves, though this was especially apparent in the pure copper films. The modulus from the unloading curves is taken since the loading curve is affected by the film roughness and is generally less reliable. The stochastic nature of defects contained within any the micropillars lend a large statistical scatter to the data, but the elastic modulus of all the multilayer films can be said to be comparable.

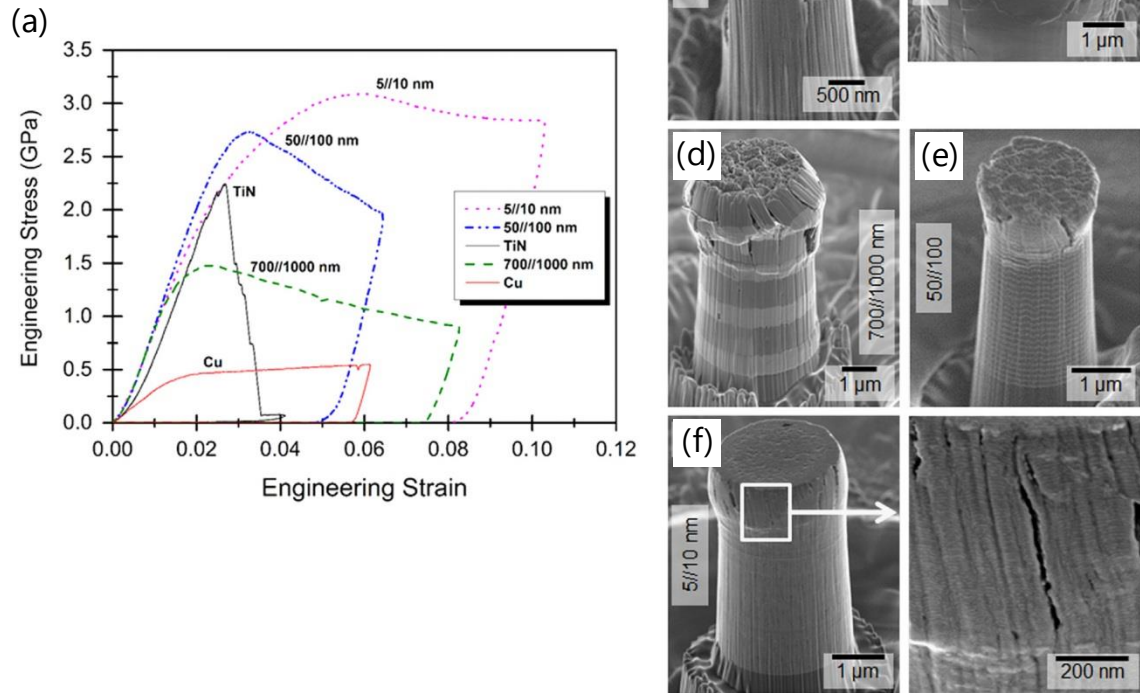


Figure 31: Room temperature micropillar compression experiments demonstrate that multilayers with small layer thicknesses can exceed the strength of either constituent material (a). The corresponding micrographs for (b) TiN, (c) copper, (d) Cu(700 nm)-TiN(1000 nm) multilayers, (e) Cu(50 nm)-TiN(100 nm) multilayers, and (f) Cu(5 nm)-TiN(10 nm) multilayers are also shown.

Reactively sputtered TiN tends to exhibit a columnar microstructure with a (111) texture when deposited using a mixture of argon and nitrogen as the sputtering gases [108]. As was the case here, the nitrogen component of the sputtering gas can be kept low in order to maintain near-stoichiometric film compositions rather than the deposition of nitrogen-rich films [110]. Shear fracture at grain boundaries has been identified as the main failure mechanism in sputtered TiN coatings on steel substrates [111]. When deposited atop a compliant substrate, hard columnar coatings can actually have the opposite of the intended effect by individual columnar grains punching into the substrate [112]. Columnar sliding can transition to fracture of the grains themselves at sufficiently high film thicknesses. Brittle fracture along TiN columnar grain boundaries and local punching of the TiN grains into the softer copper layers are seen in the cross-sectional images shown in Figure 32.

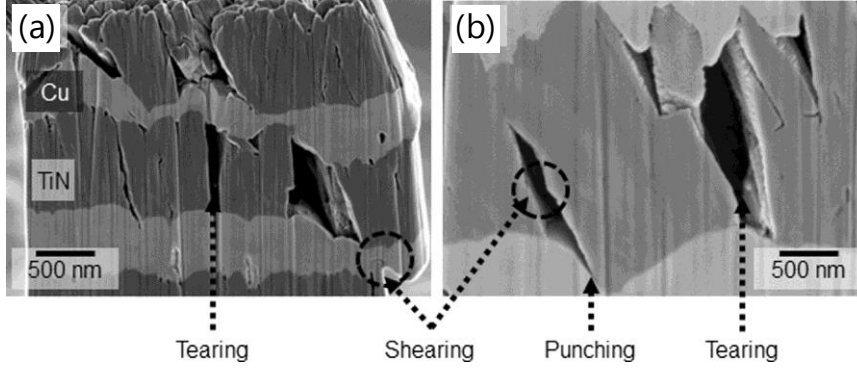


Figure 32: SEM micrographs FIB-milled cross-sections of Cu(700 nm)-TiN(1000 nm) micropillars after compression provide insight into the deformation mechanisms at work. The copper layers can be seen to have sheared, resulting in fracturing of the TiN layers along columnar grain boundaries (a). The separate TiN grains are free to rotate separately and punch into the readily deformable copper (b).

Finite Element (FE) simulations were performed of micropillar compression at room temperature. A simple model was utilized in which both the Cu and TiN layers were treated as isotropic. The model was used to predict the yield stress at the onset of plastic deformation, but not to capture the strain softening behavior observed. Doing so would necessitate the inclusion of the friable columnar grain boundaries within the TiN layers, which was beyond the capacity of such a model. The copper behavior was defined using a piecewise function to capture the transition from totally elastic behavior to a power law plastic behavior once a critical yield stress was surpassed, as given in Equation 18:

$$\varepsilon = \begin{cases} \frac{\sigma}{E}; & \sigma \leq \sigma_{ys} \\ \left(\frac{\sigma}{\sigma_0}\right)^{\frac{1}{n}}; & \sigma \geq \sigma_{ys} \end{cases} \quad \text{Equation 18}$$

where ε is the total strain, σ is the stress, E is the elastic modulus, σ_{ys} is the yield stress, n is the power-law strain hardening coefficient, and σ_0 is given by Equation 19.

$$\sigma_0 = E^n \sigma_{ys}^{1-n} \quad \text{Equation 19}$$

The elastic modulus used for copper was 120 GPa while that of TiN was 250 GPa. These values differ somewhat from those measured from the single-component reference films, but are in good agreement with a number of established literature values. A strain hardening coefficient of 0.1 was used for the simulation of pure copper while no strain hardening was considered for the multilayer films.

The model and boundary conditions used for the FE simulations is shown in Figure 33(a) while the Von Mises stress within the copper layers is displayed in Figure 33(c). A large isostatic stress is generated within the center of the micropillars while the stress decreases closer to the micropillar sidewalls. Near the center of the micropillar there is a large degree of lateral confinement provided by the resistance of the interface to shear, whereas near the micropillar surface the copper layers are no longer subject to significant lateral confinement and can bulge slightly to accommodate deformation. The model is sufficient to accurately predict the yield stress for the pure copper film, the Cu(700nm)-TiN(1000nm) multilayers, and the Cu(50nm)-TiN(100nm) multilayers, but fails to provide accurate predictions for either the pure TiN film or the Cu(5nm)-TiN(10nm) multilayers.

Due to the simplicity of the model and the treatment of each material as being fully isotropic, it is not possible to capture the more complex fracture behavior observed within the TiN layers. The model's utility is therefore limited to the prediction of the yield stress and does not provide an accurate description of the plastic deformation of the micropillars. As such it is clear that the mechanical behavior of the pure TiN films with columnar grain boundaries is not well predicted by the model. That the behavior of the Cu(5nm)-TiN(10nm) multilayers is not well predicted is somewhat more surprising. It is postulated that at these thin individual layer thicknesses other hardening mechanisms dictate the yield stress of the films.

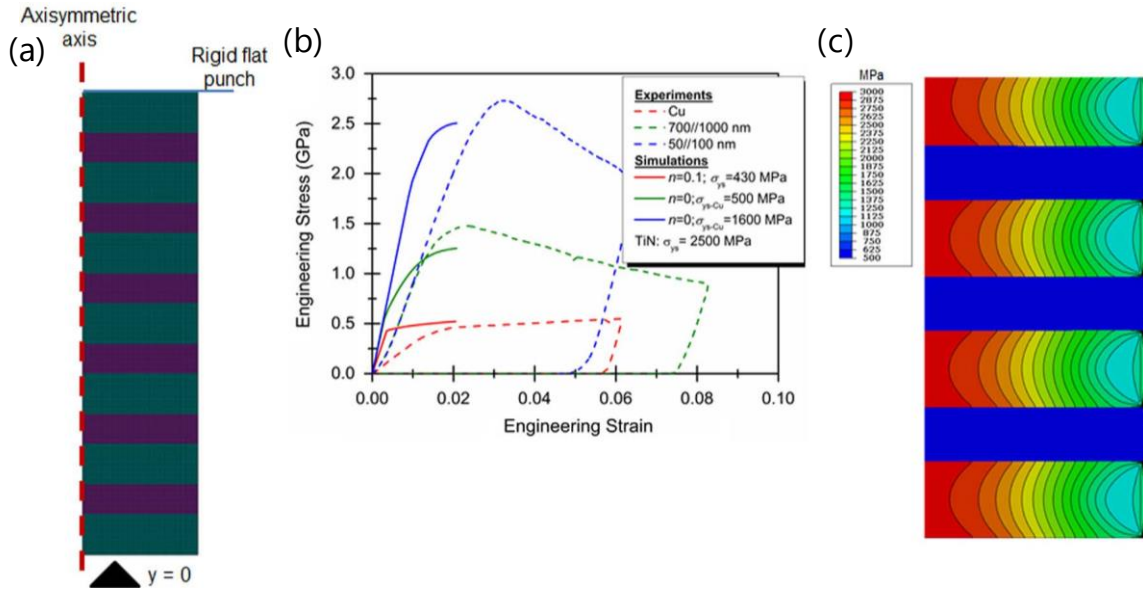


Figure 33: (a) The finite element model and constraints used to perform the simulation. (b) Good agreement between the room-temperature experimental data and the FEM simulations was achieved for the entire range of layer thicknesses tested here. (c) The Von Mises stress is highest near the center of the micropillar and decreases closer to the micropillar surface since the Cu-TiN is allowed to slide once a critical shear stress threshold is surpassed.

During the heating and temperature stabilization phases of testing, an interesting crystal growth phenomenon was observed on the sample surfaces, remote from the sample edges and micropillars prepared for mechanical testing, seen in Figure 34. Prolific growth of copper microcrystals interspersed with occasional whiskers was observed on the surface of the Cu(5nm)-TiN(10nm) sample. The Cu(50nm)-TiN(100nm) sample exhibited a similar growth phenomenon, albeit predominantly whiskers and occasional platelets. The growth rate of these whiskers and microcrystals was highest immediately after each incremental step increase in sample temperature. The growth rate decayed during the temperature stabilization phase and growth ultimately ceased several tens of minutes after a stable temperature had been reached.

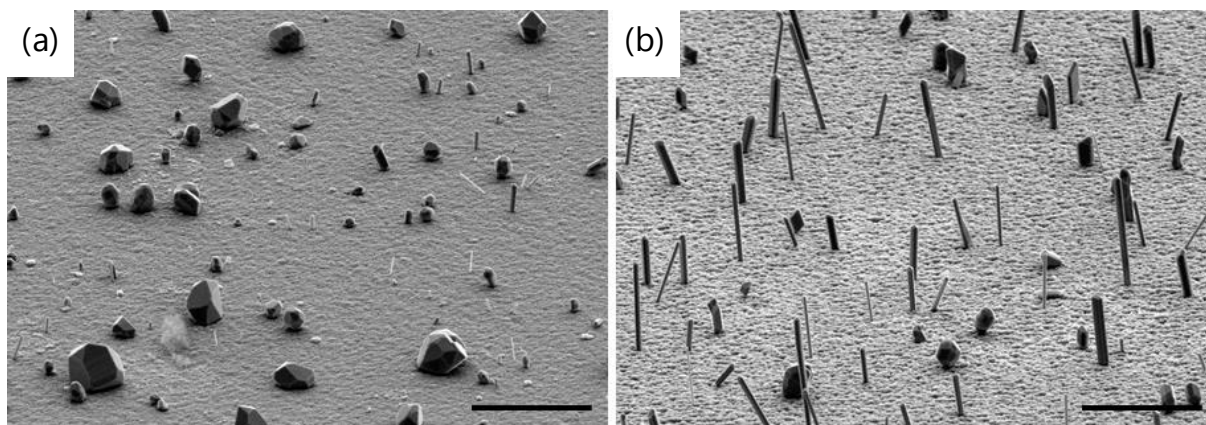


Figure 34: During the temperature stabilization process anomalous growth of microcrystals and whiskers was observed on the sample surface. The morphology of the growths is dependent upon the thickness of the bilayer thickness. The surface of the Cu(5nm)-TiN(10nm) sample is shown in (a) while the surface of the Cu(50nm)-TiN(100nm) sample is shown in (b). The growths themselves are entirely made of copper and contain sufficient volume that all of the underlying copper layers must contribute to their formation. The scale bars represent a length of 5 μm .

The majority of the whiskers, platelets, and microcrystals exhibit clearly faceted surfaces, indicating that they are highly crystalline in nature. A cross-section of one of the microcrystals shown in Figure 35 shows that, at least in the case of the microcrystal, the structure is polycrystalline. The whiskers are presumably single-crystalline in nature. In both cases the TiN layers beneath the growth are heavily fractured. A copper “root” is centered beneath the growth and penetrates many of the underlying layers.

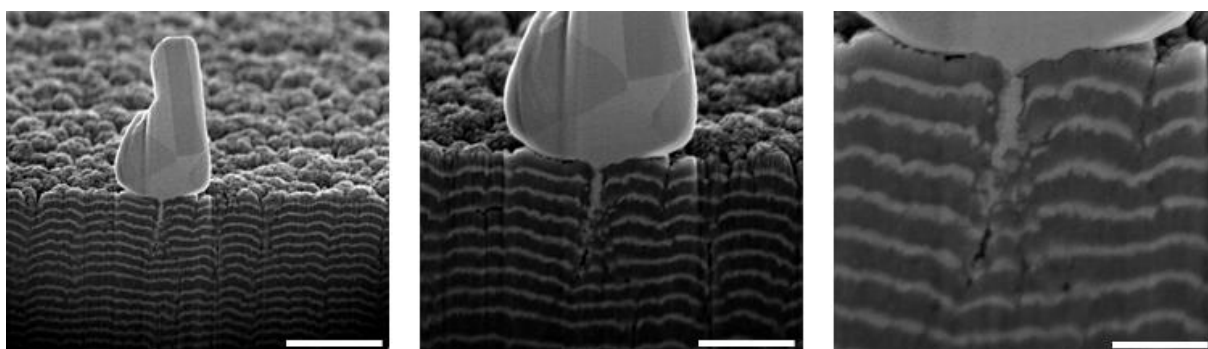


Figure 35: A cross-sectional view of a microcrystal growth on the sample surface reveals a root structure in which the TiN layers have fractured and copper from many of the underlying layers contributes material to the growth process. From left to right, the scale bars represent 1 μm , 500 nm, and 250 nm.

The micropillars themselves did not exhibit any such spontaneous growth phenomena during sample heating. No visible change in the micropillars could be observed, indicating that the driving force for whisker growth is not present within the micropillars. A related growth phenomenon was observed during the micropillar compression experiments at elevated temperatures for the Cu(5nm)-TiN(10nm) and Cu(50nm)-TiN(100nm) films in which protuberances were seen to develop on the micropillar side-walls during micropillar compression. Micrographs of representative post-compression micropillars for each of the temperatures tested are shown in Figure 36b. Representative stress-strain curves from the experiments are shown in Figure 36a. At room temperature the common trend for higher yield strength with decreasing film thickness is observed. Each multilayer film thickness also exhibits a trend for decreasing yield strength with increasing temperatures. The major difference in the stress-strain behavior between the films is the rate at which the yield stress decreases with increasing temperature. For the Cu(700nm)-TiN(1000nm) films the decrease in strength is gradual, dropping to roughly half,

and then one-quarter of the original yield strength with the two temperature increases. For the Cu(5nm)-TiN(10nm) film the relative drop in strength with increasing temperature is much more pronounced. An increase of temperature to 200°C results in the yield strength of the pillar dropping to roughly one-third of their room temperature value. At 200°C and 400°C there is no discernable strength advantage in the Cu(5nm)-TiN(10nm) film compared to the Cu(50nm)-TiN(100nm) film, despite the former being much stronger than the latter at room temperature. In the case of the Cu(50nm)-TiN(100nm) film there is also a notable change in the strain-hardening behavior of the sample. At room temperature the formation of cracks at the top of the pillar lead to a drastic drop in strength after the yield stress has been surpassed. This is also observed in the thicker films. However, once a temperature of 200°C has been reached there is instead a pronounced strain-hardening behavior of the micropillar. Since strain at these temperatures occurs almost exclusively within the copper layers, their thickness decreases significantly through the test.

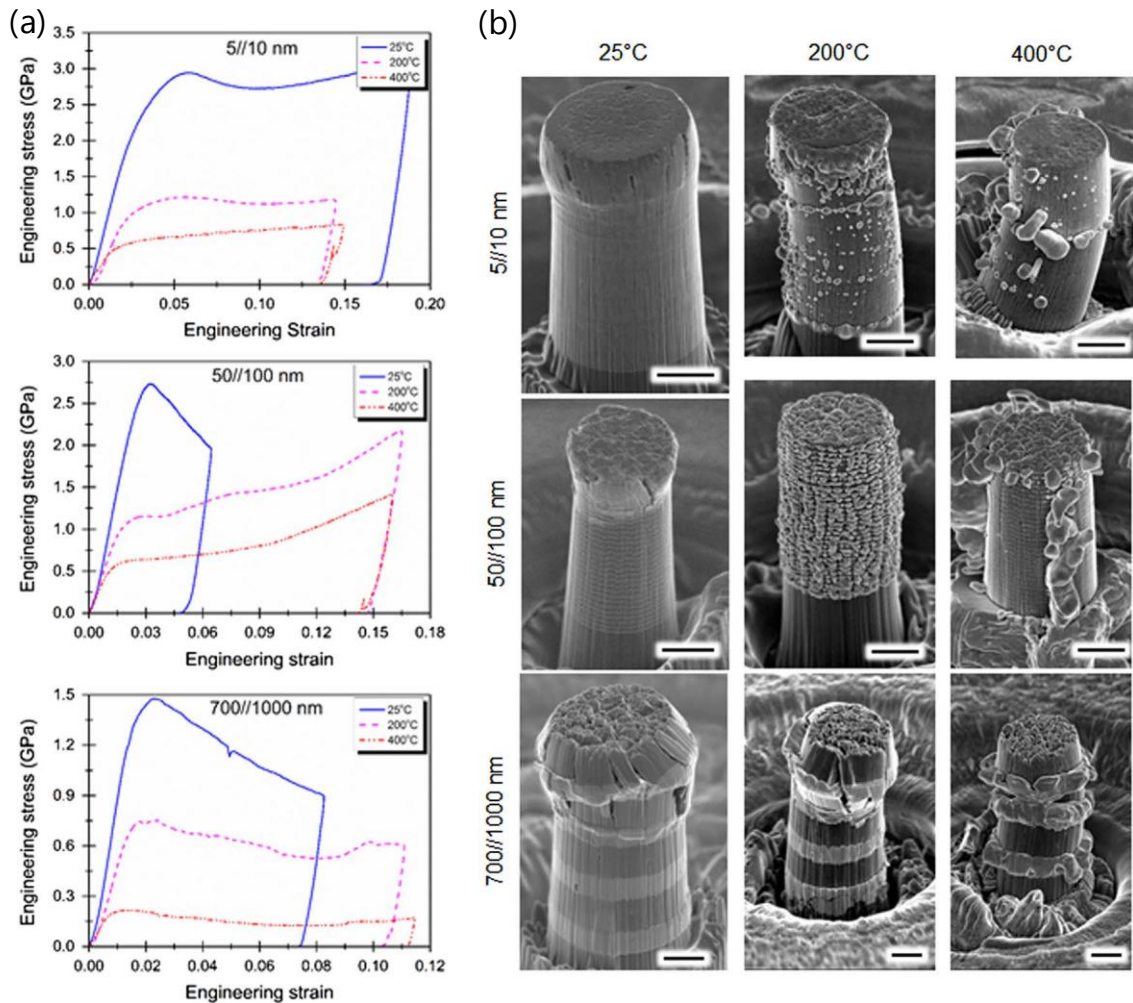


Figure 36: Characteristic engineering stress-strain curves for three thickness combinations of Cu-TiN micropillars at three temperatures (a). Corresponding post-compression SEM micrographs of the micropillars are shown in (b). Higher test temperatures and thinner copper layers result in more pronounced evidence for stress-assisted diffusion during deformation. The scale bar in all micrographs represents 1 μm.

More detailed views of the surfaces of the post-compression micropillars tested at elevated temperatures are seen in Figure 37. The thinnest layer thicknesses exhibit a number of protrusions on the sample surface which are more pronounced at higher temperatures. The diameter of these copper protrusions significantly exceeds the initial layer thickness and at many points the copper from several adjacent layers can be seen to have coalesced into larger protrusions. These protrusions also show some signs of faceting, indicating that there is recrystallization occurring within the copper no longer

contained within the micropillar. For the Cu(50nm)-TiN(100nm) film tested at 200°C there is sufficient separation that these protrusions can still be assigned to the layers of their origin despite the beginnings of coalescence. Significant rounding of the protrusions leads to a droplet like appearance, suggesting that the surface tension of the protrusions results in their rounding. At 400°C in the intermediate layer thickness films significant coalescence has occurred and the micropillar appears to have fractured internally. An interconnected network of copper penetrating the TiN layers can be inferred based on the surface inspection. The Cu(700nm)-TiN(1000nm) does not exhibit the same type of behavior as the two films with thinner layers. At room temperature the copper and TiN both exhibit vertical cracks and fracturing. At 400°C the copper layers exhibit more plastic deformation than cracking while the TiN remain more or less intact. Bulging of the copper layers is observed, but now signs of copper diffusion as with the other two samples.

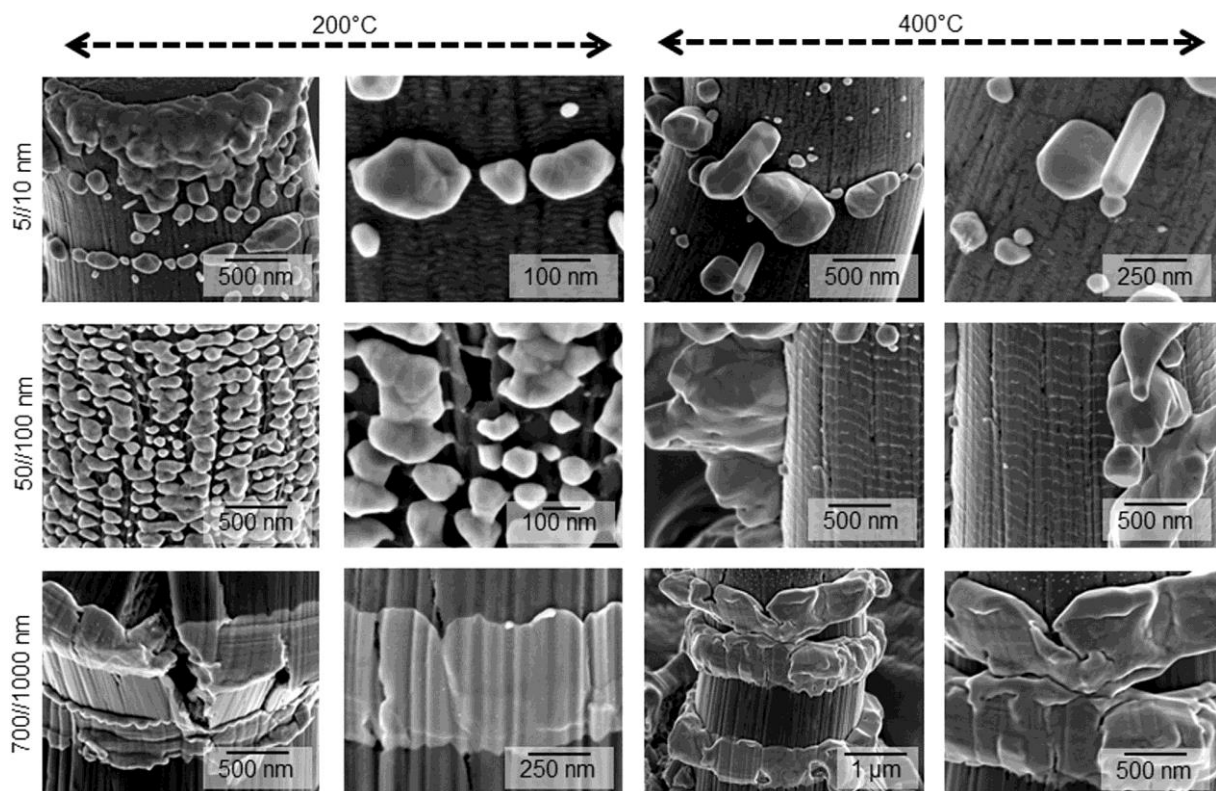


Figure 37: SEM micrographs of Cu-TiN micropillars with various layer thicknesses are shown after compression at 200°C and 400°C. Significant diffusion of copper during compressions leads to the formation of extruded protuberances at the micropillar surfaces. The volume of these protuberances is greater for the tests conducted at higher temperatures. When the layer thickness is sufficiently small, copper from adjacent layers is seen to coalesce into larger protuberances.

In order to determine the changes occurring to the internal structure of the Cu(5nm)-TiN(10nm) and Cu(50nm)-TiN(100nm) micropillars during compression, half of one post-compression micropillar of each film was removed by FIB milling to obtain a cross-sectional view. Micrographs of these cross-sections are presented in Figure 38. In the one Cu(5nm)-TiN(10nm) micropillar a shear band has formed from the upper-right-hand corner of the pillar. Fracture within the TiN layers has occurred along this band and the voids have been filled by an interconnected network of copper. The surface of the micropillar is decorated with large protuberances spanning many individual copper and TiN layers. These protuberances are connected to multiple adjacent copper layers and have coalesced into large droplets on the sidewalls of the micropillars. The Cu(50nm)-TiN(100nm) exhibits similar surface growths, but the TiN layers are sufficiently thick to provide distinct separation between the copper protuberances. At higher strains these protuberances also coalesce to form larger droplets connecting adjacent copper layers. The TiN layers do not exhibit any signs of strain while the copper layers have

been reduced to a fraction of their original thickness. At higher strains the thickness of these layer approaches that of the Cu(5nm)-TiN(10nm) film, potentially explaining the similarity between their stress-strain behavior at elevated temperatures.

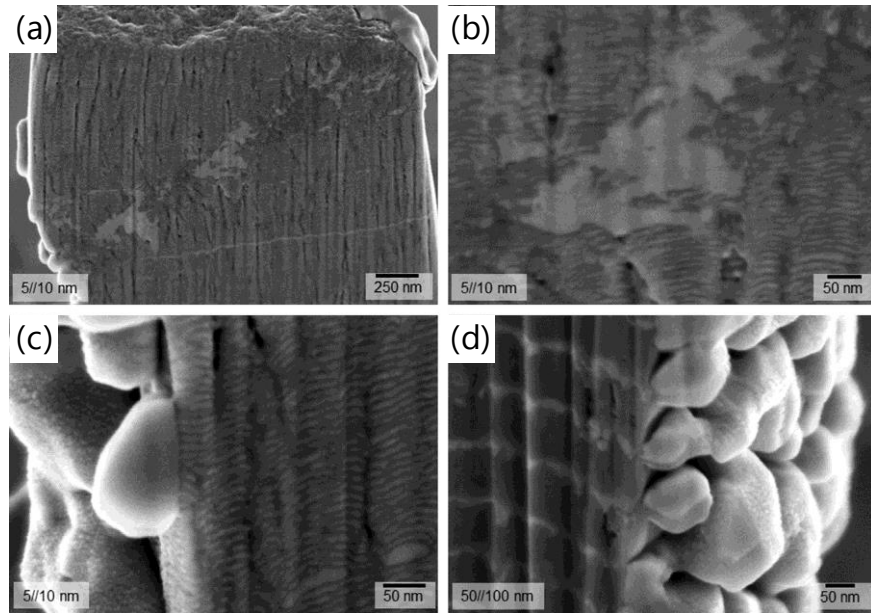


Figure 38: (a) and (b) show the filling of voids by mobile copper during shearing of the micropillar. (c) and (d) show coalescence of extruded copper on the surface of the micropillar along with a reduction of the copper layer thickness. This indicates that most of the pillar plasticity is accommodated within the copper layers while the TiN layers maintain their original thickness.

5.2.4 Discussion

The growth of whiskers, platelets, and microcrystals through heating multilayers has not yet been reported in the literature. The phenomenon bears striking similarity to the well-known formation of hill-ocks and whiskers over time in lead-free solders. For solders used in microelectronic devices the formation of whiskers poses a severe threat to device reliability as these whiskers can readily result in a short circuit and are generally undesirable. In this case, however, there is an obvious potential to exploit this phenomena to produce whisker or particle arrays. The morphology of the growths is strongly dependent upon the thickness of the individual layers used in the fabrication of the multilayer films.

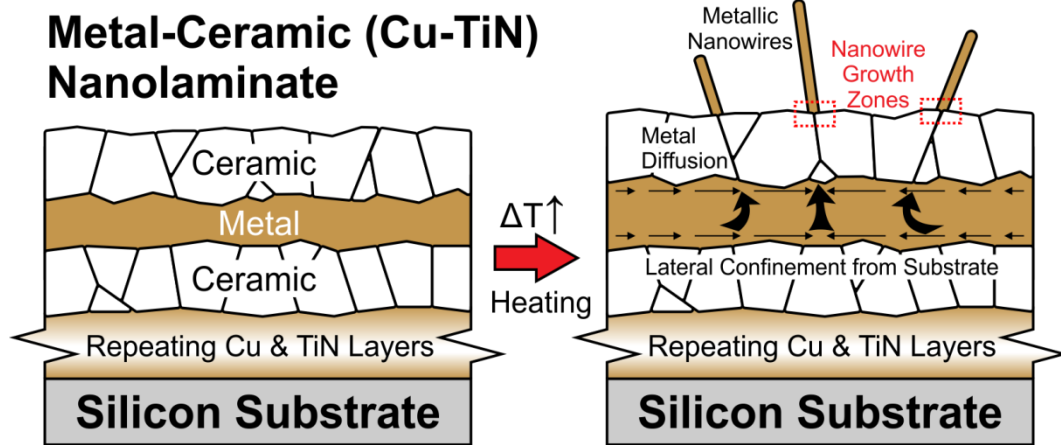


Figure 39: Increasing the temperature of the sample results in the generation of a large compressive stress within the film due to the large difference in CTE between the substrate and film. Columnar grain boundaries within the TiN layers serve as diffusion pathways for the mobile copper ions, which make their way to the upper surface to relieve the stress. Whisker growth occurs at the base of each wire or microparticle, with additional material pushing the already re-solidified material further from the surface.

At room temperature the use of thinner individual layer thicknesses is an effective strategy for increasing both the hardness and toughness of Cu-TiN sputtered films. Failure occurs along the columnar grain boundaries of the brittle TiN layers once the copper is sufficiently displaced to allow shear stresses to act on the TiN grain boundaries. Further compression results in the fractured TiN crystallites punching into the compliant copper film while shearing and tearing are observed along the TiN grain boundaries. At elevated temperatures the failure mechanism changes drastically, mainly due to softening within the copper layers and sufficiently high temperatures for copper diffusion to become a contributing factor to the overall material plasticity. This change in deformation mechanism is immediately visible even during the micropillar compression tests as copper protuberances and agglomerations form on the outside of the micropillars.

While the term “self-healing” has been used to describe this type of behavior in the past [103], this is not entirely accurate as there is no recovery of lost strength. Instead “damage-tolerant” is more precise, since flow of the softer metallic phase into voids left through brittle fracture within the ceramic component serves to prevent catastrophic failure. Instead of a sudden, brittle fracture, the ceramic components remain embedded within the diffusive metal matrix.

A quantitative explanation for the measured yield stress at room temperature is provided with reasonable accuracy using the Hall-Petch relation, given by Equation 20:

$$\sigma_{0.5\%} = \sigma_0 + k l_{Cu}^{-1/2} \quad \text{Equation 20}$$

where $\sigma_{0.5\%}$ is the 0.5% offset yield stress of the multilayers, σ_0 is the lattice resistance to slip, k is the Hall-Petch slope, and l_{Cu} is the thickness of the individual copper layers. The influence of the TiN layers is neglected in this consideration since they are assumed to behave in a perfectly elastic fashion until after the copper layers have begun to yield. The Hall-Petch constants were fit from the multilayer data, resulting in a σ_0 value of around 600 MPa and a k value of around $0.5 \text{ MPa} \cdot \text{m}^{1/2}$. The former value is in good agreement with the yield stress of the pure copper film, whereas the latter value is more than double the value reported for pure copper in the literature [113,114]. Since the calculation of Hall-Petch coefficients is performed using empirical data, this variability could be ascribed to microstructural differences between the experimental data sets and is still considered to be a reasonable value.

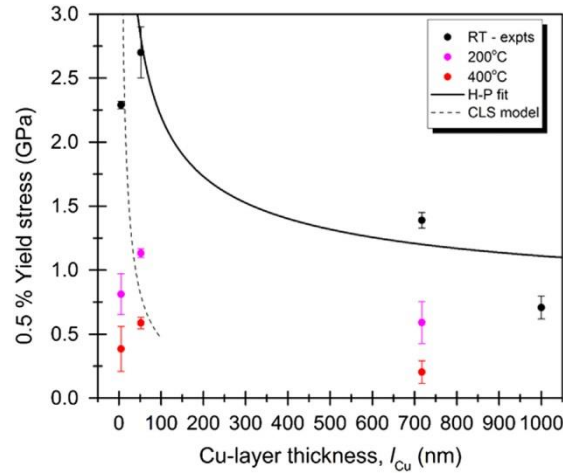


Figure 40: The experimental yield stress for the various multilayer thicknesses is plotted alongside the Hall-Petch and Confined Layer Slip models. At room temperature the Hall-Petch model provides an acceptable fit for the data, but at higher temperatures is no longer applicable. The smallest layer thicknesses exhibited yield stresses below those predicted by any standard hardening models.

For the thinnest films there is no longer an especially large gain in yield strength observed as predicted by the Hall-Petch relationship. Viewed in Figure 40 the thinnest layers exhibit a lower yield stress than the slightly thicker ones. This is in agreement with previous observations of the limit to Hall-Petch strengthening in copper, where softening has been observed at grain sizes below 30 nm [115]. No further improvement in yield stress is expected with further reduction of layer thickness. An alternative to Hall-Petch behavior is given through the Confined Layer Slip (CLS) model [116], in which the layer thickness is too confining for dislocation pileup to occur. The equation used to describe the CLS is given in Equation 21 [8]:

$$\sigma_{0.5\%} = 3.1\tau_{CLS} = \frac{Gb}{8\pi} \left(\frac{4-\nu}{1-\nu} \right) \frac{1}{l_{Cu}} \ln \left(\frac{\alpha l_{Cu}}{b} \right) \quad \text{Equation 21}$$

where τ_{CLS} is the shear stress required for a dislocation loop to pass through a single layer of copper, G is the shear modulus, b is the Burgers vector, ν is the Poisson's ratio, and α is the cutoff parameter, taken here as unity. The CLS model provides a reasonable prediction for the yield strength of the thinnest multilayers, but only at room temperature. Typically the CLS model is used to describe additional strengthening beyond the region under which the Hall-Petch hardening behavior is operative. It generally leads to a continued increase in strength, albeit at a more modest rate. These classical models are adequate to describe the room temperature stress-strain behavior, but predict drastically higher strengths than were observed at elevated temperatures.

The micrographs of the micropillar surfaces after compression at elevated temperature exhibit many telltale signs of diffusional copper flow. Rounded, droplet-like protuberances decorate the micropillar sidewalls. In cases where these growths are still separated their diameter exceeds the original film thickness, therefore any sort of dislocation-based extrusion of material is insufficient to explain their occurrence. When the strain in the micropillar is increased sufficient quantities of copper have exited the pillar to lead to coalescence into even larger growths, spanning many individual layers. With a melting temperature of 1085°C, copper has reached a homologous temperature of 0.35 at 200°C and of nearly 0.5 at 400°C. These temperatures are insufficient for bulk diffusion to be a major contributor to material deformation, but in sputtered multilayers the high density of grain boundaries and interfaces provide a significant number of pathways along which diffusion can readily occur. The more rapid loss of strength with increasing temperature for films with thinner individual layer thickness indicates that diffusion is occurring along the Cu-TiN interfaces. The micropillars themselves are not

constrained laterally; therefore no spontaneous growth of whiskers or microcrystals occurs on their surface. Instead, the direct application of load using the flat diamond punch is needed to provide the necessary driving force for diffusion.

Since diffusion of copper is the primary deformation mechanism at elevated temperatures, neither the Hall-Petch nor the Confined Layer Slip model provides an accurate estimate of the yield stress. Both of these models are built upon resistance to dislocation movement, whereas diffusion is responsible for plasticity at the elevated temperatures tested here. By adapting the equation for Coble creep, an equation relating strain rate, stress, and temperature can be obtained, given in Equation 22:

$$\dot{\epsilon} = \frac{148\Omega\delta}{kT} \left(\frac{\sigma}{d^3} \right) D_{gb} \quad \text{Equation 22}$$

where $\dot{\epsilon}$ is the strain rate, d is the average grain size, δ is the grain boundary width, Ω is the atomic volume, σ is the applied stress, D_{gb} is the grain boundary diffusion coefficient. A typical Arrhenius-type equation is used to describe the grain boundary diffusion coefficient as a function of temperature, given in Equation 23:

$$D_{gb} = D_0 \exp \left(-\frac{Q_{gb}}{kT} \right) \quad \text{Equation 23}$$

where D_0 is the pre-exponential factor, Q_{gb} is the activation energy for diffusion along grain boundaries, k is the Boltzmann constant and T is the absolute temperature. Solving the equation for strain rate for the Cu(50nm)-TiN(100nm) multilayer compressed at 200°C, a strain rate of roughly $45 \times 10^{-3} \text{ s}^{-1}$ is obtained. A stress of $\sigma = 1.13 \text{ GPa}$ (Figure 38), interface width of $\delta = 0.5 \times 10^{-10} \text{ m}$, atomic volume of $\Omega = 8.78 \times 10^{-30} \text{ m}^3$, diffusional pre-exponential factor of $D_0 = 3 \times 10^{-9} \text{ m}^2/\text{s}$, and activation energy for grain boundary diffusion $Q_{gb} = 0.64 \text{ eV}$ [117] were taken for this calculation. This value of strain rate is an order of magnitude higher than that used during the experiments and indicates that diffusion is indeed responsible for accommodating nearly the entirety of plastic deformation. At higher temperatures the case is even clearer, where the total number of diffusion pathways and diffusivity of the copper atoms is even higher.

5.2.5 Conclusions

At elevated temperatures the copper layers become significantly more compliant and the strengthening capacity of the multilayer structure is greatly diminished. Pairing a hard ceramic with a softer metal also ceases to be effective when the microstructure of the ceramic enables brittle fracture to occur, as is seen here along the columnar grain boundaries within TiN. Conventional multilayer hardening models are insufficient to describe the deformation observed at temperatures where a high homologous temperature is reached within one of the component materials. Diffusion is shown to play a significant role in the deformation of the multilayers, assisted by the high stress levels reached within the micropillar. Mechanical stress is the driving force for copper diffusion. The use of multilayer structures is shown to be a possible means for inhibiting catastrophic failure of multilayer coatings since the diffusive material can fill voids generated through brittle fracture within the ceramic layers of the film.

Contributions: FEM simulations were performed by Daniel Esqué-de los Ojos. Micropillar compression experiments and were performed with Rejin Raghavan and Jeff Wheeler. Damien Frey and Gerhard Bürki assisted with the development and operation of the elevated temperature indenter while Simon Hofstetler of Synton-MDP collaborated in the development of the heated indenter tips. Data analysis and scien-

tific discussion were the results of collaboration with Rejin Raghavan. The figures were also mainly prepared by Rejin Raghavan. A majority of these results has been published in 2014 as "Mechanical behavior of Cu/TiN multilayers at ambient and elevated temperatures: Stress-assisted diffusion of Cu" [118].

5.3 Magnesium-Niobium

5.3.1 Introduction

The magnesium-niobium materials system was selected for study in order to ascertain if the conclusions drawn from well-studied multilayer systems like copper-niobium are more broadly applicable to other materials. The magnesium-niobium system is especially interesting since interfacial energy reduction can stabilize otherwise unstable phases in one of the constituent materials. This polymorphic transformation is referred to as pseudomorphism, and can be considered an interface-stabilized allotrope. Stable pseudomorphs are formed when the sum of the strain energy due to coherency stress, the applied stress, and the energy penalty of forming dislocation arrays is minimized. Examples of materials systems which exhibit polymorphic transformation in multilayers include Mg-Nb [119], Zr-Nb [120,121], and Ti-Al [122,123]. Since the driving force for phase transformation is a reduction of interfacial energy, either of the two components can be made to adapt to the phase of the other by selecting appropriate layer thicknesses. Bi-phase transition diagrams show which phases will be present as a function of bilayer thickness and the volume fraction of one component [124]. Calculated bi-phase transition diagrams generated using a thermodynamic model for energy show good agreement with experimental work and are available for a number of materials systems [125]. The stabilization of pseudomorphs often requires a volumetric ratio other than 1:1, therefore future studies will benefit from investigating the effects of both layer thickness and volumetric ratio.

All combinations of body-centered cubic (BCC), face-centered cubic (FCC), and hexagonal close-packed (HCP) transitions have been observed, but the HCP to cubic transitions are especially of interest. Polycrystalline HCP metals tend to be brittle due to the limited number of slip systems available, whereas cubic metals can undergo significant plastic deformation before failure. By inducing a pseudomorphic transformation within a normally HCP metal it should be possible to capitalize on the metal's desirable properties while foregoing the usual drawback of limited plasticity. Magnesium is an ideal candidate for such a strategy due to its widespread use in structural applications where weight is critical. Magnesium is the lightest weight structural metal at just $\frac{1}{4}$ the density of a typical steel and $\frac{2}{3}$ the density of aluminum. Pseudomorphic BCC magnesium should allow magnesium's high specific strength and low density to be leveraged without suffering from its brittle fracture. Niobium is an ideal partner for this stabilization due to its mutual insolubility with magnesium and its BCC crystal structure, though an alternative material would be needed for applications seeking to capitalize on magnesium's low density for lightweight applications since niobium is nearly five times denser than magnesium. For these applications a FCC metal may even be a more attractive if a similar pseudomorphic stabilization of magnesium could be achieved. This work seeks to investigate the operative deformation mechanisms present in the BCC magnesium phase to determine the potential impact this phase stabilization has on the strength and ductility of a multilayer composite.

5.3.2 Experimental

Films were deposited in a sputtering chamber built by H.V.A. (High Vacuum Apparatus) Mfg. Inc. in Hayward, California, USA. Substrates are mounted to a vertical-axis rotating spindle which can be rotated to face one of four target cusps. Large (6-inch diameter) targets are positioned at a four-inch working distance from the substrates to realize a lateral sputtering configuration. The small working distance and large target size enable homogeneous film thicknesses to be deposited without rotating

the substrates during depositions. Square silicon chips with roughly 1 cm side length were cleaved from a 4-inch (100) wafer to be used as substrates. These substrates were rinsed with acetone and de-ionized water before being blow-dried with compressed air to remove particles generated in the cleaving process. A total film thickness of 5 μm was targeted, with nominal layer thicknesses of 5 nm for one film and 50 nm for the other. The sputtering conditions are given in Table 5.

After film deposition, the samples were mounted on aluminum stubs using a high-temperature silver adhesive (Aremco Pyro-Duct 597TM-A). The samples were cured at 100°C for two hours to ensure good bonding without encouraging grain growth within the film. A focused ion beam (FIB) workstation (Tescan Vela) was used for milling the micropillars using a three-step process. First, stepped circles with an outer radius of 20 μm and inner radius of 5 μm were milled using an accelerating voltage of 30 kV and a current of 6 nA, stopping when the crater floor first reached the interface between the film and the substrate. Second, an annulus was milled at 30 kV and 1.6 nA to reduce the pillar diameter and sidewall taper. Finally, a polishing circle was used under the same milling conditions as in the previous step to achieve the final pillar diameter. The same FIB workstation was used to produce the cross-sectional lamella for transmission electron microscopy (JEOL JEM-2200FS) by the lift-out process.

	film 1	film 2
nominal layer thickness	5 nm	50 nm
base pressure	$5 \cdot 10^{-7}$ Torr	$5 \cdot 10^{-7}$ Torr
deposition pressure	6 mTorr	6 mTorr
Nb deposition power	300 Watts	300 Watts
Mg deposition power	300 Watts	300 Watts
Nb cycle duration	9.30 s	93.0 s
Mg cycle duration	2.03 s	20.3 s
# of bilayer cycles	500	50
nominal film thickness	5 μm	5 μm

Table 5: Sputter deposition conditions

The film thicknesses were determined using three independent methods: step height measurement using a stylus profilometer (Altisurf 500), examination of FIB-prepared (Tescan Vela) film cross sections by both scanning (Hitachi S-4800) and transmission electron microscopy (Jeol 2200 FS), and X-Ray Reflectometry (XRR) (Bruker D8 Discover). The sputter rates were initially determined after depositing separate elemental magnesium and niobium films, each with a thickness of roughly 100 nm. A thin strip of tape was placed across each substrate prior to deposition and peeled away after deposition. The step height was then measured using a stylus profilometer. The films are referred to by their nominal individual layer thicknesses of 5 and 50 nm for the remainder of this paper, though the layer and film thicknesses determined by XRR and reported in the results section are considered to be the more accurate values.

A Bruker Discover D8 with Cu K_{α} radiation was used for both the XRR and XRD measurements. For the XRD scans an offset Bragg-Brentano arrangement was used to measure a 2θ range from 20° to 100° with a step size of 0.05°. A 2° offset was utilized for the ω - 2θ scans to suppress diffraction peaks from the single-crystalline silicon substrate. For the XRR measurements data was collected from 2θ values of 0.25° to 4.25° with a step size of 0.025° for the 5 nm films and 0.0076° for the 50 nm films. Thicker lay-

ers require improved resolution to adequately capture the narrower oscillations. The collection time was increased at higher angles to partially compensate for the decreased signal intensity.

Room temperature nanoindentation was performed using a Hysitron Ubi nanoindenter. A Berkovich indenter was used to perform indents at loads up to 10 mN, resulting in indentation depths up to a few hundred nanometers. Therefore no substrate effects are expected. All micropillar compression experiments were performed using an *in situ* indenter (Alemnis AG, Switzerland), as previously described in detail [126]. This experimental platform allows for displacement-controlled tests to be performed across a wide range of temperatures and strain rates operating *in situ* within a Zeiss DSM 962 Scanning Electron Microscope (SEM). Strain rate sensitivity (m) and activation volume (V) were determined using Strain Rate Jump (SRJ) tests as originally performed on metallic (Cu-Ni) multilayers by Carpenter *et. al* [127]. Room temperature micropillar compression SRJ tests began at baseline strain rate of $9 \times 10^{-4} \text{ s}^{-1}$. Shortly after the onset of plastic deformation the strain rate was dropped abruptly to $5 \times 10^{-5} \text{ s}^{-1}$. Subsequent jumps to strain rates of $2 \times 10^{-4} \text{ s}^{-1}$, $5 \times 10^{-5} \text{ s}^{-1}$, and $9 \times 10^{-4} \text{ s}^{-1}$ were performed once the deformation had stabilized. With four SRJs per micropillar it is possible to calculate three strain-rate sensitivity values.

Elevated temperature tests were performed at five different temperatures: 20, 72.5, 150, 200, and 250 °C. Five micropillars were compressed at each temperature to ensure sufficient statistical data could be collected. Prior to heating the first five pillars were compressed at 20 °C to establish if any microstructural changes occur within the samples during the elevated temperature tests. Both the sample and indenter were then heated to the maximum temperature of 250 °C and allowed to reach thermal equilibrium over the course of approximately one hour before compressing the next set of five micropillars. The temperature was then stepped down incrementally following the same procedure, concluding with an additional five micropillars compressed at 20 °C.

Cryogenic micropillar compression tests were also performed at -70°C and -30°C. The same *in situ* indenter used for the elevated temperature tests was modified to permit cryogenic tests to be performed as well. Both the sample and the flat-punch indenter are cooled by pumping vapor from a 25-liter cryogenic storage dewar filled with liquid nitrogen. Resistive heaters and thermocouples for temperature feedback are then used to ensure that the sample and indenter tip are in thermal equilibrium before the compression experiments are performed. A separate sample (deposited during the same sputtering run) was attached to an aluminum stub using Stycast 2850FT adhesive. The entire sample was then sputtered with a thin (<5nm) layer of gold to ensure that sufficient SEM image quality could be obtained to reliably align the sample.

All micropillars were imaged using a Hitachi S-4800 SEM both prior to compression (to determine the exact pillar dimensions) and after compression (to observe the deformation mode). As there is a slight pillar taper from annular milling, the stress was calculated using the upper diameter of each micropillar. Strain was determined using the total displacement relative to the film thickness.

5.3.3 Results

5.3.3.1 X-ray diffraction and reflectometry

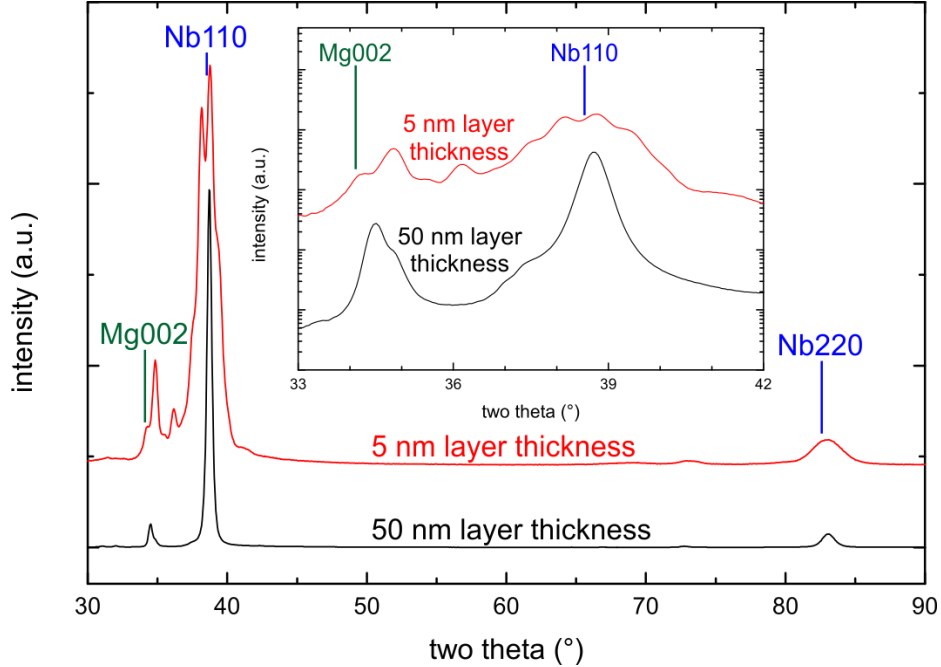


Figure 41: Bragg-Brentano XRD patterns for both 5 and 50 nm layer thicknesses in Mg-Nb multilayers. Superlattice peaks are apparent between 33° and 42° for the films with a layer thickness of 5 nm, indicating an epitaxial relationship between Mg and Nb for thin layer thicknesses.

The XRD patterns for the magnesium-niobium multilayers, shown in Figure 41, exhibit a number of interesting features. For both samples the Nb 110, Nb 220, and Mg 002 peak are much more pronounced than any other peaks. This indicates a strong 110 texture in the Nb layers, as is often observed for a BCC material prepared via physical vapor deposition (PVD). The 50 nm Mg layers exhibit a 002 texture, with the c-axis perpendicular to and the close-packed planes parallel to the substrate. The Bragg-Brentano XRD scans do not conclusively demonstrate which of the Mg pseudomorphs is present in the 5 nm film due to the presence of higher-order superlattice peaks are visible between 33° and 42°. These peaks are a product of X-rays diffracted from the superlattice, where the layer thickness effectively acts as a large unit cell [128]. Superlattice peaks are commonly observed in periodic bilayer structures with individual layer thicknesses between 1 and 15 nm [129]. Thicker layers will result in only classical XRD peaks while thinner layers tend to produce individual, broad peaks. At sub-nanometer layer thicknesses adjacent peaks can meld together to form a single, broad peak. The spacing, position, and intensity of these superlattice peaks can be used to precisely determine the layer thickness and interface roughness in superlattice structures [130]. A complex fitting operation, as described in Schuller's *New Class of Layered Materials* [128], can be conducted to obtain precise information regarding the structure of the multilayer film. For cases where only a simple estimate of the individual layer thickness is required, this can be obtained using Equation 24:

$$\sin \theta_{\pm} = \sin \theta_B \pm \frac{n\lambda}{2\Lambda} \quad \text{Equation 24}$$

where θ_{\pm} is the position of the satellite peak, θ_B is the position of the main Bragg diffraction peak, n is the order of the satellite peak, λ is the X-ray wavelength, and Λ is the bilayer thickness. Equation 24 was originally developed to utilize only the position of the first satellite peak [131], though it was later extended to include additional satellite peaks [132]. It is not uncommon for there to be some minor discrepancy between the values calculated from the satellite peaks, though in general the difference is quite small. After algebraic rearrangement of this equation the bilayer thickness for the nominally 5 nm thick layer film was calculated as 8.8 nm. This value is an average from the seven satellite peaks, which varied from 8.3 to 9.4 nm. The lattice spacing of magnesium does not change appreciably between its nominal HCP structure to its metastable BCC form, so the 002 peak position does not directly reveal which crystal structure is present. Since the films are so strongly textured the other peaks are not captured in a Bragg-Brentano scan.

The XRR curves for both samples are shown in Figure 42. The thickness of the layers can be determined simply using the Fast Fourier Transform (FFT) of each curve, or more precisely by fitting a model to the data. Using the FFT approach, frequencies of 49.9 and 94.3 nm were determined for the nominally 50 nm thick layers while frequencies of 6.1, 14.7, 20.5, and 28.7 nm were strongly detected for the nominally 5 nm thick layers. Since the FFT can contain secondary reflections it is necessary to use the simulation approach to precisely determine the layer thickness. The results of the XRR simulations are shown alongside the measured data in Figure 42.

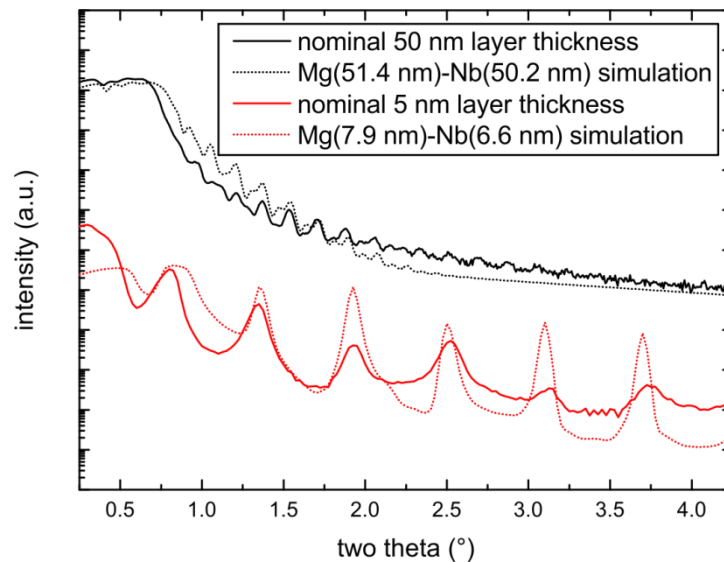


Figure 42: X-Ray Reflectometry (XRR) curves, both as measured and as simulated for Mg-Nb multilayers with nominal 5 and 50 nm layer thicknesses.

Bruker Leptos software was used to construct a simple 2D model for the simulation, consisting of alternating magnesium and niobium layers atop a silicon substrate. The layer thickness and interface roughness were the only adjustable parameters and a genetic algorithm was used to perform the necessary fitting. The film with nominally 5 nm thick layers was shown to consist of 7.9 nm thick magnesium layers and 6.6 nm thick niobium layers with an interface roughness of roughly 0.3 nm. The film with nominally 50 nm thick layers was shown to consist of 51.4 nm thick magnesium layers and 50.2 nm thick niobium layers with an interface roughness of 2.0 nm. These values are an average over the sample and are expected to vary somewhat locally. In both films the critical angle for total external reflection was somewhat lower than that calculated by simulation. This is likely due to the formation of a partial MgO layer atop the film. Fitting was also performed using a model which included a thin MgO layer, but in general the fit was inferior to the simpler model. Realistically the interface roughness would increase with distance from the silicon substrate, but for the sake of simplicity was considered to be constant among all of the layers.

5.3.3.2 Cross-sectional TEM

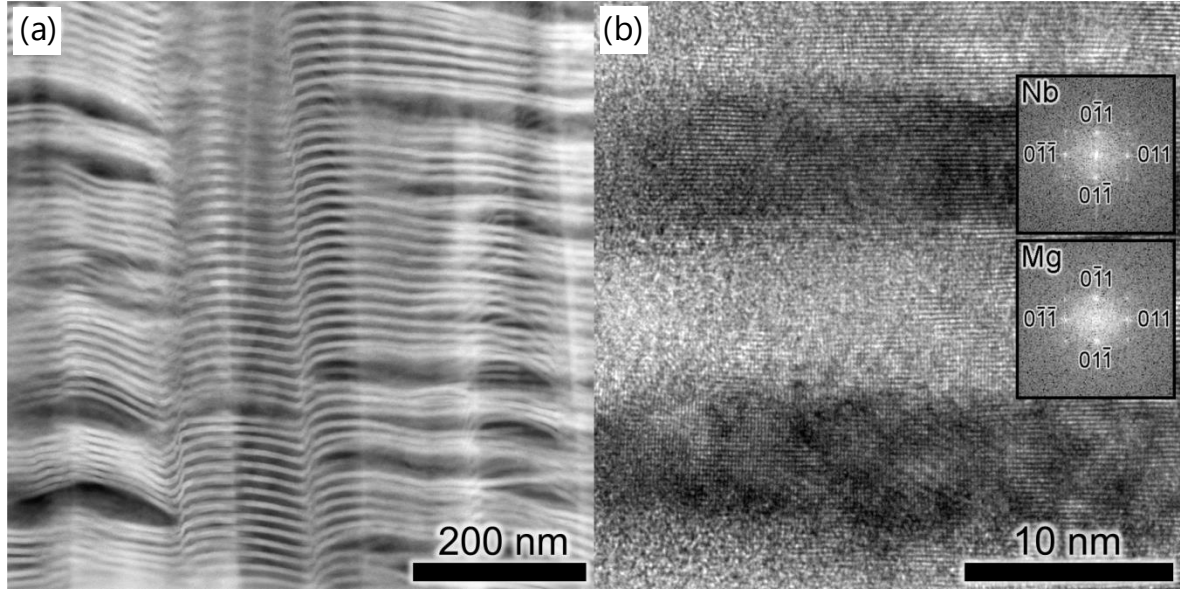


Figure 43: Cropped and rotated (a) HAADF-STEM and (b) HRTEM image with FFT inset of Mg-Nb multilayer with 5 nm layer thickness

A horizontal cross-section TEM shows a clearly defined multilayer structure as seen in Figure 43 (a). The appearance of waviness is a product of the curtaining effect produced when milling the TEM lamella with the FIB. Surface micrographs for the 5 nm layer thickness films show a characteristic brain-like wrinkle pattern, seen in Figure 44. The presence of these wrinkles makes it challenging to avoid the curtaining effect and indicates that some columnar porosity may be present within the sample. This microstructure was not observed in any of the cross-sectional views of the film, so it is considered to be a growth phenomenon present only at the film surface.

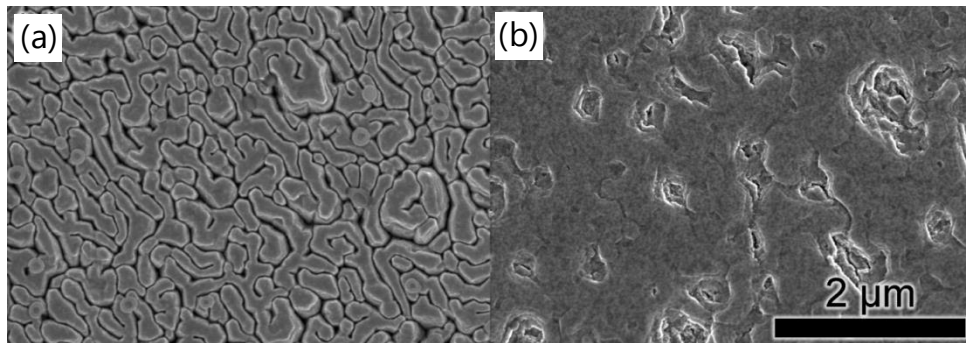


Figure 44: Characteristic surface topology of (a) 5 nm and (b) 50 nm layer thickness Mg-Nb films

The epitaxial relationship between the magnesium and the niobium layers can be observed in Figure 43(b). The magnesium layers (light) exhibit a BCC crystal structure to realize a classic cube-on-cube epitaxy, as seen in the inset Fast Fourier Transform (FFT) images.

5.3.3.3 Strain-rate jump testing

Typical stress-strain curves for the SRJ tests are shown in Figure 45. The overall length of the plastic deformation zone before the ultimate yield strength is reached tends to be short, necessitating that all

SRJs be performed before 10-15% engineering strain was reached. There is a small tail at the beginning of the loading curve which corresponds to the upper surface of the pillar conforming to the diamond flat punch as the indenter comes into contact with the micropillar. Real-time observation of the stress-strain behavior is necessary to determine when the pillar has begun to deform plastically and to determine when to initiate the next SRJ. In general the transients were not as sharp as those observed in other material systems [133], so at most four SRJs could be performed for a given micropillar. Strain rate sensitivity is observed for both 5 and 50 nm thick layers, though it is more pronounced in the 5 nm layers.

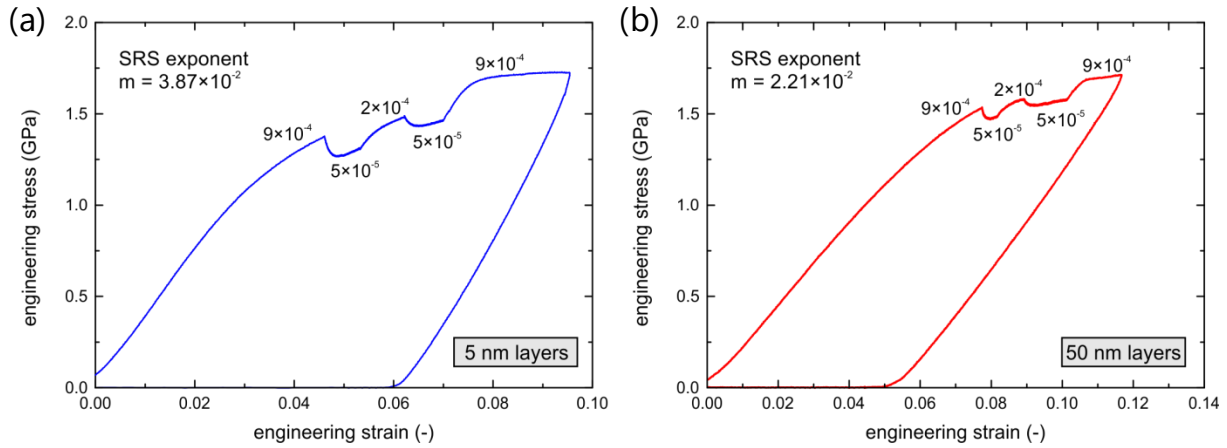


Figure 45: Strain Rate Jump (SRJ) results for Mg-Nb multilayers with (a) 5 nm layer thickness and (b) 50 nm layer thickness

The strain rate sensitivity (SRS) exponent, m , is calculated from a uniaxial strain rate jump test by using Equation 8 [134]. The results of this evaluation correspond to the visual assessment: namely that the thinner layers exhibit larger sensitivity to strain rate.

$$m = \left. \frac{\partial \ln \sigma}{\partial \ln \dot{\epsilon}} \right|_T \quad \text{Equation 25}$$

In addition to the SRS exponent, another useful metric for evaluating the operative deformation mechanism is the apparent activation volume. The apparent activation volume is inversely proportional to the strain rate sensitivity exponent and is given by Equation 7 [135].

$$V_{\text{activation, apparent}} = \frac{\sqrt{3}kT}{m\sigma_f} \quad \text{Equation 26}$$

Both the SRS and apparent activation volume will exhibit some temperature dependency, but for the sake of simplicity the results from the room temperature SRJ tests are applied to calculations at elevated temperatures as well. Taking a Burger's vector value of 0.3192 nm for the 50 nm magnesium layers, the room temperature activation volume is 5.58 times the cube of the Burger's vector. For the 5 nm magnesium layers a lattice constant of 0.3574 nm was used as calculated by density functional theory (DFT) simulations [136]. The activation volume at room temperature for the 5 nm layers is 2.78 times the cube of the Burger's vector. Activation volumes commonly interpreted as belonging to grain-boundary diffusion are typically on the order of 10 times the cube of the Burger's vector.

5.3.3.4 Elevated temperature micropillar compression

Typical engineering stress-strain curves from the elevated temperature tests are shown in Figure 46. For both samples the yield stress predictably decreases with increasing temperature, though there are differences in the general yield behavior. For the 5 nm layers the elastic region is initially linear after the pillar surface has flattened, but then exhibits a gradual transition from the elastic regime to the point of highest stress. At higher temperatures this effect is less pronounced and a steady engineering stress is observed up to engineering strains of 20%. The 50 nm thick layers exhibit a comparatively sharp transition from the elastic to plastic regime, followed a moderate strain-hardening plateau before the ultimate compressive stress is reached. At temperatures at and above 150°C a characteristic kink is observed which becomes more pronounced at higher temperatures. Reviewing the in-situ SEM videos, this kink is shown to be associated with the collapse of the lowest magnesium layer.

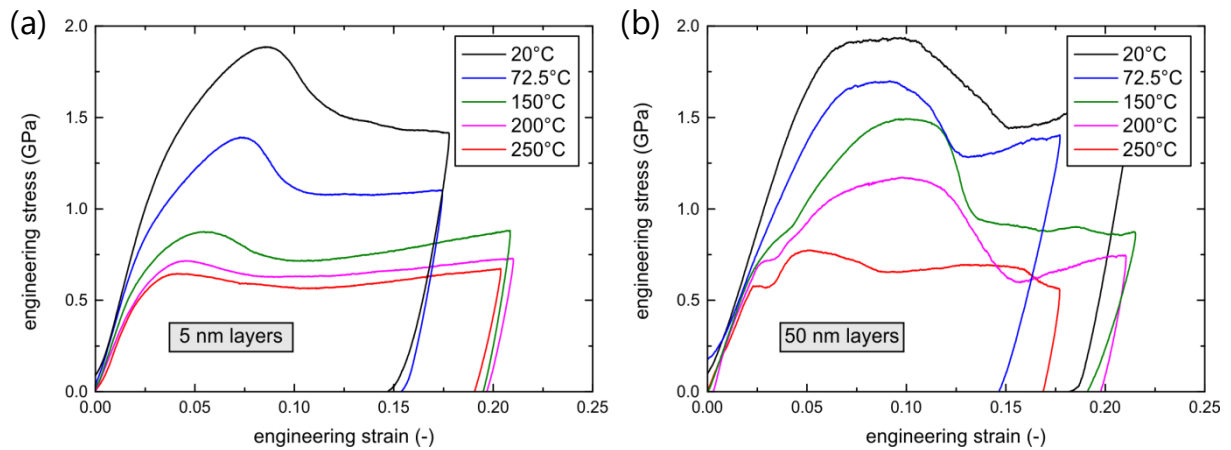


Figure 46: Engineering stress-strain curves for Mg-Nb multilayers with (a) 5 nm layer thickness and (b) 50 nm layer thickness at elevated temperatures

Post-mortem micrographs for characteristic micropillars compressed at elevated temperatures are given in Figure 47 and Figure 48. The 5 nm layer thickness samples deform in a similar fashion across the entire temperature range: plastic deformation is largely confined to the upper portion of the pillar - where taper from the FIB-milling process results in a smaller diameter and higher stress - though testing to larger total strains results in some changes at the higher temperatures. At the two lower temperatures a shear band has formed near the top of the pillar which ultimately results in a large lateral force on the rest of the pillar. This has led to the separation of the pillar from its substrate pedestal, but occurs late enough in the test as to have no impact on the yield strength calculations. At higher temperatures and large strains, beginning at 150°C, signs of magnesium extrusion and coalescence into beads on the micropillar surface can be observed.

The 50 nm layer thickness micropillars demonstrate a much more marked change in deformation mechanism with temperature. At room temperature the tapered portion of the pillar accounts for nearly all of the plastic deformation, mushrooming out as the magnesium layers deform and the niobium layers fracture. At 72.5°C the mushrooming near the top of the pillar is far less pronounced and the magnesium layer nearest the substrate has collapsed. Small, curved tendrils of magnesium have extruded from this lower magnesium layer. At temperatures of 150°C and above the mushrooming effect near the top of the pillar has become much less pronounced while all of the magnesium layers contribute to the deformation of the pillar. This is evidenced by the growth of magnesium protuberances and whiskers from the outer surface of the pillar. At 250°C many of these whiskers clearly exhibit a hexagonal cross-section and sharp kinks indicative of an internal twin boundary or stacking fault. As is observed in the 5 nm thick layer samples at 250°C, the magnesium extrusions from the micropillar have begun to coalesce when they come into contact with magnesium extruded by adjacent layers. In

all cases no growth of whiskers was observed during the roughly one-hour temperature stabilization period, but rather occurred nearly instantaneously upon the application of mechanical load.

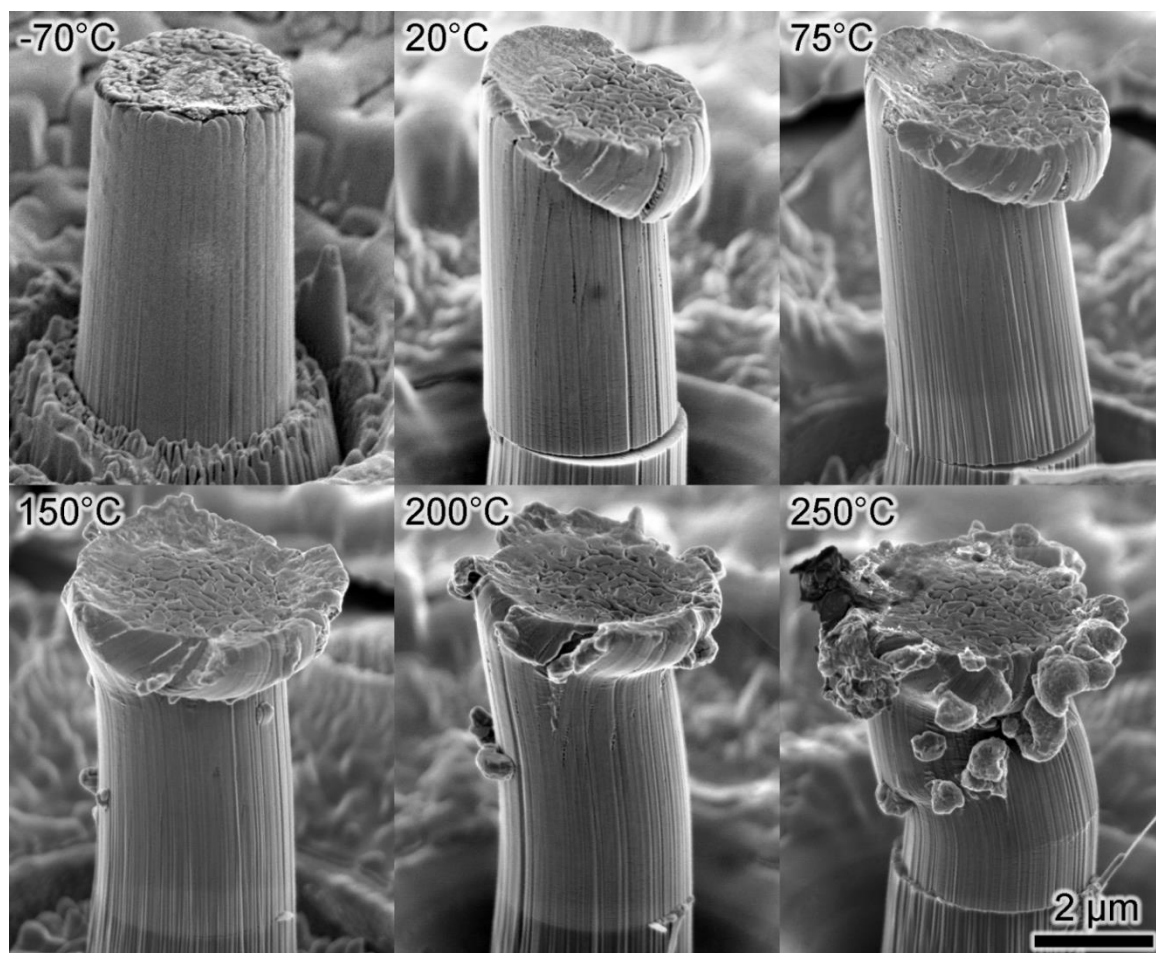


Figure 47: Micropillars with 5 nm layer thickness compressed at various temperatures

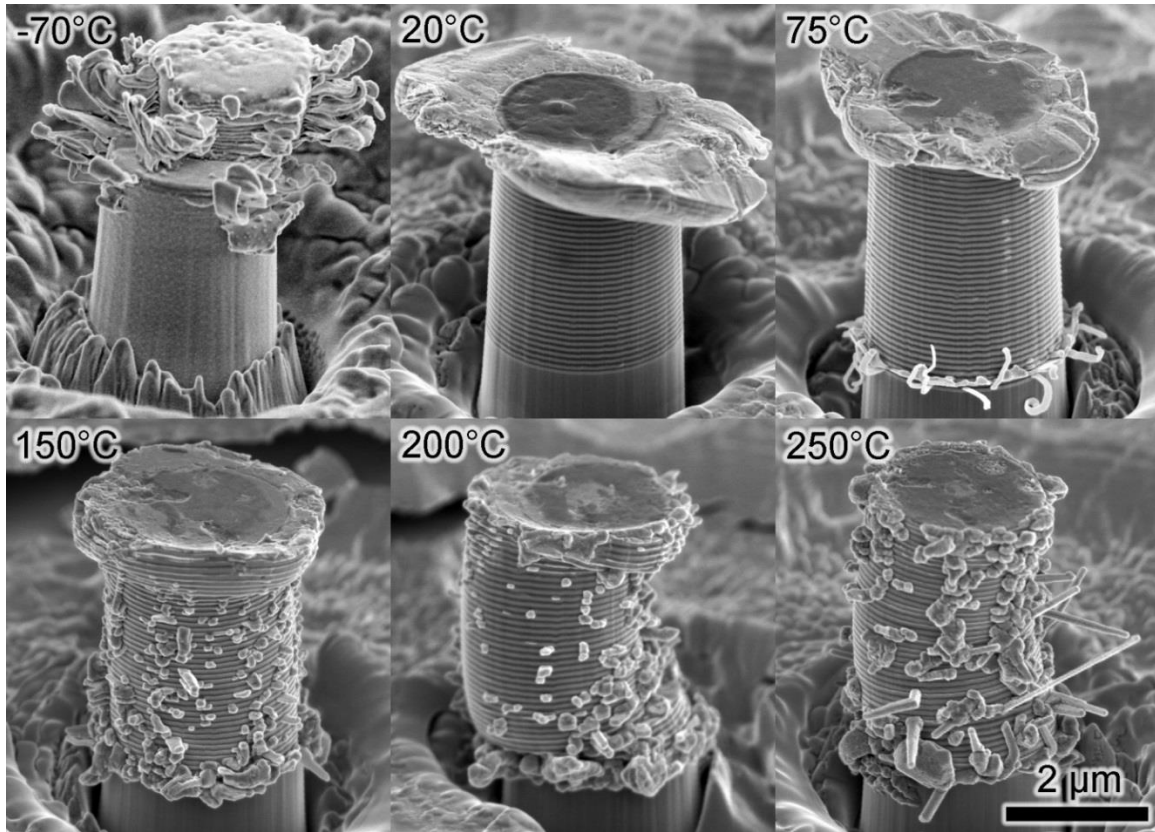


Figure 48: Micropillars with 50 nm layer thickness compressed at various temperatures

5.3.3.5 Cryogenic Temperature Micropillar Compression

All samples had to be sputtered with a thin (~5 nm) layer of gold in order to allow for sufficient image quality to perform alignment of the flat punch. The low-temperature adhesive has exceptionally poor electrical conductivity and is quite prone to charging effects in the SEM. The 5 nm films exhibit increased yield strengths with decreasing temperature as expected, allowing for successful SRJ tests to be performed at -70°C as well. The cryogenic data is presented separately in Figure 49 rather than with the elevated temperature data in Figure 46 to maintain clarity and give a better impression of the statistical variability within the cryogenic data.

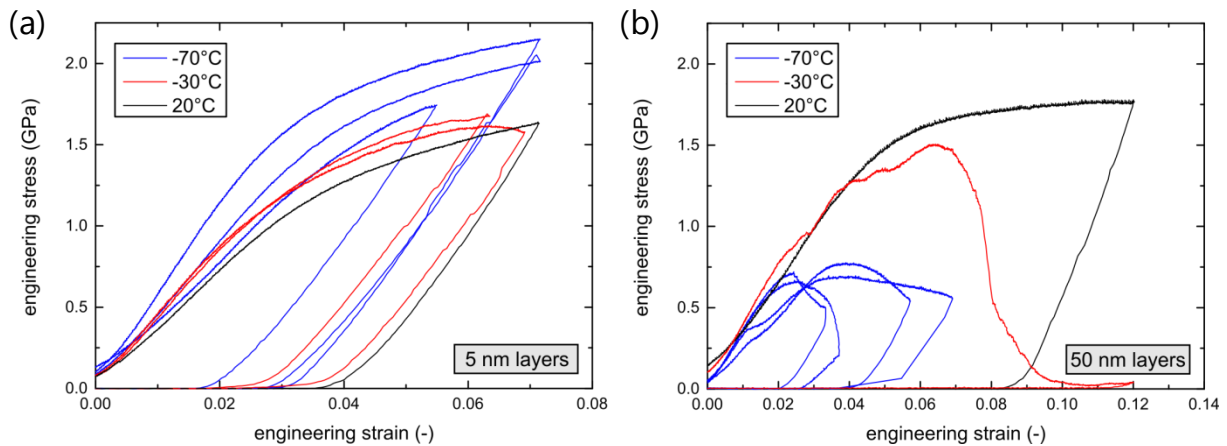


Figure 49: The Mg-Nb multilayer micropillars with 5 nm individual layer thickness (a) demonstrate increasing yield strength with decreasing temperature down to -70°C while the 50 nm Mg-Nb multilayer micropillars (b) lose strength with decreasing temperature due to the onset of brittle fracture.

The 50 nm films exhibited an unexpected, drastic reduction in yield strength. Data obtained at -30°C generally exhibited stochastic variation, with marked differences in micropillar deformation behavior from one pillar to the next. The best curve is shown in Figure 49(b). At -70°C the data was much more repeatable and exhibited less statistical variation. Brittle materials tend to exhibit higher variability in the failure stress, indicating that the material has undergone a ductile-to-brittle transition at cryogenic temperatures. The yield stress of only around 0.7 GPa is much lower than expected. In order to ensure that there were no sample alignment issues, a pillar was compressed at room temperature without changing the experimental setup. The yield strength was 1.6 GPa, only slightly below that obtained during the previous experiments. Sample misalignment can therefore be ruled out as a cause for the low yield stress. Since the stresses from thermal expansion coefficient mismatch are quite mild (10s of MPa at most), there must be some other stress concentration within the pillar leading to fracture of the magnesium layers. Minor voids or even variability within the grain boundaries is sufficient to act as a failure initiation point. The post-compression SEM micrographs in Figure 49(b) indicate that the magnesium layers account for all of the plastic deformation. As was observed in the elevated temperature experiments, the magnesium has been extruded out of the pillars. Here, however, there is no evidence for diffusion (no rounding, coalescence of adjacent layers, no formation of hexagonal structures), but rather through slip parallel to the substrate.

5.3.3.6 Activation Energy Analysis

The activation energy for the dominant deformation mechanisms was also calculated using the slope of the yield stress on an Arrhenius-style plot and the strain sensitivity exponent, as given by Equation 6.

$$Q = \frac{1}{m} R \left[\frac{\partial \ln \sigma}{\partial (1/T)} \right] \quad \text{Equation 27}$$

Activation energies for various deformation mechanisms in magnesium include 135 kJ/mol for lattice diffusion, 92 kJ/mol for both boundary and core diffusion, and 230 kJ/mol for power-law creep [137]. Though no literature data is available for the diffusion coefficient of magnesium along a magnesium-niobium interface, it stands to reason that the value would lie somewhere between the grain boundary diffusion coefficient and the diffusion coefficient for a free surface. If this is the case, an activation volume of this magnitude is not unreasonable for a diffusion-dominated deformation mechanism. The flow stress was taken as being equivalent to the 1% yield offset stress determined from the point on the loading curve at which the slope was the steepest.

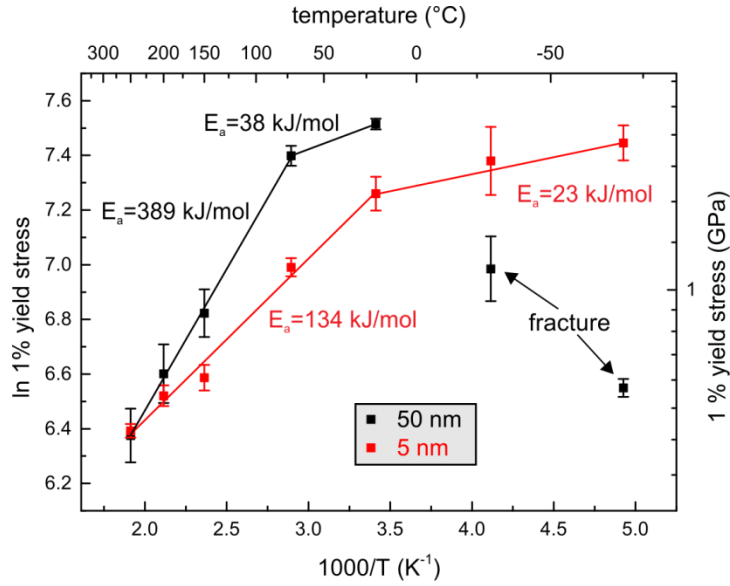


Figure 50: Arrhenius plot used for the calculation of activation energy for deformation mechanisms

5.3.4 Discussion

5.3.4.1 Microstructure

The Mg-Nb materials system was selected due to the mutual insolubility between the two materials, enabling multilayers with atomically sharp interfaces to be produced. The TEM micrographs in Figure 43 indicate that this was achieved and that the targeted BCC magnesium phase was also realized in the 5 nm layer thickness films. The preparation and imaging of TEM lamella is notably more labor-intensive than X-ray diffraction techniques, therefore the latter are preferable for determining the individual layer thicknesses and the phases present. The strong texture in sputtered films and the secondary peaks which appear for nanoscale multilayers complicate the interpretation of the XRD data, therefore TEM was used to confirm the findings.

Figure 41 shows the XRD results for both samples. When plotted linearly the Nb 110 and Nb 220 peaks are by far the most pronounced, indicating a strong 110 texture within the Nb layers. The Mg peaks are less intense due to the lower electron density in lighter elements. Phase identification can be convoluted by the presence of superlattice peaks which overlap with many of the classical XRD peaks. Significantly more superlattice peaks of higher intensity are observed here than were reported in reference [138]. This is due to the subtle differences in the precise individual layer thickness. The spacing of these peaks is very sensitive to the layer thickness and can also be used to obtain an estimate of the layer thicknesses. More precise determination of layer thickness is obtained using XRR in Figure 42.

Density Functional Theory (DFT) simulations show that BCC magnesium is metastable under thin film conditions where magnesium grows epitaxially on BCC niobium [138]. Further DFT calculations predict a stability cutoff for BCC magnesium with a layer thickness of 4.2 nm [136], a value which is exceeded by the 7.9 nm Mg layer thickness here. The thickness of the BCC Mg layers could also likely be increased further through the use of higher volume fractions of Nb. The XRR data demonstrates that the density of the films is somewhat lower than bulk material. This is seen by the lower angles at which total external reflection ceases to operate and is more pronounced for the 5 nm film than for the 50 nm film. Cross-sections of the film do not reveal any obvious porosity or voids, so the films were considered to be sufficiently dense to perform mechanical tests. The possibility of film density impacting the mechanical properties of the films should still be taken into consideration.

5.3.4.2 Mechanical Behavior

For the elevated temperature tests there is a continuous decrease in yield strength for both layer thicknesses. This result is consistent with the theory that deformation consists of both thermal and athermal components and that the yield strength of a material decreases with increasing temperature. Previous nanoindentation experiments between room temperature and 200 °C in similar Mg-Nb multi-layer films did not exhibit this trend [139], although the standard deviation of the experiments was too large to establish a clear relationship between hardness and temperature. Micropillar compression experiments provide a clearer result due to the more uniaxial stress state and the lack of large isostatic stresses from lateral confinement in nanoindentation experiments.

The overall behavior of the stress-strain curves is reminiscent of that of pure magnesium. HCP magnesium possesses a low ductility and initially high strain-hardening behavior due to the decomposition of dislocations into lower-energy, immobile arrangements [140]. At elevated temperatures magnesium exhibits limited strain-hardening capacity, resulting in rapidly reached peak stress followed by significant softening [141]. This behavior was also observed in this experiments and deformation is postulated to be dominated by the behavior of the magnesium layers. Niobium requires very high stresses to display any diffusion, regardless of the temperature, and does not contribute to the micropillar plasticity at elevated temperatures. This is also supported by the post-compression SEM micrographs which show that plasticity is largely confined to the magnesium layers, except at lower temperatures where co-deformation causes the niobium layers to crack. While the ductile-to-brittle transition temperature for pure niobium is well below the temperature range tested here [142], the introduction of even very small quantities of impurity atoms can result in the onset of brittle behavior at temperatures around -30°C [143].

In the samples with 5 nm layer thickness (those containing BCC magnesium) the pillars also exhibit a clear transition in deformation mechanism from diffusion- to dislocation-based deformation with decreasing temperature. In the 5 nm layer thickness films this transition occurs around room temperature, rather than 75°C as observed for the 50 nm layer thickness films. The general mode of failure begins with the formation of a shear band that forms from the upper edge of the micropillar. At lower temperatures this shear band behaves like a wedge and ultimately displaces the lower part of the pillar from its substrate pedestal. At higher temperatures the micropillar is capable of accommodating larger deformations without separating from the substrate pedestal. Agglomerated magnesium protuberances form on the pillar surface at higher temperatures. At the highest temperatures the silicon pedestal appears to be compromised where the stress is the highest. A long filament is often observed growing out from this point. It seems like that this filament is also a magnesium whisker, albeit much thinner than those observed in the 50 nm layer thickness samples.

The 50 nm layers exhibit a stress concentration at the top of the pillar due to taper which causes the upper part of the pillar to deform first at lower temperatures. As the temperature increases the bottom layers instead fail first, with more of a curling, extruded appearance rather than the whiskers seen from the upper layers. The stress concentration at the base of the pillar is a result of the elastic modulus mismatch between the substrate and film, otherwise known as image stress. The reduced interface roughness could also play a role as the smoother silicon-magnesium interface provides less resistance to lateral forces, whereas in the upper layers of the film a compound waviness prevents any lateral sliding. The yield stress was taken at 1% strain rather than the conventional 0.2% in order to capture yielding at the top of the pillar and not at the collapse of the bottom layer.

Contrary to prior reports of room temperature micropillar compression of similar films [139], the “smaller is stronger” mantra is not followed. There is good agreement between the values for 50 nm layer thicknesses, so presumably the 5 nm layer thickness films presented here are not entirely dense. The TEM cross-sections do not exhibit porosity or voids within the grains while the SEM micrographs indicate that the reduced density can be accounted for by the grain boundaries. It is also possible that the enhanced strain rate sensitivity of the thinner layers coupled with the relatively long testing times results in somewhat lower yield stress. Direct comparison between the two layer thicknesses is further complicated by the different magnesium phases. As such the quantitative strength values for the 5 nm films presented here should be treated with some skepticism, but the activation energy and activation volume are expected to be representative of a fully dense film. Micropillar compression is ideal for testing thin films as these types of multilayered structures are not easily realizable in bulk samples. First strain rate jump, and then variable temperature micropillar compressions tests are performed, permitting the activation energy to be calculated by using the strain rate sensitivity information gained from the strain rate jump tests. This approach of coupling SRJ tests with variable temperature testing to gain insight into the operative deformation mechanisms has been previously used in nanocrystalline nickel [144].

The Arrhenius plot of the 1% yield stress values is used together with the strain-rate sensitivity exponent calculated from the strain rate jump tests in order to calculate the activation energy of deformation, as shown in Figure 50. The 5 nm film data points are collinear in the Arrhenius plot, indicating that there is no change in the operational deformation mechanism. The activation energy of 127 kJ/mol is well above those reported for dislocation-based deformation mechanisms and agrees well with the values reported for diffusion. Diffusion can occur readily as each interface between magnesium and niobium within the multilayer film serves as a potential diffusion pathway. Experimental tensile test results for bulk magnesium and magnesium alloys performed between 423 and 773 K [141] report the activation energy for pure magnesium as ranging from 20 to 270 kJ/mol, increasing with increasing temperature. The magnesium alloy, however, remains confined between 92 kJ/mol for pipe diffusion [137] and 135 kJ/mol for lattice self-diffusion [145]. Similar activation energies between 100 and 110 kJ/mol were measured in AZ31 magnesium alloy and were attributed to either dislocation creep climb associated with pipe diffusion or simple lattice diffusion [146]. The 50 nm layer thickness films, however, exhibit a change in the activation energy 72.5°C. At lower temperatures the activation energy is around 84 kJ/mol. This value lies between those reported for dislocation movement and diffusion, indicating that both mechanisms contributing to the overall plasticity. At higher temperatures the yield strength drops drastically with increasing temperature and the activation energy reaches 389 kJ/mol, a value even beyond that reported for lattice diffusion.

Similar signs of plasticity facilitated by diffusion in multilayer micropillars have been observed previously, albeit at a lower homologous temperature. The surface extrusions were described as “tongues” of aluminum extruded from 60 nm layer thickness Al-SiC multilayers compressed at 100°C (homologous temperature of 0.4 for aluminum). [101] Interface sliding was cited as the main deformation mechanism. Interface sliding was modeled using FEM while treating the Al-SiC interface as a cohesive crack. A reduced friction coefficient was introduced after the cohesive crack is broken. The interface sliding model did not account for the asymmetry of the extrusions and the possibility of interfacial diffusion is briefly mentioned in the conclusions. Nanoindentation performed on these same layers [100] did not show the same degree of strain hardening as the lateral flow of aluminum is prevented through the surrounding material, indicating that the free surface of a micropillar is necessary for such strain hardening to occur. The bottom layer of these micropillars was also observed to deform prior to the rest of the layers and was commented upon, but no explanation was proposed. An elastic mismatch between the film and substrate is the likely culprit here as well. A recent nanoindentation study of Al-SiC multilayers demonstrate that multilayers with thinner layers exhibit inferior yield stress compared to thicker multilayers at elevated temperatures [147]. Grain boundary and interface diffusion are concluded to limit the strength of aluminum multilayers at elevated temperatures (up to 100°C).

The cryogenic tests for the 5 nm layer thickness films follow the same trend as the elevated temperature tests, with increasing strength at lower temperatures. These observations are in agreement with previous experiments in magnesium alloys. At room temperature, AZ31B magnesium alloy exhibits some ductility before fracture, whereas when cooled to liquid nitrogen (77K) and liquid helium (4.2K), fracture is entirely brittle. The strength is observed to increase continuously with decreasing temperature [148]. For bulk specimens, a brittle-to-ductile transition temperature has been reported to be as high as 200°C when ductility is provided through dynamic recrystallization [149]. No direct comparison with bulk cubic magnesium is possible as it is only stable at extremely high pressures. The 50 nm films, however, exhibit somewhat surprising yielding behavior. The yield strength is reduced drastically below that observed at room temperature. The failure mechanism here is clearly a different one than observed at room temperature and elevated temperatures, with significant glide occurring within the magnesium layers along their basal plane. The magnesium layers have fractured and been ejected out of the micropillar at higher strains. While superficially similar to the magnesium protuberances observed at elevated temperatures, there are no signs of diffusion having contributed significantly to deformation. There is no edge rounding, formation of whiskers, or coalition of adjacent layers. Instead brittle fracture has occurred at internal stress concentrations and the magnesium layers are ejected from the pillars through basal glide. At the lowest temperatures measured here fracture of the niobium layers is possible as well due to the ductile-to-brittle transition in Niobium when impurities are present.

The conventional hardening models used for describing the strength of multilayers all rely on dislocation-based mechanisms. Around room temperature the 50 nm multilayers still benefit from these strengthening mechanisms, as described by the confined layer slip model. The original model proposed by Misra *et al.* [8] was then modified to include an additional two strength contributors: elastic interface stress (f) and interactions between confined layer slip dislocations and those already present near the interfaces (C/λ).

$$\sigma_{cls} = M \left(\frac{\mu b}{8\pi h'} \right) \left(\frac{4-\nu}{1-\nu} \right) \left(\ln \frac{\alpha h'}{b} \right) - \frac{f}{h} + \frac{\mu b / (1-\nu)}{\lambda} \quad \text{Equation 28}$$

At 5 nm layer thickness, however, there is no longer sufficient space for a dislocation to bow between interfaces. Instead the properties of the interface dictate yield strength. Activation volume in BCC materials tends to be small as yield stress is strongly dependent upon temperature [150], and this effect is even more pronounced in a material with a low melting temperature like magnesium. The introduction of a large number of internal interfaces provides numerous pathways along which magnesium can readily diffuse. The use of a model based solely on dislocation movement is not valid for describing the type of behavior observed in Mg-Nb multilayers across the temperature range investigated here. Further studies are needed in both this and other materials systems in order to develop a model which can be used to predict material strength where diffusion and brittle fracture can occur.

5.3.5 Conclusions

Pseudomorphic BCC magnesium has been stabilized in Mg-Nb multilayers at thicknesses of nearly 8 nm. Micropillar compression tests at both cryogenic and elevated temperatures were used to calculate the activation energy and activation volume governing the mechanical behavior of the films. Mg-Nb multilayer films with individual layer thicknesses of 5 and 50 nm demonstrate two major deformation regimes: an elevated temperature regime where deformation is controlled by diffusional flow of magnesium and a lower temperature regime where dislocation movement and co-deformation of the layers dictates the material behavior. At cryogenic temperatures the 50 nm layer thickness films fail via

brittle fracture of the niobium layers and within the magnesium layers through glide along their basal plane. Around room temperature a combination of dislocation- and diffusion-based mechanisms are active, where enhanced plasticity prevents the type of brittle fracture and glide observed at cryogenic temperatures. At elevated temperatures deformation is dominated by diffusion, where the growth of magnesium whiskers outside the micropillar occurs during deformation. The lower-than-expected strength of the 5 nm layer thickness films is attributed to non-fully-dense magnesium layers and the relatively low strain rates applied, though the deformation mechanisms are postulated to remain unaffected relative to fully dense films.

Acknowledgements: The research leading to these results has received funding from STEEP, a Marie Curie Action Initial Training Network (ITN) of the European Union's Seventh Framework Program FP7 under REA grant agreement number 316560. The open and friendly atmosphere at both LANL and Empa has enabled this international collaboration. Elevated-temperature compression tests were performed together with Juri Wehrs, strain-rate jump tests were performed with Gaurav Mohanty, and the cryogenic tests were performed together with Cinzia Peruzzi and Daniele Casari under the supervision of Jakob Schwiadrzik. The choice of materials was suggested by Nathan Mara and Siddhartha Pathak.

6 Nanoparticle Composite Films

6.1 Introduction

Nanocrystalline metals exhibit significant hardness and ductility improvements over their coarse-grained counterparts. These exceptional mechanical properties are due to the high concentration of grain boundaries within the material. The well-known Hall-Petch relationship is used to describe the hardness improvement as a function of grain size. A number of routines exist for synthesizing nanocrystalline materials. Severe plastic deformation (SPD) processes utilize a large shear stress to generate an extremely high density of grain boundaries within the material [151]. For these processes a bulk material is subjected to large plastic strains, often repeatedly, in order to refine grain size. Nanocrystalline metals can also be produced through deposition techniques including PVD and CVD. During the initial grain nucleation phase the grain size is generally quite small, with a large number of competing nucleation sites. Grains with a favorable orientation grow more quickly and obstruct grains with a slower growth right. As the film continues to grow a strong texture develops and the grains exhibit a columnar structure. Interrupted sputtering is used to re-nucleate a number of grains and prevent a large-grained, columnar microstructure from forming.

Even when the desired nanocrystalline structure is achieved through the growth process, there is no guarantee that the material will retain this structure. Spontaneous grain growth in nanocrystalline metals has been observed at ambient temperatures, leading to a deterioration of their mechanical properties. Grain boundaries are present a high-energy arrangement, so even relatively modest diffusion rates will often result in the film consolidating to a coarser microstructure. The introduction of secondary phase particles is another strategy for material strengthening. These particles generally consist of an exceptionally hard material. Particle reinforcement is used to strengthen materials through a dislocation bowing mechanism. Crystal lattice distortion in the vicinity of the particle provides an obstacle to dislocation movement. An optimum particle size exists for strengthening at which the tradeoff between dislocation bowing and cutting through the particle is balanced.

Particle reinforcement can be produced through traditional metallurgical techniques in the form of precipitation strengthening. For alloys which have undergone extensive research and development, this is an excellent way to produce bulk quantities of precipitate strengthened materials. While the method is effective, it lacks versatility and can only be employed in material systems where the solubility of the second phase decreases upon cooling the metal from the melt. A number of methods have been developed to improve the versatility of particle strengthening and increase the number of materials systems for which it can be applied. These methods also aim to improve the control over the particle size distribution and their spatial distribution within the metal matrix. Particle reinforced metal matrix composites (MMCs) utilize the ductility and toughness of a metallic matrix while hard particles (typically ceramics, in this case a refractory metal) serve as obstacles to dislocation movement, thereby improving the hardness and modulus of the composite.

Spray atomization has been used to co-deposit metals and particle reinforcement. Sometimes this technique is described as "disintegrated melt deposition". Droplets are typically micron-sized; therefore typical interparticle spacings are on the order of several to several tens of microns [152]. Nanoscale (50 nm diameter, 1.1 volume %) Al_2O_3 has been used to reinforce magnesium in this way, resulting in improved mechanical properties and grain refinement [153]. Yamamuro et. al proposed plasma-gas-condensation (PGC) as a technique for forming monodisperse metal clusters, originally using chromium [154]. They consider the process to be an extension of colloidal particle formation as described by the LaMer model [155].

A novel method for producing nanoparticle-reinforced metal matrix composites through co-deposition is presented here. Monodisperse tungsten nanoparticles are generated using terminated gas condensation. Differential pumping conveys the nanoparticles to the main sputtering chamber, where they are embedded within a sputtered copper film. This method can be readily applied to other materials systems, enabling nanoparticle reinforced films to be deposited with the same versatility of materials choice afforded by conventional sputtering. A uniform, random distribution of nanoparticles can be achieved in a near-arbitrary sputtered matrix. A basic schematic of the deposition strategy and the potential film architectures which can be realized using this approach is shown in Figure 51.

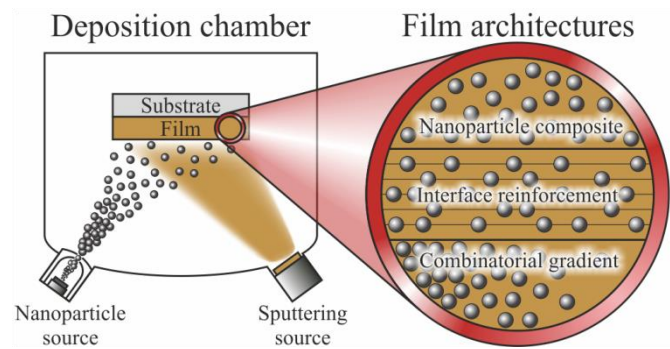


Figure 51: The co-deposition of nanoparticles and a sputtered film can be used to realize a number of film architectures. Simultaneous operation of both sources results in a nanoparticle reinforced composite. Disabling substrate rotation will produce a combinatorial gradient by varying film thickness and nanoparticle flux. Alternating deposition of nanoparticles and sputtered material is used to produce interface reinforcement using nanoparticles.

6.2 Experimental

All samples were prepared using magnetron sputtering. Samples which were tested at room temperature were deposited directly onto silicon chips with a native oxide. Silicon substrates with a diffusion barrier consisting of 100 nm of SiO_2 and 100 nm of Si_3N_4 were used for the samples intended for high temperature experiments. Conventional DC magnetron sputtering was used to prepare 1 μm thick samples due to the higher sputtering rates achievable. High power impulse magnetron sputtering (HIPIMS) was used to prepare samples with a film thickness of 500 nm and 100 nm in order to slow the sputtering rate, improve the density of the film, and reduce the formation of copper twins. Films consisting of pure copper and various concentrations of tungsten nanoparticles were prepared for all three film thicknesses. The nanoparticle flux varied across the substrate holder, enabling multiple samples of differing tungsten nanoparticle concentrations to be prepared in a single deposition by positioning the substrates at various distances from the substrate holder center.

The tungsten nanoparticles are prepared using terminated gas condensation in a separate chamber adjacent to the main sputtering chamber. Details of the nanoparticle production process used here have been described previously [156].

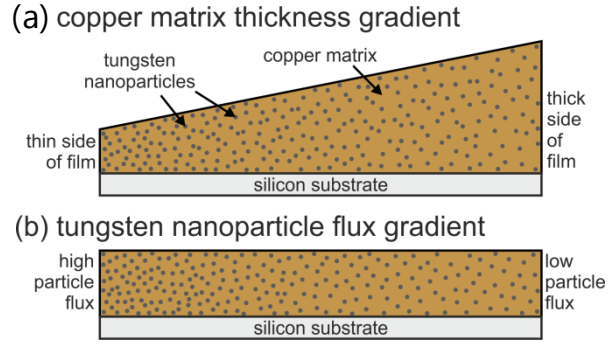


Figure 52: Two methods for achieving a particle density gradient, utilizing (a) gradients in the matrix thickness and (b) gradients in the nanoparticle flux.

Room temperature nanoindentation experiments were conducted using a Hysitron Ubi nanoindenter. A new Berkovich diamond tip was used to characterize the 100 nm-thick films since tip sharpness is of upmost importance for obtaining consistent data at such shallow indentation depths. The elevated temperature nanoindentation tests were conducted using an Anton Paar elevated temperature nanoindenter. Samples were adhered to a massive copper block using Pyroduct 597-A adhesive to ensure accurate measurement of the film modulus at elevated temperatures.

X-ray diffraction was performed using Cu-K α radiation in a Bruker Discover D8 diffractometer. The samples were clipped to a heating stage to ensure excellent thermal contact. The stage was covered by a graphite dome and a modest argon flow rate was maintained in order to ensure that the samples did not oxidize during the experiments. The temperature was increased by 100°C increments using a heating rate of 40°C per minute and maintained at each temperature for 30 minutes before progressing to the next temperature. Three scans were performed at each temperature : a quick 2° offset omega-two theta scan, a detailed scan of the copper 111 peak to be used for determining the crystallite size, and a scan of the silicon 004 peak to compare the sample temperature with that of the thermocouple in the heating stage. After a maximum temperature of 800°C was obtained the samples were allowed to return to room temperature at a cooling rate of approximately 80°C per minute before a final set of three scans was performed.

Film thickness and tungsten concentration were determined using X-ray fluorescence (XRF) with a Fischerscope X-ray XDV. The tungsten nanoparticles were assumed to be randomly and homogeneously distributed within the copper matrix, therefore comparing the relative intensity of the copper and tungsten peaks is sufficient to determine their relative concentration. Since the total quantity of tungsten is fairly low, TEM lamella were prepared for several different nanoparticle concentrations to calibrate the XRF measurements. Assuming a monodisperse particle size distribution, the average interparticle spacing can be calculated assuming a random distribution of particles with a diameter d_p , occupying a volume percentage V_p of the film using Equation 29:

$$\lambda \approx d_p \left[\left(\frac{1}{V_p} \right)^{\frac{1}{3}} - 1 \right] \quad \text{Equation 29}$$

6.3 Results

6.3.1 Tungsten nanoparticle deposition

Prior to co-depositing the tungsten nanoparticles into a sputtered copper matrix, the tungsten nanoparticles were deposited directly onto both silicon substrates and carbon film TEM grids. Both the particle size distribution and the spatial distribution of the particles across the substrate holder were determined using this method. While the entire substrate holder receives some nanoparticle flux, the area just below the center of the substrate holder receives roughly ten times more particles than the perimeter of the sample holder. This is the “focus” of the nanoparticle beam and is the ideal location for placing substrate when a high particle concentration is desired. The nanoparticles themselves are monodisperse with a mean diameter which can be readily tuned between 4 and 8 nm. No significant clustering of nanoparticles is observed into larger agglomerates. Each nanoparticle consists of a single crystal of tungsten. Immediately after deposition the nanoparticles consist entirely of tungsten. When left under atmospheric conditions for several days, the surface of the nanoparticles begins to oxidize, forming a core-shell structure. The thickness of this oxide continues to increase with time and after several months nearly the entire tungsten nanoparticles has become oxidized.

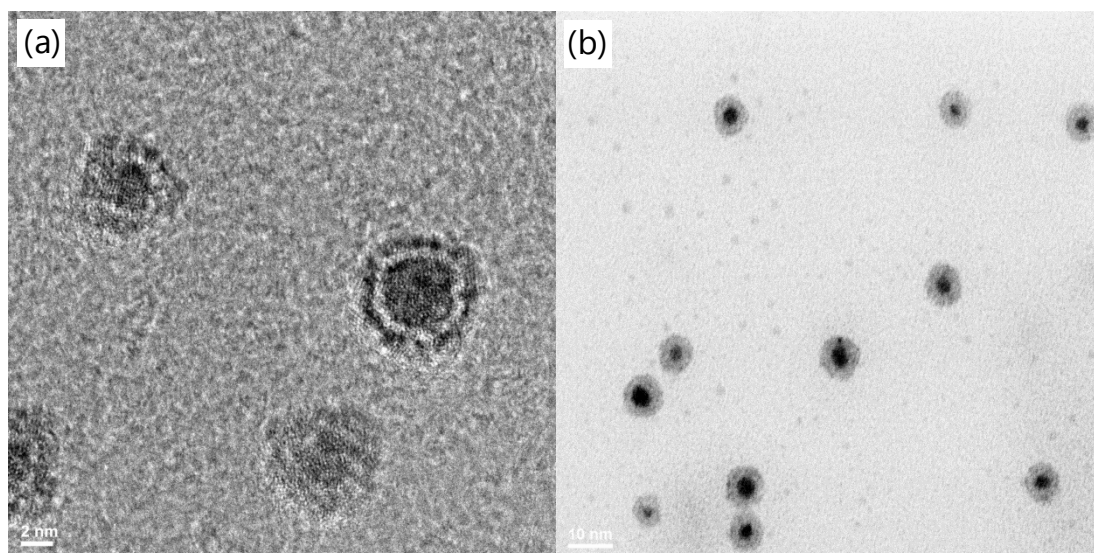


Figure 53: The tungsten nanoparticles are entirely crystalline immediately after deposition and do not appear to be agglomerations of smaller particles (a). After several days a core-shell structure begins to appear, with the shell eventually consuming a large portion of the nanoparticle (b). It is unclear if this is oxidation of the tungsten or a reaction with the carbon film on the TEM grids. When embedded in the copper films this reaction does not take place and the tungsten remains in its as-deposited state.

6.3.2 Thickness gradient sample

The thickness-gradient deposition approach was used to produce a film which varied continuously in thickness from 1.5 μm to 3 μm over a 10 cm diameter silicon wafer. Spatial variation in the tungsten nanoparticle deposition flux was also observed, with the maximum deposition density located several centimeters below the center of the wafer. XRF was used to measure the film thickness and to determine the tungsten content of the film, expressed as a consolidated tungsten thickness (the equivalent thickness if the nanoparticles were deposited and compressed into a fully dense film) to give a better impression of the nanoparticle flux across the substrate. The film thickness was confirmed using SEM observation of cross-sections prepared by FIB milling. The tungsten content, however, could not be precisely quantified with the necessary precision using XRF due to residue from the tungsten filament

used to generate the X-rays. As such it was necessary to prepare TEM lamella in which the tungsten nanoparticles could be directly observed, measured, and counted. Although time-consuming, this was essential to understanding the film microstructure as well as the distribution and density of tungsten nanoparticles within the film.

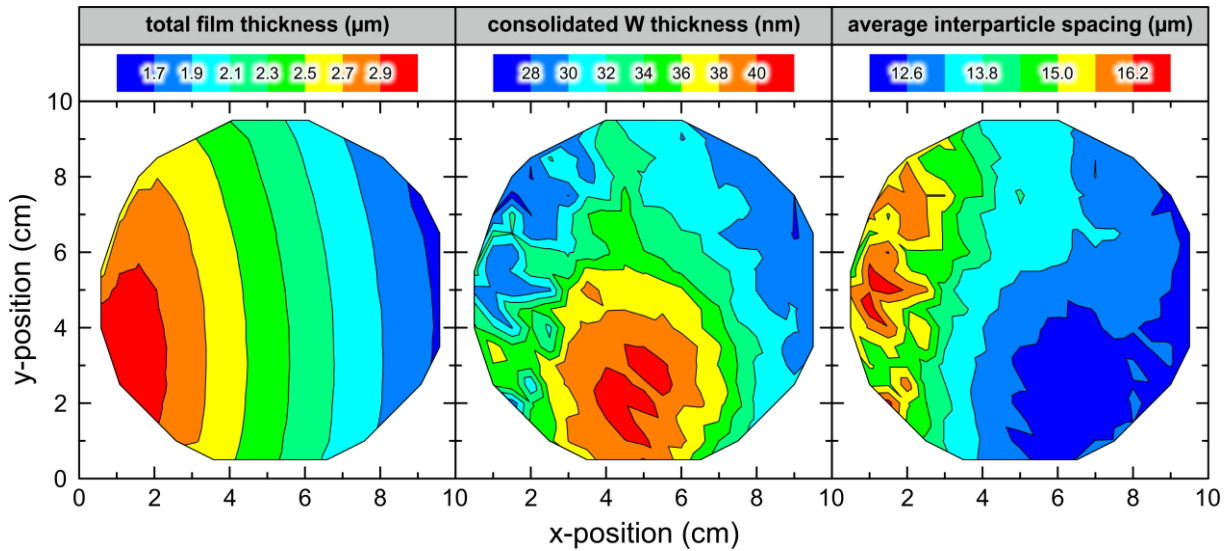


Figure 54: Film thickness, consolidated tungsten thickness, and average interparticle spacing maps

The thickness gradient film exhibits a microstructure consisting of columnar grains tilted roughly 20° angle to the surface normal. These columnar grains exhibit an exceptionally high twin density throughout the entire film thickness, with the average twin being only a few nanometers thick. The tungsten nanoparticles are present, though with far less concentration than was indicated by the XRF measurements. A number of large pores are also visible, indicating that the film may not be entirely dense. Far fewer tungsten nanoparticles are present than indicated by the XRF measurements. The nanoindentation results were somewhat compromised by the method of mounting the large substrate for indentation. This is seen especially clearly in the reduced modulus, where the compliance of the sample holder varied across the substrate. The sample needed to be moved to four different positions in order to complete the nanoindentation mapping, which is clearly seen in the form of minor disruptions to the continuity of the hardness and modulus maps. Despite the minor compliance issues, the hardness map exhibits no discernable difference in hardness as a function of nanoparticle concentration.

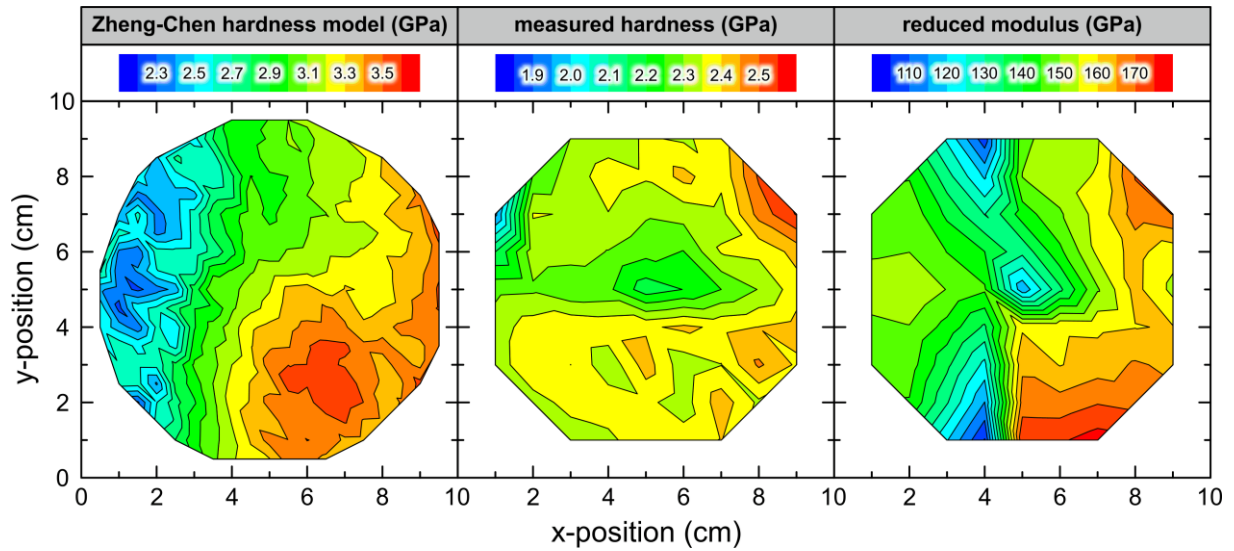


Figure 55: The Zheng-Chen hardness model predicts hardness variation between 2.2 and 3.6 GPa across the wafer. Experimentally this was not observed as the hardness was more or less independent of the nanoparticle concentration and film thickness. Hardness values varied between 2.2 and 2.4 GPa without any obvious spatial trend. The modulus values were compromised by the compliance of the sample holder.

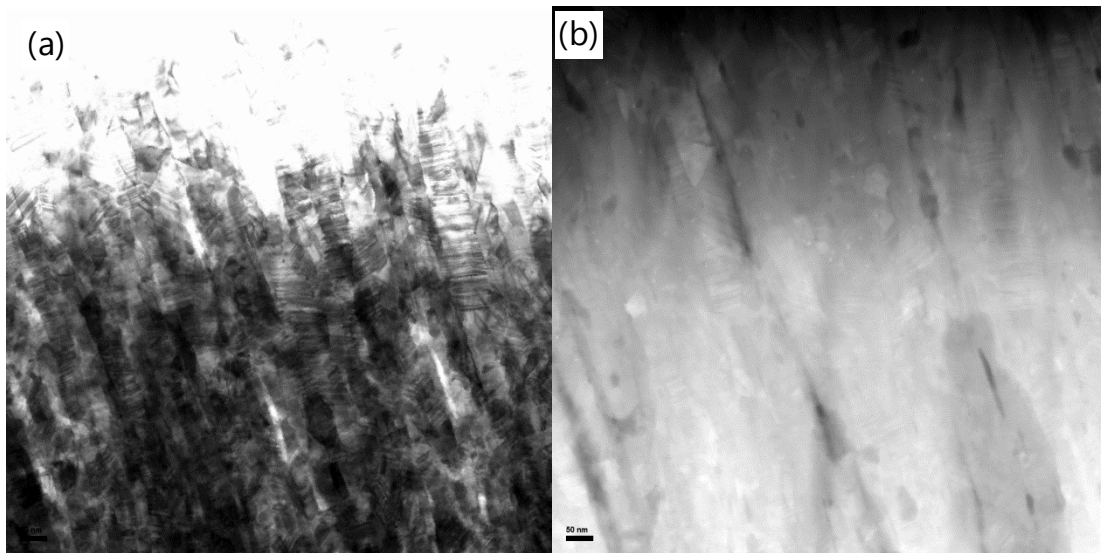


Figure 56: Using conventional DC sputtering resulted in exceptionally high twin densities (a) within the copper. Tungsten nanoparticles are readily visible in the dark-field TEM image (b), though the average particle spacing is considerably larger than the twin spacing and grain size. As such the particles have no discernable impact on the hardness of the film.

6.3.3 Nanoparticle density gradient sample

A second sample was deposited for which the substrate was rotated during deposition. This eliminated the 20° tilt to the columnar grains, though larger pores were still occasionally present along the columnar grain boundaries as in the previous sample. Two TEM lamellae were extracted from the sample: one from the center of the wafer where the nanoparticle concentration was the highest and one from the perimeter where the nanoparticle concentration was the lowest. The tungsten nanoparticle density varies by a factor of five, ranging from 0.01 volume % at the perimeter to 0.05 volume % in the center of the sample. These densities are already noticeably higher than in the film thickness gradient sample. The microstructure of the copper matrix differed somewhat between the two lamellae extraction sites. The center of the sample exhibited a columnar microstructure throughout the film's entire micron of

thickness. As with the film thickness gradient sample, twin boundaries were observed with single-digit nanometer spacing within the columnar grains. Twins were somewhat less prevalent in the nanoparticle density gradient sample and exhibited far more orientations tilted relative to the columnar grain boundaries. The TEM lamella extracted from the sample perimeter exhibits a nearly identical microstructure in the upper half of the film, while the lower half of the film possesses large grains without any obvious columnar arrangement. The perimeter of the sample is subject to an oscillating growth rate which increases when being rotated past the sputtering target and decreases at the opposite end of its rotation. It is possible that this oscillation is responsible for the larger-grained microstructure and suppression of columnar grain growth during the first half of the film deposition.

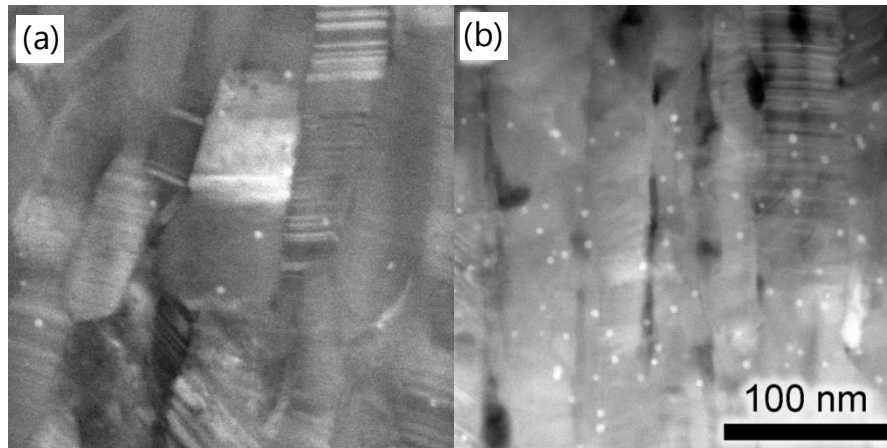


Figure 57: The nanoparticles density varies across the nanoparticle-gradient sample by a factor of five. At the sample perimeter (a) the mean interparticle distance is around 100 nm, whereas at the sample center the distance is 45 nm (b). The volume percentage of tungsten is still quite modest, ranging from 0.01 to 0.05 percent.

Close examination of the TEM lamellae reveals that the tungsten nanoparticle concentration, though constant for the upper 900 nm of the film, exhibited perturbations during the initial 100 nm of film growth. During the first 50 nm of growth the nanoparticle density is exceptionally high while no nanoparticles whatsoever were deposited during the second 50 nm. Review of the periodic mass spectrometer checks performed during the deposition indicates that the deposition flux remained constant throughout the entire duration of the deposition. It is possible that the orifice between the mass spectrometer and the main deposition chamber had become partially obstructed by a stray flake of deposited material or that the orifice had become partially congested by a nanoparticle aggregate. In neither of these cases is it obvious what alleviated the obstruction or why the nanoparticle deposition density did reach the levels it had enjoyed during the first 50 nanometers of film deposition.

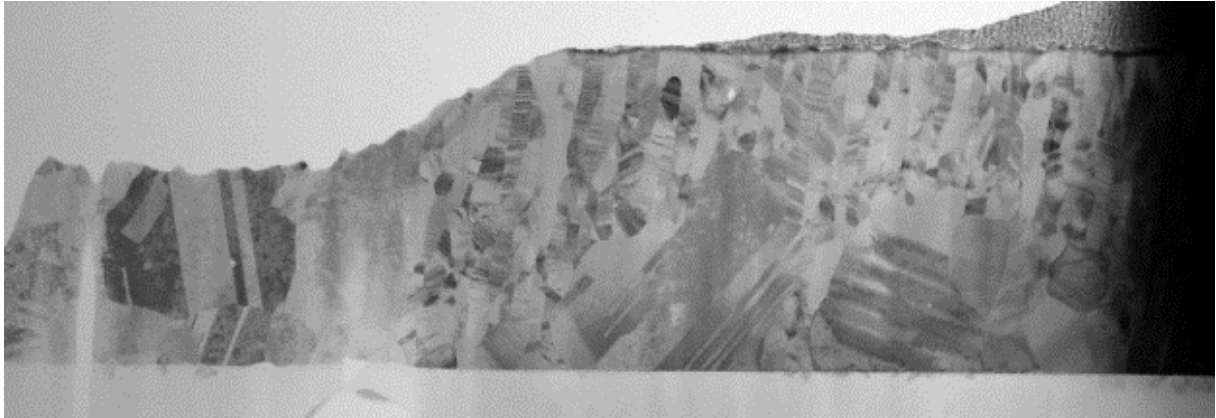


Figure 58: HIPIMS sputtering was successful at increasing the grain size while sputtering the first 500 nm of the film for the portion of the sample with low tungsten nanoparticle content. Afterwards the film microstructure largely returned to the same microstructure as in the high tungsten content region of the film, with columnar grains and plentiful nanoscale twins.

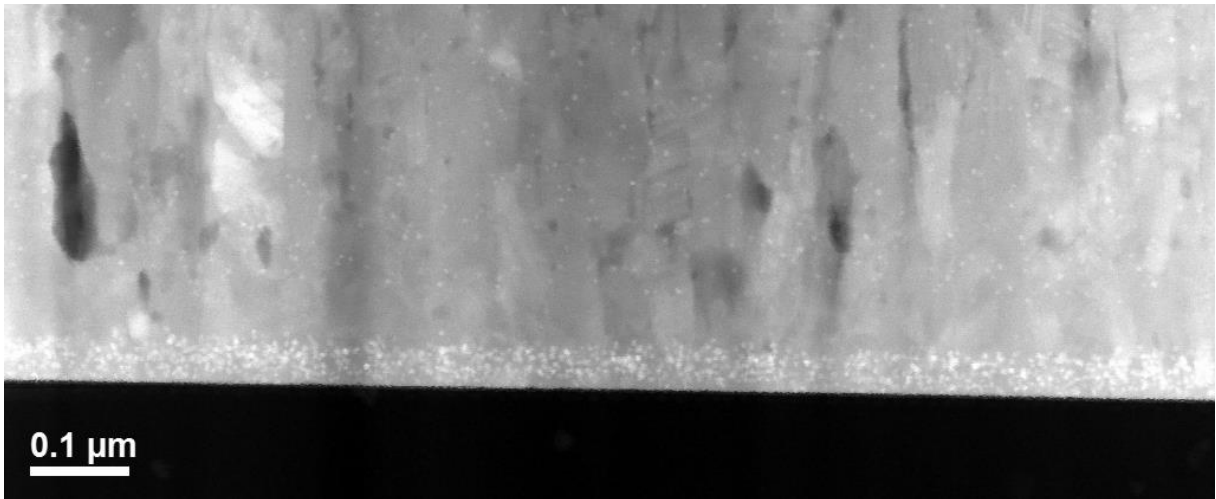


Figure 59: The initial 50 nm of the deposition exhibited an exceptionally high nanoparticle concentration. The subsequent 50 nm are devoid of any tungsten nanoparticles whatsoever. The remainder of the film contains a moderate, constant tungsten nanoparticle concentration. General difficulties with stability of the nanoparticle source motivated the exploration of thinner films in which exceptionally high nanoparticle concentrations could be achieved throughout the film thickness.

As with the film thickness gradient sample, the hardness and modulus of the film remain statistically invariable as a function of tungsten nanoparticle content. As the upper half of the film still exhibits a large twin density, it is possible that the presence of these twins and the impact of the copper microstructure still dominate any possible hardening effect exhibited by the tungsten nanoparticles.

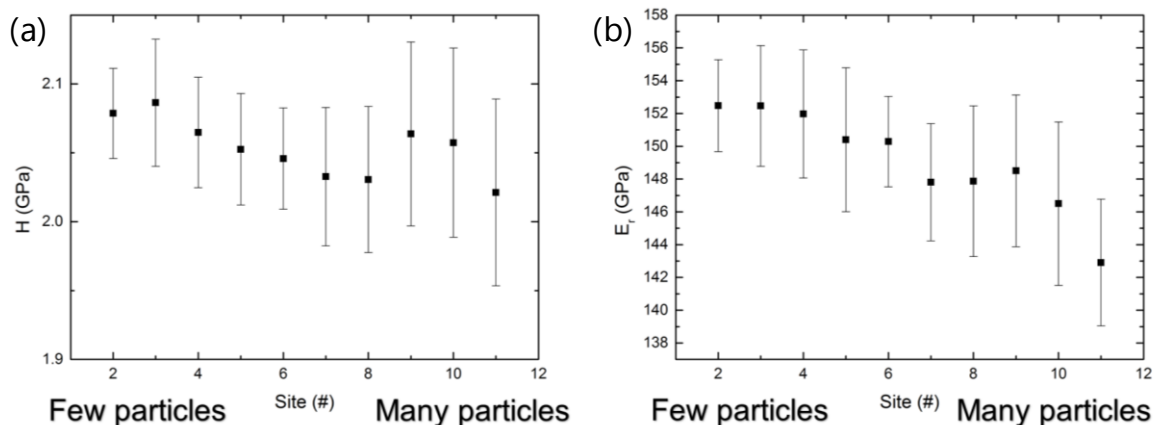


Figure 60: There is no obvious correlation between tungsten nanoparticle concentration and film hardness (a). There is a minor decrease in elastic modulus with increasing tungsten nanoparticle concentration (b), but this is likely due to a minor increase in porosity rather than any effect from the nanoparticles themselves.

6.3.4 High particle density in thin films (100 nm)

Microstructural changes within the copper film at larger film thicknesses and general stability issues with the nanoparticle deposition process motivated an attempt to achieve maximum nanoparticle densities at the expense of film thickness. An additional advantage provided by depositing such thin films is that TEM-grids could be placed adjacent to the substrates in the deposition chamber in order to readily obtain plan-view TEM images of the film, providing quick feedback regarding the achieved particle density and copper grain size. Using this strategy it was possible to obtain 0.5 volume percent tungsten, a full order of magnitude superior to the other samples. A reference sample of pure copper deposited under identical deposition conditions, barring the absence of tungsten nanoparticle conditions, was prepared as well to provide a comparison to the film containing tungsten nanoparticles.

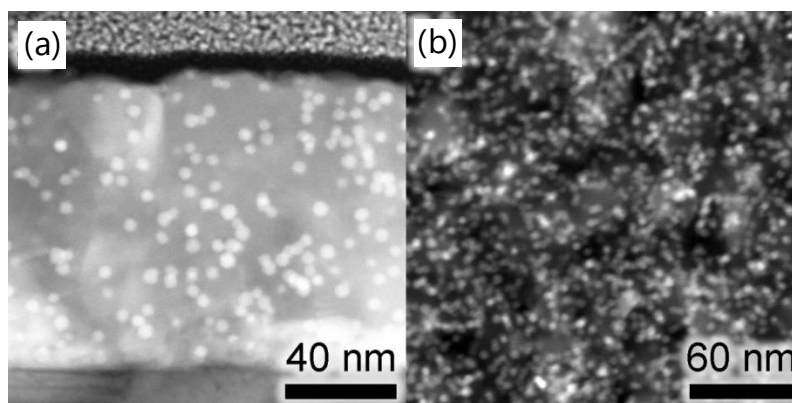


Figure 61: (a) Cross-sectional and (b) plan views of 100 nm thick copper films containing 0.5 volume % tungsten nanoparticles were successfully deposited. The monodisperse nanoparticles have an average diameter of 4.2 nm and possess a random spatial distribution, resulting in an average interparticle distance of 20 nm.

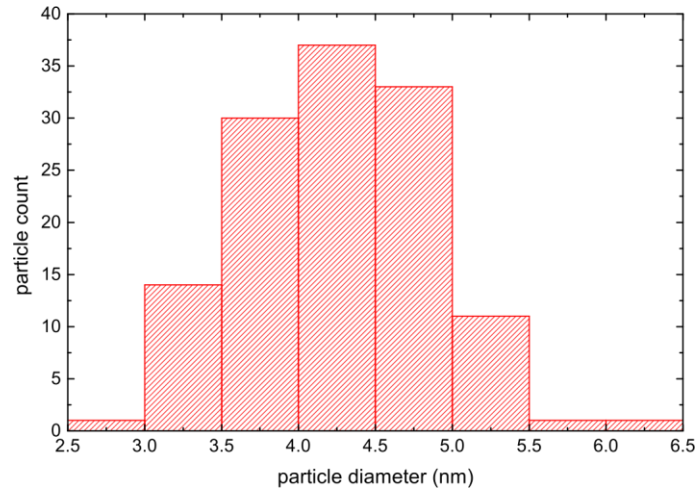


Figure 62: A histogram of 128 tungsten nanoparticles measured from the TEM cross-section lamella demonstrates a monodisperse particle size distribution with an average particle diameter of 4.2 nm.

Surprisingly high quality nanoindentation data was obtained by implementing a previously unused Berkovich diamond indenter tip. Indentation depths of less than 20 nm were insufficient for obtaining low-scatter data, while indentation depths of greater than 60 nm were eschewed because of undue substrate influence. No significant difference between either the hardness or modulus could be detected between two films. In both cases the hardness was more than double that measured for the 1 μm films. Upon measurement using XRF it was observed that the pure copper reference film was in fact only 90 nm thick while the film containing tungsten nanoparticles was 140 nm thick, despite being deposited under nominally identical conditions for the same duration. It appears that there is some cross-talk between the copper and tungsten nanoparticle deposition processes or that the sputter deposition displays greater variable in deposition rate than initially anticipated. Since there is marked increase in film hardness with decreasing film thickness, it is difficult to make a direct comparison between the two samples. The tungsten nanoparticles may still be improving the hardness of the film, but direct comparison with the pure copper reference is not possible since it gains additional hardness due to the smaller film thickness.

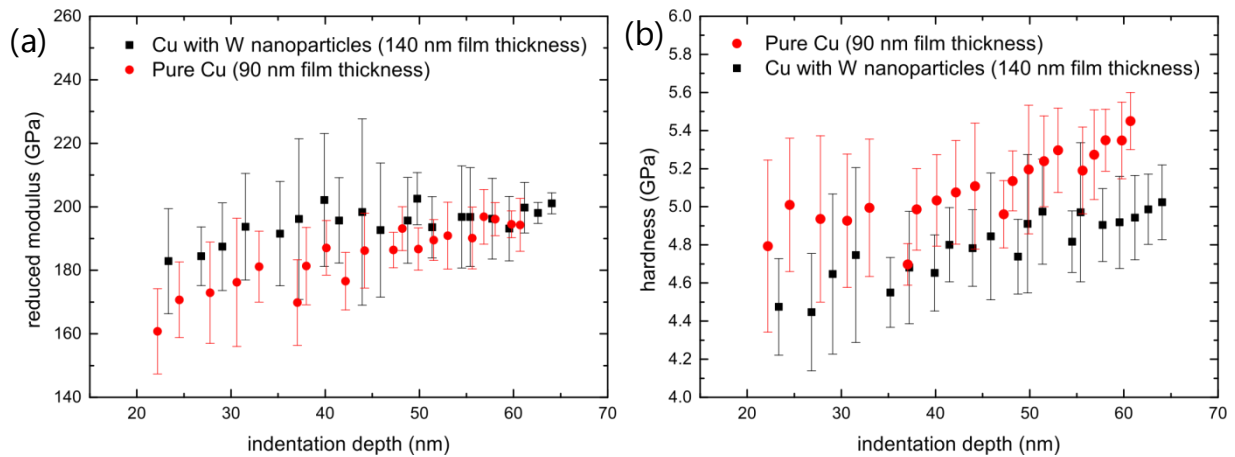


Figure 63: The modulus (a) and hardness (b) of the nominally 100 nm thick films is nearly indistinguishable. The film containing nanoparticles exhibits a slightly higher modulus and slightly lower hardness values. Since the two films do not have identical thickness it seems that the pure copper film derives its strength from its reduced dimensions while the tungsten nanoparticles provide strengthening of similar magnitude.

6.3.5 High particle density in thick films (1 μm)

A final set of two samples was sputtered in the new, larger deposition chamber. The same nanoparticle source was used as for all the previous depositions, but attached to the new PVD chamber. A nominal film thickness of 500 nm was targeted as a compromise between depositing a sufficiently thick film to perform reliable nanoindentation experiments and keeping the deposition time short enough to have a better chance of maintaining stability of the nanoparticle source. Several small area substrates (5 mm \times 5 mm) were used for nanoindentation samples. Four such substrates were placed at regular intervals starting from the center of the substrate holder moving outward to its perimeter in order to produce samples with various nanoparticle concentrations. A larger substrate (1 cm \times 1 cm) was also placed near the center of the substrate holder in order to be used for XRD experiments, where it is advantageous to have a larger area. Finally, a large rectangle (3 cm \times 5 cm) of polyamide tape was included for potential use in tensile test experiments or for Small Angle X-Ray Scattering (SAXS) experiments where X-ray transparency of the substrate is necessary.

The actual film thickness were around 1000 nm as measured by XRF, nearly double that of the nominal film thickness. Since the deposition chamber was only recently installed, it is possible that the sputtering rate calibration needs to be checked. The thicker films are advantageous both for nanoindentation and increasing the signal of the XRD experiments. The elevated temperature XRD experiments indicate a clear difference between the film containing tungsten nanoparticles and the reference film of pure copper. The film containing tungsten nanoparticle began with a slightly larger crystallite size of around 65 nanometers as determined by applying the Scherrer equation. This value remained nearly constant at temperatures up to 700°C, after which grain growth increased dramatically. A minor decrease in crystallite size is observed between room temperature and 200°C, but this is a measurement artifact associated with the peak broadening from thermal vibrations of the copper atoms around their lattice sites. For the pure copper film the same artifact is observed for the measurement at 100°C, after which considerable grain growth occurs. The grains continue to grow throughout the entire temperature range.

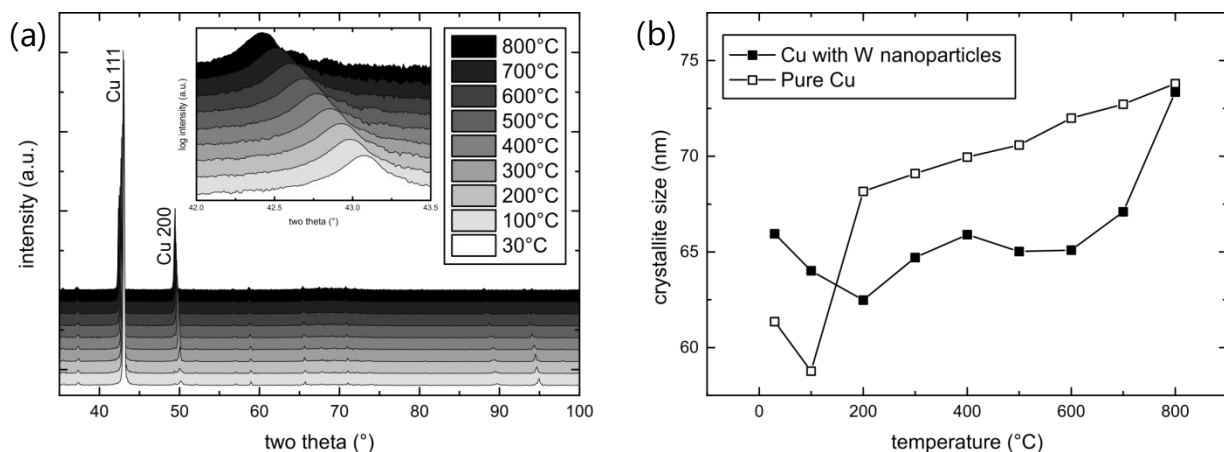


Figure 64: During heating there all XRD peaks shift to smaller angles due to the thermal expansion of the film (a). An increasing 100 component to the predominantly 111 film texture appears with increasing temperature. Grain growth is observed in the pure copper film at 200°C while it is largely stymied until temperatures above 700°C in the film containing tungsten nanoparticles (b). At 800°C the crystallite size is comparable for the two films.

For the first time the nanoindentation experiments demonstrate conclusively a difference in hardness between the pure copper film and the copper film containing tungsten nanoparticles. The nanoparticle density is sufficient to demonstrate both a hardening effect and improvement to the thermal stability of the copper microstructure through introduction of tungsten nanoparticles. This additional strength-

ening is maintained even at elevated temperatures of 100°C. Further experiments at even higher temperatures are underway to determine until which temperature the hardness advantage is preserved. Based on the XRD data, one could speculate that the pure copper film will lose strength more rapidly than the film containing tungsten nanoparticles once grain growth begins in the pure copper film at around 200°C. If this is the case, incorporation of nanoparticles into nanocrystalline metals may find application in extending the engineering applications of nanocrystalline materials through improvement of hardness and especially thermal stability.

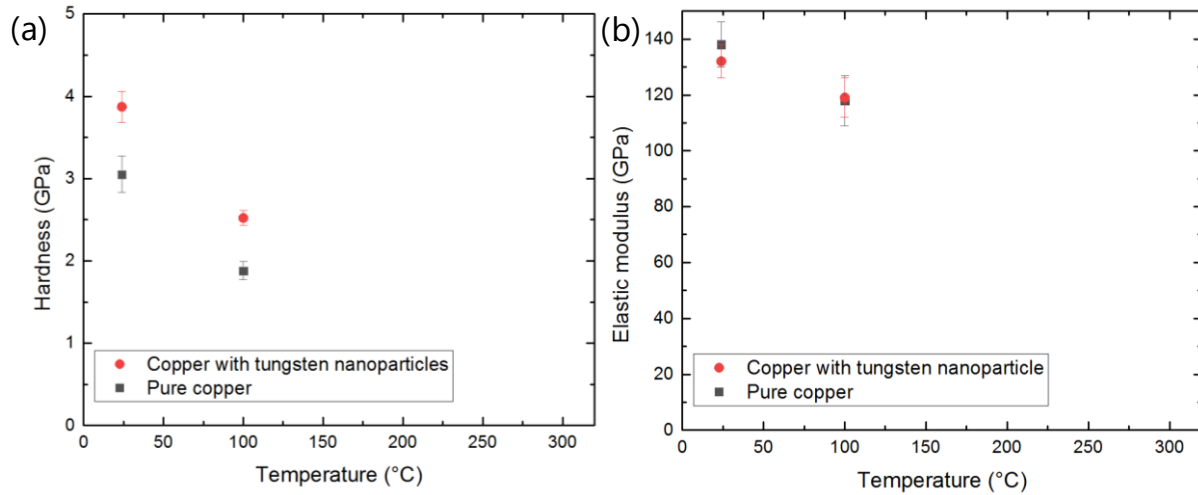


Figure 65: The hardness (a) of the copper film with tungsten nanoparticles exhibits a hardness of near 4 GPa while the pure copper reference film is just over 3 GPa. This is the first time that a hardening effect could be demonstrated through the incorporation of tungsten nanoparticles in copper using this co-deposition process. The hardening effect is maintained at elevated temperatures of up to 100°C. Further experiments at 200°C and 300°C are underway. The modulus (b) between the two films is indistinguishable and decreases from 135 GPa to 120 GPa with the initial temperature increase to 100°C.

6.4 Discussion

At sufficiently high tungsten nanoparticle concentrations it is possible to increase the film hardness beyond that which is achievable using microstructure alone in a pure copper film. This effect is only observable when the average interparticle spacing for the tungsten nanoparticles is smaller than the copper grain size. The tungsten nanoparticles appear to be randomly distributed throughout the film and were observed at both grain boundaries and enclosed within copper grains. Any re-nucleation effect in the copper film as a result of the introduction of tungsten nanoparticles is therefore expected to be minor.

Not only do tungsten nanoparticles provide a hardening effect, they also serve to stabilize the microstructure of the copper film through grain boundary pinning. This was confirmed through both elevated temperature XRD experiments and annealing of TEM lamella. The XRD experiments indicate that for copper films containing tungsten nanoparticles grain growth is largely suppressed until temperatures beyond 800°C, whereas for pure copper films appreciable grain growth is detected already at temperatures below 200°C. If grain boundary pinning is the mechanism through which the tungsten nanoparticles stabilize the film microstructure, the tungsten nanoparticles would be expected to be located predominantly at grain boundaries after extended exposure to elevated temperatures.

The film thickness also has a strong impact on the measured film hardness. Repeatable, qualitatively good indentation data was successfully obtained from films with a thickness of less than 100 nm using

a sharp Berkovich indenter. At these small film thicknesses the proximity of the indenter tip to the substrate results in significant interaction between the two. In this case, where the substrate is notably harder than the film being tested, the measured hardness increases significantly with decreasing film thickness. The particle size distribution is monodisperse. The particle diameter can be more precisely controlled using a quadrupole mass filter, but this would come at the expense of impacting the deposition rate. Since the particle size distribution is already narrow, there is no real reason to utilize the mass filter. The particle size is better adjusted by modifying the condensation length of the nanoparticle source.

A round robin investigation aimed at determining the reliability and repeatability of nanoindentation was performed in which 33 laboratories measured the hardness and modulus from 1.5 μm thick copper films [157]. The average reported hardness was 2.59 GPa and the average reported modulus was 144.5 GPa. For the entire data set the standard deviation for hardness was 15% while the standard deviation for modulus was 19%. Considered collectively the data is reasonable, but comparing results between individual laboratories shows a significant difference, with hardness values varying by up to a factor of two and modulus values approaching a factor of three. A drastic (power law) increase in hardness was observed with decreasing film thickness for copper films measured by nanoindentation [158]. The 1 μm thick film had a hardness of only 1.7 GPa while the 180 nm thick film reached a hardness of 2.7 GPa. The trend in modulus is less clear and generally hovered around 100 GPa (minimum 93 GPa, maximum 113 GPa). Extremely high hardness values (10 GPa) were measured on beam sputtered copper films with a thickness of 250 nm [159]. Modulus values of 135 GPa were reported for the same films. A linear correlation between hardness and modulus was established.

High twin densities can drastically improve the film hardness without having an effect on either the density or electrical properties of the film. Twins effectively provide many of the same advantages associated with a nanocrystalline grain structure, but are generally more stable. Sputtered nanotwinned copper covering large areas was first reported in 2006 [160] at Lawrence Livermore. Stacking faults and twins had been observed in sputtered nanocrystalline and UFG copper deposited at sputter rates up to 11 nm/s [161]. These early efforts were plagued by high intrinsic stresses. Micropillars with a height of 2 μm were created with a high density of nanotwins parallel to the film-substrate interface [162]. The nanotwins were achieved by utilizing higher sputter rates (1 nm/s) than normal. Nanocrystalline copper grains were sputtered at 0.2 nm/s while the standard sputter rate was given as 0.5 nm/s. Sputter rate changes were achieved through variations in sputter power.

Although the nanoparticles do not appear to be effective at pinning dislocations, there is evidence that they do pin grain boundaries. Copper films containing nanoparticles did not exhibit any appreciable grain growth after having undergone the same annealing process. Instead of directly contributing to the strength of the films, the nanoparticles enhance the thermal stability of the nanocrystalline grains. The films can thereby benefit from the Hall-Petch effect over a wider range of temperatures. This is especially useful as many nanocrystalline materials have been shown to exhibit significant grain growth even at room temperature, precluding their use for engineering applications.

6.5 Conclusions and Outlook

The incorporation of tungsten nanoparticles into nanocrystalline copper has been shown to increase both the hardness and thermal stability of the film. This effect arises only once a critical particle concentration has been surpassed; at lower concentrations the introduction of tungsten nanoparticles has no discernable impact on the mechanical properties of the film. In addition to the strengthening effect, the tungsten nanoparticles stabilize the copper microstructure at elevated temperatures. Grain growth is suppressed until temperatures of above 800°C, as opposed to 200°C in pure copper. While these re-

sults were all obtained specifically within the copper-tungsten materials system, they are postulated to be generally applicable to a wider range of materials combinations. As such the use of nanoparticles for microstructure stabilization is especially appealing in nanocrystalline metals where spontaneous grain growth has been observed even at room temperature. The strength and ductility gains obtained through the Hall-Petch effect could then be maintained for extended time periods under a wider range of temperatures. This improvement could potentially extend the number of engineering applications for nanocrystalline metals, where temporal and thermal stability issues have restricted their use.

While the main finding in this work is certainly the benefit to metallic films obtained through the incorporation of nanoparticles, the particles themselves benefit from the matrix as well. Left exposed standard atmospheric conditions, tungsten nanoparticles show appreciable oxidation after the course of just a few days. Prolonged exposure results in the formation of a core-shell nanoparticle, where the crystalline metal core is surrounded by an oxide shell. Even more extensive exposure, in the range of several months, can result in the metal nanoparticles oxidizing entirely. By embedding the nanoparticles within a matrix this oxidation is largely prevented, preserving the crystalline nature and dimensions of the nanoparticles in the as-deposited state. This is important not only for the preservation of the mechanical properties of the nanoparticles, but also for potential optical applications where the properties vary drastically with even small changes in particle diameter.

Despite the considerable progress achieved in the film deposition process, there is still plenty of room for improvement through increasing the nanoparticle density deposited within the film. At present the highest nanoparticle content achieved is still below one volume percent. In the short term this can be improved by focusing the nanoparticle beam onto a smaller area and reducing the flux at which the matrix is deposited. In the long term large-area depositions are of interest and it will be necessary to increase the nanoparticle yield. Acceptance of a higher variability in nanoparticle diameter would also be useful for increasing particle yield, especially for mechanical applications where the exact nanoparticle size is not as critical.

Tungsten nanoparticles were co-deposited into a sputtered copper matrix to form a nanoparticle-containing metal matrix composite film. There are no technological barriers preventing this fabrication technique from being used with nearly any material combination which can be deposited via sputtering. The nanoparticles are randomly and uniformly distributed throughout the film and do not appear to have any major impact on the microstructure of the film. Considerable particle concentrations approaching one volume percent have been achieved, though further refinement of the deposition process shows promise for even larger volume fractions of nanoparticles. At low concentrations these particles do not appear to have any impact on the mechanical properties of the film. Initial thermal annealing experiments indicate that the particles do, however, provide pinning points for grain boundaries. As such, this introduces the possibility for the particles to be used as a means of stabilizing the copper film microstructure at elevated temperatures. At higher particle concentrations a hardening effect was observed, demonstrating that the nanoparticles can provide a reinforcement effect in addition to their thermal stabilization effect. A critical particle concentration is needed to ensure that nanoparticles are present not only along the grain boundaries, but also within the grains to provide an obstacle to dislocation movement.

7 Strengthening Mechanisms in Sputtered Films

In the previous three chapters the mechanical properties of sputtered thin films were improved through the use of several different film architectures. Each of these film architectures utilizes a different strengthening strategy, but all share the common approach of attempting to provide resistance to dislocation movement in the form of some type of obstacle. In order to evaluate the effectiveness of each strategy it is useful to establish a metric through which the various film architectures can be compared, both within the framework of this dissertation and in the context of the established scientific literature. Film hardness as determined by room-temperature nanoindentation is an ideal metric for comparison owing to the broad amount of literature available, the ease and speed with which such experiments can be conducted, and the applicability of such experiments to a wide variety of materials. Since all of the films presented here contain two components, treating one component as the base material and the other as the reinforcing material enables a meaningful comparison to be made. The intrinsically softer film component is considered to be the base material while the harder of the two components is considered as the reinforcement. The measured film hardness is normalized to the hardness of a film consisting of just the base material. Wherever possible the normalizing hardness value was taken from a pure film with a large microstructure to minimize the hardening effect of grain boundaries within the pure material. Since the copper-tungsten materials system was investigated in this work through compositional gradient thin films, multilayer films, and nanoparticle-reinforced composites, it is the standard baseline for comparison. Additional materials systems from this work are included as well as cases from the literature to set the relevance of this work in an appropriate context.

The mechanical properties of these films are not only a function of the film architecture, but also of the conditions under which the mechanical tests took place and the type of test used. For bulk materials the use of deformation mechanism maps is a well-established method to evaluate the conditions under which particular strengthening mechanisms are effective. Variable temperature and variable strain rate testing have begun to gain traction with the micromechanical testing community as they provide not only information about the material strength under these conditions, but also provide insight into the operative deformation mechanisms under these conditions. Multilayer thin films present a particularly interesting class of materials for these investigations since the interface density is easily modulated by simply adjusting the individual layer thickness. For room temperature experiments there are established models for the strengthening mechanisms operating as a function of layer thickness. Up until now these mechanisms have all relied upon resistance to dislocation movement, but these mechanisms are insufficient to describe the behavior of multilayer films tested at extreme temperatures and strain rates, particularly in cases of exceptionally thin individual layers. For metals with a low melting temperature, diffusion along multilayer interfaces can be a significant stress-relief mechanism, even at room temperature when the strain rates are sufficiently slow.

Several different strategies of achieving stronger sputtered films have been presented, including co-sputtering, sequential sputtering to produce multilayer films, and co-deposition of condensed nanoparticles and sputtered films to produce a particle-reinforced metal matrix composite. Several different materials systems were investigated using each of these architectures in order to ensure that the findings from each could be applied as more general principles beyond each specific system. The copper-tungsten materials system was investigated using each of the three architectures, acting as a universal system to investigate potential strengthening mechanisms. The immiscibility of copper and tungsten along with their widely differing mechanical properties made this system the ideal candidate for such a comparison. The nanoindentation results for sputtered copper-tungsten thin films of all three film architectures are presented in Figure 66.

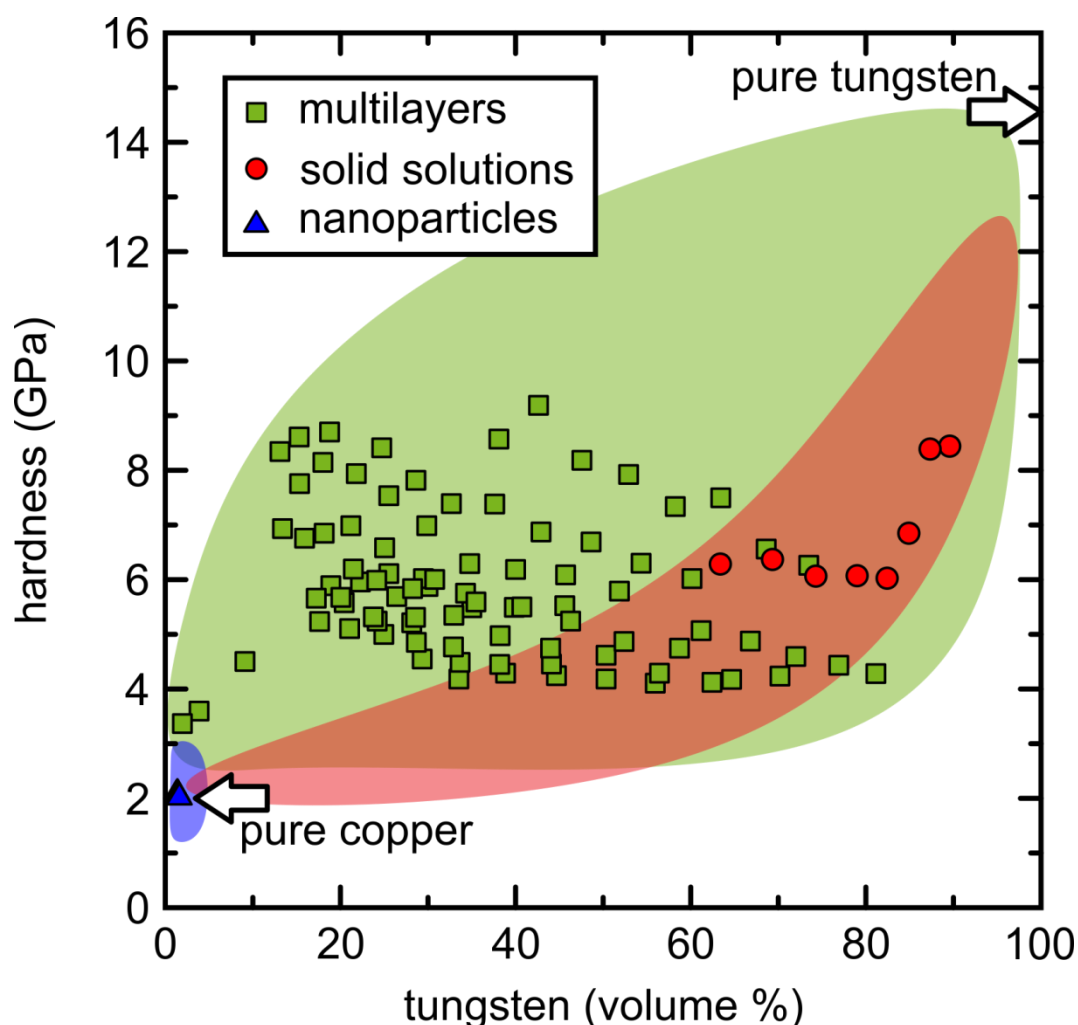


Figure 66: The Ashby plot of hardness versus tungsten content for Cu-W composites demonstrates the potential for the deposition architectures investigated in this work. Co-deposition of nanoparticles into a sputtered matrix utilizes the lowest volume of reinforcing material, but serves rather to pin grain boundaries in place rather than harden the film. Multilayers provide the largest strengthening due to their incorporation of the highest interface density and excellent adjustability through variation of the individual layer thicknesses. Substitutional solid solutions offer the least strengthening and are more useful for “phase diagram on a chip” combinatorial investigation.

Multilayers, solid solutions, and nanoparticle metal matrix composites all possess radically different structures, yet by presenting the data as a function of tungsten content a meaningful Ashby plot can be generated to enable comparison. By far the most data was collected for the multilayer films, where the use of two orthogonal wedge samples enabled a large number of different layer thicknesses and tungsten contents to be investigated with just a few deposition runs. This data spans more than 80% of the potential tungsten content range and exhibited hardness values which differ by more than a factor of three, depending mainly on the individual layer thicknesses used. The combinatorial approach for co-sputtering a lateral compositional gradient was useful for investigating the potential for solid solution strengthening in the copper-tungsten materials system. More than 30% of the potential tungsten contents were investigated here. Finally, tungsten nanoparticles embedded in a copper matrix were used to investigate the potential of this novel deposition technique for film hardening. Despite the implementation of a combinatorial approach, low particle deposition rates prevented tungsten contents above one volume percent from being achieved. As such this architecture is less interesting for providing additional film hardness, but rather seems suited for stabilizing the copper microstructure at elevated temperatures. All the measured data is presented as symbols in Figure 66 while the approximate range of hardness and tungsten content accessible through each film type is presented as

a correspondingly colored cloud behind the data. While this data is specific to the copper-tungsten materials system, the general trends are predicted to be applicable for other similar materials combinations as well.

7.1 Co-Sputtered Thin Films

Co-sputtering enables any materials which can be sputtered to be combined in arbitrary concentrations. One of the most attractive applications for co-sputtered films is the potential for producing a “phase diagram on a wafer”, a lateral compositional gradient which covers a large portion or the entirety of the phase diagram between two or three components. The phases and microstructure present within the deposited film depend strongly on the deposition conditions. For reactive elements it is possible for a number of phases to be present within the film, both equilibrium phases and otherwise. While co-sputtering permits films spanning a large range of chemical compositions to be prepared in a single deposition, this method is not without its shortcomings. Control over film microstructure is difficult, the oblique impingement angles of the deposited material can lead to porosity and directional growth, and film thickness can vary. The formation of metastable phases is quite common as sputtering is a process which takes far from thermodynamic equilibrium. The sputtered ions, particularly under room temperature deposition conditions, have a very limited surface mobility. Directional growth is especially problematic for the surface roughness, which needs to be kept quite small in order to perform nanoindentation.

7.1.1 Rule-of-Mixtures

A simple rule of mixtures following the Voigt model is generally sufficient for understanding the reduced modulus of co-sputtered films. The elastic modulus of the metastable solid solutions prepared by co-sputtering tends to be predicted well by the lower bound of a simple rule of mixtures. The hardness is a more complex value and is influenced greatly by the film microstructure while excessive surface roughness interferes with the measurement of hardness. As neither of these two parameters can be actively controlled during deposition it remains challenging to separate their individual contributions when interpreting the hardness data.

7.1.2 Solid Solution Strengthening

Solid solution strengthening often has far less influence on the film mechanical properties than other contributing factors. The tungsten content is generally a better predictor of the film strength. Metastable solid solutions arise commonly during co-deposition of otherwise immiscible materials, especially when the substrate is not heated during the deposition. Limited atom mobility on the substrate encourages the formation of nanocrystalline solid solutions. The strength of these solid solutions depends on the microstructure and texture of the film, both of which are difficult to control. This is especially true when using co-sputtering and a stationary substrate to produce a lateral compositional gradient combinatorial film. In general the modest contributions of solid strengthening can be neglected in materials systems where other strengthening mechanisms are present.

7.1.3 Grain Size Strengthening

The strength of metals tends to increase with decreasing grain size, as described by the well-known Hall-Petch relationship. As opposed to other strengthening mechanisms, grain size strengthening does not have any detrimental effect on ductility and, depending on the nature of the grain boundaries, can even lead to improved ductility. For the case of the copper-tungsten compositional gradient film, a

BCC crystalline solid solution was formed across the entire range of compositions investigated. SEM inspection of faceted features on the film surface suggested that the grain size generally decreased with increasing copper content, which was later confirmed through both XRD and TEM investigations. Three unique sites were found to exhibit especially strong diffraction peaks and were subsequently selected for further TEM investigation. There was not, however, any strong correlation between the grain size and the film hardness. For co-sputtered films the grain size is difficult to control and does not appear to be a determining factor in the hardness of metastable solid solutions.

7.1.4 Superposition of Hardening Mechanisms

The superposition of hardening mechanisms has been suggested as a method of simply adding the hardening contributions of several mechanisms in order to obtain the total film hardness. Using this method drastically overestimated the hardness for the co-sputtered films and does not appear to be applicable for such films. The main prerequisite for the validity of this approach is for each of the hardening mechanisms in consideration to operate independently of the others. This does not appear to be the case for the films in question, where the other potential hardening mechanisms either interfere or are not operative. In cases in which the different hardening mechanisms operate on similar length scales the superposition method is likely to be inaccurate and overestimate the hardening contribution of each mechanism.

7.2 Multilayer Thin Films

Multilayer thin films have long been recognized for their potential to provide drastic strength improvements of their single-component counterparts. The nanoscale mantra “smaller is stronger” also largely holds true in multilayers of all types with improved mechanical properties being observed as the individual layer thickness is reduced. This improvement to both strength and ductility appears to be near-universal for a wide variety of materials systems, leaving many open questions regarding the origin of strengthening in multilayer films. In 1994 Chu and Barnett proposed a model for hardening in coherent multilayers (superlattices) in which the difference in shear moduli provides resistance to dislocation glide [163]. Coherency strain at the interface was not included in this model, but had been previously proposed as a hardening mechanism in coherent multilayers [164]. A method for determining the flow stress within the individual components of a multilayer, and not just the hardness of the composite, has been developed using Cu-Ni multilayers [165]. Widespread adaptation of this approach has not yet been realized since experimental values of in-plane stress, uniaxial compressive flow stress, elastic modulus, and hardness are required. These results then need to be combined with extensive finite element simulations, which is both difficult and time-consuming. Plastic flow in one component of multilayers has been shown to reduce the flow stress of the other component through deposition of dislocation at the interface in the case of Cu-Ni multilayers [166].

Incoherent interfaces, those in which no obvious mechanisms of dislocation transmission across an interface, also exhibit exceptional hardness values. In this case a different argument has been developed in which it is not a difference in elastic moduli or the elastic strain at the interface which are responsible for strengthening, but rather the resistance of the interface to dislocation crossing. When subject to enough stress, dislocation transmission can occur even in unlike crystal lattices with highly incoherent interfaces. Even the very concept of strengthening through resistance to dislocation movement has been called into question with observed hardening in ceramic-ceramic multilayers, where little to no plasticity is observed prior to fracture. Enhanced toughness in ceramic superlattices has been observed and correlates well with hardness enhancements, suggesting that the toughening and hardening mechanisms may be correlated [167]. Materials combinations utilizing one hard and one soft material

have become especially popular in research since the mechanical behavior of the composite can provide especially strong hardening effects.

When the difference in hardness and elastic modulus of the two component materials is large the stress distribution within the micropillar is far from homogeneous. In addition to the stress concentrations at the top and bottom of the micropillar, there is also a large lateral stress variation. When compressed to high strains brittle failure occurs in the harder of the two materials, especially in cases where columnar grain boundaries are present in the harder phase. Columnar grain boundaries potentially contain porosity in reactively sputtered ceramic films and can act as a point of origin for brittle fracture in multilayers [168]. Larger scatter in the experimental data is expected once brittle fracture begins to occur. A large stochastic component arises and the strength of the material will be better described by fracture mechanics (Weibull statistics, etc.). Brittle fracture will only occur when the harder of the two materials is subjected to a significant lateral tensile load. Again, this arises in micropillar compression more readily than in nanoindentation, where the tensile stresses are generally less severe due to lateral confinement. In nanoindentation experiments delamination between the individual layers or between the film and the substrate are observed [169]. When the softer material flows into and fills the cracks in the brittle material, the term "self-healing" has been somewhat erroneously applied [170]. Even when the soft material flows around the fractured hard layer there is no actual recovery of strength, but rather just a resistance to catastrophic failure of the composite.

Brittle failure of multilayer micropillars can also be strongly influenced by the volume fractions of the two film components. The impact of non-identical volume fractions has been largely neglected in the literature, opting instead to utilize a standard identical volumetric ratio of the two film components. One notable exception here is the study of Al-SiC nanolaminates by nanoindentation at elevated temperatures [102]. The film hardness was shown to decrease with decreasing volume fraction of aluminum across all temperatures. The hardness of films with thin individual layers decreased more rapidly with increasing temperature, indicating that an interface-related deformation mechanism exhibits high temperature sensitivity. Indeed, the use of variable temperature testing has evolved into a technique not only for ascertaining the materials behavior at different temperatures, but also into understanding the deformation mechanisms at work by analyzing the temperature sensitivity of the multilayers.

7.2.1 Temperature-Dependent Deformation in Multilayers

The classical models for strengthening in multilayers are all based on mechanisms which provide resistance to dislocation movement. Similar strengthening effects have been observed in ceramic-ceramic multilayers, calling into question whether this strengthening effect is truly dislocation mediated in all cases [132]. The general trend of increasing strength with decreasing layer thickness down to just a few nanometers is widely accepted, though there remain many open questions regarding the origin of this strengthening. Room temperature nanoindentation data is widely reported in the literature due to the simplicity of the experimental setup, the minimal sample preparation required to obtain data, and the ease and quickness of collecting large data sets. At room temperature most metals are well below their melting temperature and it has been sufficient to consider their behavior solely in terms of dislocation-based deformation mechanisms. As variable temperature testing becomes more commonly, entirely different failure mechanisms have been observed which indicate that diffusion governs the material strength. This is especially apparent for micropillar compression experiments, where the signs of diffusion are readily apparent on the micropillar sidewalls. For nanoindentation this is not nearly as apparent since the only free volume toward which the mobile atoms can readily diffuse is present in porosity and at grain boundaries in non-fully dense films.

In an effort to better understand the operative deformation mechanisms at these small length scales, experimental efforts are now being focused on extending the range of temperature and strain rates at which the film mechanical properties are being tested. Expanding the range of testing conditions has led to the observation of new failure mechanisms in these films which differ depending on the type of experiment used to ascertain the film's mechanical properties. In nanoindentation various crack types have been observed as a function of the strain rate [103], where even at room temperature the multilayers exhibit a crack-filling phenomenon. Elevated temperature micropillar compression experiments have resulted in the growth of whiskers, microcrystals, and extruded volumes of metals on their side-walls. Strong evidence of diffusion-mediated deformation at elevated temperatures, collected in the form of SEM observation and analysis of the activation energies and activation volumes, has been obtained. Current models of soft-hard multilayer combinations assume that failure is dictated by deformation in the soft material phase, but the cryogenic micropillar compression experiments presented here suggest that this is not always the case. Particularly when impurities or a high density of grain boundaries are present within the hard phase, it is possible for brittle fracture of the harder material phase to occur. This is evidenced by an increase in the statistical scatter in yield strength at lower temperatures and cross-sections of compressed micropillars. Models encompassing more than the three primary dislocation-based strengthening mechanisms summarized by Misra [8] are needed to adequately address the types of deformation mechanisms which can occur in new material combinations and across a wider range of testing conditions. A phenomenological plot of the primary strengthening and deformation mechanisms as a function of individual layer thickness and homologous temperature, inspired by the popular deformation maps, is presented in Figure 67. This figure is intended to be largely schematic as there are transitions between the different areas where multiple deformation mechanisms are active. The onset of diffusion-based mechanisms is also highly dependent upon the applied strain rate and the micropillar geometry, so Figure 67 is intended to represent the general mechanisms operative within a limited range of strain rates. Lower strain rates would result in the migration of the brittle-to-ductile and dislocation-to-diffusion boundaries to the left, toward lower temperatures.

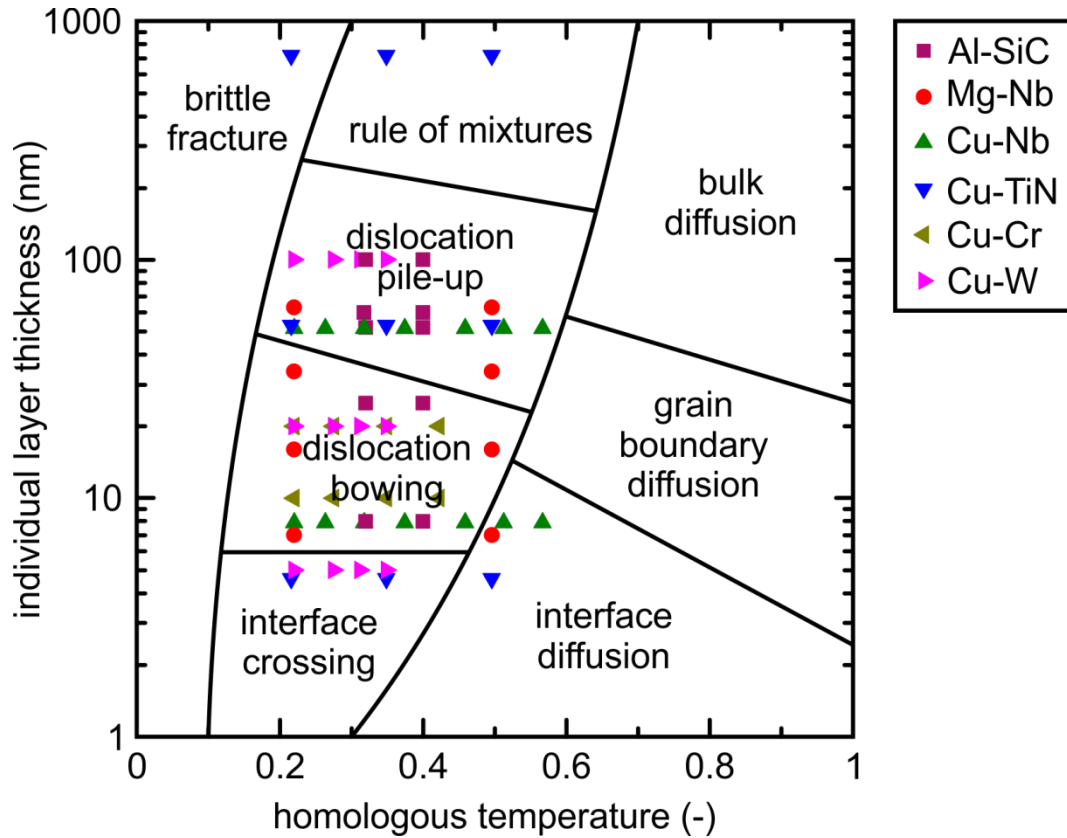


Figure 67: The appropriate model for describing the mechanical behavior of a multilayer depends on the individual layer thickness and the homologous temperature of the material. At higher temperatures diffusion plays a central role in the deformation of multilayers. Incoherent interfaces act as diffusion pathways, leading to material softening at larger layer thicknesses than are observed at room temperature. Brittle fracture within the harder phase can occur at low temperatures for multilayers containing hard-soft material combinations. The majority of the existing literature for variable temperature micropillar compression of soft-hard multilayer material combinations can be reasonably well described by dislocation pile-up and dislocation bowing models utilizing appropriate fitting coefficients. Data are presented for Al-SiC [101,171], Mg-Nb (this work), Cu-Nb [172], Cu-TiN (this work) [118], Cu-Cr [173], and Cu-W [174].

A number of deformation mechanisms have been proposed to describe the behavior of multilayers, but the three most prevailing are dislocation pile-up, dislocation bowing, and interface crossing. The first two of these models predict an increase in yield strength with decreasing layer thickness and generally describe the data well with minimal fitting parameters. As the layers become thinner the strengthening effect begins to deteriorate, especially when tests are conducted at elevated temperatures or low strain rates. Dislocation climb has been identified as the primary deformation mechanism in Cu-Nb multilayers with layer thickness below 25 nm [172], indicating that diffusion along the interface may not occur as easily as in the Mg-Nb system. A rudimentary dislocation mechanism map expressing flow stress in micropillars as a function of layer thickness was developed to include confined layer slip, dislocation transmission, and dislocation climb within a fixed range of strain rates. Diffusion along the interfaces is cited as the limiting factor for strengthening and a layer thickness of 25-35 nm is identified as offering the highest strength at 400°C for the Cu-Nb system. The prevalence of dislocation-based mechanisms for describing multilayer behavior is fully justified when viewing the literature seen in Figure 67. The vast majority of data available in the literature falls within these models, though some data near the edge of the dislocation bowing and dislocation pile-up regimes has necessitated the use of diffusion-based mechanisms to describe the material behavior. For especially low strain rates, as exemplified through creep tests, this diffusion behavior can be observed even at room temperature for metals with lower melting temperatures.

Even at room temperature, significant creep has been observed in multilayers. In the case of Ag-Fe multilayers, a clear trend of increasing creep rates was observed for decreasing layer thickness [175]. Stress exponent values for power law creep ranging from 2 to 32 were observed, leading the authors to conclude that dislocation glide-climb processes were responsible for the creep. The exceptionally high stress exponents were observed in multilayers with a periodicity of 60 nm, indicating that almost no creep takes place whatsoever. The interfaces were suggested to be the pathway along which diffusion occurs, in keeping with the observed trend of higher creep rates for thinner layers. In multilayers with layer thicknesses below 15 nm steady-state creep is reached quickly and allowed grain-boundary sliding to be identified as the primary deformation mechanism in Ag-Cu multilayers [176]. Creep was postulated to become increasingly relevant as the layer thickness is further reduced and the strain rate is decreased. Elevated temperature studies of nanoscale multilayers remain relatively scarce since the high number of interfaces, coupled with the available thermal energy, can readily result in the decomposition of the multilayer structure. Mixing of the layers, formation of intermetallic compounds, or spinodal decomposition are all possible. Tensile tests on Cu-Nb multilayers with individual layer thicknesses of 40, 60, and 75 nm were performed at temperatures of up to 700°C, where grain-boundary sliding was determined to be the prevalent deformation mechanism [177]. At higher strain rates the strain rate exponent decreases, suggesting that power-law creep is the dominant mechanism. The diffusion coefficient along an interface of two materials is generally higher than the bulk diffusion coefficient and can differ from the grain boundary diffusion coefficient [178].

The relevance of diffusion to multilayer deformation is highlighted especially clearly by comparing nanoindentation and micropillar compression results. At elevated temperatures films tested via micropillar compression will fail at lower stresses than those tested via nanoindentation. Micropillars are surrounded by a large free volume toward which mobile atoms can readily diffuse. Diffusion as a stress relief mechanism is not available in nanoindentation simply due to the geometric confinement of the tested volume. The large compressive stress experienced beneath the indenter tip is constrained by the surrounding film. Incoherent interfaces presumably have a diffusion coefficient close to that of a grain boundary since there is free volume which is conducive to atoms hopping. A totally coherent or epitaxial interface however, probably does not offer a diffusion pathway any more significant than bulk diffusion. At elevated temperatures, the hardness to yield stress ratio increases due to the diffusional pathways available in micropillar compression [101]. The lateral constraint in nanoindentation is greatly reduced in micropillar compression, especially when the ratio of layer thickness to pillar diameter is high. In this case the softer phase accommodates nearly all of the plastic deformation [171]. The critical ratio also depends on the homologous temperature since interface diffusion can promote further plasticity in the soft phase of a micropillar. Diffusion is available as a deformation mechanism in micropillars where the lack of lateral constraint and availability of a large free surface on the pillar sidewalls offer a convenient stress-relief pathway which is largely unavailable using nanoindentation due to the surrounding film. Micropillar compression is therefore an ideal technique for investigating diffusion-based deformation and potentially for determining the diffusion coefficient along the multilayer interface. Systematic study of pillar deformation as a function of multilayer orientation would be useful in this regard.

7.3 Nanoparticle Metal Matrix Composites

Although the co-deposition technique for producing nanoparticle metal matrix composites is still largely under development, the films produced thus far are sufficient to gain the first insights into the behavior of this type of film architecture. Somewhat surprisingly, especially considering the widespread adaptation of precipitate strengthening in precipitate-strengthened alloys, there was no observed hardening effect upon the introduction of tungsten nanoparticles into a copper matrix. The total volume of tungsten nanoparticles remains somewhat modest at less than one volume percent due to the low deposition rates associated with the nanoparticle condensation process. The potential strengthen-

ing effect of the nanoparticles is overshadowed by the hardening due to the fine-grained structured of the copper film. It is hypothesized that the tungsten nanoparticles disturb copper grain growth during the deposition process and are therefore predominantly located along grain boundaries within the copper. This positioning is ideal to provide Zener pinning under conditions where copper grain growth would normally occur. XRD and TEM data collected during sample annealing demonstrate that the nanocrystalline grain structure is indeed preserved in the samples containing tungsten nanoparticles while extensive grain growth occurs in pure copper samples deposited under identical conditions. This indicates that while the nanoparticles do not strengthen the copper film directly, that they may be able to extend the range of temperatures at which grain boundary strengthening can be exploited. Ultimately the incorporation of nanoparticles could be used to stabilize nanocrystalline metals where spontaneous grain growth and deterioration of mechanical properties would occur.

8 Summary and Outlook

The principal focus of this work was the investigation of the mechanical properties of sputtered thin films utilizing a combinatorial approach. To this end three main sputtered film architectures were studied: lateral compositional gradient films, periodic bilayer multilayer films, and nanoparticle metal matrix composites. The copper-tungsten materials system was investigated for all three architectures while several additional materials systems were investigated using the former two film architectures. A broad spectrum of materials characterization techniques was utilized to ascertain the film composition and structure. Among these techniques were scanning electron microscopy, transmission electron microscopy, X-ray fluorescence, X-ray diffraction, X-ray reflectometry, and energy dispersive X-ray spectroscopy. Mechanical characterization was conducted using nanoindentation and micropillar compression. New insight regarding the fundamental deformation mechanisms within the films was obtained through implementation of variable strain rate and variable temperature testing. Both cryogenic and elevated temperature tests were conducted in addition to a number of transient methods including strain-rate jump, stress relaxation, and creep tests. The combinatorial approach to sample deposition and testing proved to be highly effective; this approach enabled far more progress to be achieved than could have been using a traditional sample-by-sample approach.

Co-sputtered lateral compositional gradient samples offer an excellent opportunity to study a large spread of chemical compositions between two or more materials. Given the geometric constraints of the sputtering chamber used for sample deposition, roughly 50% of the compositional range of a binary system could be produced in a single deposition, as was performed here to investigate copper-tungsten and zirconium-niobium combinations. Co-sputtered samples rarely demonstrated any appreciable solid solution strengthening. This effect tends to be rather small and is typically overshadowed by microstructural effects. Annealing the samples would allow equilibrium phases to precipitate and likely improve hardness. The elastic properties of the films tend to follow the lower bound of a simple rule of mixtures. Ternary and higher-order compounds can also be prepared, as demonstrated with the aluminum-copper-nickel materials system. Although the emphasis of this work was the investigation of the mechanical properties of thin films, they are also well suited for investigating other properties as highlighted by the laser ablation portion of the study. Increasing the number of components reduces the total portion of the compositional range which can be covered per experimental run. Studies of films containing three or more components are better facilitated using an alternative method to co-sputtering. In this method thickness-gradient layers are deposited using a shutter system to first produce a multilayer film structure which can be subsequently annealed to facilitate intermixing of the layers into a homogeneous film.

The introduction of variable temperature and variable strain rate testing techniques were applied to copper-titanium nitride and magnesium-niobium multilayers. Both cryogenic and elevated temperature micropillar compression experiments were conducted, shedding light not only on the temperature-dependent behavior of these materials, but also on the fundamental deformation mechanisms governing their strength. At high strain rates and low temperatures failure was shown to occur through fracture of the intrinsically stronger phase, highlighting the inhomogeneous stress fields present in multilayer films. At elevated temperatures diffusion-based mechanisms were shown to accommodate plastic deformation through enhanced diffusion along the material interfaces. These findings were used to produce a schematic deformation mechanism map for multilayer films in which layer thickness, temperature, and strain rate determine whether brittle fracture, dislocation movement, diffusion, or a combination of mechanisms lead to material failure. In the magnesium-niobium materials system a pseudomorphic phase of cubic magnesium was observed when the layer thickness was kept below eight nanometers. The orthogonal wedge stack sample geometry was demonstrated as a powerful tool for generating mechanical data and can be readily extended to collect phase data necessary for construction of bi-phase diagrams for interface-stabilized pseudomorphic materials.

The third sample architecture investigated was a nanoparticle-containing metal matrix composite in which tungsten nanoparticles were co-deposited with sputtered copper. At room temperature this film did not exhibit any exceptional mechanical properties when compared to pure copper films deposited under identical conditions. The tungsten nanoparticles are likely situated at grain boundaries, where they have little direct impact on the strength of the film. These particles do, however, have a significant impact on the film behavior at elevated temperatures. Grain growth is greatly inhibited through Zener pinning in nanoparticle-containing films at temperatures where grain growth readily occurs in pure copper films. As such the inclusion of nanoparticles through co-deposition is proposed as a method for stabilizing the grain size and maintaining the attractive mechanical properties of nanocrystalline materials at elevated temperatures. This was demonstrated to be effective in copper up to temperatures of 800°C. This approach could also be applied to nanocrystalline materials where grain growth has been shown to occur spontaneously even at room temperature, opening the possibility for exciting new applications of nanostructured films.

Throughout this work the combinatorial method has been demonstrated as an effective means for studying the mechanical properties of thin films. The combinatorial approach was applied to the three different film architectures (lateral compositional gradients, periodic bilayers, and nanoparticle composites) to provide a sizable data set with reduced experimental effort. A number of novel findings have been presented in this work, though, as is often the case in science, each answered question opens the possibility for further research and experimentation. Several of the potential paths for continued exploration of the topics treated in this thesis are described below.

The copper-tungsten materials system was demonstrated to form a metastable solid solution when deposited as a thin film by co-sputtering. The lateral compositional gradient approach could be extended to the copper-rich portion of the phase diagram, where a FCC solid solution is present rather than the BCC solid solution investigated here. The transition region between crystal structures is an especially interesting area for mechanical investigation. While the Reuss model rule-of-mixtures was sufficient for predicting the film hardness in the BCC solid solution regime of the copper-tungsten materials system, it is not intuitively clear what effect the change in crystal structure would have on this trend.

For the case of multilayer copper-tungsten the mechanical properties were shown to be well-predicted by calculating the hardness of the individual copper and tungsten layers and averaging the two values. Historically the strength of similar films has been calculated considering the strength of the weaker component alone. At least for the copper-tungsten system, this approach has been demonstrated to be insufficient. The absence of any clear interaction between the copper and tungsten layers is surprising since co-deformation of the layers is necessary. A universal model which can predict the hardness of multilayers made of non-equal volumetric fractions for arbitrary materials would contribute greatly to our understanding of the mechanical behavior of multilayer structures. The orthogonal wedge sample geometry offers an ideal means for doing this. In this work only two regions of individual layer thickness and ratio between the multilayer components were investigated. Extending this to cover all layer thicknesses between several nanometers to one micron with material ratios up to 10:1 would be an excellent starting point. The confounding effect of intrinsic stress variation within the film could be counteracted by using a shutter system rather than obliquely positioned sputtering targets for film preparation.

The orthogonal wedge geometry also offers great promise for studying metastable pseudomorphs in multilayers. With this sample geometry it is possible to develop the bi-phase diagram for metastable pseudomorphs. This would otherwise be very difficult to achieve experimentally as the typical length scale of single-digit nanometers can be somewhat difficult to control precisely using sputtering. Early reports on the existence of interface-stabilized pseudomorphs in multilayers indicated that an abrupt

transformation occurs at the critical thickness; the entire layer is present as a single phase. More recent investigations suggest that a more gradual transition is possible in which a mixture of both crystal phases is possible. Examination of a gradual thickness gradient will enable better understanding of the pseudomorphic transition and the precise experimental determination of the bi-phase diagram.

From a strictly experimental point of view, there is still plenty of room for improvement for variable temperature and strain rate testing of small-scale materials. Extending the range of operating temperatures for micromechanical testing apparatus deep within the cryogenic range will allow for more fundamental materials studies to be performed with less interference from thermal processes. This will help to reduce the gap between atomistic simulations and experimental data. Increasing the range of strain rates which can be investigated will have a similar effect at improving the comparability between atomistic simulations and experiments, hopefully establishing a means through which fundamental deformation mechanisms can be more thoroughly understood. In conclusion, there are still plenty of open questions which remain in the field of thin film micromechanics. Combinatorial methods, innovative new test apparatus, and novel film architectures will enable further insight in the bright future of this exciting field.

9 Bibliography

- [1] X.-D. Xiang, COMBINATORIAL MATERIALS SYNTHESIS AND SCREENING: An Integrated Materials Chip Approach to Discovery and Optimization of Functional Materials, *Annu. Rev. Mater. Sci.* 29 (1999) 149–171. doi:10.1146/annurev.matsci.29.1.149.
- [2] R.B. Van Dover, L.F. Schneemeyer, R.M. Fleming, Discovery of a useful thin-film dielectric using a composition-spread approach, *Nature*. 2655 (1998) 2653–2655. doi:10.1038/32381.
- [3] K. Kennedy, T. Stefansky, G. Davy, V.F. Zackay, E.R. Parker, Rapid Method for Determining Ternary-Alloy Phase Diagrams, *J. Appl. Phys.* 36 (1965) 3808. doi:10.1063/1.1713952.
- [4] J.J. Hanak, The “Multiple-Sample Concept” in Materials Research: Synthesis, Compositional Analysis and Testing of Entire Multicomponent Systems, *J. Mater. Sci.* 5 (1970) 964–971. doi:10.1007/BF00558177.
- [5] R. a Potyrailo, K. Rajan, K. Stowe, I. Takeuchi, B. Chisholm, H. Lam, Combinatorial and High-Throughput Screening of Materials Libraries: Review of State of the Art Combinatorial and High-Throughput Screening of Materials Libraries: Review of State of the Art, (2011) 579–633. doi:10.1021/co200007w.
- [6] S.H. Oh, M. Legros, D. Kiener, P. Gruber, G. Dehm, In situ TEM straining of single crystal Au films on polyimide: Change of deformation mechanisms at the nanoscale, *Acta Mater.* 55 (2007) 5558–5571. doi:10.1016/J.ACTAMAT.2007.06.015.
- [7] T. Zhu, J. Li, Ultra-strength materials, *Prog. Mater. Sci.* 55 (2010) 710–757. doi:10.1016/j.pmatsci.2010.04.001.
- [8] A. Misra, J.P. Hirth, R.G. Hoagland, Length-scale-dependent deformation mechanisms in incoherent metallic multilayered composites, *Acta Mater.* 53 (2005) 4817–4824. doi:10.1016/j.actamat.2005.06.025.
- [9] W.R. Tyson, Theoretical strength of perfect crystals, *Philos. Mag. A J. Theor. Exp. Appl. Phys.* 14 (1966) 925–936. doi:10.1080/14786436608244763.
- [10] J.M. Wheeler, D.E.J. Armstrong, W. Heinz, R. Schwaiger, High temperature nanoindentation: The state of the art and future challenges, *Curr. Opin. Solid State Mater. Sci.* 19 (2015) 354–366. doi:10.1016/J.COSSMS.2015.02.002.
- [11] A. Anders, A structure zone diagram including plasma-based deposition and ion etching, *Thin Solid Films*. 518 (2010) 4087–4090. doi:10.1016/J.TSF.2009.10.145.
- [12] J.A. Thornton, Influence of apparatus geometry and deposition conditions on the structure and topography of thick sputtered coatings, *J. Vac. Sci. Technol.* 11 (1974) 666–670. doi:10.1116/1.1312732.
- [13] M. Khojasteh, V. V Kresin, Influence of source parameters on the growth of metal nanoparticles by sputter-gas-aggregation, *Appl. Nanosci.* 7 (2017) 875–883. doi:10.1007/s13204-017-0627-2.
- [14] R. Spolenak, L. Sauter, C. Eberl, Reversible orientation-biased grain growth in thin metal films induced by a focused ion beam, *Scr. Mater.* 53 (2005) 1291–1296. doi:10.1016/j.scriptamat.2005.07.030.
- [15] J. Mayer, L.A. Giannuzzi, T. Kamino, J. Michael, TEM Sample Preparation and FIB-Induced Damage, *MRS Bull.* 32 (2007) 400–407. doi:10.1557/mrs2007.63.
- [16] X.D. Xiang, X. Sun, G. Briceño, Y. Lou, K. a Wang, H. Chang, W.G. Wallace-Freedman, S.W. Chen, P.G. Schultz, A combinatorial approach to materials discovery., *Science*. 268 (1995) 1738–1740. doi:10.1126/science.268.5218.1738.
- [17] P.R. Subramanian, D.E. Laughlin, Cu-W (Copper-Tungsten), in: T.B. Massalski (Ed.), *Bin. Alloy Phase Diagrams*, Second Edi, Materials Park, Ohio, 1991: pp. 76–79.
- [18] B. Predel, Cu-W (Copper-Tungsten), *SpringerMaterials - Landolt-Börnstein Database*. 5d (1994) Volume 5d: Cr-Cs-Cu-Zr. doi:10.1007/b4775.

- [19] a. G. Cullis, J.M. Poate, J. a. Borders, The physical state of implanted tungsten in copper, *Appl. Phys. Lett.* 28 (1976) 314. doi:10.1063/1.88766.
- [20] N. Radir, B. Gr, D. Gracin, T. Car, Preparation and structure of Cu - W thin films, *Thin Solid Films.* 228 (1993) 225–228. doi:10.1016/0040-6090(93)90604-N.
- [21] H.F. Rizzo, T.B. Massalski, M. Nastasi, Metastable crystalline and amorphous structures formed in the Cu-W system by vapor deposition, *Metall. Trans. A.* 24 (1993) 1027–1037. doi:10.1007/BF02657233.
- [22] M. Nastasi, F.W. Saris, L.S. Hung, J.W. Mayer, Stability of amorphous Cu-Ta and Cu/W alloys, *J. Appl. Phys.* 58 (1985) 3052. doi:10.1063/1.335855.
- [23] B. Cantor, R.W. Cahn, Metastable alloy phases by co-sputtering, *Acta Metall.* 24 (1976) 845–852. doi:10.1016/0001-6160(76)90051-1.
- [24] N. Saunders, A.P. Miodownik, J. Rangiha, Use of vapour co-deposited thin films containing concentration gradients in the rapid assessment of phase equilibria in binary and ternary alloy systems, *J. Mater. Sci. Lett.* 6 (1987) 1179–1181. doi:10.1007/BF01729174.
- [25] N. Saunders, A.P. Miodownik, Phase formation in co-deposited metallic alloy thin films, *J. Mater. Sci.* 22 (1987) 629–637. doi:10.1007/BF01160780.
- [26] J.M. Poate, Formation of substitutional alloys by ion implantation in metals, *Appl. Phys. Lett.* 25 (1974) 698. doi:10.1063/1.1655366.
- [27] a. G. Dirks, Metastable solid solutions in vapor deposited Cu–Cr, Cu–Mo, and Cu–W thin films, *J. Vac. Sci. Technol. A Vacuum, Surfaces, Film.* 3 (1985) 2618. doi:10.1116/1.572799.
- [28] R.L. Zong, S.P. Wen, F. Zeng, Y. Gao, F. Pan, Nanoindentation studies of Cu–W alloy films prepared by magnetron sputtering, *J. Alloys Compd.* 464 (2008) 544–549. doi:10.1016/j.jallcom.2007.10.033.
- [29] F.T.N. Vüllers, R. Spolenak, From solid solutions to fully phase separated interpenetrating networks in sputter deposited “immiscible” W–Cu thin films, *Acta Mater.* 99 (2015) 213–227. doi:10.1016/j.actamat.2015.07.050.
- [30] K. Chang, D. Music, M.T. Baben, D. Lange, H. Bolvardi, J.M. Schneider, Modeling of metastable phase formation diagrams for sputtered thin films, *Sci. Technol. Adv. Mater.* 6996 (2016) 1–10. doi:10.1080/14686996.2016.1167572.
- [31] K. Chang, M. to Baben, D. Music, D. Lange, H. Bolvardi, J.M. Schneider, Estimation of the activation energy for surface diffusion during metastable phase formation, *Acta Mater.* 98 (2015) 135–140. doi:10.1016/j.actamat.2015.07.029.
- [32] A. Schäfer, G. Menzel, The structural and electrical properties of Metglas and amorphous metal films, *Thin Solid Films.* 52 (1978) 11–21. doi:10.1016/0040-6090(78)90250-X.
- [33] J. Zhao, A Combinatorial Approach for Structural Materials, *Adv. Eng. Mater.* 3 (2001) 143–147. doi:10.1002/1527-2648(200103)3:3<143::AID-ADEM143>3.0.CO;2-F.
- [34] N. Radić, M. Stubicar, Microhardness properties of Cu–W amorphous thin films, *J. Mater. Sci.* 33 (1998) 3401–3405. doi:10.1023/A:1013201817300.
- [35] W. Oliver, G. Pharr, An improved technique for determining hardness and elastic modulus using load and displacement sensing indentation experiments, *J. Mater. Res.* 7 (1992) 1564–1583. doi:10.1557/JMR.1992.1564.
- [36] C.M. Müller, S. Parviainen, F. Djurabekova, K. Nordlund, R. Spolenak, The as-deposited structure of co-sputtered Cu-Ta alloys, studied by X-ray diffraction and molecular dynamics simulations, *Acta Mater.* 82 (2015) 51–63. doi:10.1016/j.actamat.2014.08.066.
- [37] P. Scherrer, Bestimmung der Größe und der inneren Struktur von Kolloidteilchen mittels Röntgenstrahlen, *Nachrichten von der Gesellschaft der Wissenschaften zu Göttingen, Math. Klasse.* 1918 (n.d.) 98–100. <https://eudml.org/doc/59018#.WCG1ku1onzE.mendeley> (accessed November 8, 2016).
- [38] A. Monshi, Modified Scherrer Equation to Estimate More Accurately Nano-Crystallite Size Using

- XRD, World J. Nano Sci. Eng. 02 (2012) 154–160. doi:10.4236/wjnse.2012.23020.
- [39] L. Vegard, Die Konstitution der Mischkristalle und die Raumfüllung der Atome, Zeitschrift für Phys. 5 (1921) 17–26. doi:10.1007/BF01349680.
- [40] M.G.M. Miranda, E. Estévez-Rams, G. Martínez, M.N. Baibich, Phase separation in Cu₉₀Co₁₀ high-magnetoresistance materials, Phys. Rev. B. 68 (2003) 014434. doi:10.1103/PhysRevB.68.014434.
- [41] D. Tabor, The Hardness of Metals, ClarendonP, 1951. <https://books.google.ch/books?id=jsLRAAAAMAAJ>.
- [42] U.K. Vashi, R.W. Armstrong, G.E. Zima, The Hardness and Grain size of consolidated fine tungsten powder, Metall. Trans. 1 (1970) 1769–1771. doi:10.1007/BF02642027.
- [43] N. Kosarev, M. Khazin, R. Apakashev, N. Valiev, Mechanical Properties of Micro- and Nanostructured Copper Films, J. Mater. Sci. Chem. Eng. 01 (2013) 7–10. doi:10.4236/msce.2013.15002.
- [44] R. Fleischer, Substitutional solution hardening, Acta Metall. 11 (1963) 203–209. doi:10.1016/0001-6160(63)90213-X.
- [45] T.H. Courtney, Mechanical behavior of materials, Waveland Press, 2005.
- [46] R.L. Smialek, G.L. Webb, T.E. Mitchell, Solid solution softening in BCC metal alloys, Scr. Metall. 4 (1970) 33–37. doi:10.1016/0036-9748(70)90139-0.
- [47] T.J. Rupert, J.C. Trenkle, C.A. Schuh, Enhanced solid solution effects on the strength of nanocrystalline alloys, Acta Mater. 59 (2011) 1619–1631. doi:10.1016/j.actamat.2010.11.026.
- [48] T.D. Shen, C.C. Koch, Formation, solid solution hardening and softening of nanocrystalline solid solutions prepared by mechanical attrition, Acta Mater. 44 (1996) 753–761. doi:10.1016/1359-6454(95)00178-6.
- [49] A. Reuss, Berechnung der Fließgrenze von Mischkristallen auf Grund der Plastizitätsbedingung für Einkristalle., ZAMM - Zeitschrift Für Angew. Math. Und Mech. 9 (1929) 49–58. doi:10.1002/zamm.19290090104.
- [50] J. Meijer, Laser beam machining (LBM), state of the art and new opportunities, J. Mater. Process. Technol. 149 (2004) 2–17. doi:10.1016/j.jmatprotec.2004.02.003.
- [51] M.D. Shirk, P.A. Molian, A.P. Malshe, Ultrashort pulsed laser ablation of diamond, J. Laser Appl. 10 (1998) 64. doi:10.2351/1.521822.
- [52] C.P. Grigoropoulos, Transport in Laser Microfabrication, Cambridge University Press, Cambridge, 2009. doi:10.1017/CBO9780511596674.
- [53] K. Sokolowski-Tinten, J. Bialkowski, A. Cavalleri, D. Von der Linde, A. Oparin, J. Meyer-Ter-Vehn, S.I. Anisimov, Transient states of matter during short pulse laser ablation, Phys. Rev. Lett. 81 (1998) 224–227. doi:10.1103/PhysRevLett.81.224.
- [54] A. V. Pakhomov, M.S. Thompson, D.A. Gregory, Laser-induced phase explosions in lead, tin and other elements: Microsecond regime and UV-emission, J. Phys. D: Appl. Phys. 36 (2003) 2067–2075. doi:10.1088/0022-3727/36/17/308.
- [55] S. Fähler, H.U. Krebs, Calculations and experiments of material removal and kinetic energy during pulsed laser ablation of metals, Appl. Surf. Sci. 96–98 (1996) 61–65. doi:10.1016/0169-4332(95)00466-1.
- [56] X. Xu, K.H. Song, Phase change phenomena during high power laser-materials interaction, Mater. Sci. Eng. A. 292 (2000) 162–168. doi:10.1016/S0921-5093(00)00996-5.
- [57] G. Heise, M. Englmaier, C. Hellwig, T. Kuznicki, S. Sarrach, H.P. Huber, Laser ablation of thin molybdenum films on transparent substrates at low fluences, Appl. Phys. A Mater. Sci. Process. 102 (2011) 173–178. doi:10.1007/s00339-010-5993-5.
- [58] S.N. Aqida, D. Brabazon, S. Naher, Z. Kovacs, D.J. Browne, Laser micro-processing of amorphous and partially crystalline Cu 45Zr48Al7 alloy, Appl. Phys. A Mater. Sci. Process. 101 (2010) 357–

360. doi:10.1007/s00339-010-5829-3.
- [59] O. a. Bulgakova, N.M. Bulgakova, V.P. Zhukov, A model of nanosecond laser ablation of compound semiconductors accounting for non-congruent vaporization, *Appl. Phys. A Mater. Sci. Process.* 101 (2010) 53–59. doi:10.1007/s00339-010-5757-2.
 - [60] S. Rung, A. Christiansen, R. Hellmann, Influence of film thickness on laser ablation threshold of transparent conducting oxide thin-films, *Appl. Surf. Sci.* 305 (2014) 347–351. doi:10.1016/j.apsusc.2014.03.082.
 - [61] E. Matthias, M. Reichling, J. Siegel, O.W. Kading, S. Petzoldt, H. Skurk, P. Bizenberger, E. Neske, The Influence of Thermal-Diffusion on Laser-Ablation of Metal-Films, *Appl. Phys. a-Materials Sci. Process.* 58 (1994) 129–136. doi:10.1007/Bf00332169.
 - [62] C.P. Kothandaraman, S. Subramanyan, *Heat and Mass Transfer Data Book*, New Academic Science, 2012. <https://books.google.ch/books?id=yjUBLgEACAAJ>.
 - [63] O. Benavides, O. Lebedeva, V. Golikov, Reflection of nanosecond Nd:YAG laser pulses in ablation of metals, *Opt. Express.* 19 (2011) 21842. doi:10.1364/OE.19.021842.
 - [64] M. Hafner, W. Burgstaller, A.I. Mardare, A.W. Hassel, Aluminium-copper-nickel thin film compositional spread: Nickel influence on fundamental alloy properties and chemical stability of copper, *Thin Solid Films.* 580 (2015) 36–44. doi:10.1016/j.tsf.2015.03.018.
 - [65] S.A. Rebegea, K. Thomas, V. Chawla, J. Michler, M.C. Kong, Laser ablation of a Cu–Al–Ni combinatorial thin film library: analysis of crater morphology and geometry, *Appl. Phys. A Mater. Sci. Process.* 122 (2016) 1–9. doi:10.1007/s00339-016-0608-4.
 - [66] C.R. Mayer, L.W. Yang, S.S. Singh, J. Llorca, J.M. Molina-Aldareguia, Y.L. Shen, N. Chawla, Anisotropy, size, and aspect ratio effects on micropillar compression of Al[SiC] nanolaminate composites, *Acta Mater.* 114 (2016) 25–32. doi:10.1016/j.actamat.2016.05.018.
 - [67] J. Wang, a. Misra, An overview of interface-dominated deformation mechanisms in metallic multilayers, *Curr. Opin. Solid State Mater. Sci.* 15 (2011) 20–28. doi:10.1016/j.cossms.2010.09.002.
 - [68] W.A. Jesser, J. Kui, Misfit dislocation generation mechanisms in heterostructures, *Mater. Sci. Eng. A.* 164 (1993) 101–110. doi:10.1016/0921-5093(93)90647-W.
 - [69] J. Wang, C. Yang, P.D. Hodgson, Strain gradients in Cu–Fe thin films and multilayers during micropillar compression, *Mater. Sci. Eng. A.* 651 (2016) 146–154. doi:10.1016/j.msea.2015.10.105.
 - [70] G. Janeschitz, Plasma-wall interaction issues in ITER, *J. Nucl. Mater.* 293 (2001) 1–11. doi:10.1016/S0022-3115(00)00623-1.
 - [71] Y. Shimomura, ITER and plasma surface interaction issues in a fusion reactor, *J. Nucl. Mater.* 363–365 (2007) 467–475. doi:10.1016/j.jnucmat.2007.01.215.
 - [72] F. a. Garner, M.L. Hamilton, T. Shikama, D.J. Edwards, J.W. Newkirk, Response of solute and precipitation strengthened copper alloys at high neutron exposure, *J. Nucl. Mater.* 191–194 (1992) 386–390. doi:10.1016/S0022-3115(09)80072-X.
 - [73] I.J.C. Team, The impact of materials selection on the design of the International Thermonuclear Experimental Reactor (ITER), *J. Nucl. Mater.* 212–215 (1994) 3–10. doi:10.1016/0022-3115(94)90027-2.
 - [74] G. Vieider, M. Merola, F. Anselmi, J.P. Bonal, P. Chappuis, G.D. Orco, D. Duglue, European development of prototypes for ITER high heat flux components, *Fusion Eng. Des.* 50 (2000) 135–143. doi:10.1016/S0920-3796(00)00238-6.
 - [75] G. Pintsuk, S.E. Brünings, J.-E. Döring, J. Linke, I. Smid, L. Xue, Development of W/Cu—functionally graded materials, *Fusion Eng. Des.* 66–68 (2003) 237–240. doi:10.1016/S0920-3796(03)00220-5.
 - [76] A. Misra, M.J. Demkowicz, X. Zhang, R.G. Hoagland, The Radiation Damage Tolerance of Ultra-High Strength Nanolayered Composites, *JOM.* 59 (2007) 62–65. doi:10.1007/s11837-007-0120-

6.

- [77] S. Wen, R. Zong, F. Zeng, Y. Gao, F. Pan, Evaluating modulus and hardness enhancement in evaporated Cu/W multilayers, *Acta Mater.* 55 (2007) 345–351. doi:10.1016/j.actamat.2006.07.043.
- [78] H.C. Barshilia, K. Rajam, Characterization of Cu/Ni multilayer coatings by nanoindentation and atomic force microscopy, *Surf. Coatings Technol.* 155 (2002) 195–202. doi:10.1016/S0257-8972(02)00008-7.
- [79] M.T. Johnson, P.J.H. Bloemen, F.J. a Den Broeder, J.J. De Vries, Magnetic anisotropy in metallic multilayers, *Reports Prog. Phys.* 59 (1996) 1425–1426. doi:10.1088/0034-4885/59/11/002.
- [80] C.-C. Huang, T.-C. Chiang, T.-H. Fang, Grain size effect on indentation of nanocrystalline copper, *Appl. Surf. Sci.* 353 (2015) 494–498. doi:10.1016/J.APSUSC.2015.06.135.
- [81] L. Zhu, G. Li, H. Wang, B. Xu, D. Zhuang, J. Liu, Microstructures and nano mechanical properties of the metal tungsten film, *Curr. Appl. Phys.* 9 (2009) 510–514. doi:10.1016/j.cap.2008.05.003.
- [82] H. Holleck, V. Schier, Multilayer PVD coatings for wear protection, *Surf. Coatings Technol.* 76–77 (1995) 328–336. doi:10.1016/0257-8972(95)02555-3.
- [83] S.J. Bull, A.M. Jones, Multilayer coatings for improved performance, *Surf. Coatings Technol.* 78 (1996) 173–184. doi:10.1016/0257-8972(94)02407-3.
- [84] W.J. Clegg, Controlling cracks in ceramics, *Science* (80-.). 286 (1999) 1097–1099. doi:10.1126/science.286.5442.1097.
- [85] W.J. Clegg, K. Kendall, N.M. Alford, T.W. Button, J.D. Birchall, A simple way to make tough ceramics, *Nature.* 347 (1990) 455–457.
- [86] C. Subramanian, K.N. Strafford, Review of multicomponent and multilayer coatings for tribological applications, *Wear.* 165 (1993) 85–95. doi:10.1016/0043-1648(93)90376-W.
- [87] H. Holleck, M. Lahres, P. Woll, Multilayer coatings-influence of fabrication parameters on constitution and properties, *Surf. Coatings Technol.* 41 (1990) 179–190. doi:10.1016/0257-8972(90)90166-A.
- [88] P.H. Mayrhofer, C. Mitterer, L. Hultman, H. Clemens, Microstructural design of hard coatings, *Prog. Mater. Sci.* 51 (2006) 1032–1114. doi:10.1016/j.pmatsci.2006.02.002.
- [89] S.C. Tjong, H. Chen, Nanocrystalline materials and coatings, *Mater. Sci. Eng. R Reports.* 45 (2004) 1–88. doi:10.1016/j.mser.2004.07.001.
- [90] J.R. Greer, J.T.M. De Hosson, Plasticity in small-sized metallic systems: Intrinsic versus extrinsic size effect, *Prog. Mater. Sci.* 56 (2011) 654–724. doi:10.1016/j.pmatsci.2011.01.005.
- [91] Y.P. Li, G.P. Zhang, On plasticity and fracture of nanostructured Cu/X (X = Au, Cr) multilayers: The effects of length scale and interface/boundary, *Acta Mater.* 58 (2010) 3877–3887. doi:10.1016/j.actamat.2010.03.042.
- [92] W. Guo, E. Jägle, J. Yao, V. Maier, S. Korte-Kerzel, J.M. Schneider, D. Raabe, Intrinsic and extrinsic size effects in the deformation of amorphous CuZr/nanocrystalline Cu nanolaminates, *Acta Mater.* 80 (2014) 94–106. doi:10.1016/j.actamat.2014.07.027.
- [93] S.M. Han, M.A. Phillips, W.D. Nix, Study of strain softening behavior of Al-Al3Sc multilayers using microcompression testing, *Acta Mater.* 57 (2009) 4473–4490. doi:10.1016/j.actamat.2009.06.007.
- [94] M. a. Phillips, B.M. Clemens, W.D. Nix, Microstructure and nanoindentation hardness of Al/Al3Sc multilayers, *Acta Mater.* 51 (2003) 3171–3184. doi:10.1016/S1359-6454(03)00128-9.
- [95] M.A. Phillips, B.M. Clemens, W.D. Nix, A model for dislocation behavior during deformation of Al/Al3Sc (fcc/L12) metallic multilayers, *Acta Mater.* 51 (2003) 3157–3170. doi:10.1016/S1359-6454(03)00127-7.
- [96] D. Bhattacharyya, N.A. Mara, P. Dickerson, R.G. Hoagland, A. Misra, Compressive flow behavior of Al-TiN multilayers at nanometer scale layer thickness, *Acta Mater.* 59 (2011) 3804–3816.

- doi:10.1016/j.actamat.2011.02.036.
- [97] D.R.P. Singh, N. Chawla, G. Tang, Y.L. Shen, Micropillar compression of Al/SiC nanolaminates, *Acta Mater.* 58 (2010) 6628–6636. doi:10.1016/j.actamat.2010.08.025.
 - [98] G. Tang, Y.L. Shen, D.R.P. Singh, N. Chawla, Indentation behavior of metal-ceramic multilayers at the nanoscale: Numerical analysis and experimental verification, *Acta Mater.* 58 (2010) 2033–2044. doi:10.1016/j.actamat.2009.11.046.
 - [99] I. Knorr, N.M. Cordero, E.T. Lilleodden, C.A. Volkert, Mechanical behavior of nanoscale Cu/PdSi multilayers, *Acta Mater.* 61 (2013) 4984–4995. doi:10.1016/j.actamat.2013.04.047.
 - [100] S. Lotfian, J.M. Molina-Aldareguia, K.E. Yazzie, J. Llorca, N. Chawla, High-temperature nanoindentation behavior of Al/SiC multilayers, *Philos. Mag. Lett.* 92 (2012) 362–367. doi:10.1080/09500839.2012.674220.
 - [101] S. Lotfian, M. Rodríguez, K.E. Yazzie, N. Chawla, J. Llorca, J.M. Molina-Aldareguia, High temperature micropillar compression of Al/SiC nanolaminates, *Acta Mater.* 61 (2013) 4439–4451. doi:10.1016/j.actamat.2013.04.013.
 - [102] S. Lotfian, C. Mayer, N. Chawla, J. Llorca, A. Misra, J.K. Baldwin, J.M. Molina-Aldareguia, Effect of layer thickness on the high temperature mechanical properties of Al/SiC nanolaminates, *Thin Solid Films.* 571 (2014) 260–267. doi:10.1016/j.tsf.2014.06.022.
 - [103] W.M. Mook, R. Raghavan, J.K. Baldwin, D. Frey, J. Michler, N.A. Mara, A. Misra, Indentation fracture response of al–TiN Nanolaminates, *Mater. Res. Lett.* 1 (2013) 102–108. doi:10.1080/21663831.2013.783515.
 - [104] J. Li, Y. Shacham-Diamand, J.W. Mayer, Copper deposition and thermal stability issues in copper-based metallization for ULSI technology, *Mater. Sci. Reports.* 9 (1992) 1–51. doi:10.1016/0920-2307(92)90011-O.
 - [105] J.M. Wheeler, J. Michler, Invited Article: Indenter materials for high temperature nanoindentation, *Rev. Sci. Instrum.* 84 (2013) 101301. doi:10.1063/1.4824710.
 - [106] R. Rabe, J.M. Breguet, P. Schwaller, S. Stauss, F.J. Haug, J. Patscheider, J. Michler, Observation of fracture and plastic deformation during indentation and scratching inside the scanning electron microscope, *Thin Solid Films.* 469–470 (2004) 206–213. doi:10.1016/j.tsf.2004.08.096.
 - [107] A. Misra, R.G. Hoagland, Effects of elevated temperature annealing on the structure and hardness of copper/niobium nanolayered films, *J. Mater. Res.* 20 (2005) 2046–2054. doi:10.1557/JMR.2005.0250.
 - [108] B. Pécz, N. Frangis, S. Logothetidis, I. Alexandrou, P.B. Barna, J. Stoemenos, Electron microscopy characterization of TiN films on Si, grown by d.c. reactive magnetron sputtering, *Thin Solid Films.* 268 (1995) 57–63. doi:10.1016/0040-6090(95)06692-6.
 - [109] H. Zhang, B.E. Schuster, Q. Wei, K.T. Ramesh, The design of accurate micro-compression experiments, *Scr. Mater.* 54 (2006) 181–186. doi:10.1016/j.scriptamat.2005.06.043.
 - [110] R. Banerjee, R. Chandra, P. Ayyub, Influence of the sputtering gas on the preferred orientation of nanocrystalline titanium nitride thin films, *Thin Solid Films.* 405 (2002) 64–72. doi:10.1016/S0040-6090(01)01705-9.
 - [111] S. Bhowmick, Z.H. Xie, M. Hoffman, V. Jayaram, S.K. Biswas, Nature of contact deformation of TiN films on steel, *J. Mater. Res.* 19 (2004) 2616–2624. doi:10.1557/JMR.2004.0339.
 - [112] S. Math, S.J. Suresha, V. Jayaram, S.K. Biswas, Indentation of a hard film on a compliant substrate: film fracture mechanisms to accommodate substrate plasticity, *J. Mater. Sci.* 41 (2006) 7830–7837. doi:10.1007/s10853-006-0455-3.
 - [113] A. Misra, M. Verdier, Y.C. Lu, H. Kung, T.E. Mitchell, M. Nastasi, J.D. Embury, Structure and mechanical properties of Cu-X (X = Nb,Cr,Ni) nanolayered composites, *Scr. Mater.* 39 (1998) 555–560. doi:10.1016/S1359-6462(98)00196-1.
 - [114] H. Huang, F. Spaepen, Tensile testing of free-standing Cu, Ag and Al thin films and Ag/Cu multilayers, *Acta Mater.* 48 (2000) 3261–3269. doi:10.1016/S1359-6454(00)00128-2.

- [115] V.Y. Gertsman, M. Hoffmann, H. Gleiter, R. Birringer, The study of grain size dependence of yield stress of copper for a wide grain size range, *Acta Metall. Mater.* 42 (1994) 3539–3544. doi:10.1016/0956-7151(94)90486-3.
- [116] W.D. Nix, Mechanical properties of thin films, *Metall. Trans. A.* 20 (1989) 2217–2245. doi:10.1007/BF02666659.
- [117] J. Horváth, R. Birringer, H. Gleiter, Diffusion in nanocrystalline material, *Solid State Commun.* 62 (1987) 319–322. doi:10.1016/0038-1098(87)90989-6.
- [118] R. Raghavan, J.M. Wheeler, D. Esqué-de los Ojos, K. Thomas, E. Almandoz, G.G. Fuentes, J. Michler, Mechanical behavior of Cu/TiN multilayers at ambient and elevated temperatures: Stress-assisted diffusion of Cu, *Mater. Sci. Eng. A.* 620 (2014) 375–382. doi:10.1016/j.msea.2014.10.023.
- [119] B. Ham, X. Zhang, High strength Mg/Nb nanolayer composites, *Mater. Sci. Eng. A.* 528 (2011) 2028–2033. doi:10.1016/j.msea.2010.10.101.
- [120] G.B. Thompson, R. Banerjee, H.L. Fraser, Predicting pseudomorphic phases in multilayers: Hexagonal-closed-packed Nb in Nb/Zr, *Appl. Phys. Lett.* 84 (2004) 1082–1084. doi:10.1063/1.1647687.
- [121] W.P. Lowe, T.H. Geballe, NbZr multilayers. I. Structure and superconductivity, *Phys. Rev. B.* 29 (1984) 4961–4968. doi:10.1103/PhysRevB.29.4961.
- [122] D. Van Heerden, D. Josell, D. Shechtman, The formation of f.c.c. Titanium in titanium-aluminum multilayers, *Acta Mater.* 44 (1996) 297–306. doi:10.1016/1359-6454(95)00159-5.
- [123] R. Ahuja, H.L. Fraser, Microstructural transitions in Titanium-Aluminum thin film multilayers, *J. Electron. Mater.* 23 (1994) 1027–1034. doi:10.1007/BF02650371.
- [124] S.A. Dregia, R. Banerjee, H.L. Fraser, Polymorphic phase stability in thin multilayers, *Scr. Mater.* 39 (1998) 217–223. doi:10.1016/S1359-6462(98)00144-4.
- [125] J.C. Li, W. Liu, Q. Jiang, Bi-phase transition diagrams of metallic thin multilayers, *Acta Mater.* 53 (2005) 1067–1071. doi:10.1016/j.actamat.2004.11.004.
- [126] J.M. Wheeler, P. Brodard, J. Michler, Elevated temperature, *in situ* indentation with calibrated contact temperatures, *Philos. Mag.* 92 (2012) 3128–3141. doi:10.1080/14786435.2012.674647.
- [127] J.S. Carpenter, A. Misra, M.D. Uchic, P.M. Anderson, Strain rate sensitivity and activation volume of Cu/Ni metallic multilayer thin films measured via micropillar compression, *Appl. Phys. Lett.* 101 (2012). doi:10.1063/1.4739521.
- [128] I.K. Schuller, New Class of Layered Materials, *Phys. Rev. Lett.* 44 (1980) 1597–1600. doi:10.1103/PhysRevLett.44.1597.
- [129] M. Callisti, T. Polcar, Combined size and texture-dependent deformation and strengthening mechanisms in Zr/Nb nano-multilayers, *Acta Mater.* 124 (2017) 247–260. doi:10.1016/j.actamat.2016.11.007.
- [130] E.E. Fullerton, I.K. Schuller, H. Vanderstraeten, Y. Bruynseraede, Structural refinement of superlattices from x-ray diffraction, *Phys. Rev. B.* 45 (1992) 9292–9310. doi:10.1103/PhysRevB.45.9292.
- [131] A.H. Eltoukhy, J.E. Greene, Compositionally modulated sputtered InSb/GaSb superlattices: Crystal growth and interlayer diffusion, *J. Appl. Phys.* 50 (1979) 505–517. doi:10.1063/1.325643.
- [132] Q. Yang, C. He, L.R. Zhao, J.P. Immarigeon, Preferred orientation and hardness enhancement of TiN/CrN superlattice coatings deposited by reactive magnetron sputtering, *Scr. Mater.* 46 (2002) 293–297. doi:10.1016/S1359-6462(01)01241-6.
- [133] J. Wehrs, M.J. Deckarm, J.M. Wheeler, X. Maeder, R. Birringer, S. Mischler, J. Michler, Elevated temperature, micro-compression transient plasticity tests on nanocrystalline Palladium-Gold: Probing activation parameters at the lower limit of crystallinity, *Acta Mater.* 129 (2017) 124–137. doi:10.1016/j.actamat.2017.02.045.
- [134] E. Hart, Theory of the tensile test, *Acta Metall.* 15 (1967) 351–355. doi:10.1016/0001-

6160(67)90211-8.

- [135] Q. Wei, S. Cheng, K.T. Ramesh, E. Ma, Effect of nanocrystalline and ultrafine grain sizes on the strain rate sensitivity and activation volume: Fcc versus bcc metals, *Mater. Sci. Eng. A*. 381 (2004) 71–79. doi:10.1016/j.msea.2004.03.064.
- [136] A. Kumar, I.J. Beyerlein, J. Wang, First-principles study of the structure of Mg/Nb multilayers, *Appl. Phys. Lett.* 105 (2014). doi:10.1063/1.4893700.
- [137] H.J. Frost, M.F. Ashby, *Deformation-mechanism maps: the plasticity and creep of metals and ceramics*, Pergamon Press, 1982. <https://books.google.ch/books?id=s9BRAAAAMAAJ>.
- [138] A.R. Junkaew A, Ham B, Zhang X, Talapatra A, A. Junkaew, B. Ham, X. Zhang, Stabilization of bcc Mg in Thin Films at Ambient Pressure: Experimental Evidence and ab initio Calculations, *Mater. Res. Lett.* 1 (2013) 161–167. doi:10.1080/21663831.2013.804218.
- [139] S. Pathak, N. Velisavljevic, J.K. Baldwin, M. Jain, S. Zheng, N.A. Mara, I.J. Beyerlein, Strong, Ductile, and Thermally Stable bcc-Mg Nanolaminates, *Sci. Rep.* 7 (2017) 8264. doi:10.1038/s41598-017-08302-5.
- [140] Z. Wu, W.A. Curtin, The origins of high hardening and low ductility in magnesium, *Nature*. 526 (2015) 62–67. doi:10.1038/nature15364.
- [141] A. Galiyev, O. Sitdikov, R. Kaibyshev, Deformation Behavior and Controlling Mechanisms for Plastic Flow of Magnesium and Magnesium Alloy, *Mater. Trans.* 44 (2003) 426–435. doi:10.2320/matertrans.44.426.
- [142] M.A. Adams, A.C. Roberts, R.E. Smallman, Yield and fracture in polycrystalline niobium, *Acta Metall.* 8 (1960) 328–337. doi:10.1016/0001-6160(60)90118-8.
- [143] M.L. Grossbeck, H.K. Birnbaum, Low temperature hydrogen embrittlement of niobium II—Microscopic observations, *Acta Metall.* 25 (1977) 135–147. doi:10.1016/0001-6160(77)90117-1.
- [144] G. Mohanty, J.M. Wheeler, R. Raghavan, J. Wehrs, M. Hasegawa, S. Mischler, L. Philippe, J. Michler, Elevated temperature, strain rate jump microcompression of nanocrystalline nickel, *Philos. Mag.* 95 (2014) 1878–1895. doi:10.1080/14786435.2014.951709.
- [145] P. Shewmon, F. Rhines, Rate of self-diffusion in polycrystalline magnesium, *J. Met.* (1954). <http://www.osti.gov/scitech/biblio/4408928>.
- [146] H.-K. Kim, W.-J. Kim, Creep behavior of AZ31 magnesium alloy in low temperature range between 423 K and 473 K, *J. Mater. Sci.* 42 (2007) 6171–6176. doi:10.1007/s10853-006-1162-9.
- [147] L.W. Yang, C. Mayer, N. Chawla, J. Llorca, J.M. Molina-Aldareguía, Deformation mechanisms of ultra-thin Al layers in Al/SiC nanolaminates as a function of thickness and temperature, *Philos. Mag.* 96 (2016) 3336–3355. doi:10.1080/14786435.2016.1219075.
- [148] X.D. Jiao, Mechanical Properties of Low Density Alloys at Cryogenic Temperatures, *AIP Conf. Proc.* 824 (2006) 69–76. doi:10.1063/1.2192335.
- [149] T. Al-Samman, G. Gottstein, Dynamic recrystallization during high temperature deformation of magnesium, *Mater. Sci. Eng. A*. 490 (2008) 411–420. doi:10.1016/J.MSEA.2008.02.004.
- [150] G. Taylor, Thermally-activated deformation of BCC metals and alloys, *Prog. Mater. Sci.* 36 (1992) 29–61. doi:10.1016/0079-6425(92)90004-Q.
- [151] A. Azushima, R. Kopp, A. Korhonen, D.Y. Yang, F. Micari, G.D. Lahoti, P. Groche, J. Yanagimoto, N. Tsuji, A. Rosochowski, A. Yanagida, Severe plastic deformation (SPD) processes for metals, *CIRP Ann.* 57 (2008) 716–735. doi:10.1016/J.CIRP.2008.09.005.
- [152] M. Gupta, F.A. Mohamed, E.J. Lavernia, Heat transfer mechanisms and their effects on microstructure during spray atomization and codeposition of metal matrix composites, *Mater. Sci. Eng. A*. 144 (1991) 99–110. doi:10.1016/0921-5093(91)90214-8.
- [153] S.F. Hassan, M. Gupta, Enhancing physical and mechanical properties of Mg using nanosized Al₂O₃ particulates as reinforcement, *Metall. Mater. Trans. A*. 36 (2005) 2253–2258. doi:10.1007/s11661-005-0344-4.

- [154] S. Yamamuro, K. Sumiyama, K. Suzuki, Monodispersed Cr cluster formation by plasma-gas-condensation, *J. Appl. Phys.* 85 (1998) 483–489. doi:10.1063/1.369476.
- [155] V.K. LaMer, R.H. Dinegar, Theory, Production and Mechanism of Formation of Monodispersed Hydrosols, *J. Am. Chem. Soc.* 72 (1950) 4847–4854. doi:10.1021/ja01167a001.
- [156] E. Pérez-Tijerina, M. Gracia Pinilla, S. Mejía-Rosales, U. Ortiz-Méndez, A. Torres, M. José-Yacamán, Highly size-controlled synthesis of Au/Pd nanoparticles by inert-gas condensation, *Faraday Discuss.* 138 (2008) 353–362. doi:10.1039/b705913m.
- [157] D.T. Read, R.R. Keller, N. Barbosa, R. Geiss, Nanoindentation round robin on thin film copper on silicon, *Metall. Mater. Trans. A Phys. Metall. Mater. Sci.* 38 A (2007) 2242–2248. doi:10.1007/s11661-007-9177-7.
- [158] Z.H. Cao, P.Y. Li, H.M. Lu, Y.L. Huang, X.K. Meng, Thickness and grain size dependent mechanical properties of Cu films studied by nanoindentation tests, *J. Phys. D: Appl. Phys.* 42 (2009). doi:10.1088/0022-3727/42/6/065405.
- [159] T.-H. Fang, W.-J. Chang, Nanomechanical properties of copper thin films on different substrates using the nanoindentation technique, *Microelectron. Eng.* 65 (2003) 231–238. doi:10.1016/S0167-9317(02)00885-7.
- [160] A.M. Hodge, Y.M. Wang, T.W. Barbee, Large-scale production of nano-twinned, ultrafine-grained copper, *Mater. Sci. Eng. A.* 429 (2006) 272–276. doi:10.1016/j.msea.2006.05.109.
- [161] S.D. Dahlgren, Columnar grains and twins in high-purity sputter-deposited copper, *J. Vac. Sci. Technol.* 11 (1974) 832. doi:10.1116/1.1312763.
- [162] J.Y. Zhang, G. Liu, J. Sun, Comparisons between homogeneous boundaries and heterophase interfaces in plastic deformation: Nanostructured Cu micropillars vs. nanolayered Cu-based micropillars, *Acta Mater.* 61 (2013) 6868–6881. doi:10.1016/j.actamat.2013.07.065.
- [163] X. Chu, S.A. Barnett, Model of superlattice yield stress and hardness enhancements, *J. Appl. Phys.* 77 (1995) 4403–4411. doi:10.1063/1.359467.
- [164] P.B. Mirkarimi, S.A. Barnett, K.M. Hubbard, T.R. Jervis, L. Hultman, Structure and mechanical properties of epitaxial TiN/V_{0.3}Nb_{0.7}N(100) superlattices, *J. Mater. Res.* 9 (1994) 1456–1467. doi:10.1557/JMR.1994.1456.
- [165] M.D. Gram, J.S. Carpenter, P.M. Anderson, An indentation-based method to determine constituent strengths within nanolayered composites, *Acta Mater.* 92 (2015) 255–264. doi:10.1016/j.actamat.2015.04.002.
- [166] M.D. Gram, J.S. Carpenter, E.A. Payzant, A. Misra, P.M. Anderson, X-Ray Diffraction Studies of Forward and Reverse Plastic Flow in Nanoscale Layers During Thermal Cycling, *Mater. Res. Lett.* 1 (2013) 233–243. doi:10.1080/21663831.2013.843602.
- [167] R. Hahn, M. Bartosik, R. Soler, C. Kirchlechner, G. Dehm, P.H. Mayrhofer, Superlattice effect for enhanced fracture toughness of hard coatings, *Scr. Mater.* 124 (2016) 67–70. doi:10.1016/J.SCRIPMAT.2016.06.030.
- [168] J.M. Molina-aldareguia, S.J. Lloyd, M. Odén, T. Joelsson, L. Hultman, W.J. Clegg, Deformation structures under indentations in TiN/NbN single-crystal multilayers deposited by magnetron sputtering at different bombarding ion energies, *Philos. Mag. A.* 82 (2002) 1983–1992. doi:10.1080/01418610208235710.
- [169] N. Verma, V. Jayaram, Role of interface curvature on stress distribution under indentation for ZrN/Zr multilayer coating, *Thin Solid Films.* 571 (2014) 283–289. doi:10.1016/J.TSF.2014.06.001.
- [170] S. Lotfian, J.M. Molina-Aldareguia, K.E. Yazzie, J. Llorca, N. Chawla, High-temperature nanoindentation behavior of Al/SiC multilayers, *Philos. Mag. Lett.* 92 (2012) 362–367. doi:10.1080/09500839.2012.674220.
- [171] L.W. Yang, C. Mayer, N. Li, J.K. Baldwin, N.A. Mara, N. Chawla, J.M. Molina-Aldareguia, J. Llorca, Mechanical properties of metal-ceramic nanolaminates: Effect of constraint and temperature, *Acta Mater.* 142 (2018) 37–48. doi:10.1016/J.ACTAMAT.2017.09.042.

- [172] J. Snel, M.A. Monclús, M. Castillo-Rodríguez, N. Mara, I.J. Beyerlein, J. Llorca, J.M. Molina-Aldareguía, Deformation Mechanism Map of Cu/Nb Nanoscale Metallic Multilayers as a Function of Temperature and Layer Thickness, *JOM*. 69 (2017) 2214–2226. doi:10.1007/s11837-017-2533-1.
- [173] R. Raghavan, J.M. Wheeler, T.P. Harzer, V. Chawla, S. Djaziri, K. Thomas, B. Philippi, C. Kirchlechner, B.N. Jaya, J. Wehrs, J. Michler, G. Dehm, Transition from shear to stress-assisted diffusion of copper-chromium nanolayered thin films at elevated temperatures, *Acta Mater.* 100 (2015) 73–80. doi:10.1016/j.actamat.2015.08.016.
- [174] J.M. Wheeler, R. Raghavan, V. Chawla, J. Zechner, I. Utke, J. Michler, Failure mechanisms in metal-metal nanolaminates at elevated temperatures: Microcompression of Cu-W multilayers, *Scr. Mater.* 98 (2015) 28–31. doi:10.1016/j.scriptamat.2014.11.007.
- [175] X.Y. Zhu, X.J. Liu, F. Zeng, F. Pan, Room temperature nanoindentation creep of nanoscale Ag/Fe multilayers, *Mater. Lett.* 64 (2010) 53–56. doi:10.1016/J.MATLET.2009.10.003.
- [176] S.P. Wen, R.L. Zong, F. Zeng, Y. Gao, F. Pan, Nanoindentation investigation of the mechanical behaviors of nanoscale Ag/Cu multilayers, *J. Mater. Res.* 22 (2007) 3423–3431. doi:10.1557/JMR.2007.0423.
- [177] N.A. Mara, T. Tamayo, A. V. Sergueeva, X. Zhang, A. Misra, A.K. Mukherjee, The effects of decreasing layer thickness on the high temperature mechanical behavior of Cu / Nb nanoscale multilayers, *Thin Solid Films*. 515 (2007) 3241–3245. doi:10.1016/j.tsf.2006.01.036.
- [178] A.C. Lewis, D. Van Heerden, D. Josell, T.P. Weihs, Creep deformation in multilayered and microlaminate materials, *JOM*. 55 (2003) 34–37. doi:10.1007/s11837-003-0191-y.

Curriculum Vitae

Personal Information

Name: Keith Bennett Thomas
Gender: male
Date of birth: 12 August 1988
City of birth: Albuquerque, New Mexico, USA
Nationality: American
E-mail: trickyfish75@yahoo.com

Education

July 2013 – August 2018	Eidgenössische Technische Hochschule Zürich (ETHZ) Zürich, Switzerland PhD in Materials Science
October 2010 – December 2012	Friedrich-Alexander Universität Erlangen-Nürnberg (FAU) Erlangen, Germany Master's Degree in Materials Science
August 2006 – May 2010	New Mexico University of Mining and Technology (NMT) Socorro, United States of America Bachelor's Degree in Mechanical Engineering

Publications and Presentations

Peer-reviewed journal publications

K. Thomas, R. Schoeppner, B. Könnnyü, M. Polyakov, L. Petho, R. Spolenak, J. Michler, Preservation of nanocrystalline strengthening in copper films at elevated temperatures through the incorporation of tungsten nanoparticles, (undergoing preparation for submission).

K. Thomas, G. Mohanty, J. Wehrs, A.A. Taylor, S. Pathak, D. Casari, J. Schwiedrzik, N. Mara, R. Spolenak, J. Michler, Elevated and cryogenic temperature micropillar compression of magnesium-niobium multi-layer films, *Journal of Materials Science*. (under review).

G.B.J. Cadot, **K. Thomas**, J.P. Best, A.A. Taylor, J. Michler, D.A. Axinte, J. Billingham, Investigation of the microstructure change due to phase transition in nanosecond pulsed laser processing of diamond, *Carbon* N. Y. 127 (2018) 349–365. doi:10.1016/j.carbon.2017.10.030.

K. Thomas, A.A. Taylor, R. Raghavan, V. Chawla, R. Spolenak, J. Michler, Microstructure and mechanical properties of metastable solid solution copper-tungsten films, *Thin Solid Films*. 642 (2017) 82–89. doi:10.1016/j.tsf.2017.09.007.

S.A. Rebegea, **K. Thomas**, V. Chawla, J. Michler, M.C. Kong, Laser ablation of a Cu–Al–Ni combinatorial thin film library: analysis of crater morphology and geometry, *Appl. Phys. A Mater. Sci. Process.* 122 (2016) 1–9. doi:10.1007/s00339-016-0608-4.

R. Raghavan, J.M. Wheeler, T.P. Harzer, V. Chawla, S. Djaziri, **K. Thomas**, B. Philippi, C. Kirchlechner, B.N. Jaya, J. Wehrs, J. Michler, G. Dehm, Transition from shear to stress-assisted diffusion of copper-chromium nanolayered thin films at elevated temperatures, *Acta Mater.* 100 (2015) 73–80. doi:10.1016/j.actamat.2015.08.016.

S.K.P. Veerapandian, S. Beuer, M. Rumler, F. Stumpf, **K. Thomas**, L. Pillatsch, J. Michler, L. Frey, M. Rommel, Comparison of silicon and 4H silicon carbide patterning using focused ion beams, *Nucl. Instruments Methods Phys. Res. Sect. B Beam Interact. with Mater. Atoms.* 365 (2015) 44–49. doi:10.1016/j.nimb.2015.07.079.

R. Raghavan, J.M. Wheeler, D. Esqué-de los Ojos, **K. Thomas**, E. Almandoz, G.G. Fuentes, J. Michler, Mechanical behavior of Cu/TiN multilayers at ambient and elevated temperatures: Stress-assisted diffusion of Cu, *Mater. Sci. Eng. A*. 620 (2014) 375–382. doi:10.1016/j.msea.2014.10.023.

Oral presentations

14th November 2016 - 2016 Empa PhD Symposium - *Thin Film Mechanics using Combinatorial Materials Science* – Dübendorf, Switzerland

Poster presentations

ECI Conference - Nanomechanical Testing in Materials Research and Development V – October 4-9, 2015 - Albufeira, Portugal - *Diffusion-based deformation in high temperature micropillar compression of Mg-Nb multilayers*

ECI Conference - Nano- and Micromechanical Testing in Materials Research and Development IV – Olhão, Portugal – October 7-11, 2013 – *Compositional and Thickness Gradients in Sputtered Metallic Films*